In-situ Analysis of Nanoscale Deformation Mechanism in Mutable Collagenous Tissue

Jingyi Mo

A thesis submitted for the degree of Doctor of Philosophy

School of Engineering and Materials Science

Queen Mary University of London

September 2017

Declaration

I, Jingyi Mo, confirm that the research included within this thesis is my own work or that where it has been carried out in collaboration with, or supported by others, that this is duly acknowledged below and my contribution indicated. Previously published material is also acknowledged below.

I attest that I have exercised reasonable care to ensure that the work is original, and does not to the best of my knowledge break any UK law, infringe any third party's copyright or other Intellectual Property Right, or contain any confidential material.

I accept that the College has the right to use plagiarism detection software to check the electronic version of the thesis.

I confirm that this thesis has not been previously submitted for the award of a degree by this or any other university.

Signature:

Date:

Abstract

Echinoderms, for example sea cucumber, contain a unique collagenous tissue, with special biomechanical properties, which could near-instantly change their mechanical state (going from stiff to soft, and vice versa, in less than a second). However, the structure-function relation has so far not been exploited. Understanding how the material design of mutable collagenous tissue (MCT) enables this remarkable dynamical mechanical behaviour will help enable development of new biomaterials with adaptable mechanical properties.

Currently, it is hypothesised that MCT can rapidly form crosslinks between the collagen fibrils and stiffen the interfibrillar matrix under neural control, but this had never been shown directly. In this thesis, we carried out an experimental study of quantifying how the interfibrillar matrix response to stimuli agents, to generate active forces and change conformation using a synchrotron *in situ* X-ray nanomechanical imaging method.

By the uncovering of the mechanisms of active force generation, a valuable guideline, which could be applied in bioinspired constructs that response to external stimuli, can be obtained.

Acknowledgements

First and foremost, I would like to express my sincere gratitude to my primary supervisor Dr. Himadri Gupta for his support and encouragement throughout the four-year period of my PhD. By giving me chance to pursue and conduct various projects, I have learned immense knowledge on multiple scientific areas from him. I couldn't have achieved what I have been able to do without his help. I would also like to thank my secondary supervisor Professor Wen Wang for his insightful suggestions and ideas. I am truly grateful.

I would also like to thank the School of Engineering and Materials Science (SEMS) at Queen Mary University of London (QMUL) and the Chinese Scholarship Council (CSC), without their financial support, I would never have been able to come to London pursuing a Ph.D.

All the beamline scientists from I22 Diamond Light Source (I22, DLS, UK), ID02 European Synchrotron Radiation Facility (ID02, ESRF, France) and μ-Spot BEESY II (Berlin, Germany) are gratefully acknowledged. I could not have completed the project without the continuous assistance from you. Particularly, I would like to thank Dr. Sylvain Prevost at ESRF for his great efforts in instrumental preparation and data analysis. My gratitude is also extended to Professor Maurice Elphick, Dr. Ettore Barbieri and Dr. Nick Terrill for all the inputs in every stage of my research.

I must also acknowledge the technicians at the SEMS workshop – Dougie Thomson, Dennis Ife and Vince Ford – who offered help in designing and manufacturing the experimental device, and Jun Ma

who has been extremely helpful in developing the LabView-control programmes.

The work in this thesis is also motivated and inspired by our research group, including Li, Andrew, Sheetal, Liisa, and Yanhong. Without their precious help, especially during the experiment sessions in Synchrotron, it would be impossible for me to conduct this research.

Last, but certainly not least, I must give tremendous and deep thanks to my family. They have always been there whenever I needed support and company. My achievement means nothing without them.

I dedicate this thesis to my parents (Ping and Guangnan) and my beloved pet (Xiaobai) for their unstinting support and unconditional love.

I love you all dearly.

Publications, Poster presentations

Following papers were published or presented at scientific meetings based the work presented in this thesis:

Publications

- Mo, Jingyi, Sylvain F. Prévost, Liisa M. Blowes, Michaela Egertová, Nicholas J. Terrill, Wen Wang, Maurice R. Elphick, and Himadri S. Gupta. "*Interfibrillar stiffening of echinoderm mutable collagenous tissue demonstrated at the nanoscale*." Proceedings of the National Academy of Sciences (2016): 201609341.

- Mo, Jingyi, Sylvain F. Prévost, Liisa M. Blowes, Michaela Egertová, Nicholas J. Terrill, Wen Wang, Maurice R. Elphick, and Himadri S. Gupta. "*An experimental study of the ability to change viscoelastic state in MCT*." 2017 (In preparation).

- Mo, Jingyi, Nicholas J. Terrill, Wen Wang, Maurice R. Elphick, and Himadri S. Gupta. " *In-situ customized imaging of active force generation mechanisms using customized microinjection and microfluidics device in situ imaging active force generation in MCT*." 2017 (In preparation).

Poster presentations

- Mo, Jingyi et al. *Adaptable Mechanics of Mutable Collagenous Tissue at the Nanoscale*. Poster presented at the SEMS Research Graduate Poster Show/Industrial Liaison Forum. 14/November/2014, London, UK

- Mo, Jingyi et al. *Active force generation in mutable collagenous tissue*. Poster presented at Diamond Synchrotron Radiation User Meeting 2015, 2-3/September/2015, Oxfordshire, UK

- Mo, Jingyi et al. *Echinoderm connective tissue as a dynamic mechanically responsive biomaterial: insights from synchrotron small-angle X-ray scattering with in situ tensile testing*. Poster presented at the 10th World Biomaterials Congress, 17-22/May/2016, Montreal, Canada.

- Mo, Jingyi et al. *Echinoderm connective tissue as a Natural Dynamic Biomaterial*. Poster presented at the 3rd London Echinoderm Network, 6/ September/2016, London, UK

Table of Contents

List of Abbreviations

SEM	Scanning electron microscopy
TEM	Transmission electron microscopy
SAXS	Small Angle X-ray Scattering
WAXD	Wide Angle X-ray diffraction
FT-IR	Fourier-transform infrared spectroscopy
ASW	Artificial sea water
KASW	Artificial sea water with high K^+ concentration
CaF-ASW	Ca^{2+} -free artificial sea water
SURFs	Sea urchin fibrillar domains
NSF	Novel stiffening factor
MCT	Mutable collagenous tissue
ECM	Extracellular matrix
Gly	Glycine
GAGs	Glycosaminoglycans
PGs	Proteoglycans
FACIT	Fibril-associated interrupted triple helices
MMP	Matrix metalloproteinases
TIMP	Tissue inhibitor of metalloproteinase
Ach	Acetylcholine
JLC	Juxtaligamental cell
3D	Three dimensional
2D	Two dimensional

List of symbols

ε	Strain
σ	Stress
$\boldsymbol{q}$	Scattering vector
2θ	Scattering angle
λ	Wavelength
ε_T	Tissue strain
ε_F	Fibril strain
E_T	Tangent modulus
Φ_1	Fibril volume fraction
ρ_1	Fibril aspect ratio
E_F	Fibril elastic modulus
E_{IF}	Interfibrillar modulus
G_{IF}	Shear modulus of the interfibrillar matrix
E_{IF}	Tensile modulus of the interfibrillar matrix
ρ	Aspect ratio
F	Overlap/D ratio
σ_T	Tissue stress
τ_1	Short time scale parameter
τ_2	Long time scale parameter
σ_M	Load bearing by matrix

List of Figures

Chapter 1 : Motivation

In materials engineering, the interest in stimuli-responsive and mechano-adaptive polymers and composites, where the mechanical properties can be changed via exposing to different physiological conditions, in an active and long-running focus, especially in the context of biomimicry and biomedical material, including controlled-released drug delivery, biosensors, scaffolds ("smart hydrogels") for tissue engineering and smart implants [1-5]. While great effort has been dedicated to investigating the design and implementation of stimuli-sensitive systems, most of the current synthetic systems are commonly triggered by non-biologically relevant stimuli which cannot always be easily achieved *in-vivo*, for example pH, voltage and temperature [6-8]. Therefore, recently, the approach of biomimicking where one imitates the mechanisms present in natural systems, giving polymers and composites adaptable functions through incorporation of bioactive molecules (proteins and peptides), are becoming increasingly popular and prevalent [9, 10]. In this regard, we consider the material design of a remarkable natural nanocomposite, a special collagenous tissue from the sea cucumber dermis, both to understand it from a structural mechanical point of view as well for (longer-term) understanding how to use it as a template of new stimuli-responsive "intelligent" biomedical materials.

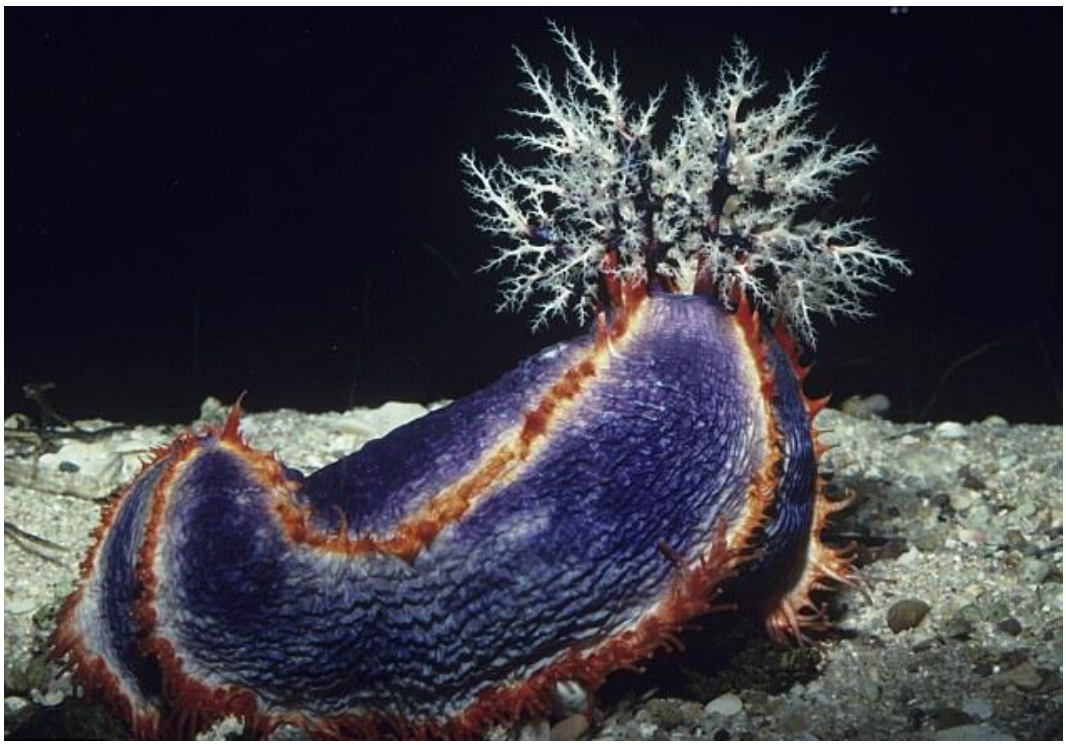

Figure 1.1 *Image of sea cucumber with tentacles extended (species: Pseudocolochirus) (from http://www.gettyimages.co.uk).*

Sea cucumber (**Figure 1.1**) is a type of echinoderm containing a unique collagenous tissue with the remarkable capacity of changing its mechanical properties (going from soft ↔ stiff nearly instantly [11]), which gives it the name **mutable collagenous tissu**e (MCT) [11, 12]. MCT can be found in other echinoderms, for example, starfish, sea urchin and sea lily [11]. Because of its ability to change its mechanical state, MCT helps echinoderms to move, maintain posture or feed on prey. This special mutability endows MCT-based tissues with the ability to work in a manner similar to muscle – despite constituting largely of collagen, and it is the only collagen-based tissue with this remarkable property [13]. Whilst it is believed that neural system plays a role in MCT remarkable mutability by secreting macromolecule and increasing the extent of crosslinks, the precise nanoscale mechanism has not been analysed and investigated directly.

Therefore, in the thesis, we describe and analyse the structure-function relations underpinning the mutability mechanism at the nanoscale.

The gap in the understanding of these structure-function relations of MCT is due to the indirect nature of mechanical and structural methods used to try and understand the mechanisms at the nanoscale. Owing to the length scale (sub-micron and nanometre) at which active forces are generated in MCT, it is difficult to measure and analyse the mechano-active processes directly. Additionally, the conventional high resolution structural methods, for example scanning electron microscopy (SEM), transmission electron microscopy (TEM) and confocal microscopy, are (largely) static (especially at very high resolutions and energies) and not suitable for imaging "live" mechanical processes. Therefore, it is impossible for us to directly image the molecular level stiffening and de-stiffening mechanisms in real time, in response to action of bioactive molecules, using the techniques mentioned above. In this regard, *in situ* small-angle X-ray diffraction (SAXD) combining with mechanical testing can overcome those drawbacks by providing information for the deformation of the fibrillar-level composite in MCT, including fibril strain, interfibrillar spacing and orientation [14-18].

The research objectives for this thesis include:

1) To measure the structural changes of **freeze-thawed MCT** specimen at the molecular and fibrillar level using quasi-static mechanical testing, combining with synchrotron X-ray radiation (**Chapter 5**).
2) To quantify the interfibrillar stiffening mechanism of viable MCT using **quasi-static mechanical testing**, and to model this

mechanism using the composite model of interfibrillar cohesion regulating by crosslinks (**Chapter 6**).

3) To quantify the nanoscale mechanisms of viable MCT **viscoelastic** behaviour, by measuring fibril and interfibrillar sliding during stress relaxation, to model these mechanisms and extract the loads bearing by fibrils and interfibrillar matrix (**Chapter 7**).
4) To quantify the viable MCT nanoscale mechanisms of **force generation**, by measuring fibrillar deformation and the force generating in real-time during chemical-induced stiffening and softening (**Chapter 8**).

Chapter 2 : Structure and Mechanics of Collagen

2.1General introduction of collagenous tissue and their functions

Collagen, sourced from Greek (kolla, means “glue”), is the most abundant protein in both vertebrates (e.g.: mammals) and invertebrates (e.g.: echinoderms). Broadly speaking, it functions like a natural “bio-glue” that keeps the integrity of living bodies. Based on their architecture, mammalian collagenous tissues can be divided into the following groups: (i) loose areolar tissues (such as lining of the blood vessel[19]); (ii) reticular tissue (in lymph nodes, bone marrow and endotenon tissue inside mammalian tendon [20-22]); (iii) fibrous tissues such as tendons and ligaments [20, 23, 24]; and (iv) cartilage and mineralized tissues such as bone and dentin [23]. As a mechanical backbone for nearly every organ in living bodies, collagen is versatile structurally and mechanically, which helps cater for various functional demands. For example, in tendon and ligament, collagen functions like a passive spring that transmits the force from muscles to bones and thus regulates loads during locomotion, providing mechanical stability for living bodies [23]. While in bone, collagen comprises the organic matrix coexisting with the mineral phase, and confers to bones their high toughness and fracture resistance [25-28]. The biomechanical versatility of collagen-containing tissues mainly results from specializations or variations in their complex hierarchical structure [25]. Examples include the plywood structure of mineralized collagenous fibrils in bone, enabling increased fracture crack length and high fracture resistance [28], multidirectional fibre orientation in skin to resist loads in different orientations [29], and formation of layered tubular structures in arteries and veins [30]. A summary overview of these tissues will be provided at the end of this chapter.

We first describe the hierarchical architecture of collagenous tissues in general.

2.2Composition of collagenous tissue

From a compositional viewpoint, collagenous tissues comprise of an extracellular matrix (ECM) – comprising collagen fibrils, water, proteins, and glycosaminoglycans (GAGs)/ proteoglycans – in which cells are embedded [23, 31]. Collagen molecules are triple helical chains (series of [Gly-X-Y]) [32, 33]. Proteoglycans (PGs), presented on the surface of collagen fibrils, are composed by a single polypeptide with one or more glycosaminoglycan (GAG) chain(s) bounded covalently[34]. Fibrous components (density and organization of collagen fibrils) and extrafibrillar component (amount and type of glycoproteins, proteoglycans and associated glycosaminoglycans (GAGs)) both played a fundamental role in alteration of mechanical properties for the whole tissue [23, 35]. For example, tendon contains a high amount of collagen fibril compare to other tissue, these collagen fibrils are arranged in parallel arrays along the loading direction, which will provide maximal resistance to external forces. While in cartilage tissue, high content of GAGs plays

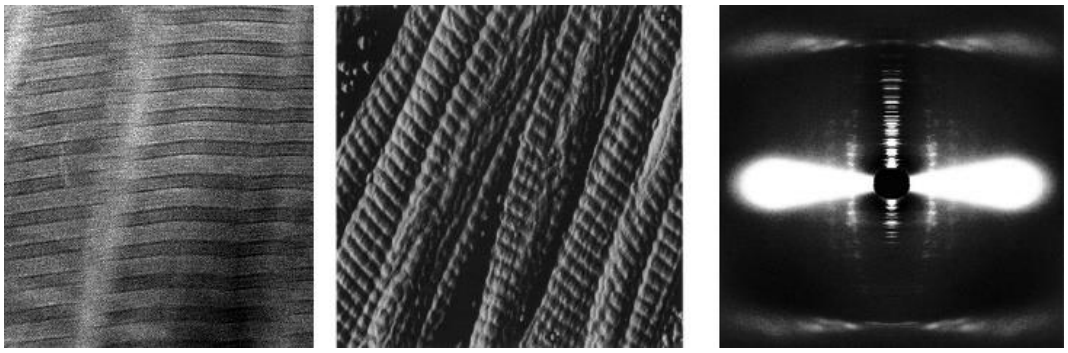

a vital role of hydration enable the capacity of resisting compression.

Figure 2.1 *Different imaging technique used to characterise microstructure of collagen Left: Electron microscopy image of tendon collagen fibrils. The contrast with different grey level shows the*

characteristic D-period of 67 nm; Middle: Atomic force microscopic images of collagen fibrils from the same tissue; Right: X-ray diffraction image from tendon tissue. The series of Bragg's reflection peaks in the centre arise from the axial D-periodicity of 67 nm. Adapted from [23]

2.2.1 Types of collagen

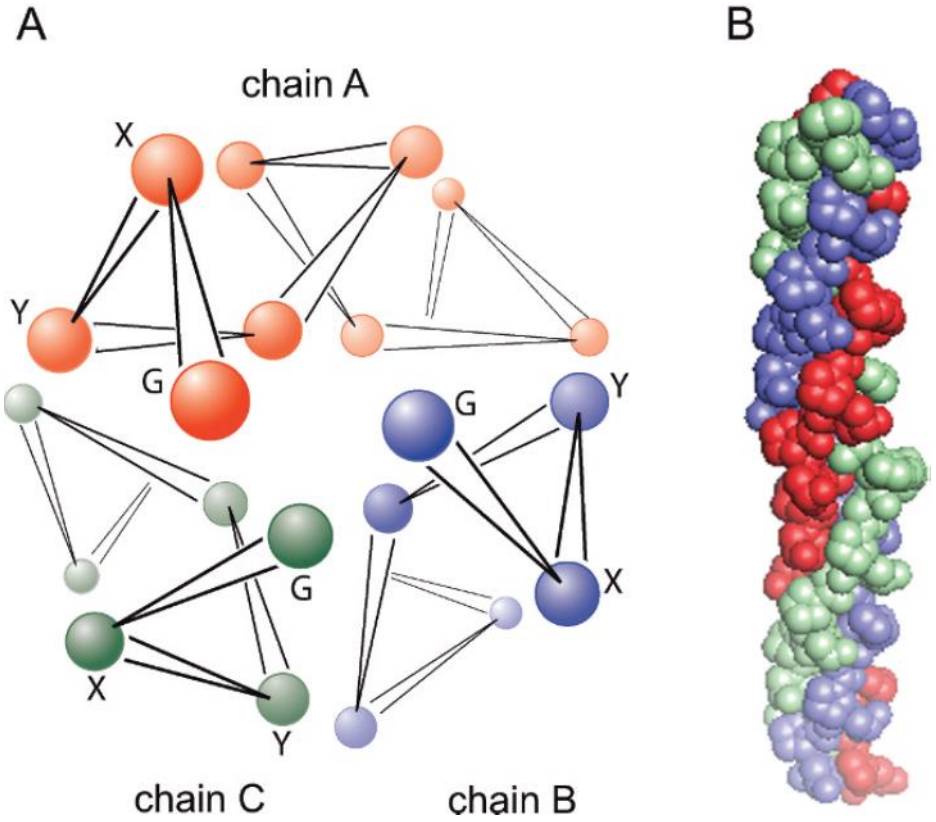

Figure 2.2 Schematic diagram of collagen molecule *(A) Viewed from the top of the three-polypeptide chains A, B and C. (B) Viewed from the side of the three-polypeptide chains, showing the right handed helical twist. Adapted from [23].*

Collagen can be divided according to their structure into fibrillar and non-fibrillar collagen. In vertebrates, there are currently 28 different proteins, some with one or more distinct polypeptide α-chain, which are recognised as collagens [36]. The fibrillar collagens are characterized by possessing striated nanofibrils with a repeating banding period of 64–67 nm (depending on the type of tissue), while the form of non-fibrillar collagen varies a lot, they normally

assembled into a wide array of other supramolecular structures, for example, the sheet like networks and antiparallel arrays [37-39].

Most collagens are of the fibrillar type, and will form fibrils which then bundle into fibres that provide high tensile mechanical strength. Fibrillar collagens (type I, II, III, V, XI, XXIV) have an uninterrupted triple helical domain [2]. The characteristic collagen (types I, II, III, and minor types V and XI) is the main structural protein of skin, tendon, bone, cartilage, and other tissues [7]. Type I collagen has the highest tensile strength (17.1 GPa, cortical bone [40]) and is found in bone, ligament, skin and tendon. Type II is principal structural component of cartilage. Aggregation and association laterally – at multiple scales – between each subunit increases the mechanical properties, and these are usually the result of post-translational modifications like cross-linking.

In the next subsections, we compare – at the molecular level only – the fibrillar and non-fibrillar collagen types. Hierarchical architectures of collagen – from the molecular to macroscopic level – will be covered subsequently.

2.2.2 Fibrillar collagens

The most striking ultrastructural feature of fibrillar collagen is the repeating banded structure of the fibril (the D-period ~ 64-67 nm) for both vertebrates and invertebrates. This periodicity, arising from the axial arrangement of tropocollagen molecules which are staggered by a constant distance of multiples D = 67 nm [23], is the shared commonality for collagen fibrils from both vertebrates and invertebrates. Such arrangement gives rise to low electron density (gap G) and high electron density (overlap O) packing regions inside

the fibril, which will lead to a characteristic striated pattern in scanning electron microscopy images, transmission electron microscopy images and small-angle X-ray diffraction pattern. Details on the structural arrangement are given in the subsequent subsection on the hierarchical architecture of collagenous tissues.

All fibrillar collagen molecules are constituted by three polypeptide α chains, but the nature of these chains varies between types. In vertebrate family, collagen type II and III are homotrimeric, consisting of three identical triple helical molecules: for examples type II is composed by three α1-chain (chain composition [α1(II)]3). Others are heterotypic, consisting of two or three different type of α-chain: for example, the most abundant vertebrate collagen, type I, is formed from one α1(I) and two α2(I) polypeptides [8], which can be written as [α1(I)]2[α2(I)]. Not all collagens from vertebrates have the same composition of α chains as invertebrate collagens. Mammalian collagens shares some similarities with those from invertebrates. For example, echinoid collagen is heterotrimer, including two α1 and one α 2 polypeptides, which is same as those of type I collagens from mammalian tissue.

The classical fibrillar collagen (types I, II, III, V, XI, XXIV, XXVII) displays a characteristic molecular structure that consisting of a long, continuous region account by $[Gly\text{-}X\text{-}Y]_n$ repeat flanked at both N- and C-termini by telo- and pro-peptides [23, 36], with molecular weights of ~100 kDa [41]. Among them, type I-III is a relatively abundant collagen while types V and XI are quantitatively minor [42]. Type I, III and V can be found in many non-cartilage tissues for instance: skin, tendon, bone, cornea and ligament; type II and XI are found in a limited amount in cartilage and cornea respectively.

Collagens types I-III, V, and XI has similar, containing a long triple-helical region with~1000 amino acids or ~330 [Gly-X-Y] sequence / α chain.

In terms of synthesis, collagens are all first synthesized as larger precursors, the procollagens, with large N- and C-termini propeptide regions [23, 36]. Followed by the cleavage of N-propeptides and C-propeptides through specific proteinases, these procollagens will be tailored into collagens. In facilitating the assembling of the triple-helical trimers, each molecule has an axial shift by one-quarter of its length relative to its nearest neighbour, with the resulting form of the banded fibrils with a constant D-periodicity.

The fibril diameter is an important factor mediating the structural properties of collagenous tissue [42]. For example, tendon tissue, constituted by type I collagen, tends to have a fibril with relatively large diameter as it is appropriate for the integrity of the tissue [42], while for corneal tissue the situation is the opposite as the transparent property of cornea results from a thin and highly regular diameter of the fibrils [23, 42].

2.2.3 Nonfibrillar collagens

Non-fibrillar collagen also contains three polypeptide α-chains, with molecular weights more than 100 kDa. However, the triple-helical regions of non-fibrillar collagens are interrupted by non-helical sectors [41], while fibrillar collagen contains a uninterrupted triple helical regions. Unlike fibrillar collagen, containing at least two genetically distinct α-chains, non-fibrillar collagen are constituted by three genetically identical α-chains [41, 43, 44].

Based on the protein structures and the gene organizations, non-fibrillar collagen can be divided into several subfamilies, including fibril-associated interrupted triple helices (FACITs) (IX, XII, XIV, XVI, XIX, XX, XXI and XXII), network forming (IV, VIII and X), trans-membrane collagens (XIII, XVII, XXIII and XXV), endostatins (XV, XVIII) and anchoring fibrils (VII), beaded filament forming (VI) [36, 44-48].

The FACIT collagens, whose α-chains are constituted by numbers of short helical domains and separated by non-helical regimes, are closely related and cross-linked either with fibrillar collagens or basement membranes and tissue joint and were characterised by a short and distinct domain presented near the carboxyl-terminal of the molecule [44, 45]. For example, in cartilage tissue, type IX, the first member ever found of this subfamily, is covalently bonded with collagens II/XI [23]. All FACITs are homotrimers except collagen IX, which was formed by α 1(IX) α 2(IX) α 3(IX) heterotrimer.

As an example, collagen IV is a typical network forming collagen, it forms an interlaced network with three-dimensional structure in basement membranes. Unlike fibril forming collagens, the basement membrane collagens retain the C- terminal. The network is established firstly by head-to-head interactions of two trimers, following by the stabilization of the resultant hexamers via covalent crosslinking [49, 50]. The hexamers finally form extended networks. Type VIII is a main constituent for Descement's membrane, contributing to a transparent cornea [51]. Type X, presenting in the growth plate of cartilage, is proposed to form a network that similar to collagen VIII [52].

Trans-membrane collagens, including collagens XIII, XVII, XXIII, and XXV, have a helical region interrupted by non-helical regions. Collagens XIII, XVII and XXIII are believed to be related to cell adhesion structure, for example, hemidesmosomes, which links ECM to the cytoskeleton [48]. Type XXV have been proposed to be associated with β-amyloidogenesis, leading to the neuronal degeneration in Alzheimer disease [48, 53, 54].

Type XV is found to be closely associating and interlinking with banded collagen fibrils at the basement membranes zone. Proteoglycan core protein in epithelial basement membranes is type XVIII collagen [55-57]. They regulate the cell migrations via releasing endostatins, thereby control the growth of tumour and blood vessels [36].

Collagen VI forms a filamentous network in ECM, creating structural links with cells in most tissue [36, 50]. Its collagen molecules were constituted by a short triple helix, with beaded repeats of 105 nm in length [58]. This type of beaded filament forming collagen functions as organizing matrix components by interacting with extracellular matrix proteins.

2.3Hierarchical structure of collagenous tissues

Particularly for the fibrillar-forming collagens, the tissues they comprise are characterized by multiple levels of complex structural organization, driven by a combination of physicochemical self-assembly and cell-driven assembly. The hierarchical structure of collagen includes many levels, from collagen molecule, fibril to fibre and some higher level like fascicle of tendon tissue (**Figure 2.3**).

In general, collagen molecules forms crosslinks to produce a larger unit which is visible in electron microscopy, the collagen fibril. Bunch of fibrils will then progressively organize into fibres. Group of fibres forms the primary fibre bundle (subfascicle), which then in turn aggregate into secondary fibre bundle (fascicle). The tertiary fibre bundles, composed by fascicle, will finally make up the tendon tissue. At the fascicular level, all the subunits were surrounded by endotenon to keep their mechanical stability and integrity.

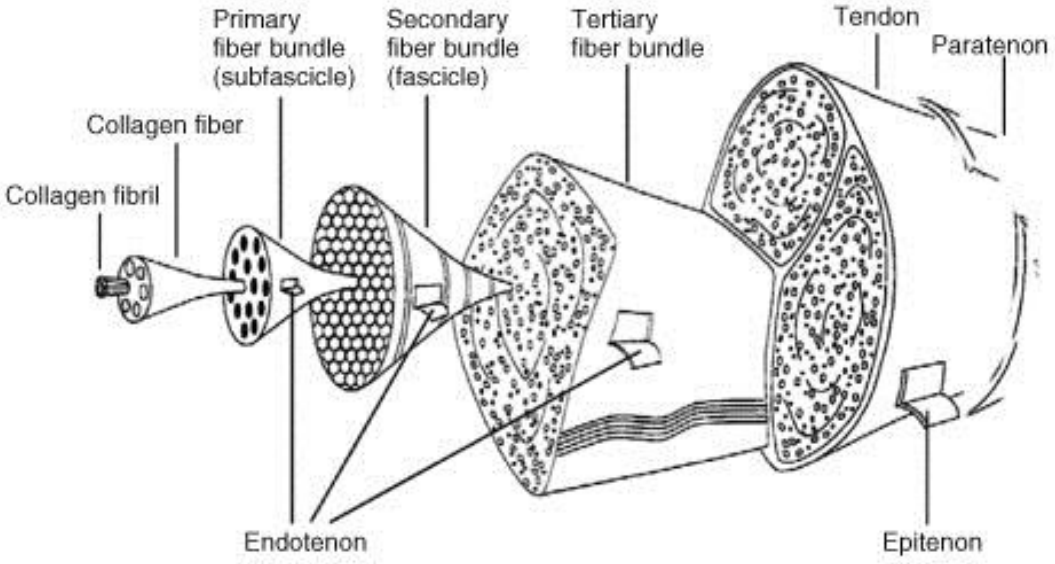

Figure 2.3 Hierarchy of tendon tissue, *showing series of subunits for tendon, from fibril, fibre, fascicle and finally tendon tissue from nano- to macro-scale (note that fibril was assembled from molecule with a staggered manner)[24].*

2.3.1 Collagen molecules

At the molecular level, collagens are composed by three α-helical polypeptide chains, each of which were formed by a series of three amino acid repeating blocks [Gly-X-Y], where the first amino acid is glycine (Gly) and the second is most often proline (Pro) and the third 4-hydroxyproline (4Hyp). The amino acid unit [Gly-X-Y] allows helical collagen α-chains to form a right-handed triple-helical

supercoiled structure (**Figure 2.2**), with the glycine residues (which are small) fitted in the centre of the helix and X and Y residues exposed. These triple helix [Gly-X-Y] were stabilized due to two effects: (1) increased hydrogen bonding between different residues and (2) steric effects coming from the pyrrolidine rings. Such "coil-coiled" forming process leads to a cylindrical rod-like molecule with ~300 nm in length and ~1.5 nm in diameter.

The assembly of procollagen molecule is completed via several steps of post-translational modifications in the endoplasmic reticulum (ER). These steps include the lysyl- and prolyl-hydroxylation and O-linked glycosylation of the individual preprocollagen chains, the formation of trimeric procollagens, disulphide bridges formation, prolyl cis–trans isomerization and folding of the triple helix. The N-propeptides will be cleaved in the trans-Golgi network (TGN) afterwards, following which the pro-collagen molecules from last step will be moved to fibripositors (FB), where C-propeptides are cleaved. Pro-collagen is then packed into secretory vesicles before secreting to the extracellular matrix (ECM), where they will assemble into larger collagen fibrils.

2.3.2 Molecular packing in collagen fibril

Collagen molecule forms fibril in an entropy driven fashion. The resulting self-assembly process leads to the change of spacing of residues within the fibril via burying hydrophobic residues into the interior and polar side-chain [23]. The monomers assemble with the axial D-stagger described previously (see **Figure 2.5**), and in the orthogonal direction to the monomer axis, form a quasi-hexagonal arrangement [23]. This axial D-stagger is driven by electrostatic and hydrophobic interactions between amino-acid residues along the

collagen molecules axis, leading to a lateral shift in alignment between adjacent rows of tropocollagen molecules. As a result of the axial stagger and the gaps, the overall packing of the fibril shows regions of high molecular packing (overlap) and low molecular packing (gap) regions, which was first explained by a consensus model known as the Hodge-Petruska model [59] (**Figure 2.4**). In model, five collagen molecules are aggregated with a staggered manner: one unit of dark and light banding pattern (the periodic electron density profile) can be divided as a 'gap region' (G~ 0.54D (36 nm)), where four molecules are presented, and 'overlap region' (O ~ 0.44D (31 nm)), where all five molecules are presented. In some tissue, for example, cornea, molecules could be grouped into microfibrils (with diameter of 4 nm), which are tilted by around 15° to the long axis of collagen fibril [23]. Compare to tendon tissue where collagen molecules are largely in parallel to the main fibril direction, such a tilting in cornea contributes to a decrease in D-spacing from 67 nm to 65nm.

From this one-dimensional electron density periodicity of the molecular density profile along the fibril axis, a strong meridional diffraction signal arises in X-ray diffraction, in the small-angle (and – wavevector) regime due to the large length scale of D compared to atomic spacings.

This fibrillar arrangement is stabilized when collagen molecules form covalent crosslinks between each other, which forms from amino acids lysine and hydroxyl lysine presenting in their telopeptide regions. N-terminal process of procollagen III, V and XI are either slow or incomplete, leading to a large surface area on N-terminal which prohibits collagen fibril from growing thicker, with other collagen

molecules being buried inside the fibrils. Such mechanics of fibril growth can be applied to collagen I/III (skin), I/V (cornea) and II/XI (cartilage). Though it is difficult to isolated intact collagen fibril from vertebrate, it had been previously shown that type I collagen from vertebrate cultured in vitro had the similar spindle-shaped ends as those fibrils from invertebrates.

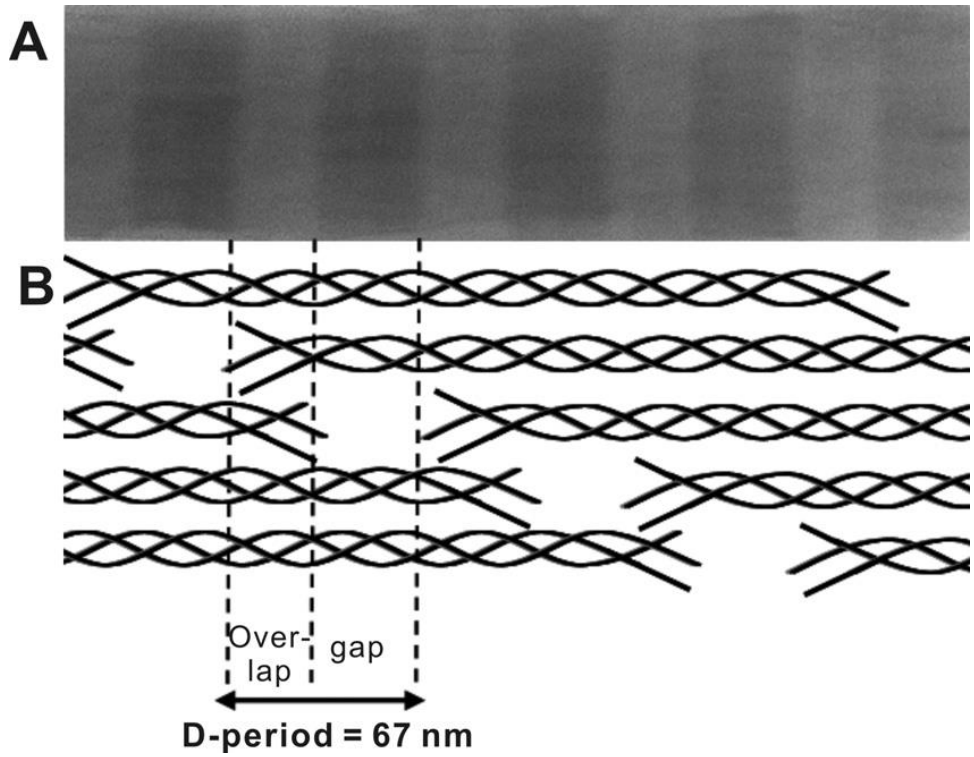

Figure 2.4 Organization of collagen molecules *(A) Transmission electron microscopy (TEM) image of single fibrils with the 67 nm D-period visible. (B) Schematic representation of the two-dimensional axial arrangement of collagen molecules in a microfibril. The D-period originates from the staggered aggregation of the collagen molecules in microfibrils [59].*

2.3.3 Collagen fibres

At the next length scale microns, the self-assembly process of fibre is simpler, comparing to molecules and fibril at the nanoscale: ordered collagen fibrils of 100-200 nm diameter are bundled and aggregated into 50-100 μm fibres (**Figure 2.5**)[16, 23, 60], whose stability and integrity of fibre geometry was maintained by interfibrillar and

intrafibrillar crosslinks via a GAGs-rich matrix both between and within fibres. Collagen fibres were held and covered by a thin sheath layer: endotenon. Bunch of fibres forms fibres bundle, which in turn inherits the characteristics of fibril by functioning to store elastic energy, transmit forces applied, maintain integrity of living body.

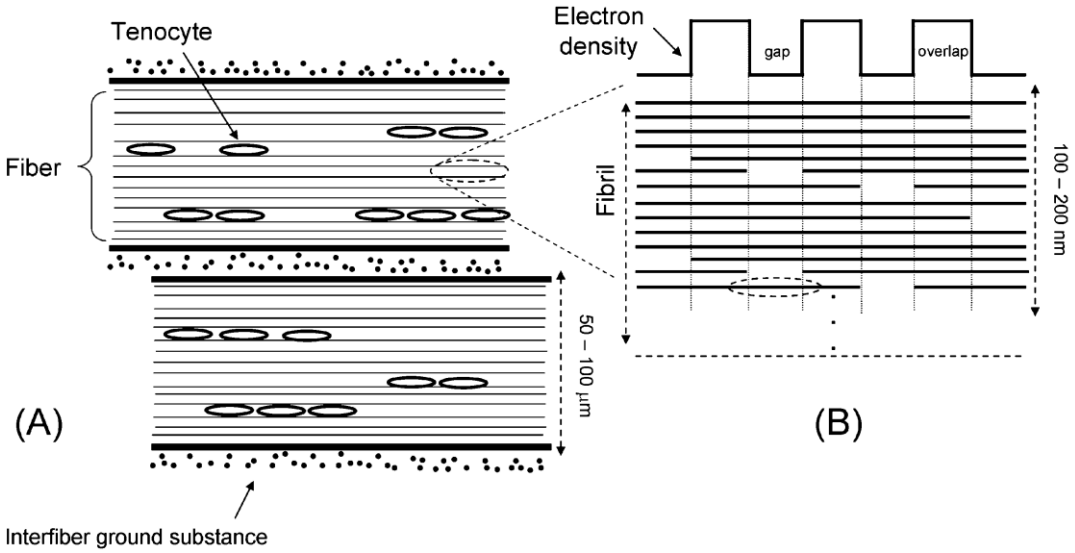

Figure 2.5 Schematic diagram of tendon tissue*, showing the multi-units hierarchy from (A) microscale down to (B) nanoscale. In (A), at the fibrous level, ordered fibrils form 50 µm diameter fibre (also termed fibril bundles) that lies parallel to its neighboured fibre. Within fibre, tendon cells (tenocytes, denoted as ellipsoid) lying next to each other parallelly. (B) A zoom-in schematic diagram of single collagen fibril, showing the staggered arrangements of collagen molecules. The resulting fluctuated electron density profile along the fibril axis will contributes to a strong X-ray diffraction signal [23].*

2.4 Mechanical properties of collagenous tissue

Fibril-forming collagen is the key elements that provides structural supports for both vertebrates (primarily type I and II, for example: stretchable skin, stiff bone) and invertebrate (for example: sea cucumber dermis, compass depressor ligament of sea urchin) [61, 62]. Such collagen-based tissues generally are anisotropic, have a much stronger mechanical strength along the longitudinal fibre axis in comparison to strength under perpendicular direction [23].

Mechanical properties of collagenous tissue, assembled from molecules, fibril, fibre and finally the entire tissue, are dependent on arrangements of subunits one different hierarchy level. Whilst the macroscale mechanics of collagenous tissue have been well documented, the quantitative studies for the deformation mechanisms at the nano- and micro levels were less investigated.

The main experimental systems used in such studies are unidirectional collagenous tissues like tendon, while some work on planar two-dimensional tissues like skin [63] has been carried out. For type II collagenous tissues like cartilage, most of mechanical modelling considers the material as a two-phase poroelastic system without explicit consideration of the fibrous collagenous structure.

2.4.1 Mechanical properties of collagen fibres (Microscale)

At one length scale below the macroscopic, collagenous tissues are comprised of collagen fibres of about 10-50 microns in diameter separated by an interfascicular matrix [16]. Their mechanical properties are rate-dependent, exhibiting viscoelastic behaviours during stretching or relaxation, i.e. the Young's modulus varies when different strain rate was applied in stretch-to-failure experiment.

A typical example of stress vs. strain curve from tendon tissue is depicted in **Figure 2.6**, exhibiting a 'J-shaped' non-linear elastic properties with three different zones, the toe, heel and linear region [23]. The "toe" region (up to ~ 2%) is where the stress increases slowly and exponentially along with applied strain. It represents the straightening of collagen fibre crimps which could be visualised with light microscope techniques [64]. As the physiologic loads accumulating, the "heel" region will turn up, which the stress

increases steadily with strain as the ordering of lateral packing and elongation of fibrils within fibres. Further strain applied to tendon specimen led to a linear increase of stress and this region is called "linear" region. The slope within this region is the elastic modulus E_t of tendon tissue. The yield point, which tendon start to deform plastically, occurs at around 4-6%. Collagen fibres begin to fail microscopically when the yield point is passed. Such a deformation is non-reversible. Tendon tissue fails between 8-14% strain, depending on the state of tissue and the type of mechanical tests.

Time resolved *in situ* mechanical deformation combined with confocal microscopy imaging (in the length scale of 10-100 μm), have been performed to investigate the viscoelastic behaviours of tendon fibres [16, 65-75]. Screen and co-workers used laser confocal microscope to image the movements of tendon cells as markers for microscale tissue strain [76-80]. They reported the local strains of rat-tail tendon fibre were always much smaller than the overall strain via the shifts of fluorescently labelled cell within fibre using laser confocal microscopy [77]. The strain within fibres is less then strain within fibres, which implies that collagen fibres sliding rather than fibre shrinkage, will then become the dominant deformation mechanism of fibres after the point where crimps of fibres were completely removed [74].

Robinson et al. compared the mechanical behaviours of tendon fascicles from normal mice and genetically modification induced the absence of proteoglycans (decorin) mice, and found out that the present of proteoglycan had an influence on viscoelastic mechanism via reducing strain rate sensitivity [68]. The analysis of the micromechanics of tendon had shown that altered composition of non-

collagenous (e.g.: proteoglycans) matrix is correlated to intra- and inter fibre sliding, which in turns demonstrated that these components in matrix did have an effect in modulating shear transferring [81].

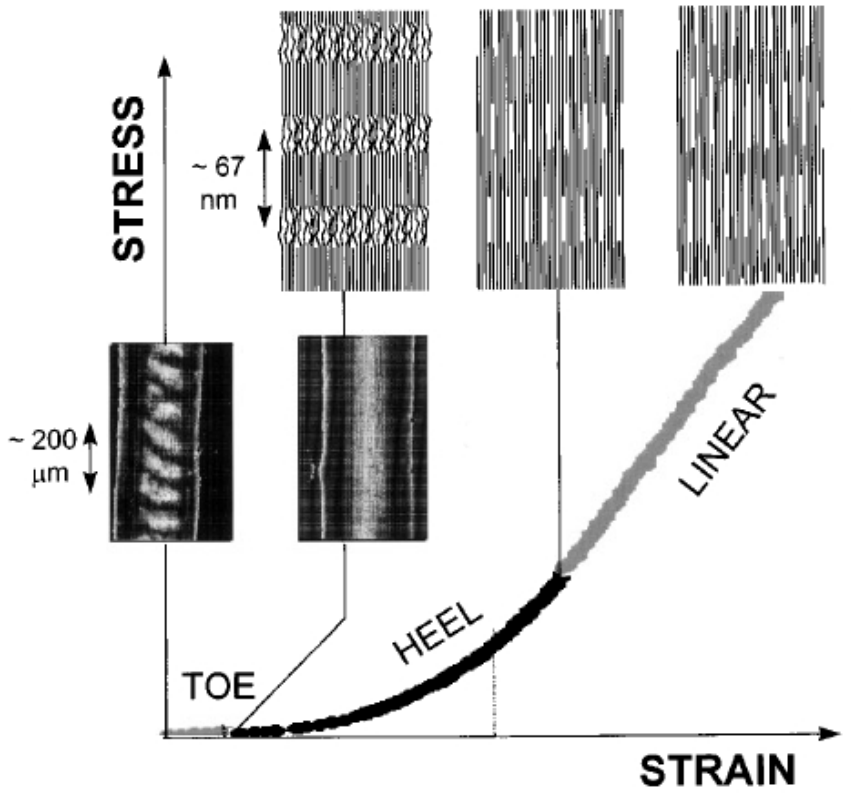

Figure 2.6 Typical stress strain curve for collagenous tissues. *The tangent modulus is increasing slowly with a concave upward tendency known as the "toe" region. On the fibre level, when tissue is not submitted to force, the fibres are somewhat wavy with different orientations. The degree of fibre straightness will go up as the stretch ratio is increasing. Meanwhile, the direction of fibre will gradually become unified. This process of fibre reorientation is known as the fibre recruitment. At the next stage of heel region, on the molecule level, the kinks in the gap zone of triple helix bundles also are removed out step-by-step as the tissue was elongated. After the collagen fibres and 'gap zones' are completely straightened, the elastic region begins. All changes in this range are reversible and if stress is removed, the strain will back to the original point. Adapted from [23]*

2.4.2 Mechanical properties of collagen fibrils

Collagen fibrils, in a range of tissues, can potentially be analysed for their deformation mechanisms via the tracking of changes in their fibrillar structure, or via single fibre measurements using atomic force microscopy and related methods. Molecular and supramolecular structural analysis methods, like wide angle X-ray diffraction (WAXD) and small angle X-ray scattering/diffraction (SAXS/SAXD), have been used in combination with mechanical testing probes to investigate the fibrillar ultrastructure (nanoscale) of collagenous tissue like tendons. The changes at fibrillar level resulting from external deformation can be derived indirectly from the changes of X-ray pattern. Details on the methodology are presented in a subsequent **Chapter 4**, as it will be a main technique used in this PhD project.

The X-ray techniques had been first applied to study the fibrillar structure of collagenous tissue ever since 1940s [82-84], by which collagen molecules were described to be aggregated in a crystallized manner within fibrils [83, 84]. Mosler and co-workers pioneered investigations into collagen nanomechanics via *in situ* high-brilliance synchrotron experiments in the 1980s. They combined high-brilliance synchrotron X-ray radiation with mechanical testing to investigate the collagen fibril elongation mechanics under mechanical deformation [85-87]. Synchrotron sources can generate high intensity of X-ray beam, which leads to good signal statistics for the diffraction pattern, thus enabling detection of small changes in the ultrastructure of collagenous tissue within a short time scale (0.5-100s). Their results show that there are two mechanisms involved in straining of fibril during deformation, which first includes the elongation of collagen molecule and secondly the sliding of collagen molecules. The D-

period of fibril increased from ~67.0 nm to ~67.6nm in the first regimen of deformation, then the D-period increases further due to the slippage of collagen molecule [86]. Sasaki and Odajima [88] studied the substructural changes induced by tension for bovine tendon using small angle X-ray scattering (SAXS).

Fratzl and co-workers did a detailed study of the tension induced strain at both fibrillar and tissue level simultaneously, by inferring the changes of X-ray pattern of collagen and reading of tissue elongation [89-92]. They proposed that the stress strain plot for tendon tissue can be divided into three regions, which includes the toe region, where the crimps at macroscopic level were removed, the heel region, where the lateral spacing within fibril was organised, and the linear region, where the fibrils was stretched and slippage within fibres.

Combining the fibre-level confocal and fibrillar X-ray scattering techniques, more recently the relaxation dynamics at fibrillar level was correlated with the fibre level to obtain a better understanding of viscoelasticity of tendon hierarchically [16]. The confocal microscope and the time resolved in-situ microtensile testing within SAXD were used to evaluate the strain at both fibrillar and fibre level. By coupling Voigt model with Maxwell in series, model had been computed and applied to the experimental results, showing that both inter-fibre and inter-fibrillar fibril relaxation had a clear two stage exponential decaying behaviour, which indicates that the shear strain was transferring within these two level via the soft organic matrix [16]. Further study on fibril from invertebrates by Shen at al. have shown that the relaxation time constant at tissue level was larger than fibrillar level, which indicates that relaxation at the tissue level is regulate by non-collagenous proteoglycan matrix [93].

Scanning microscope, such as the atomic force microscope, is another probe to image and study the nanoscale mechanics of biological specimen. The mechanical behaviour of dried type I collagen (obtained from human fibroblasts) fibrils responding to the monotonically increasing load was investigated by Graham and co-workers using AFM, and the peak value of Young's modulus for fibril was found to be ~32 MPa at strain level equals 4% [94]. Eppell et al. pioneered the study for mechanical response of hydrated collagen fibril isolated from sea cucumber dermis (close to its native state) using a micro-mechanical device called 'MEMS Mechanical Testing Platform'. A stress strain curve was obtained and the Young's modulus of hydrated collagen fibril was found to be ~550 MPa [95]. Marco and co-workers made the first step studying the mechanical properties of type I collagen fibrils extracting from native rat tail tendon (vertebrate) using AFM nanoindentation [96]. They reported that the Young's modulus of single type I collagen fibril obtained from native rat tail tendon is ranging from 5-11.5 GPa.

2.4.3 Mechanical properties of collagen molecules

X-ray diffraction and diffraction combining with simultaneous mechanical tests can be applied to study the hierarchical structure of collagen at the molecular level. The lateral molecular spacing of collagen can be acquire from a short sample to detector distance or the wide-angle X-ray diffraction. Mosler and co-workers proposed that the deformation mechanism of collagen fibril includes two mechanisms: firstly, molecules deformed homogeneous when the external forces was introduced and the ratio of length for 'gap' vs. 'overlap' remained the same during this process. Secondly, the slippage of molecules with respect to each other. Using the

experimental setup described above, the molecular strain ε_m can be determined via the changes of helical pitch.

Using a similar approach, Sasaki and co-workers considered that the deformation at the fibrillar and molecular level occurred concurrently, by measuring the changes of X-ray pattern. They obtained a linear stress-strain curve collagen molecules from bovine tendon and found out the value of collagen molecules Young's modulus of 2.9 ± 0.1GPa [97]. Later, they further investigated the molecular deformation mechanism by identifying and verifying the contribution of elongation of molecules, the change of gap/overlap ratio, the slippage between neighboured molecules. Their results suggested that the major mechanism for molecular deformation is the elongation of collagen molecules, and the other two mechanisms are subsidiary, occurring simultaneously with the elongation of molecules[88].

To summarised, the deformation mechanics of tendon and ligament includes: "toe region", elastic region, and a macroscopic fracture. In the low strain regime, the curvy nature of fibril and fibre initial will uncrimped, together with straining of collagen molecules (triple helix). The slippage of fibril and molecules will become primary that predominates as loads progressively applied.

2.5 Properties of collagen can be tailored

2.5.1 Basic mechanical properties

When external force F is subjected to a material, for example, tensile loads, the force will cause object to elongate together with the loading direction. By definition, the term stress σ is the applied force divided by cross-sectional area of this object. Strain ε is the reaction of a material in response to external force, which is defined as the amount

of elongation divided by the original length. The mechanical properties of a material can be examined by stress-strain curve firstly.

Figure 2.7 shows the mechanical property of collagenous tissues subjected to tensile force. The region where stress increases with strain proportionally is the elastic regime (light grey) and the slope within this region is defined as the Young's modulus (stiffness) of this material. The area under the stress-strain curve indicates the toughness of the material. Here, bone has a lower toughness comparing to tendon.

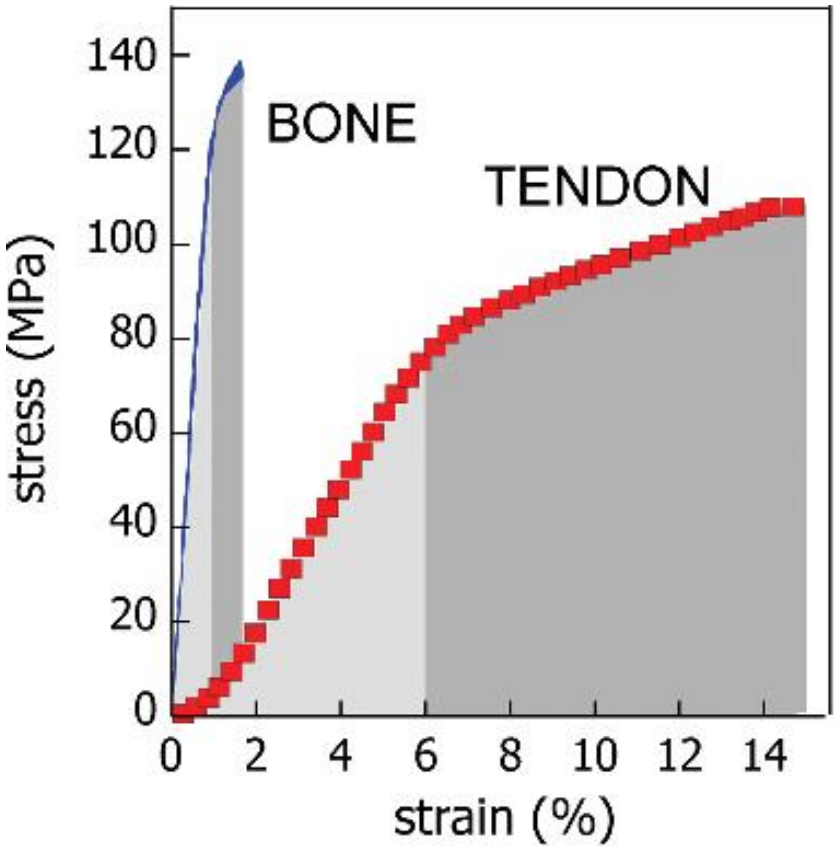

Figure 2.7 *Representative stress-strain curves of two different types of collagenous tissue, bone and tendon [23]. The light grey region corresponds to the elastic deformation while the darker grey region indicates the inelastic deformation of these two tissues.*

Two similar, yet distinct mechanical tests had been widely used to inspect the time dependent properties of material: stress-relaxation and creep. Stress-relaxation is the case when stress decreases under a fixed strain while creep is when strain increases under a constant stress.

The bulk mechanical properties of collagenous tissue vary widely, from the tough mineralized tissues such as bone and dentin to the soft tissue like cartilage, skin, tendon and ligament. To understand how the organisation of collagen fibrils and composition of ECM may influence the mechanical behaviours of collagenous tissue, we need to consider the structure-function relationship by separating individual components from the system of collagenous tissue.

The components in collagenous tissue system can be divided to two groups: (i) **collagen fibrils**, which can be considered as an elastic component, will serve to bear strain along the loading direction. In general, collagenous tissue is anisotropic, tensile property tends to be higher if the external loads applied along the longitudinal fibrillar axis. In addition to the organization of fibrils, it had been proved that the density of fibril (volume fraction of fibril) has a positive correlation with overall tensile strength of a tissue [98]; (ii) **the interfibrillar matrix** which give viscoelastic properties to the whole tissue. Interfibrillar matrix is a gel-like hydrated component with a large fraction of proteoglycans.

2.5.2 Cartilage

Cartilage is constituted by type II collagen, which makes up 40% of its dry weight. Collagen fibrils, along with hydrated proteoglycans and molecules in ECM, have a substantial role in the mechanical properties of cartilage. Glycosaminoglycans (GAGs) are the key

structural components that regulate the hydration state of cartilage: due to their polyanionic characteristic, large aqueous volume can be held and locked. Cartilage thus has the capacity to resist compressive loading by being endowed with GAG-enriched matrix, which act in a manner similar to sponges, being always negatively charged and creating an osmotic swelling pressure, which repels collagen fibrils from each other [47]. Thus, it is observed that cartilage collagen fibrils are generally in the state of tensile pre-strain [48, 49].

As a result of the structure described above, cartilage exhibits time-dependent mechanical properties (a combination of viscoelasticity and poroelasticity) [99-101]. The mechanical properties depend on the interaction of elastic and viscous components in the collagen fibrils and interfibrillar matrix. Functionally, cartilage is designed to bear high and repetitive forces in a nondamaging manner, and to transmit force with low friction coefficient from the surface of the articulating joint to the to the underlying subchondral bone [102]. Beyond the nanoscale structure of the ECM, cartilage also exhibits tissue gradients in fibrillar and GAG density, hydration and fibrillar orientation, being divided into a superficial (at surface) zone, transitional zone and a deep zone of fibrils oriented normal to the cartilage/bone interface and which have a layer of calcified cartilage leading to a strong interface. The low turnover of cartilage, as well as its complex hierarchy, makes its healing and repair process a challenge.

2.5.3 Skin

Skin is an outer collagenous tissue that covers vertebrates, protecting the underlying organs and tissue, e.g.: muscle, bones, tendon and ligament. It is a complicated multi-layer tissue which can be divided into three layers roughly: the epidermis (0.06–1.00 mm), the dermis

(1–4 mm) and the hypodermis [103, 104]. As a key structural constituent of skin tissues, collagen (mainly type I and III) account for ~77% of their fat-free dried weight [105] and it is these collagens that provides the overall mechanical properties [106].

Like other collagenous tissue, skin tissue behaves mechanically as a viscoelastic solid. This tissue is often considered as a low strain-rate sensitive biomaterial with extraordinary tear resistant ability to protect living body from getting attacked by predator[63, 107]. Their building block – fibrils- are curved and randomly ordered initially, and will be recruited and rotated into the loading axis to allow large amount of shape shifting. To evaluate its mechanical behaviour, several loading method applied to this system, for example, tensile [108], suction [109, 110] and torsion [111-113]. The values of Young's modulus for this tissue varies by a factor of hundred, depending on the type of tests. For example, modulus of skin tissue is reported to be from 4.6 - 20 MPa in tensile experiment [108], from 0.42 MPa - 0.85 MPa in torsion experiment [113].

2.5.4 Bone

The hierarchy of bone tissue has been well established in several review articles [25-28]. Their hierarchical structure includes: (i). Osteons and Haversian system (microscale: 10-500 μm); (ii). Lamellae (sub-microscale: 1-10 μm); (iii). Bunch of mineralized fibrils formed fibre (between sub-microscale to nanoscale: ~300 nm to 1 μm); (v). molecules (sub-nanoscale: a few hundred nanometres). Their overall functionality (high stiffness and toughness) is resulting for the assembly at various levels within bone tissue.

The mechanical properties of mineral-collagen fibrils had been considered to be similar as those fibrils from tendon and ligament from soft tissue. However, in bone tissue, there is an additional mineral phase (carbonated apatite) which could provide strength to support the posture and bear considerable loads.

The principal constituents of bone include type I collagen fibrils, mineral and water [114]. The mineral (inorganic) phase lying within the fibril sharing the same orientation, the longitudinal axis, with the collagen fibril (organic phase). The mechanical properties of collagen fibril from bone are assumed to be similar as those from soft tissues (tendon and ligament), given the fact that they both composed by type I collagen. The additional components, the mineral (carbonated apatite), which other tissue doesn't have, is providing bone tissue extra strength for load bearing [26].

However, the rule of material designing, whether it is synthetic or natural, emphasized a system that comprised by two phases, which one is considered as a reinforcing element for the other. Comparing the relatively low modulus but large fracture strain of collagen (1 GPa, 10%) and the high modulus but small fracture strain of mineral (135 GPa, 0.1%), bone — the combination of these two — reaches a balance by keeping both a high modulus (though sacrifice small amount) and an increased fracture strain (a measurement of toughness) and making it both stiff (bone) and tough (collagen) [115].

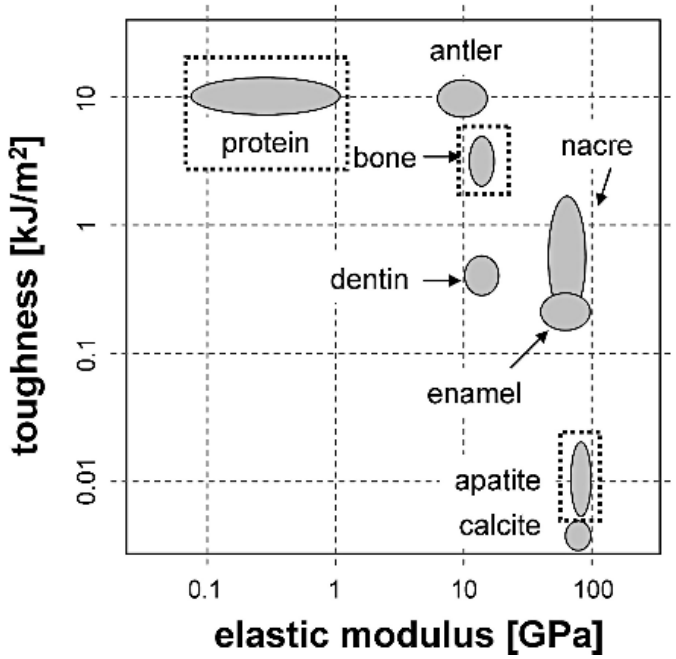

Figure 2.3 An Ashby plot showing the mechanical properties *(y-axis: toughness; x-axis: stiffness) of different nature material. Mineralized tissues composed by protein and apatite calcite, including dentin and bone, endowing with both a relatively high stiffness and toughness [28, 116].*

2.5.5 Tendons and ligaments

Tendons (joint attaches bone to muscle) and ligaments (joint attaches bone to bone attachment) both are fibrous collagenous tissue, which and their main function is with standing musculoskeletal force, thus helping to guide the locomotion of body and maintain the stability of joint capsules[23, 117].

Their hierarchical structure , from collagen molecules (300 nm long, 1.5 nm wide), fibrils (50–200 nm wide), fibre (50-300 μm wide), then to fibre bundles and finally to a dense, closely packed fascicle orientated parallel to the longitudinal axis (in some cases ligaments may not be completely parallel), facilitates them with high tensile strength (~100 – 140MPa) and stiffness (~1.0 –1.5GPa) [118].

Such mechanical properties are well suited for carrying frequent a uniaxial high tensile load create by muscle to bone or bone to bone

with appropriate joint movement, (or, in ligaments, the joint movements can be restricted within a certain range). Tendons and ligaments are type-I based (lesser amounts of proteoglycans and glycoproteins) collagenous tissue and their collagen content is generally greater than 75%. Their mechanical behaviour, under quasi-static tensile stretching, exhibits non-linear elastic properties (so called the “J”-shaped stress strain curve) [119-121], which indicates that they not only have high strength and stiffness at large strain region, but also have greater compliance at the small stress level. Such a great compliance is reasonable for the capacity of energy absorption.

Chapter 3 : Structure and Mechanics of mutable collagenous tissue

3.1 General introduction of MCT

As role of structural supportive material for organs, most collagen is relatively stable in the physiological timescales of a few seconds to minutes [62]. The definition of mutability of collagenous tissues for vertebrate (e.g.: mammals) is to change their mechanical properties (i.e. stiffness, tensile strength, elasticity and viscosity) via altering the properties of collagen fibrils or tuning the composition of ECM (e.g. relative proportion of collagen/PGs). Such changes normally are slow and irreversible, occurring in all mammalian collagenous tissue over their lifetime, e.g.: aging of skin via nonenzymatic cross-linking. We note one exception, which is the uterine cervical remodelling during pregnancy of mammal, which is reversible and relatively faster (over a period of weeks or months) compare to other process. It is controlled by hormone levels and immune-mediated inflammation and will result in a loss of strength for the preparation of giving birth.

In contrast to slow mutability in the class of Mammalia, some invertebrates have a unique collagenous tissue – the mutable collagenous tissue (also called mutable connective tissue: MCT). Compare to the classical collagenous tissue, MCT could undergo reversible and irreversible changes to its mechanical properties, i.e. stiffness, tensile strength, elasticity and viscosity, in an extremely short timescale, from less than 1s to few minutes [62] (**Figure 3.1**). This mutability, found in the class of animals known as *echinoderms* (e.g. sea cucumbers, starfish and brittle stars), was first recognised and then studied as early as 1914 by Hermann Jordan via investigating the

response of sea cucumber body wall to different external stimulus, including chemicals treatment (e.g. cocaine) and physical treatment (e.g. changes of voltage) [122].

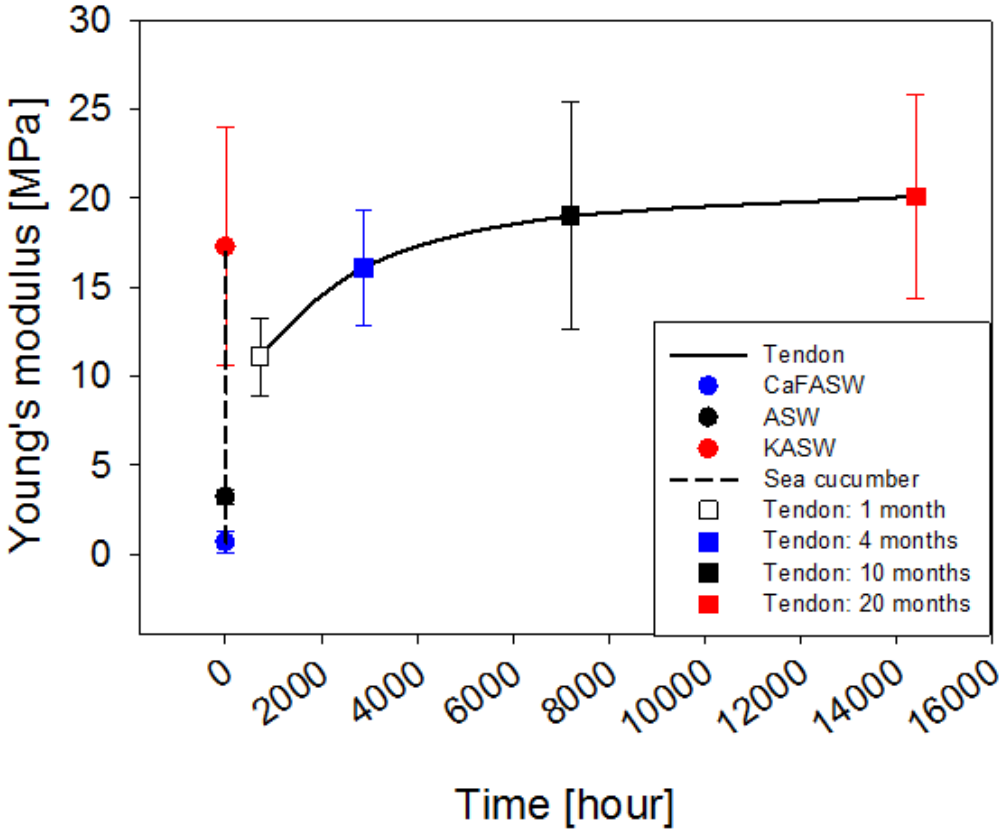

Figure 3.1 *The mechanical properties of sea cucumber dermis [123], a representative of MCT, in comparison of the "conventional" collagenous tissue, tendon [124](CaFASW: calcium-free artificial sea water; ASW: artificial sea water; KASW: potassium-enriched artificial sea water).*

Subsequently, there was some controversy over the mechanisms of MCT, specifically about whether it is a “catch muscles” or a “catch connective tissues”. Von Uexkull proposed that the catch apparatus (CA) of echinoid, which could change its stiffness in a passive way, is a kind of “catch muscles” as it resembles the function of molluscs [125]. Subsequently, it was reported that collagen is the primary component of the MCT system whilst muscle cells just account a

small amount comparing to collagen, and hence, such a small compositional fraction could not lead to such a huge increase of stiffness for the entire tissue. Further analysis of MCT physiological responses led most of the researchers to believe that variable tensility of MCT is controlled directly by the neural system, via regulating different components in ECM, and are coordinated with the activities of muscle contraction and relaxation [126-128] for locomotion of the entire animal. The idea of neural control is supported by the experiments done by Birenheide and Motokawa by anaesthetizing crinoid and observed no reaction in response to external stimuli [129]. No reaction to stimuli was observed in anaesthetized cirri (plural of crinoid). These data clearly establish that nervous control (mediated via nerves with cholinergic receptors) is critical to the functioning of catch connective tissue (a synonym for MCT) which can change its mechanical properties.

Evidence of this mutability (changes of mechanical properties) are usually measured and analysed by means of (mainly biomechanical) testing methods. Trotter et al. for example, quantified the elastic modulus of sea cucumber (*C. frondosa*) dermis and found out the elastic modulus can change from 3 MPa (compliant state) to 25 MPa (standard state), then to 42 MPa (stiff state) with external stimuli [130]. The neurosecretory cells, containing large electron-dense granules, are believed to be a part of it neural system which directly correlated to mutability of MCT. These cell bodies were named as juxtaligamental cells [131].

3.2 Examples of MCT from echinoderms

MCT presents in all five distinct classes of echinoderms [11]. It is believed that the presence of MCT plays a key role to the evolutionary

success of echinoderm [132]. Specifically, MCT provides support of animal body form and posture, aids feeding in an energy-efficient manner in starfish, brittle stars and crinoids and enabling them to escape if under threat in the forms of autotomy (removal of body parts, as also seen in other creatures like lizards) and evisceration (removal of viscera or internal organs [62]). Examples of MCT including the arm ligaments of brittle star, sea urchin compass depressor ligaments (CDL), spine ligaments (catch apparatus) and tooth ligaments [133-137], the body wall of starfish and the dermis tissue from sea cucumber [138-140].

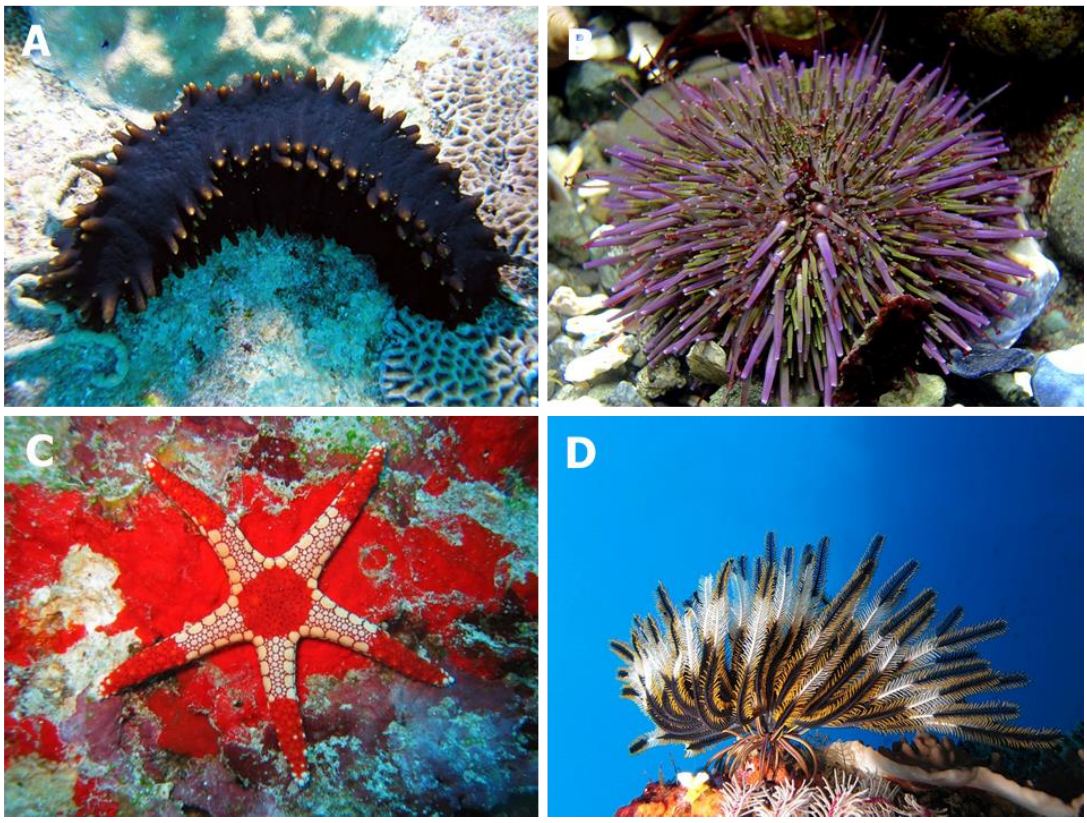

Figure 3.2 Example different kinds of echinoderms *(A) Sea cucumber; (B) Sea urchin; (C) Starfish; (D) Sea lilies. (Sourced from Internet)*

3.3 The Mechanics of MCT

To evaluate the mechanics of mutability, different mechanical testing techniques have been applied to this adaptable mechanical property

induced by employing different stimuli agent such as potassium ion. The mechanical tests of MCT can be categorised into in quasi-static and dynamic mechanical tests, including quasi-static tensile test, dynamic test (creep [141-143], stress relaxation [144], shear [145, 146] and cyclic loading [132, 146]), among which, the most commonly and widely used methods are creep and tensile tests. However, the data obtained with different methods on varied species are often descriptive and normally very difficult to compare. Besides, most of the mechanical data are patchy and largely qualitative. In the literature, the shear modulus of specimen changed from standard state of ~80 kPa to compliant state ~ 0.8 kPa for tensile test [145]. The main disadvantage of all methods is that they can't correlate the in-situ structural changes together the mechanical deformation.

In the follow section, we will focus on developing simple mechanical tests to evaluate the complicated structure that enables the mutability.

3.4 Structure and composition of MCT

3.4.1 Collagen fibril

Fairly extensive static ultrastructural analysis of MCT tissue, mainly using electron microscopy, exists [147-149]. Studies have shown that collagen from echinoderms have several similarities with type I collagen from vertebrates, including the segment long spacing (SLS) crystallinity, distribution of positive and negative charged amino acids along fibrils etc [150]. Fibril from echinoderms have linear mass distribution along the fibril direction, measuring from fibril tip projections by varying the length of collagen fibril, which means that fibrils isolated from echinoderm collagen are in a shape of symmetrically paraboloidal forms. Such finding was reported by

Thurmond and Trotter [151] analysing the molecular orientation of echinoderms fibril, and their results show that these fibrils changed their orientation in the middle of a fibril and the N terminal ends are pointing towards the ends of the nearest fibrils, differing from that of vertebrate type I collagen, which are asymmetrical bipolar with one C-terminal and one N-terminal end.

Electron microscopy imaging techniques (SEM, TEM) had been applied to investigate the ultrastructure of the echinoderms collagen fibrils [133, 151-153]. The value of D-period for sea cucumber and sea urchin CDL was studied by Trotter and co-workers and the value, ranging from 65 – 67 nm, is found out to be close to type I collagenous tissue (tendon and ligament). Similar results had been reported by Ferrario and co-workers, using TEM to evaluate isolated fibrils from sea cucumbers, sea urchins and starfish, the value was reported as reported to be 66±1.6 nm, 62.7±2.8 nm and 63±4.7 nm respectively [154]. Electron microscopy images of the transverse section of sea urchin ligament shows that the cross section of fibril is circular, with a diameter ranging from 20-750 nm. Such a wide variation in term of fibril diameter is also found in sea cucumber dermis section, with a maximum value of 400 nm. Notably, however, the chain composition for each species varies, for example the collagen molecule of holothurian *Cucumaria frondosa* and the starfish *Asterias amurensis* was constituted by three identical polypeptide chains [$(1\alpha)_3$] (homotrimer), whilst the collagen molecule for sea urchin is a heterotrimer, composed by [$(1\alpha)_{2,}(2\alpha)_1$][155-157].

In contrast to the collagen of adult mammalian tissues such as rat tail tendon, single collagen fibrils from sea cucumber dermis tissue or compass depressor ligaments of sea urchin can be isolated and

extracted from tissue in a relatively straightforward protocol, without harsh treatments and morphological damage: treatment with cation chelator and then extracted in water [158]. All echinoderms fibril has a tapered end at both side, with a shape of spindle. The aspect ratio of length to diameter of collage fibril is constant of ~2000 [159].

In addition to studying the static ECM morphology of MCT, some recent electron microscopy imaging work has attempted to characterize the changes in fibrillar structure under mechanically standard, soft and stiffened states. Ribeiro at al. carried out an exhaustive analysis for a typical MCT- the CDL of sea urchin *Paracentrotus lividus* microstructure in different chemical-induced mechanical state, they revealed that the organization of collagen fibril arrays of CDL became denser when mechanical state was shifted from standard to stiffened (**Figure 3.3**). Such a reduction of intrafibrillar spacing might come from the increase of cohesion between adjacent collagen fibrils. The stiffening effector molecules for example stiparin (see below), may facilitate the mutability by serving as cross-linker to bring two neighbouring fibrils together and thereby increase the interfibrillar cohesion [147].

The mechanism regarding to echinoderms mutability are yet to be defined because: (i) -harsh environment of the vacuum microscopic chamber and the specimen preparation procedure including fixation, dehydration and staining may lead to a biological structure that far from its native state.(ii) a comprehensive research that considers both the properties of interfibrillar matrix as well as the collagen fibril itself is needed and (iii) these measurements are – by their nature – static and cannot capture the dynamics of mutable connective tissue change

of state.

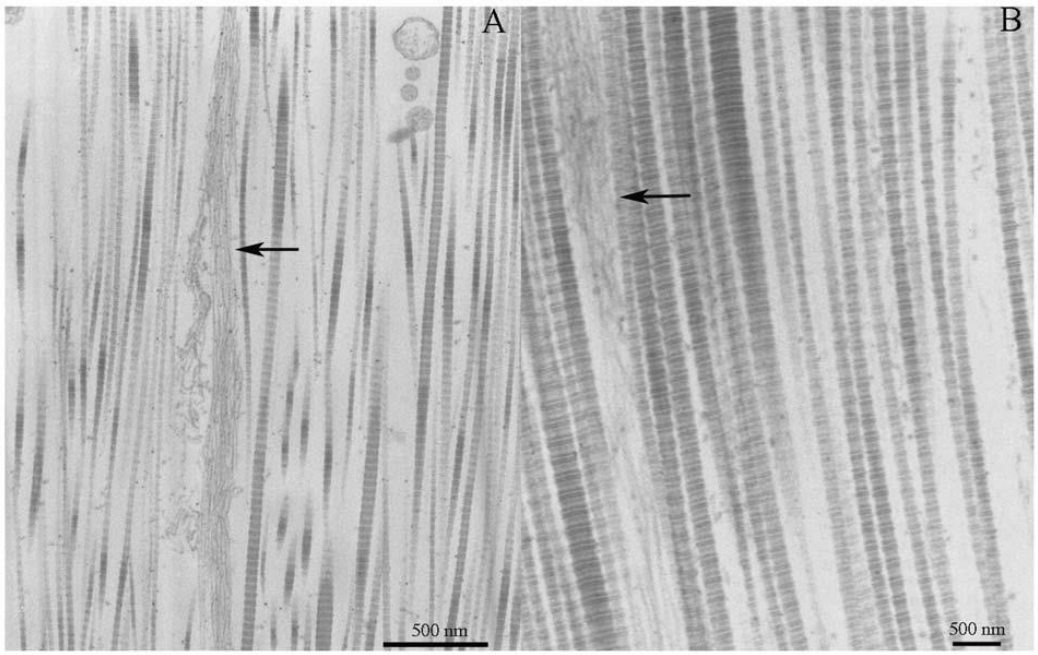

Figure 3.3 TEM micrographs*: Organization of the MCT collagen fibril in standard and stiff state (A) stiffened tissue; (B) standard tissue, obtained from compass depressor ligaments [133]*

3.4.2 GAGs/proteoglycans function as a site for interfibrillar bridges

Proteoglycans (PGs) are observed in all fibril-forming collagenous tissue in all mammal. They are usually composed of a single polypeptide with one or more polyanionic sulphated glycosaminoglycan (GAG) chain(s) attached on the surface of collagen fibrils covalently [160]. The biochemistry of MCT had been recently investigated by Ribiero and co-workers using spectroscopic methods like Fourier transform infrared (FT-IR) and confocal Raman microscopy [161]. The experimental data revealed, firstly, that type I collagen from bovine tissue and isolated compass depressor ligaments (CDLs) of a sea urchin *Paracentrotus lividus*, exhibiting similar FT-IR and confocal Raman spectra (**Figure 3.4**). This indicates the resemblance of chain composition and molecular organization between type I collagen from vertebrate and the CDL from

invertebrates. Secondly, the assay described in Bjornsson et al. 1998 [162] was utilize to identify the proteoglycans/ GAGs from CDL, following by a comparison with GAGs from shark cartilage Chondroitin sulphate. As expected, their results confirmed that the CDL collagen fibrils attached GAGs were sulphated, similar to that of

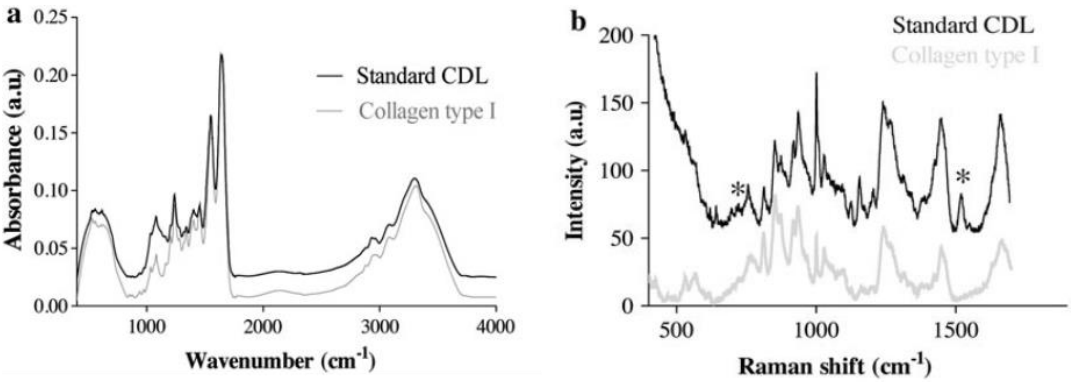

shark cartilage.

Figure 3.4 *(a) Fourier transform infrared (FT-IR) spectra and a (b) Raman microscopy spectra of a standard CDL (black) and the control Bovine Collagen type I (grey)*

To understand the structure-function relations hierarchically, the isolation and extraction of subunit fibril have been investigated for years. However, protocols to obtain single fibrils from tendon without damaging their mechanical performance are absent. Due to the lack of permanent bonds either between collagen fibrils or in the ECM was found in MCT, it is relatively easy to isolate echinoderm collagen fibril from tissue, compared to tendon or ligament tissue from vertebrates where the presence of permanent association renders this difficult [150, 163-165] . Therefore, given the relatively labile environment around the fibrils in terms of these weak bonds, it was hypothesized that during the change of mechanical state in MCT, the amount of bonds between collagen fibrils as cross-links with ECM is changing dynamically, for example, clusters of weak bonds will form

and break when the stiffness of tissue is converting from one state to the other [165]. PGs and GAGs might not be involved in echinoderm mutability directly., as Ribeiro and co-workers found out that no statistical differences of GAGs content was found between different mechanical state [161]. It was then hypothesized that PGs might be involved in mutability *indirectly* by serving as a binding sits for some bioactive molecules, which would induce interfibrillar cohesion for two adjacent collagen fibrils and thereby contribute to the increase of tissue stiffness. The role of these bioactive molecules is discussed further in the next sections.

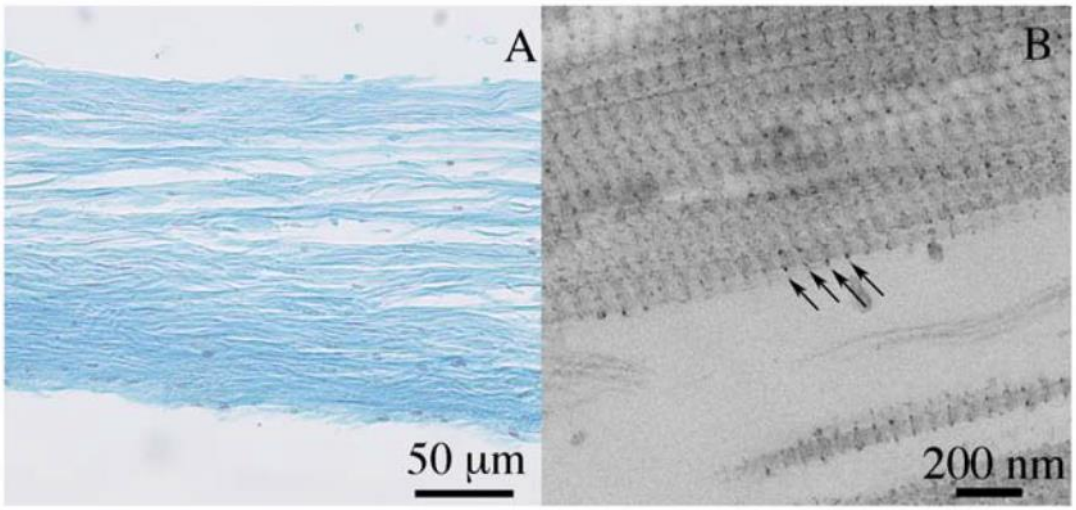

Figure 3.5 Proteoglycans attached with collagen fibrils *(A) collagen fibrils of the CDL were staining with alcian blue, the precipitates were attached to the surface of fibril; (B) the regular spacing of precipitates, each of them were allocated within one D-period, at the same position (arrows: proteoglycans)[133]*

3.4.3 Juxtaligamental cells

At the cellular level, a striking characteristic of MCT histologically is that all MCT contains a type of cell resembling neurosecretory-cells [62, 166], where the neurotransmitters was secreted. These cells contain large electron-dense granules, and are named as

juxtaligamental cells (JLC), with their congregations are also termed as juxtaligamental nodes. Due to their ubiquity in MCT-tissues, they have been considered as a candidate that contributes the mutability mechanism for a long time [167-169]. Indeed, as will be described in the subsequent sections, early researchers (till around the mid-1990s) tended to believe a direct chemical action on the ECM was the mechanism for MCT-state change [170]. The mechanical properties were believed to be controlled regulating by the concentration of Ca^{2+} in ECM. The current concept is that MCT-mutability is controlled by Ca^{2+} dependent cellular processes, coordinating with JLCs. As bioactive molecules (including stiparin, tensilin, and novel stiffening factor (NSF) etc.) were produced and secreted from JLCs, and were related to the interfibrillar cohesion *in vitro*, it was deduced that such molecules might be involved in the regulation of the mechanical state of the entire tissue. According to this view, these molecules can be stored in granules inside juxtaligamental cells and will prevent or facilitate its interaction with fibrils, enabling neighbour fibril to slide or hold together with each other. It should be noted that while this is the currently accepted belief in the echinoderm community, there is no direct evidence for this, nor much quantitative details of the process *in vivo*.

From a spatial-structural perspective, investigations using electron microscopy have shown that the JLCs are in a close contact with motor neurones in at least three of the five echinoderm classes (crinoids, echinoids and ophiuroids) [11]. More recent studies by Ribeiro, Barbaglio et al. [133], using the compass depressor ligament (CDL) of *Paracentrotus lividus* as a model tissue, observed both variations in electron density (light and dark) and shape (round and ovoid) in the membrane-bound electron-dense granules in the JLCs. The mean diameter of the light one was found to be larger than the dark counterparts, and the dark granules were more common than light ones in all mechanical states.

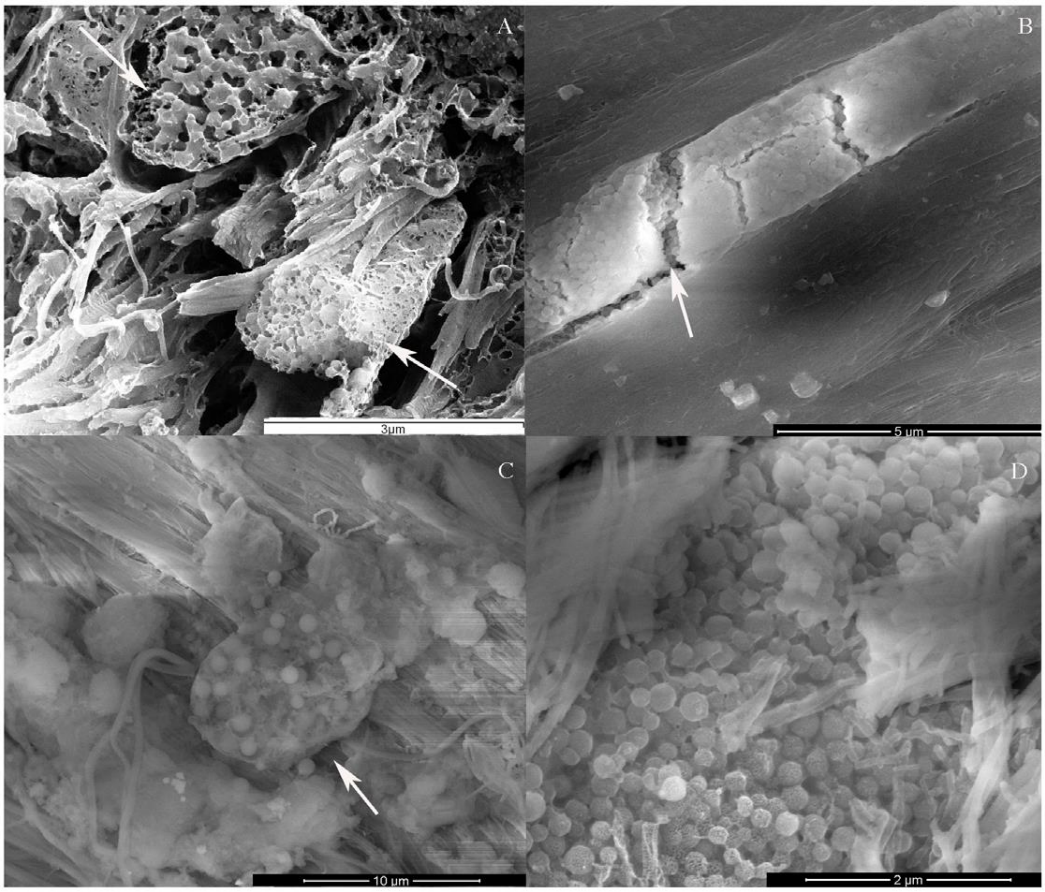

Figure 3.6 Morphology of Juxtaligamental cells *(A) cryo-scanning electron microscopy (CSEM) image for a section of JLC, cutting transversely (arrow: presence of JLCs); (B-D) gun-environmental scanning electron microscopy (FEG/ESEM) images of JLCs[133]*

To summarize, it is widely accepted that JLCs are neurosecretory-like cells that directly controlling the mechanical properties of MCT via secreting of effector molecules. Intensive investigation had been carried out using different imaging technique [171-175] to determine the organization and morphology of the juxtaligamental nodes histologically, however, the precise mechanisms between the nervous system and juxtaligamental cells are yet to be defined as the specimens prepared for transmission electron microscopy or other techniques were far away from their native state.

3.5 Mechanisms of MCT

We now review the various mechanisms that have been proposed for the change of state of MCT in echinoderms, in approximate chronological order.

3.5.1 The ionic hypothesis

Initial research into the variable mechanical properties of MCT focussed on the change of (viable or in-vivo) tissue to changes in chemical composition of the immersing solutions. It was rapidly found that upon immersion into solution of varying ionic strength that the stiffness of the echinoderm changed quickly. Much subsequent research, mainly by Motowaka [136, 142, 176-178] and colleagues, and also by Wilkie and co-workers [143, 167, 169, 179] used a 3-way classification to describe such altered states – compliant, standard, and stiff states – based on which type of ionic solution was used. Monovalent (K^+) and divalent (Ca^{2+}) ion concentration of the bathing media were primarily used, with a standard state being immersed in artificial sea water (ASW). Broadly, lowering the amount Ca^{2+} ion has a plasticising (softening) effect and levelling up the K^+ ion concentration has stiffening effect [132]. It should be noted that the

terminology used in the biological literature is not always consistent with standard materials-science usage – "plasticizing" being used sometimes as a catch-all term for "softening" (reducing modulus) or actual structural liquefaction of the tissue. Detailed numbers will be discussed in detail later.

3.5.2 K^+ ions

Wilkie [11] summarized existing views in stating that elevated potassium ion concentration in creep tests (constant load) leads to an increase in strain rate, leading to tissue rupture [142, 143, 180]. An increase in stiffness (from 0.77 MPa to 3.1 MPa) of the sea cucumber dermis when immersing in ASW with high concentration of potassium ions (KASW) had been reported [132]. A more recent study by Motokawa and his colleagues[181] showed evidence of increases in stiffness (measured by dynamic tests) of 66% from baseline levels of 0.51 MPa on immersion in KASW (a corresponding increase of 206% from a baseline of 1.71 MPa was also observed after mechanical stimulation of the tissue).

3.5.3 Ca^{2+} Ions

Wilkie (1978) studied that calcium ions (Ca^{2+}) in effecting the reversible stiffness mechanism of MCT quantitively [145]. MCT sitting in sea water with high concentrations of Ca^{2+} was found to have higher stiffness compared with normal sea water while in Ca^{2+} chelating solution, was unanimously found to have lower stiffness [167, 177, 182-184]. Szulgit et al discovered that the stiffness of inner dermis of *Cucumaria frondosa* increased from 14 kPa to 70 kPa when changing the bathing solution from Ca^{2+}- chelated to ASW (with normal Ca^{2+} concentration) [145]. In terms of a structural explanation, in the early 1990s it was proposed that the calcium ions could alter the

inter-fibrillar interaction directly by linking negatively charged macromolecules. Alternatively, both mechanisms could be involved in.

3.6 Rejection of the ionic hypotheses and alternative explanations

Till the middle of 1990s, it was believed that interfibrillar cohesion was mediated by the intake of cations/ or some cholinergic agents (for example: K^+, Ca^{2+} and acetylcholine) via directly binding two adjacent collagen fibrils, which the negatively charged GAGs or other macromolecules are attached. It was proposed that sole action of Ca^{2+} on the physical crosslinking of the negatively charged macromolecules in the interfibrillar matrix) was largely disproved when it was shown that MCT could change mechanical properties in the absence of changes in Ca^{2+}, specifically by Szulgit and Shadwick (1994), Trotter and Koob (1995) and Trotter and Chino (1999) [185-187]. As their experiments showed that the MCT tensility in the presence of a normal Ca^{2+} can be changed by drugs that interfere with calcium-dependent cellular processes. The evidence thus now supports the idea that Ca^{2+} is significant cell-derived stiffening agent that regulates the stiffness of MCT (cellular calcium regulation hypothesis). Then the model favoured by many reports is that the calcium levels, as a key modulator of compliance, regulate cellular events (other than the release of Ca^{2+}) like secretion of stiffening and destiffening factor to the ECM.

The current hypothesis is that this effect is indirect, due to the stimulus of K^+ ions (a known neuroactive agent in both humans and echinoderms) on the nerve cells (or JLCs) which in turn release stiffening or destiffening factors. However, it is still an open question if K^+ ions may have also a direct effect on the viscosity of the extracellular matrix in addition to indirect effects through the nervous

system, as charged ions can be envisaged to physically crosslink the extrafibrillar matrix and change the mechanical properties, probably increasing stiffness due to increased crosslinking in the extrafibrillar matrix.

3.7 Action of Effector molecules

It is hypothesized but not directly demonstrated currently that the mutability of echinoderms collagenous tissue is directly related to the interfibrillar cohesion [62]. Several candidates of effector molecules which have effects on mechanical properties of MCT had been partly identified and isolated over these years, including large extracellular glycoproteins, smaller granular proteins and putative neuropeptides.[186, 188-191].

3.7.1 Stiparin

Stiparin (source: Latin "stipare", means "to pack together"), a 375kDa glycoprotein that inducing the fibrils aggregation, was first identified and purified by Trotter et al in 1996 from the extracts of sea cucumber inner dermis (species: *Cucumaria frondosa)*[192]. They approached the question of effector molecule identity by testing the ability of tissue extract fractions to bind and aggregate isolated intact *Cucumaria frondosa* collagen fibrils (with GAG and proteoglycans attached) *in vitro*. It was found that stiparin was effective in aggregating collagen fibrils which had been isolated and extracted from the dermis, but the molecular mechanism is yet unclear. Specifically, the authors pointed out that it was not possible to differentiate between the possibilities that this protein causes the packing of the fibrils by a) directly binding two fibrils together, b) binding one fibril and forming multimers with the neighbouring fibril (which also has a stiparin molecule bound to it) or c) by binding

molecules to receptor sites on the fibrils which repel other fibrils in the native states (a form of shielding) leading to aggregation. Lastly, it should be noted that stiparin does not actually change the mechanical properties of whole tissue samples, and it is thus proposed that its key role is as a weak "scaffolding" separating fibrils in the intact tissue, with the resulting open architecture making it easier for mechano-effector molecules to diffuse into the space between fibrils and cross-link them or the interfibrillar matrix. It is therefore believed to be relevant to the mutability mechanism [189, 191, 193], but does not play the critical role of cross-linking the fibrillar/interfibrillar matrix. It should be noted that these structural mechanisms are largely hypothetical inferences rather than direct demonstrations.

3.7.2 Tensilin

Koob and co-workers isolated the biologically active fractions from cell-lysed *Cucumaria frondosa* inner and outer dermis via the gel filtration column [189]. A plasticising protein was isolated and purified, with a molecular mass for <15kDa and a cell-derived stiffening protein with a molecular mass for ~38kDa. They further summarised that these plasticisers and stiffeners were release by granular cells since neither of them can be derived from ECM directly, and the isolation required the dermis cell lysate (freeze-thawed process). This contributed to the hypothesis that tensilin, which was secreted from cells, are regulatory molecules and can bring about changes in MCT mechanical properties. This protein can increase tissue stiffness, which was, however, measured by an unusual and indirect manner. Specifically, the time required for a dermis sample to bend a certain distance, with and without exposure to tensilin, was calculated. It was found that this time increased by 33.4% for tensilin-

incubated dermis samples. Later, in 2002, Tipper, Trotter, Koob and colleagues characterized, sequenced and purified a protein which is found to induce both tissue stiffening and collagen fibrils aggregation, known as Tensilin [188].

All these evidences have led to the hypothesis that tensilin is a stiffening factor in MCT. A model for this hypothesis is presented in **Figure 3.7**.

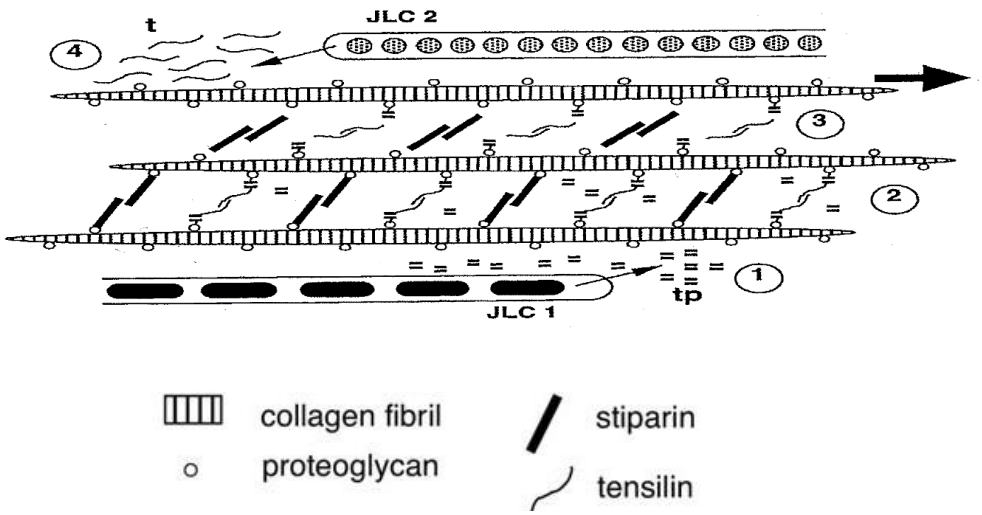

Figure 3.7 Model of the tensilin stiffening hypothesis. *Destiffening or plasticizing agent (tp) was released from type I juxtaligamental cell (JLC 1) (1) which will lead to a degradation of tensilin – GAGs crosslinks (2). Fibril will slide out from one to the other due to the lack of interfibrillar crosslinks (3). The stiffness of MCT will be restored when tensilin is secreted from the other type of juxtaligamental cell (JLC 2) [62].*

Another tensilin-like protein was also purified from another sea cucumber species, *Holothuria leucospilota* [194]. This H-tensilin was shown to aggregate collagen-fibrils and induce stiffening of holothurian dermis. It is noteworthy that H-tensilin did not induce the stiffest state (~130 kPa, achieved by K^+) in MCT and can only increase stiffness for tissue that is already soft by 3-15 folds (80 kPa), suggesting that different mechanisms are required to induce the stiff state [194].

Analogies have been drawn between tensilin and other proteins involved in structural alterations of ECM tissue in the animal kingdom. Specifically, in mammals the uterine cervical remodelling during pregnancy and parturition involves increases levels of TIMPs (inhibitor of metallopeptidase) to control the extent of collagen and other matrix protein degradation [195]. Sequence analysis of tensilin cDNA showed a significant similarity (21% - 36% amino-acid identity) between mammalian tissue inhibitors of matrix metalloproteinases (TIMPs) and tensilin [196]. Since tensilin is found to induce both tissue stiffening and aggregation of collagen fibrils, Ribeiro et al. hypothesised that the matrix metalloproteinases (MMPs) may be involved in MCT mutability, and that regulatory mechanism in MCT was evolved from a MMP-TIMP system[196]. They claimed that if the assembly of cross-links multimers and the release of ECM-degrading MMPs was in a balance, the amount of cross-links will be regulated by controlling the level of TIMPs. The alteration in stiffness observed would thus result from secreting existing intracellular TIMPs to the ECM.

3.7.3 Other possible proteins acting as mechanoeffectors

Yamaand coworkers [197] isolated and partly purified another stiffening agent, which had the ability to further increase the stiffness of H-tensilin treated specimens and produce the stiffest state of 5.5 kPa (**Figure 3.8**). However, this agent did not stiffen the specimen which is already soften by CaF-ASW (in contrast to tensilin), which suggested that several factors are responsible for a specific mechanism, either from soft to standard or from standard to stiff.

Molecular mass of NSF (novel stiffening factor) was estimated using gel filtration to be 2.4 kDa [197]. They revealed that this stiffening agent had no effect on either compliant MCT or muscle tissue from sea cucumber. This protein was then named as novel stiffening factor (NSF).

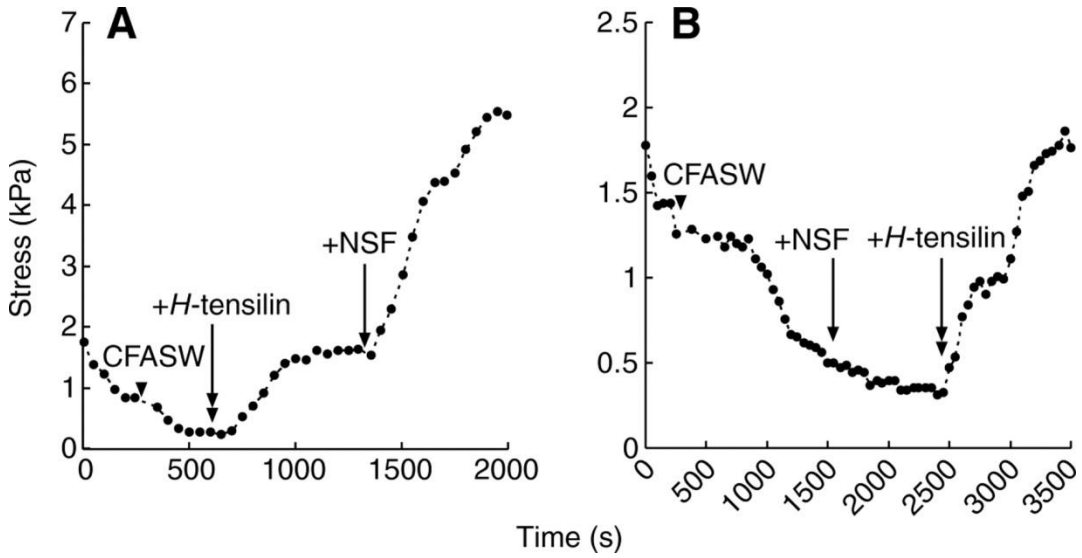

Figure 3.8 Mechanical properties of sea cucumber dermis in response to novel stiffening factor and H-tensilin. *(A)The specimens are first treated in ASW, then to CaF-ASW, and followed by the injection of H-tensile, where the stiffness of specimen increased. NSF was added after the stress began to be levelling off, a clear increase of stiffness is observed. (B) Followed by the immersing solution exchange to CaF-ASW, NSF was firstly introduced, where the stress did not increase [191].*

3.8 Summary: Proposed Ultrastructural Models of MCT Action

Qualitative ideas as to the supramolecular structural models of MCT have evolved since 1980s [168, 198]. Synthesis/consensus qualitative model is presented in **Figure 3.9**. The major component of all echinoderm MCTs is the network of extracellular discontinuous and parallel, spindle like collagen fibrils that are interconnected by interfibrillar bridges [62]. GAGs on the collagen fibril surfaces serve as binding sites for interfibrillar crosslink subunits. MCT stiffness is known to be under neural control and is modulated by the secretion of

molecules (JLC type I) that promote interfibrillar crosslink formation (i.e. stiffen the tissue) or molecules that reversely inhibit cohesion (i.e. soften tissue by decreasing the number of interfibrillar crosslinks and allowing the fibrils to slide between each other; JLC type II) [62, 133, 199, 200].

Numbers of crosslinks formation and inhibition related proteins or peptides including tensilin, stiparin and NSF etc, which was believed to be released by JLCs had been identified or partly purified since 1995. The ratio between bridge formation and inhibition of interfibrillar cohesion is thought to determine the mechanical state of the tissue [134].

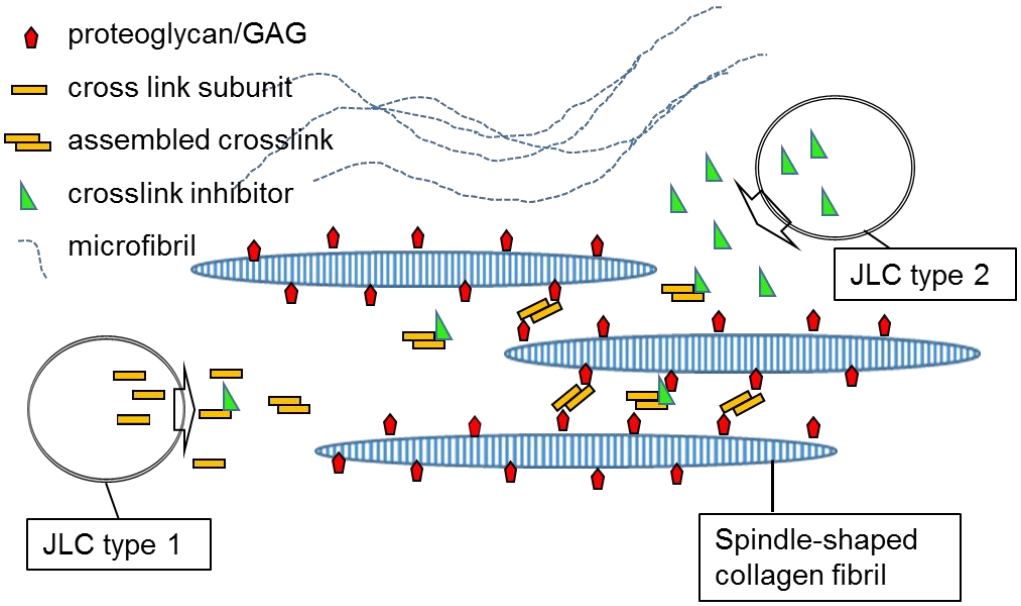

Figure 3.9 Model of MCT at the fibrillar level. MCT constituted by discontinuous and spindle-shaped collagen fibrils with PGs/GAGs attached to their surface*. GAGs are serving as a binding site for the bioactive effector molecules. Microfibrils are presented on the boundary of fibril bundles. Stiffening stimuli leads to the releasing (white arrow) bridging agent (cross-links subunits) which enhancing the fibril aggregation by forming the assembled cross-links. The stiffness of tissue will then increase subsequently. In response to softening stimuli, the secretion of bond breaking molecule from another type of cell (JLC type 2) within the system leads to a decrease*

of interfibrillar cross-links and thereby lowering the load bearing property of the tissue.

3.9 Open questions about the MCT mechanism

The mutability of MCT is proposed to be modulated by interfibrillar cohesion. The research question is to understand the kinetics and mechanics of stiffening/destiffening mechanism of MCT. Existing methods categorised the change of mechanical properties at large scale whilst it cannot measure the structural changes at the molecular and supramolecular level *in situ*. The limitations of the various techniques currently used to testify the active force generation mechanism of MCT are summarised in **Table 3.1** [133, 135, 144, 184]. Conventional techniques do not provide structural changes on the nanoscale components of the fibrils and interfibrillar matrix in response to addition of molecules in real time. Therefore, a multidisciplinary approach, where state-of-the-art nanomaterial imaging techniques using synchrotron X-ray radiation is combined with the effects of specific neuropeptides found in the starfish body wall, will be used to answer this question.

Table 3.1 *Comparison of in situ X-ray nano-mechanical imaging with other techniques*

Technique	Hierarchy	*In-situ* testing	Detecting the effects of treatment	Both structure & mechanics
Mechanical testing (creep, tensile and cyclic loading)	No	No	Yes	Mechanics

SEM, TEM and confocal microscope	Yes	No	No	Structure
In-situ mechanical testing with SAXD/ WAXD	Yes	Yes	Yes	structure & mechanics

Chapter 4 : Introduction to methodology and design of in-situ mechanical tester

4.1 X-Ray Scattering and Diffraction

X-rays are a form of transverse electromagnetic radiations, like visible light, but of much shorter wavelength, from 0.01 nm to 10 nm (corresponding to the frequency from 3×10^{16} Hz to 3×10^{19} Hz and energy from 120 keV to 120 eV) [201]. In 1895, X-rays were first discovered by a German physicist named Wilhelm Roentgen, and subsequently due to its high penetrating ability and material-specific attenuation, applied to a range of areas, for example in medical imaging to detect skeletal damage in the human body. In particular in the area of physical characterisation of material ultrastructure, X-rays have been used to investigate the molecular arrangement of both crystalline, semicrystalline and amorphous materials, initiated with the discovery of X-ray diffraction by Max von Laue and the Braggs.

Whether a material can diffract/scatter X-rays is related to its structural arrangements at atomic/molecular level. If a material had crystalline order, i.e. repetition of a particular molecular arrangement (such as when collagen molecules in tendon organized in a quasi-hexagonal manner transverse to the fibril axis [23]) with spacing in the order of few Angstroms, these repetitions lead to a periodically fluctuating electron density profile. When an X-ray primary beam is incident on such materials, the repetitive electron density fluctuation will lead to a signature spatial pattern for scattered light arising from constructive and destructive interference of scattered waves. These spatial variations can be detected if the spacing of repeating units is of the same order of magnitude as the wavelength of incident X-ray

beam, as expected from physical grounds: too small a spacing relative to the X-ray wavelength, and the material will appear solid and homogeneous from the perspective of the beam. The spatial pattern of scattered X-ray radiation captured by X-ray detectors (a diffraction pattern, in the case of crystalline materials) are sensitive to structure at the nanoscale, and therefore capable of providing ultrastructural information for a material indirectly, in the domain of reciprocal space [202]. All these characteristics make X-ray diffraction and scattering an ideal technique for studying the ultrastructure of material under 100 nm, which is far beyond the ability of conventional light microscopy (although newer super resolution microscopy methods can achieve sub-100 nm resolution [203]).

Imaging methods including, but not limiting to, scanning electron microscopy (SEM) transmission electron microscopy (TEM) and atomic force microscopy (AFM) and X-ray diffraction which had been employed to correlate the material design of biological tissues at the nanoscale to their mechanical properties and functionality at the macroscopic level. Among which, X-ray scattering and diffraction techniques allow quantitative and non-destructive investigation of hierarchically structured systems which give scattering and diffraction patterns from both wide-angle X-ray diffraction (WAXD) regime and small angle X-ray scattering (SAXS) regime where detailed information on the internal structure can be revealed. The specific advantage of WAXD and SAXD for biological materials is that this structural information can be obtained from tissues in/close to native state, which could avoid potential artefacts producing from complex specimen pre-treatment (for example, in TEM).

4.2 Theoretical background

The electrons are the basic elements that scatter X-rays. Here, the following interaction is considered as an elastic scattering process. When X-rays are incident into an atom, the electrons of atom are accelerated by the electromagnetic field of the X-rays, as a result of which the electrons oscillate at the same frequency as the incident X-rays and become emitters. Hence, re-directed electromagnetic X-rays are generated from atoms, with each atom now serving as a wave source. Most of the scattering is destructive interference, however, at some particular angles in-phase wave can add up via constructive interfere.

Scattering and diffraction both occur while waves are re-directed and interacting with particles. They are caused by the same core physical principle – emission of electromagnetic radiation, at the same wavelength as that of the incident radiation, but under slightly different geometric conditions. Scattering refers to the signal emitted after interaction of electromagnetic waves with spatially disordered particles. In contrast, diffraction happens waves interact with crystalline or partially crystalline matter, and is a specialized case of scattering, as it can be defined as the result of constructive and destructive interference of a large number of scattered rays from the individual crystalline units of the material.

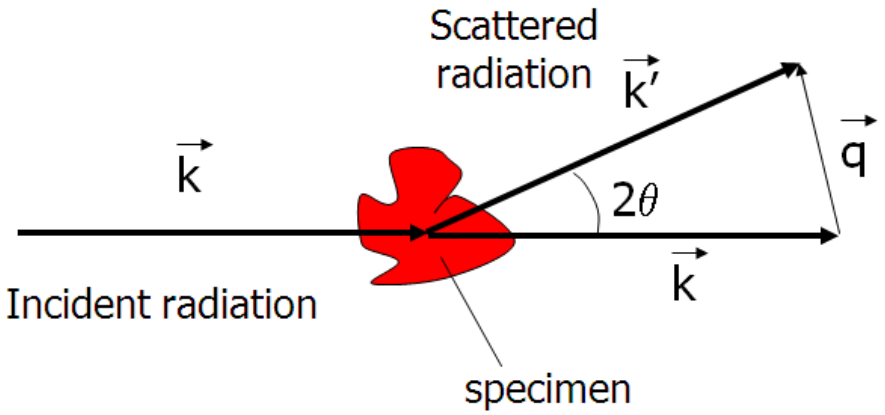

Figure 4.1 *Elastic X-ray scattering: Schematic representing how the scattering vector q is defined relative to the incident beam (k) and scattered beam (k'), with 2θ the scattering angle between the two wave-vectors k and k'.*

The intensity of diffraction is plotted as a function of the scattering vector ***q***, which is the difference between the incident and scattered beam ***k*** – ***k***' (**Figure 4.1**). Consider such a transmitting process as purely elastic, without any energy loss, the absolute values of the incident and scattered beams are equal and in this case, it can be shown that the following relation holds:

$$\boldsymbol{q = \frac{4\pi}{\lambda} \cdot \sin\frac{2\theta}{2}} \qquad \textbf{Equation 4.1}$$

where it can be seen that ***q***, the scattering vector in reciprocal space, has inverse dimensions to real space. The physical meaning of 2θ (the scattering angle) can be clarified by the well-known Bragg's law, which is reviewed below.

4.2.1 Bragg's law

The Bragg construction considers interference of scattered X-rays between adjacent planes of atoms (or larger scale repeating units) and defines critical angles at which constructive interference occurs. As shown in **Figure 4.2**, $2d \sin(2\theta/2)$ is the path difference between the

X-ray beam diffracted by adjacent lattice planes with spacing D. Hence, Bragg's Law can be written as:

$$\lambda = 2 \cdot \frac{d_{hkl}}{n} sin\,\theta \qquad \textbf{Equation} \qquad \textbf{4.2}$$

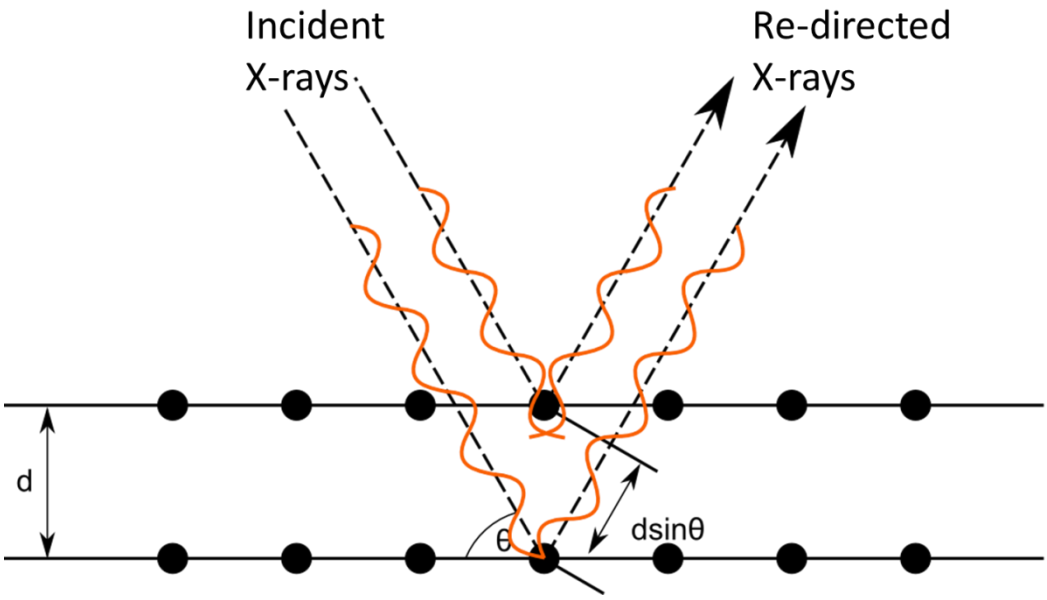

Figure 4.2 *Schematic description of Bragg's Diffraction Law (http://www.met.reading.ac.uk/pplato2/h-flap/phys7_1.html)*

where θ is the diffraction angle, *n* is an integer which refers to the order of reflection, (*hkl*) are the Miller indices of the crystallographic plane and d_{hkl} is the interplanar spacing between planes. It is shown that, for the specific angles θ_n for which satisfied Bragg's law to form a constructive interference of scattered radiation, the magnitude of scattering vector q is inversely proportional to the lattice spacing d.

$$\boldsymbol{q = n\frac{2\pi}{d}} \qquad \textbf{Equation 4.3}$$

where *d* is the distance between lattice planes and n is the integer corresponding to the diffraction peak. It is emphasized that d does not have to be of atomic dimensions: in the current project, the D~65-67 nm axial periodicity (~100 times larger than atomic dimensions) of the

collagen meridional stagger gives rise to diffraction peaks in the small-angle regime (SAXD).

In this thesis, SAXD and wide-angle X-ray diffraction (WAXD) will refer to diffraction peaks arising from periodicities at the nano- and molecular scale respectively. Small-angle X-ray scattering (SAXS) will, in contrast, refer to the diffuse scattering arising from the shape of the fibrils at the nanoscale. Usually, the distinction between SAXD [201] and WAXD [204] is defined via a Bragg angle: SAXD/SAXS refers to low scattering angles (< 5° usually), whilst WAXD refers to diffraction at larger Bragg angles [202]. Switching from SAXS (or SAXD) to WAXD or vice versa is readily by adjusting the sample to detector distance.

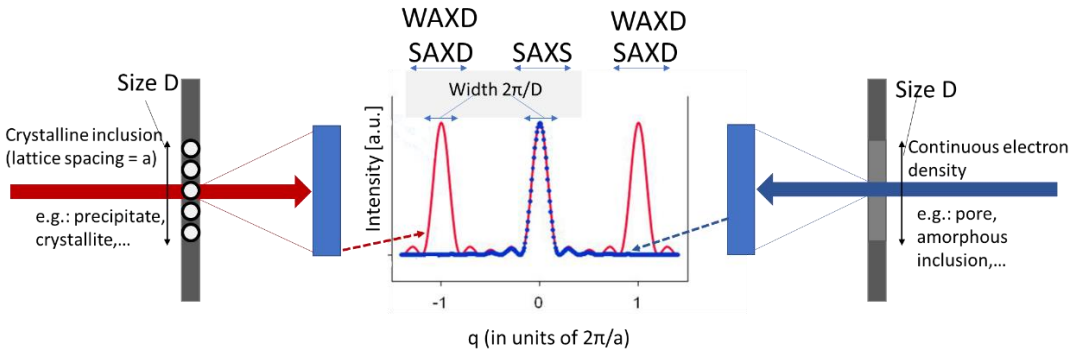

Figure 4.3 *The principles for SAXS and WAXD. Size of crystal lattice denoted as D with an inter-atomic spacing of a. After lecture notes from Oskar Paris and Peter Fratzl.*

The main theoretical principles of small angle X-ray scattering was pioneered by André Guinier in 1930s following his work on metallic alloys [202]. Later in 1960s, this method became more important in the research of biomolecules in solution, as it can provide structural information for the overall geometry and inter-molecular structure from the diffuse scattering when the crystalline structure is absent. Packages such as DAMMIN or other computational tools currently can solve structures of biomolecules in solution [205]. When

combined with high brilliance synchrotron radiation, SAXD can be applied to real time investigations on interaction and the conformational changes occurring at the nanometre scale for materials including polymers, fibre, metals and biological materials.

Theoretically, the scattering intensity is given as:

$$\mathrm{I}(\vec{q}) = \mathrm{C}\frac{d\Sigma}{d\Omega}(\vec{q}) = \frac{C}{V}\left|\int_V \rho(\vec{r})\exp(iqr)\,d^3\,\vec{r}\right|^2 \qquad \textbf{Equation 4.4}$$

where ρ(r) is the electron density distribution, q is the scattering unit vector (definition shown in **Figure 4.1**), V is the volume of specimen, and C is a scaling constant corresponding to the experimental setup and the detector used. The term in the bracket is the Fourier transform of electron density ρ(**r**). The integral is a three-dimensional spatial integral over the entire space.

Equation 4.4 is a three-dimensional vector field in reciprocal space. For SAXS, the 2D scattering pattern observed (**Figure 4.4**) is a 2D planar slice through that field, oriented perpendicular to the X-ray beam [206]. The pattern captured by an areal gas-filled or CCD detector [207] perpendicular to the incident X-ray beam. Whilst the specifics of the 2D pattern depend sensitively on the details of the electron density distribution ρ(**r**), some general qualitative and semi-quantitative statements hold on the relation between the characteristics of the SAXS pattern and the size, shape and the scattering volume of nanoparticles. Firstly, dimensions of the SAXS pattern are inversely correlated with sizes in real-space, with a broadened scattering signal inversely proportional to the dimensions of the scattering object in the real space (**Figure 4.4**). As the SAXS pattern is three-dimensional, by rotation of the specimen information on the dimensions in different

directions can be obtained. For a simple rod without internal spacing, as shown in **Figure 4.4**, a long cuboid (B<<H) would produce an elliptical intensity distribution, which is wide in the horizontal direction and narrow vertically, with the following relations:

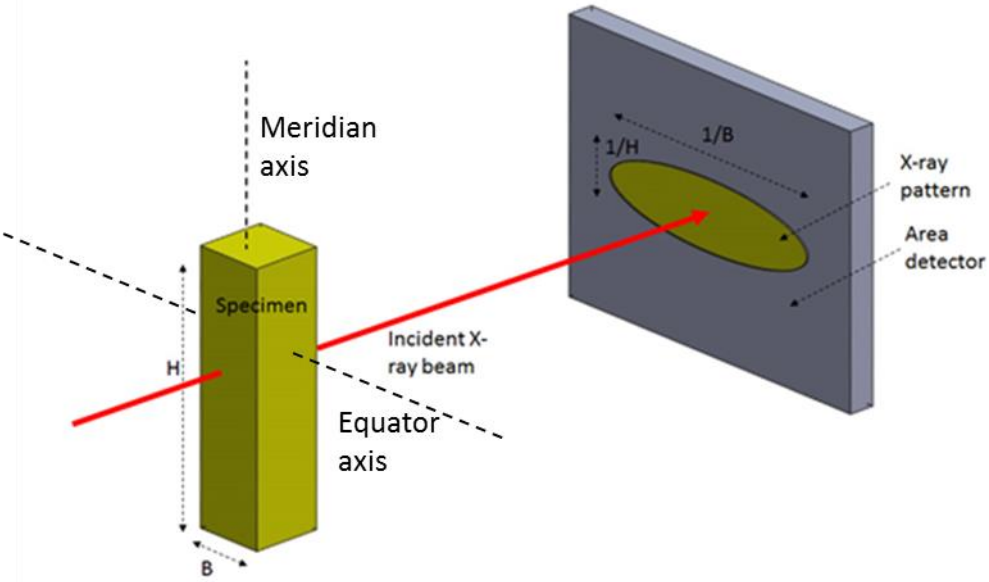

Figure 4.4 Correlation between real space and the reciprocal space. *Schematic representing the SAXS and SAXD pattern that is obtained from a fibril that has a length L, where the reciprocal space is inversely proportional to the real space*

$q_y \propto \frac{2\pi}{H}, q_x \propto \frac{2\pi}{L},$ **Equation 4.5**

where H is the height and B is width of the scattering object.

For those nanoparticles with crystalline structure (e.g.: the collagen fibril shown in **Figure 4.5**), the characteristics of the small-angle X-ray diffraction (SAXD, distinct from the general SAXS pattern) are dependent on (a) the periodicity (b) the lateral and horizontal dimensions of the repeating units. As the X-ray scattering pattern is

the Fourier transform of the electron density distribution in real space, for the case of an array of collagen fibrils in real space, the X-ray intensity in reciprocal space is the convolution of the fibril (cylinder) and internal lattice spacing. Note that here, the lateral packing relates to the fibrils and not to the internal quasi-hexagonal packing of molecules inside a fibrils [23]. The formula for the X-ray scattering of an ordered lattice-like structure (in the plane transverse to the fibril axis) is therefore

$$I(q_z, \boldsymbol{q}_\perp) = \left| \int dq_z e^{iq_z z} \int d\boldsymbol{q}_\perp e^{i\boldsymbol{q}_\perp \cdot \boldsymbol{r}_\perp} \rho(r_z, \boldsymbol{r}_\perp) \right|^2$$

Because the electron density is periodic on the lattice in the $\mathbf{r}_\perp$ plane, the second integral can be written as

$$\int d\boldsymbol{q}_\perp e^{i\boldsymbol{q}_\perp \cdot \boldsymbol{r}_\perp} \rho(r_z, \boldsymbol{r}_\perp) = \sum_m^N e^{i\boldsymbol{q}_\perp \cdot \boldsymbol{r}_{m\perp}} \int d\boldsymbol{q}_\perp e^{i\boldsymbol{q}_\perp \cdot \boldsymbol{r}'_\perp} \rho(r_z, \boldsymbol{r}'_\perp)$$

where the second integral is over the unit cell in the transverse plane, and (assuming finite density in the fibril and zero outside) is nonzero only within the fibril ($r'_\perp$<R). It can therefore be readily seen (as shown in, e.g., [208]) that in reciprocal/Fourier space, the equatorial diffraction pattern is the product of the cylinder (fibril) transform multiplied by the interference function of the quasi-hexagonal lattice, deriving from the lateral arrangement of collagen fibrils [208]. While a perfect lateral ordering of fibrils in the transverse plane would imply a series of higher order peaks (as is found in tissues like cornea), in many collagenous tissues, the lateral ordering is never a perfect crystalline lattice, and no clear peak is observed, with disorder and possible variation in fibril diameter simplifying the small angle X-ray equatorial pattern to a diffuse intensity. Experimentally, this is the

case for MCT-tissue (as will be seen in the subsequent Chapters). As shown in **Figure 4.5**, the most noticeable banding patterns were symmetrically distributed around the elongated disk presented in the middle, and are meridional lines/arcs separated by $2\pi/D$. The central elongated disk reflects the form factor of the fibre (the cylinder transform referred to earlier), and its extent on the q_x and q_y directions is related to the radius and fibril length, respectively. Further, there is a diffuse peak at larger equatorial wave-vectors (q~40 nm^{-1}; not shown), related to the lateral spacing of tropocollagen molecules within the fibril [209].

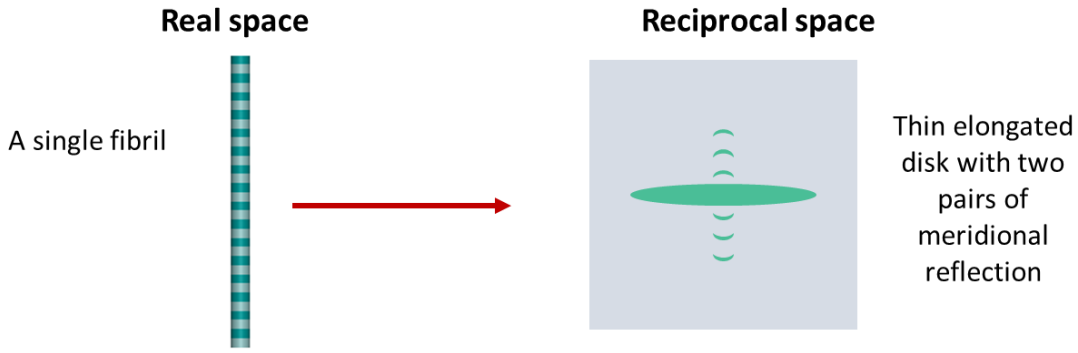

Figure 4.5 Correlation between real space and the reciprocal space of a single fibril. *Schematic representing collagen fibril (left) with its "finger print" D-banding SAXS pattern (right)*

The variation in SAXD patterns from tissues with fibrillar collagen arrays, in terms of the qualitative differences of angular anisotropy, are simply categorized as shown by **Figure 4.6**. Assume the scattering volume and the electron density of each fibril are the same. Where the fibrils are in parallel to the directions of the beam one would see a thin elongated disc or ellipse shaped with narrow arcs intensity distribution oriented to the fibril axis (**Figure 4.6A**; the same as in **Figure 4.5**). However, when there are multiple directions that the fibrils can be oriented at (termed a degree of "misorientation"), the SAXD pattern is an angularly weighted superposition of patterns of the type shown in

Figure 4.6A. This is shown in **Figure 4.6B**, where one observes a more rounded ellipse in the central SAXS regime along with broadened meridional SAXD arcs. This is because as the sum of narrow ellipses with meridional layer-lines oriented in different directions is (approximately) a broadened elliptical pattern and a wider angular range for the meridional arcs. Finally, **Figure 4.6C** shows the case when there is no single predominant orientation of fibrils, the diffraction pattern is less anisotropic and tended to become a circle, concurrently the extent of arcing is increased. It should be noted that such increasing isotropy can reflect the presence of multiply oriented layers of fibrils (individually well oriented) at the tissue/lamellar level above a few microns, if the pattern arises from the X-ray beam intersecting multiple such zones. Such a scenario can occur in collagenous layered tissues like vertebrate skin, artery walls or the sea cucumber dermis (the subject of the current work). However, it should be kept in mind that increased randomness of microfibrils or fibrils can also occur at the micron- and sub-micron scale, and the combined effect at both levels cannot usually be deconvoluted if the

X-ray beam passes through multiple tissue zones.

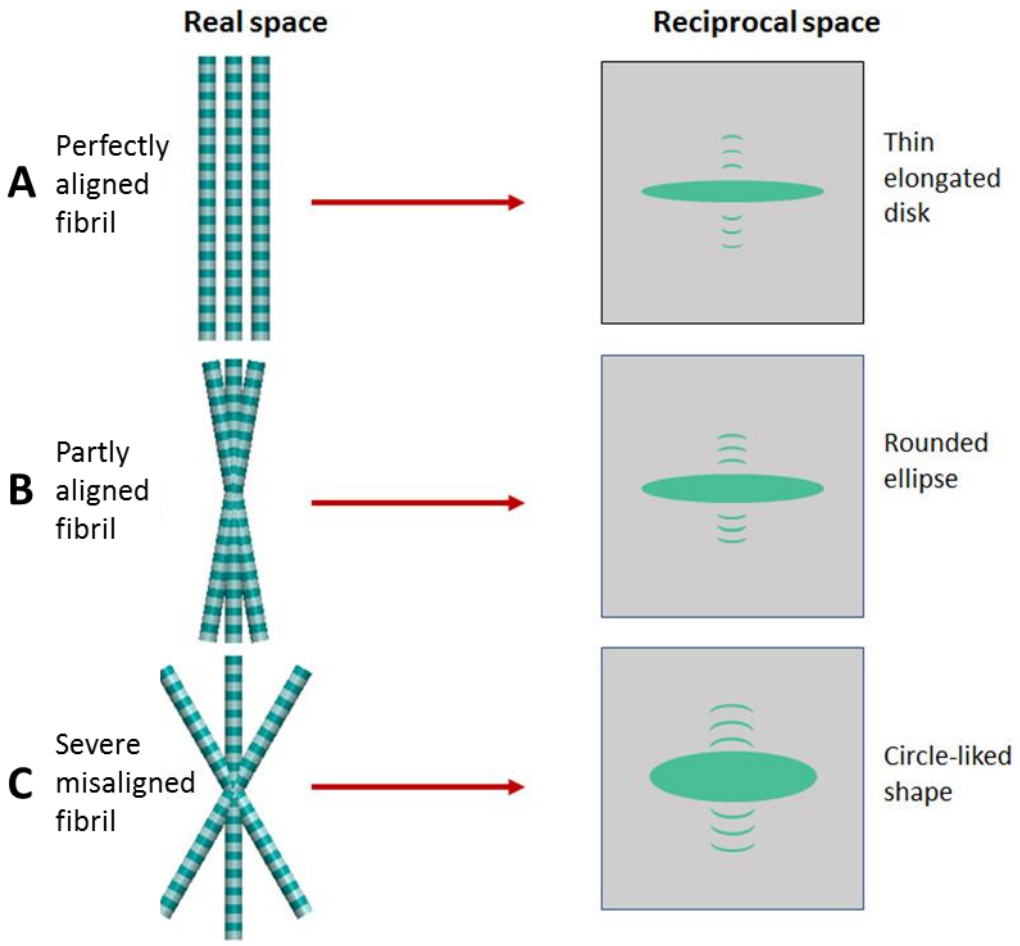

Figure 4.6 *Correlation between real space and the reciprocal space of a group of fibrils with different degree of order. A) perfectly aligned fibrils, B) Partly aligned fibrils, C) Severe misaligned fibrils.*

4.3 Characteristic SAXD patterns of mammalian type I collagen

The structure of collagen molecules at the molecular and fibrillar level is characterized by an extensive degree of ordering, which leads to a complex and rich structure in the reciprocal space of scattering patterns. From this structure, which the size, shape and orientation of the molecules/fibrillar aggregates can be derived, in principle. The Hodge – Petruska model [210] is the most widely accepted schema for explaining the axial banding pattern of 64-67 nm in fibril (D-period).

Molecules are aggregated into staggered fibril array with ~300 nm and ~1.5 nm length and width respectively. All collagen fibrils are constituted by gap and overlap regions. At the starting point of first row, the second collagen molecule had an axial displacement of 0.625D (~40 nm) compared to the first one, when moved to next row, all molecules were shifted by D (~67 nm), leading to a 0.375D (~27 nm) of overlapping region (**Figure 4.7**). Following this gap-overlap fashion, collagen molecules were organised in a staggered manner side by side. The width of the gap and overlap region, was denoted as the D-period (~65-67 nm typically, depending on the tissue type and its hydrated state). In terms of SAXD patterns, this regularly fluctuating electron density profile is similar to a 1-dimensional lattice. The fraction *f* of the unit cell which is in the overlap (O) zone is O/(O+G) = O/D and the fraction 1-*f* in the gap (G) zone is G/(O+G) = G/D.

A typical two-dimensional SAXS pattern from a widely studied mammalian type I collagen tissue (rat tail tendon) is shown in **Figure 4.7**. The meridional diffraction shown in the centre is corresponding to the D period of collagen fibrils. And the equatorial diffuse scattering is due to the lateral spacing d_m between two adjacent collagen molecules.

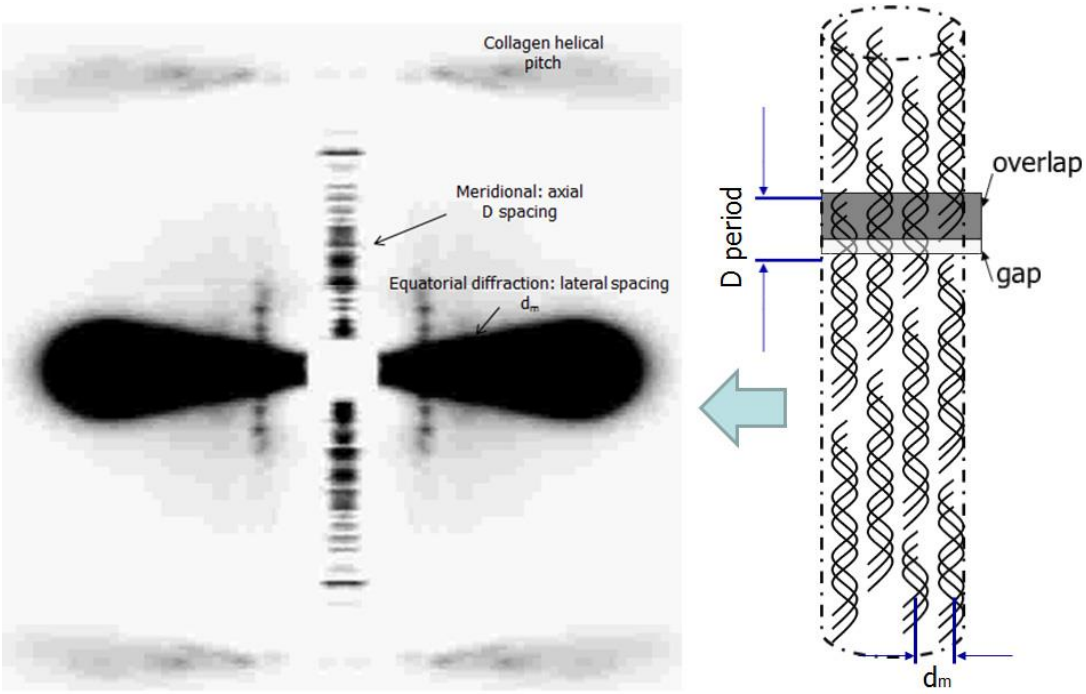

Figure 4.7 X-ray scattering pattern of a collagen fibril and a schematic of a fibril. *The meridional diffraction patterns are resulted from the axial spacing D of a fibril while the equatorial diffraction patterns arise from by the lateral spacing* d_m.

4.3.1 *In situ* SAXD nanomechanics on collagenous tissue

In situ SAXD nanomechanics refers to the measurement of mechanical changes at the fibrillar level, via analysis of structural changes in the SAXD pattern as external mechanical loads are applied. The use of X-ray scattering/diffraction method combining with mechanical deformation was first introduced by R. Hosemann, T. Nemetschek et al. in 1970s by monitoring the elongation of fibril and molecules under strain [211, 212]. In the 1980s, Nemetschek and co-workers started to work on the high-brilliance synchrotron X-ray techniques combing with *in situ* mechanical deformation to investigate the changes in fibrillar structure and molecular spacing during mechanical deformation [213, 214]. They exploited the higher intensity of synchrotron X-ray sources compared to lab sources (exposure time: seconds vs hours) to measure the *real-time* collagen

structural changes at fibrillar and molecular level during mechanical testing (**Figure 4.8**). We now review how the 2D SAXD pattern from collagenous tissues is analysed to obtain changes in fibril strain, orientation and ordering.

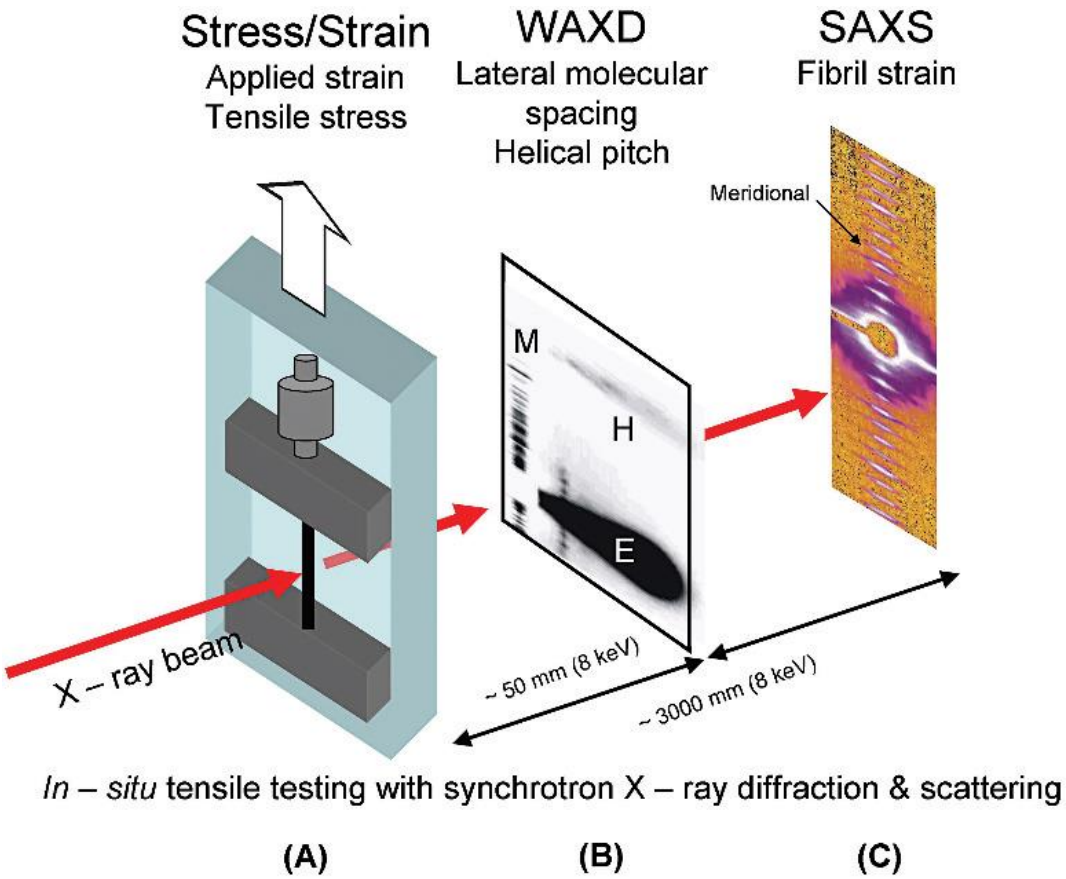

Figure 4.8 The schematic representation of in-situ mechanical testing combing with high brilliance synchrotron X-ray technique *(A) Specimen was mounted in a tensile tester machine, arrow shows the direction of external load. (B) The representative schema shows the molecular structural information including the molecular lateral spacing and helical pitch, with small sample-to-detector distance.(M: meridional signal; E: equatorial signal; H: collagen helix pitch signal) (C) The representative schema shows the large-scale structural information such as the D period of fibril, with longer sample-to-detector distance[23].*

4.3.1.1 SAXD data and evaluation

X-ray diffraction patterns are quantitative 2D images or bitmaps of intensity. To reduce the data to forms which can be fitted with models of the nanostructure, these 2D patterns – which are experimental realizations of the idealized schematics shown in **Figure 4.6** – are usually transformed to a polar coordinate system (q,χ), where the q-direction is along the radial direction and the χ-axis is along the azimuthal direction. Subsequently, the intensity is averaged either radially or azimuthally to produce intensity line profiles $I(q)$ or $I(\chi)$, which can be fitted to models to determine parameters like the fibrillar-D period, relative order and disorder in the tissue as well as degree of angular misorientation. Such data reductions are carried out by means of software such as Fit2D [215] or DAWN [216], which have graphical user interfaces (GUIs) and the capacity for batch processing of multiple SAXD patterns using macros or scripting routines. In what follows we will describe the data reduction and fitting process for the meridional collagen SAXD pattern in both radial and azimuthal directions. In Fit2D, the SAXD pattern azimuthally were averaged across a sector of 360º angular width, with centring along the vertical (tensile stretch) axis and with a wavevector range from 0.18nm^{-1} to 0.75nm^{-1}. Arising from meridional stagger D of collagen molecules in the fibril, the Bragg peaks were identified qualitatively from the position expected (**Figure 4.9**)

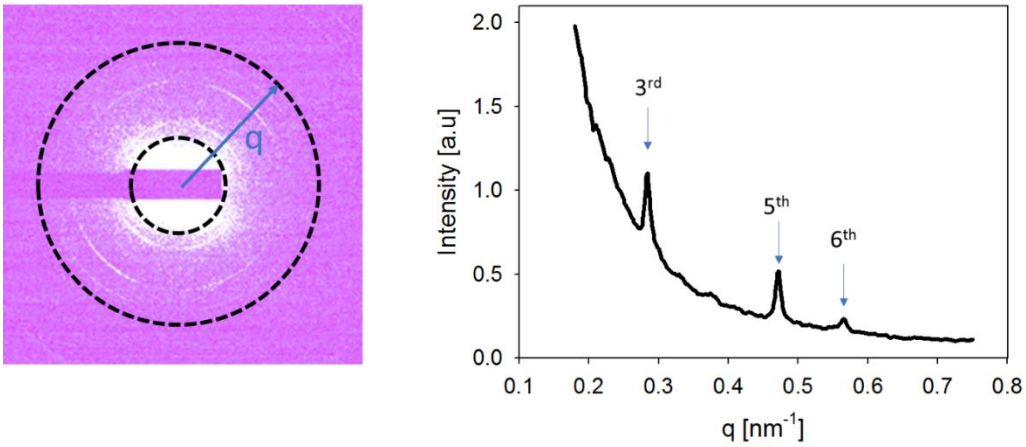

Figure 4.9 *Left: 2D SAXD pattern from stretched sea cucumber (Holothuria edulis) dermis with showing the discrete reflections arising from the collagen D period; Right: Averaged integrated intensity profile in the radial directions in the angular region denoted in right.*

4.4 Synchrotron techniques

We now describe the operational principle of synchrotrons, which for the purposes of this thesis are intense sources of X-rays which can be used for measurements of SAXD patterns from collagen with high temporal and/or spatial resolution. The basic concept of a synchrotron is that accelerated electrons emit high intensity electromagnetic radiation, and when accelerated to near relativistic speeds emitted radiation is focussed into narrow cones along the direction of motion, effectively forming beams [217]. To generate this state of accelerated electrons, there are three components for a synchrotron: the linear accelerator, the booster and the storage ring (**Figure 4.10**).

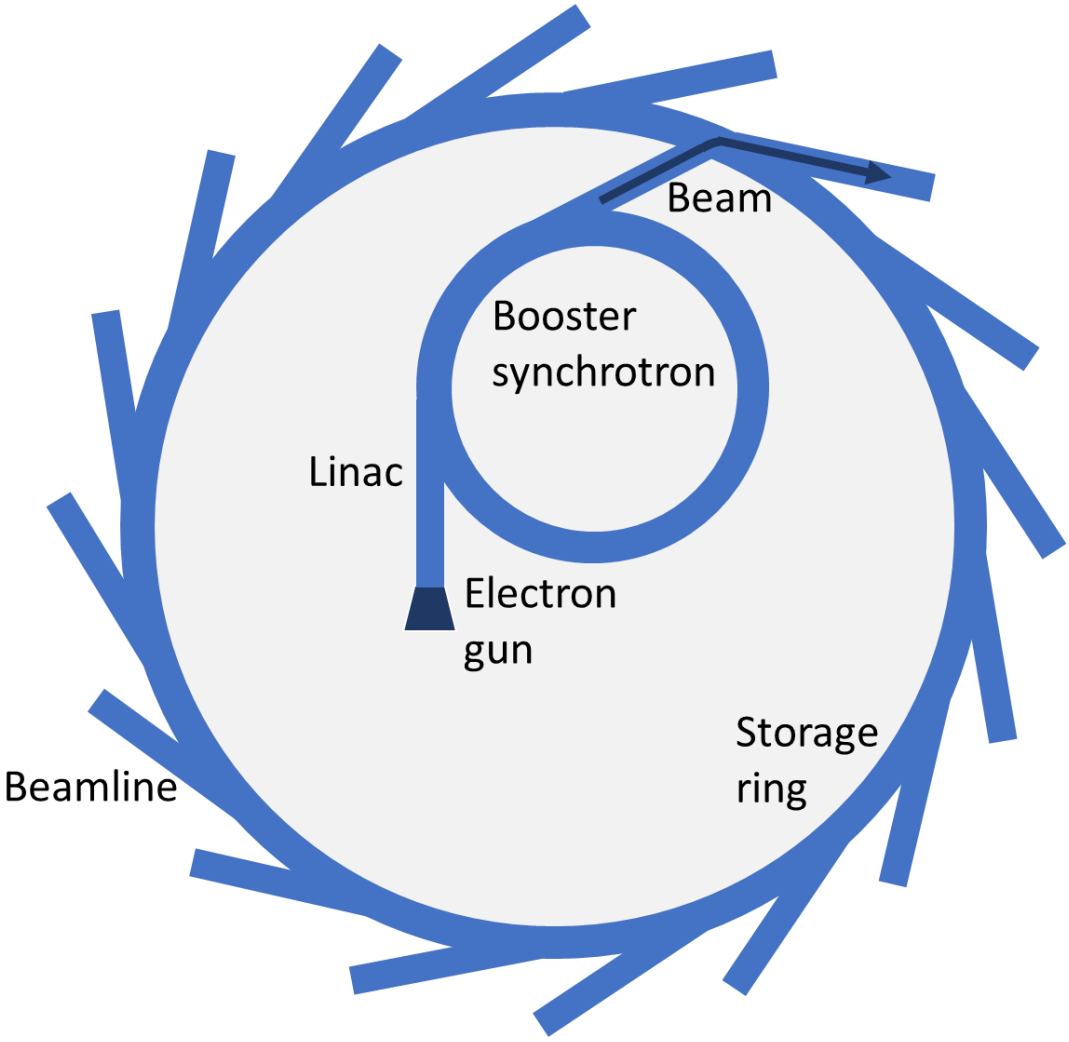

Figure 4.10 *Representative schema of Synchrotron facility, electron gun, linear accelerator (Linac), booster, storage ring and the beamline are shown.*

Within the ring, electrons will be accelerated to a speed which is close to the speed of light. Then, synchrotron light will be guided through to the beamlines which are placed at tangents to the storage ring. A beamline is essentially an end-station for the X-rays being emitted from the storage ring, where optics and other instrumentation are used to shape the beam into a form suitable for the user's experiments.

There are three main components for one beamline: an optics hutch, an experimental hutch and a control room [218]. The optics hutch is where the filtering of various wavelengths provided by the

synchrotron light occurs, by means of optical lenses – such as multilayer Bragg mirrors – together with focussing of X-ray beam (additional focussing can occur in the experimental hutch). In the experimental hutch, the X-ray beam (in a shape and size suited for the user's experiment) will be applied to the specimen for the specific experiment, and (sometimes more than one) X-ray detectors (like CCD-detectors) are used to capture the SAXS or WAXD pattern. In the μ-Spot beamline at BESSY II, detectors like, MAR Mosaic or RAPID detectors are used [207]. The control room, as the name suggests, is where the user-scientists control the experiment from remote control computers, cameras and other devices. The necessity of a separate control room is due to the radiation health-hazard posed by a high-intensity X-ray beam inside the experimental and optics hutch, which implies that no scientists can be in these rooms at the same time the experiment is happening.

Synchrotron sources have been in use since the early 1960s, and most currently available synchrotrons are denoted as third-generation synchrotron sources (still newer sources, such as free-electron lasers, are not covered here) [217, 219]. Third generation synchrotron sources can focus to very small cross-sections, with the order of microns and below. Synchrotron radiation can allow a multitude of physical parameters to be imaged because synchrotron sources cover almost the whole spectrum of electromagnetic radiation from infrared (wavelength from 10 to 0.10 nm) to hard X-rays (wavelength from 0.10 to 0.01 nm) [219, 220]. Advances in synchrotron technology have been mainly in the intensity and brilliance of the X-rays produced, combined with advances in optics to generate highly focused beam sizes and increased sensitivity of detectors. Brilliance is

an important measurement of quality of the beam source [218] and can be defined quantitatively as:

$$Brilliance = \frac{Photons}{Seconds \cdot mrad^2 \cdot mm^2 \cdot 0.1\%BW}$$

where "seconds" refers to the number of photons produced by the source per second, "mrad" is the angular divergence of the photons, "mm^2" refers the cross-sectional area of the beam and 0.1BW refers to the photons falling within a bandwidth (BW) of 0.1% of the central wavelength or frequency.

In order to localize the structural information (e.g. from X-ray scattering) from a specific microscale region in the tissue (position-resolved experiments), we need a small beam at the specimen position and a low beam-divergence in order to minimize contributions from the direct beam at low wave-vectors (particular in the case of small angle diffraction) [221]. With lab sources like rotating-anode generators, it is found that a practical lower limit to beam size is ~100 μm [222]. Led by these developments, many third-generation synchrotrons with microfocus SAXS/WAXD beamlines have been built within these years, such as the μ-Spot beamline at BESSY II (Berlin, Germany), and BL I22 beamline at Diamond Light Source (DLS) (Harwell, UK), and the beamline ID02 European Synchrotron Radiation Facility (ESRF) (Grenoble, France) [223, 224]. These beamlines have introduced several cutting-edge developments in instrumentation (high-throughput beamlines such as for solution SAXS, robotic arms etc.) to the field of synchrotron-related materials research, which include a wide range of materials from metals through carbon nanotubes to polymers and biopolymers.

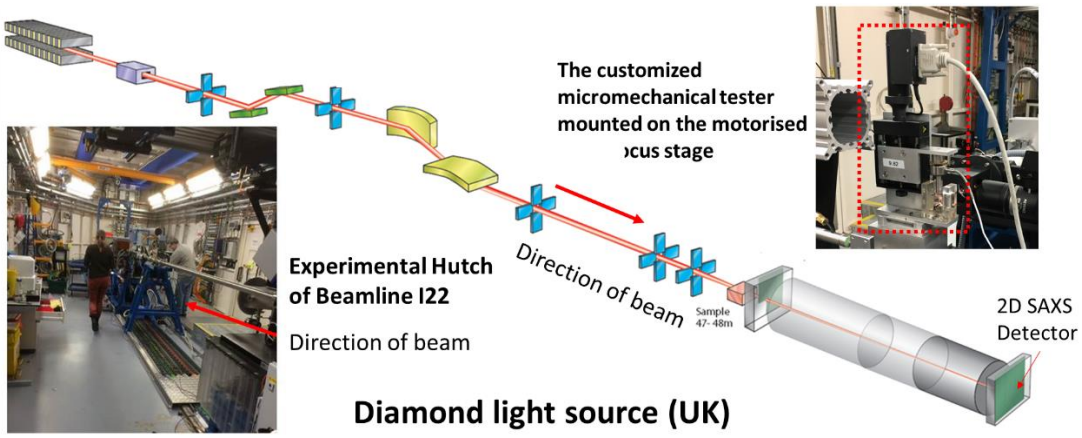

Figure 4.11 *An example layout of beamline (I22, Diamond Light Source). (Schema in the centre was taken from: http://www.diamond.ac.uk/Beamlines/Soft-Condensed-Matter/small-angle/I22/specs.html)*

4.5 Micromechanical Testers for Soft Collagenous Tissue

Here we describe the micromechanical test device used to carry out *in situ* synchrotron SAXD tests. The overall tester-frame (**Figure 4.12**), including subsystem 1 and 2, was designed as part of a preceding PhD by Yi Zhang [225] to test a stiffer, calcified tissue (arthropod cuticle). In the current project, parts of the system, both hardware and software, including sample grips, fluid chamber, fluid exchanging system and the relevant control software, were modified to meet the requirements of testing sea cucumber dermis tissue.

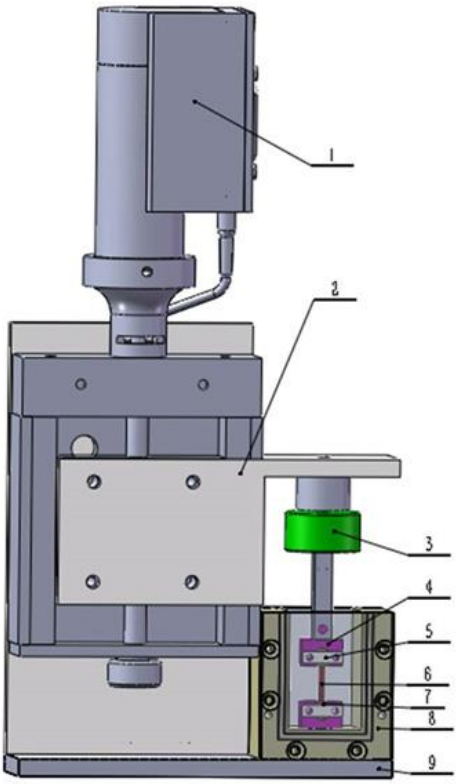

Index	Name
1	M 126.DG1 Motor
2	Arm for holding load cell
3	Load cell (110N)
4	Upper sample holder
5	Sample gripping piece
6	MCT specimen
7	Bottom sample holder
8	Fluid chamber
9	Base

Figure 4.12 *3D assembly schema of micromechanical testing device, suitable for synchrotron SAXD or WAXD at the beamline.*

We first review the special considerations needed when designing a tester for a synchrotron beamline:

The tester needs to be as compact as possible. This is because of the space limitation on the microfocus stage at I22, where only 100 mm is available between the beam inlet and the diode. The width of the stage should be about the similar size to fit. The usual large mechanical testing rigs like Instron™ etc. are widely used in different kind of mechanical testing in materials-research labs, including tensile, compression, cyclic loading with ranges of applications for different materials. However, they are not ideal for synchrotron measurements due to their lack of portability and large size compared to the limited space available in beamlines.

Stress ranges from 0-30 MPa and a large tissue strain ranging from 0-120% needs to be measurable, as these correspond to the tensile deformation characteristics of MCT-containing tissue (**Chapter 2**). As sample dimensions are ~1 mm^2, the load cell should be capable of measuring loads of 30 MPa $\times$ 10^{-6} m^2 = 30 N. In contrast to mineralized tissues like cuticle [225] and bone [226, 227], the large tissue strains and much lower stiffness of the sea cucumber dermis (~10s of MPa vs GPa for bone; **Chapter 2**) mean that strain measurements from motor-grip displacements are sufficient to determine strain, without needing video extensometry.

The tester should contain a fluid chamber, which can be combined with a syringe pumping system (**Chapter 6**), who contains two solutions, to introduce different fluid environment to MCT-containing specimens and thereby inducing reversible softening or stiffening of tissue. Therefore, the main requirement for the fluid-chamber is that it should be water-tight. Furthermore, X-rays get attenuated in water and degrade the signal quality [228]. Hence the fluid chamber should be as flat as possible in the direction of the X-ray beam, to provide the X-ray beam a short pathway (~ mm) between the inlet and outlet to reduce the beam absorption by the fluid.

4.5.1 Sub system 1- Motorised linear encoder stages

The high-resolution M126.DG1 motor was bought from Physik Instrumente (PI) Ltd, UK (**Figure 4.13A**). This motor has a large travel range of 25 mm and can sustain a maximum stress up to 50N, with minimum incremental motion down to 0.1 μm and a maximum rate up to 15 mm/s. A Mercury DC motor controller (C-863.11, Physik Instrumente Ltd, UK) was applied to control and record the

displacement of the motor, from which the tissue strain of specimen can be determined (**Figure 4.13 B**).

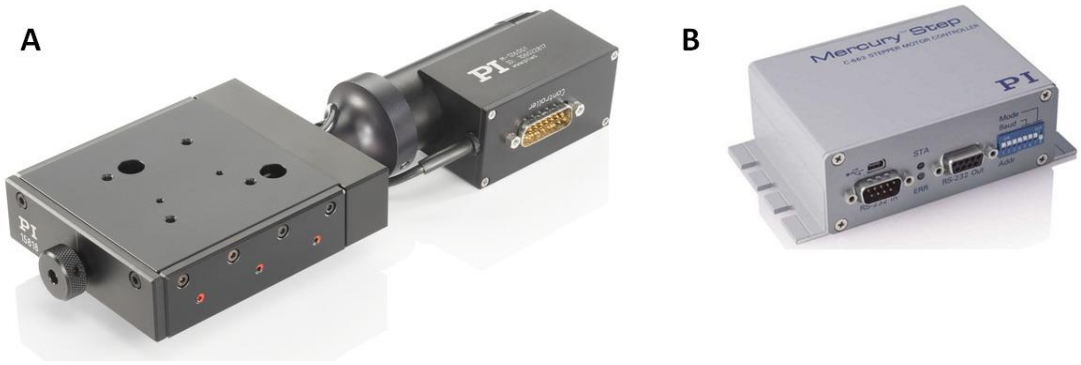

Figure 4.13 *(A) Motorised linear stage (M-126.DG1) with crossed roller used for the micro-tensile tester, and (B) motor controller (C-863 Mercury Servo) used for the micro-tensile tester. (Images are from PI website, http://www.physikinstrumente.co.uk/).*

4.5.2 Subsystem 2 – Load cell

A load cell (Type SLC31/00025; maximum 110N load) from RDP Electronics Ltd (West Midlands, UK) was used as part of the system (**Figure 4.14**). An additional load cell amplifier equipped with a USB plug directly connecting to the PC (Mantracourt Electronics Limited, UK) was used to amplify the signal. Before starting the mechanical testing, two-point calibration of the amplifier (Mantracourt Electronics Limited, UK), software, must be processed to ensure the correct reading.

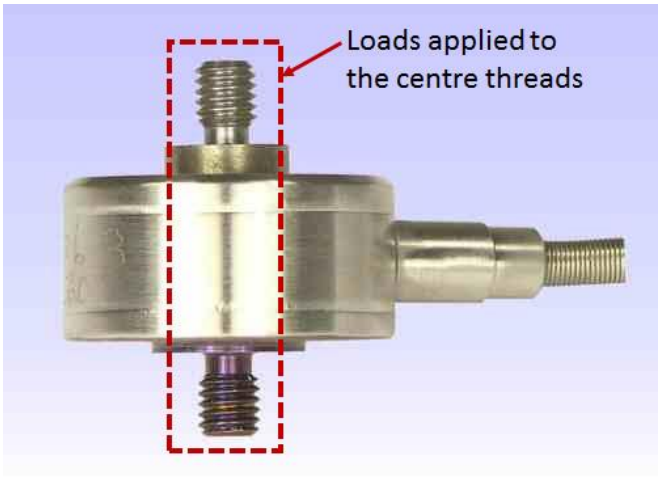

Figure 4.14 *Load cell (SLC31/00025) used for the micro-tensile tester. Measurement transducer from the stress applied to the thread.*

4.5.3 Subsystem 3 – Sample grips

A conventional sample grip, made from medical grade stainless steel, with a length of 14.5 mm and width of 8 mm was designed for the holding MCT specimens during the mechanical test (**Figure 4.15**). Like other hydrated soft biomaterials, MCT specimen is slippery and hard to clamp. To get a proper gripping, without damaging, additional friction is needed. This can be simply done by adding a sandpaper piece onto the gripping face. M2 screws were used to tighten the grips and the sample holder.

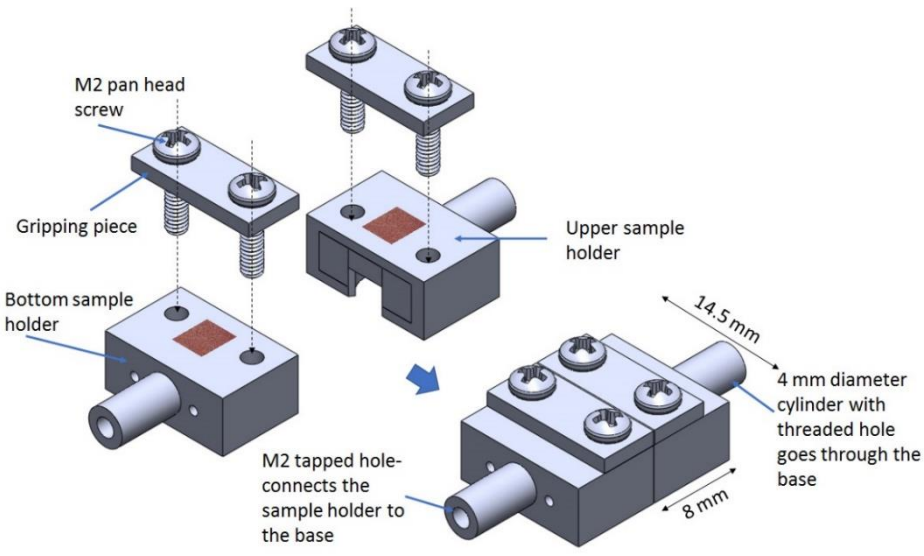

Figure 4.15 *Sample grips for tension made by stainless steel. Sand paper were shown in dark red on the surface of sample holder.*

4.5.4 Subsystem 4 – Fluid chamber

The fluid chamber is used for providing MCT specimen a physiological condition that close enough to induce active force generation, by incubating specimens in different chemical stimulation agent. Besides, the fluid volume for in-let and out-let X-ray beam path should be minimised to avoid over-absorption of beam intensity. Therefore, two protruding tubes were added into the front and back window of the chamber (**Figure 4.16** and **Figure 4.17**). The extruded tube on the back window (**Figure 4.16**) is manufactured to be adjustable, capable of moving back and forward, to ensure the most suitable experimental set-up. A rubber O-ring is used to avoid fluid leakage during the mechanical tests. Tubes are covered with a thin layer of Ultralene, which is relatively high transmittance to X-rays. All components are made from medical rated stainless steel.

To enable the function of fluid exchange, a syringe pumping system, which will be demonstrated in detail in **Chapter 8**, was manufactured and to collaborate with fluid chamber.

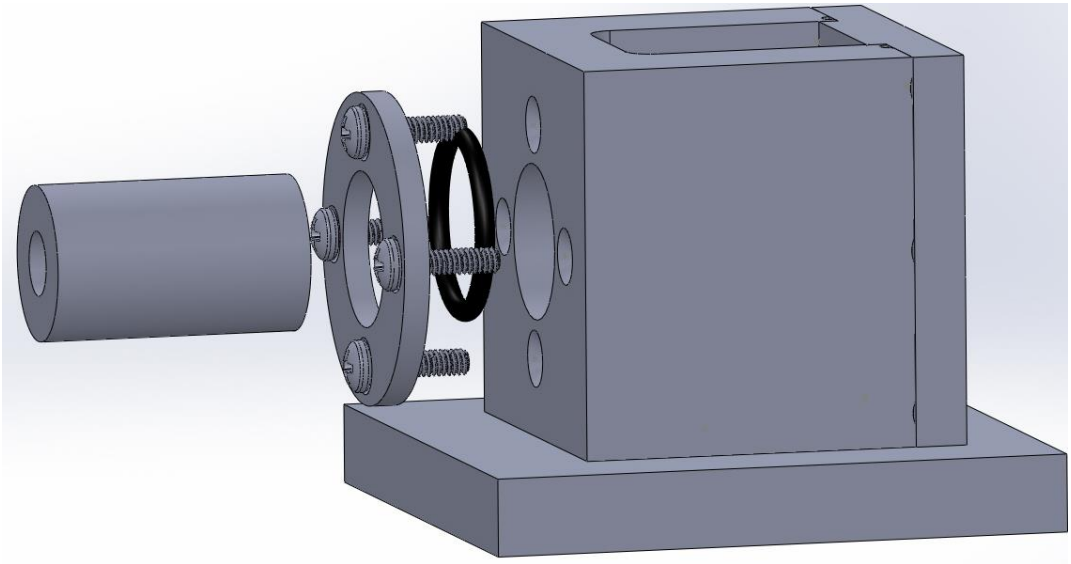

Figure 4.16 *Schematic representation showing the back side of the fluid chamber, the adaptable tube on the left will be stabilized and locked by the hollow part and O-ring with 4 M2 screws.*

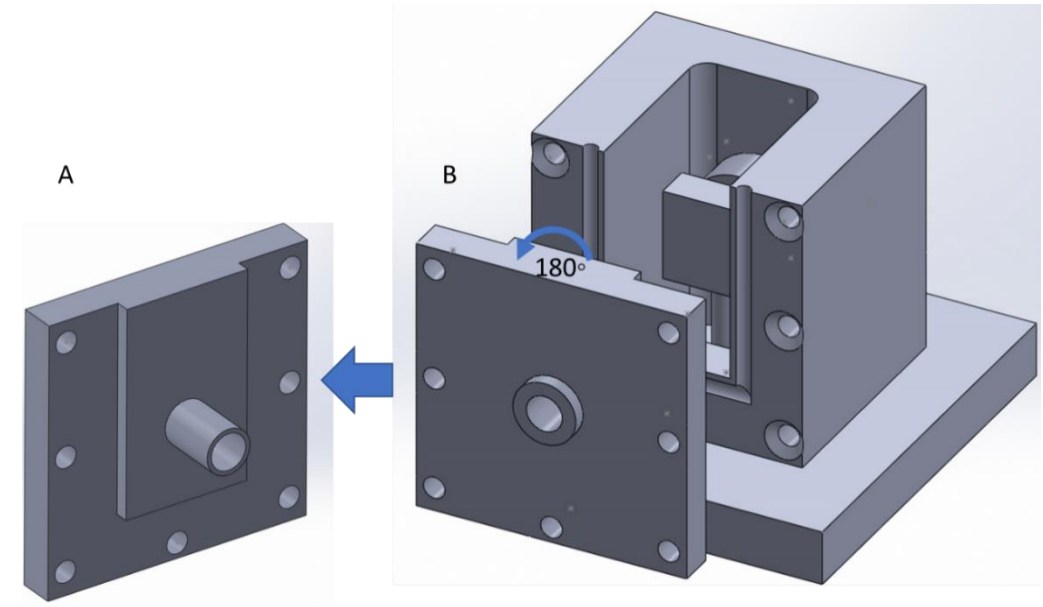

Figure 4.17 *Schematic representation showing the front side of the fluid chamber.*

Chapter 5 : Deformation mechanics of freeze - thawed mutable collagenous tissue demonstrated at the nanoscale

5.1 Introduction

The development of new mechanoresponsive biomaterials capable of interacting with and substituting the function of natural tissues such as skin or nervous tissue is a major current goal of biomedical engineering. Such materials can serve as matrices for tissue engineering of soft tissues [1], and in acting as synthetic muscle replacements generating active forces, as in cardiac pacemakers. A very promising approach to this goal is the development of "biomimetic" materials whose architecture is inspired by natural biological systems with adaptive mechanical properties. In this regard, the mutable connective tissue (MCT) of echinoderms like sea cucumber, which could enable active force generation and exhibit the remarkable capability to rapidly change (in ~1 s) its mechanical and viscoelastic properties [4, 5], is a good example of stimuli-responsive material in natural biological system.

As explained in **Chapter 1**, collagenous tissues have a hierarchical structure from the macroscopic down to the molecular (~Angstrom) and supramolecular (~nanometre) length scales. To investigate the structure at the smallest length scales, techniques like diffraction and scattering are applied with X-ray radiation of wavelengths of the order of the molecular spacings. However, prior to application of *in situ* x-ray methods to viable MCT, it is necessary to validate both i) whether the collagenous tissue in MCT is at sufficient density and degree of organization to give the expected SAXD pattern, and ii) whether the changes in SAXD patterns, on macroscopic loading, are in line with

the expected peak shifts and other changes described in the previous **Chapter 4**. Hence, in this proof-of-concept study, we will investigate whether, using freeze-thawed (nonviable) MCT, at the high X-ray flux of synchrotron sources can enable measurable analysis of time-resolved nanoscale mechanics of MCT-containing sea cucumber dermis during macroscopic mechanical deformation.

5.2 Methods and materials

5.2.1 Methods

In order to localize the structural information (e.g. from X-ray scattering) from a specific microscale region in the tissue (position-resolved experiments), we need a small beam at the specimen position and a low beam divergence in order to minimize contributions from the direct beam at low wave-vectors (particular in the case of small angle diffraction) [201]. With lab sources like rotating anode generators, it is found that a practical lower limit to beam size is ~100 μm [229]. To obtain the monochromatic X-ray beam with size down to submicron level, modern X-ray multilayer mirror optics were used [229]. Led by these developments, many third-generation synchrotrons with microfocus SAXS/WAXD beamlines have been built within these years, such as the μ-Spot beamline at BESSY II (Berlin, Germany). These beamlines have introduced several cutting edge developments in instrumentation (high throughput beamlines, robotic arms etc.) to the field of materials research, which include a wide range of materials from metals through carbon nanotubes to polymers and biopolymers [230].

As an example, **Figure 5.1** shows a schematic representation of the SAXS/WAXD/XRF setup at the MuSpot beamline (BESSY II, Berlin, Germany). A monochromatic X-ray beam interacted with the specimen and then the scattered X-ray photons were then detected by an MAR detector. Depending on the distance between sample and detector (at a typical wavelength of λ ~ 1Å), either a WAXD pattern (distance ~ 5-30 mm) or a SAXS pattern (distance ~ 500 -5000mm) can be acquired [230].

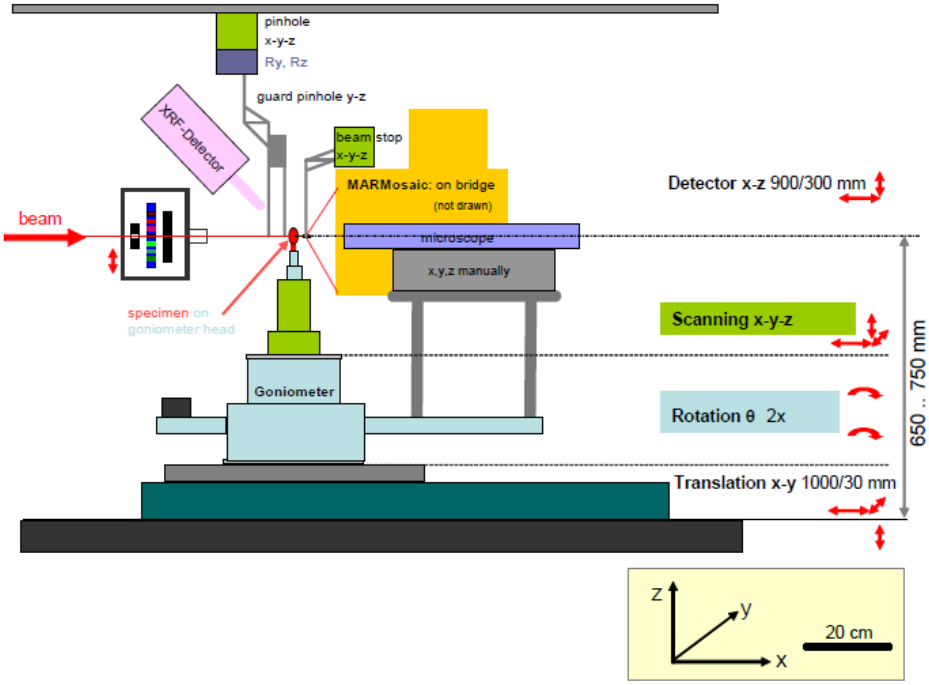

Figure 5.1 *Experimental setup for scanning micro-focus SAXS in μ-Spot beamline at BESSY II (adapted from μ-Spot beamline user manual)*

5.2.2 *In situ* micromechanical experiment of MCT at a synchrotron beamline

The micromechanical test frame is designed for small loads (relative those experienced by metals and ceramics), typical for biological tissues, and uses load cells with ratings from 20 N to 100 N typically. A customized LabVIEW interface on a control PC is used to control the applied tissue strain from motor – displacements, read the load

values and apply specified loading protocols [226, 231-233]. DC motors (Physik Instrumente, Karlsruhe, Germany) are used to apply external strain to the sample. To keep the sample wet when testing, two options were considered. The first uses a fluid chamber construction around the sample, but has the disadvantage that the X-ray beam is absorbed to a significant extent due to the path length in artificial sea water (ASW). We are currently working on modifying this chamber to reduce the path length. The second method, used in the experiments reported here, combines a medical saline bag with a length of plastic tubing, an adjustable metal clamp to regulate the flow rate, and a pipette at the end of the tube to constantly drip saline (artificial sea water or ASW) onto the tissue during the test. Tissue paper placed around the bottom of the tester is used to absorb the excess liquid.

Since it is not possible for user-scientists to be in the same hutch where the experiments are running due to high doses of X-rays, therefore, to control the *in situ* tester and control PC remotely, the Remote Desktop software was installed both the host (control) PC (in the experimental hutch) and the remote (beamline) PC (in the control cabin) and the two were connected through internal Ethernet connections in the MuSpot beamline. The remote (beamline) PC was also used for all commands related to SAXS/WAXD acquisition.

The data acquisition system at the MuSpot beamline uses the instrument control software SPEC [234]. In a Unix environment, single commands inside a SPEC-session can be used for acquiring a single SAXS image, driving motors connected to components of the beamline like the beamstop or sample stage, and to carry out a 1D or 2D SAXS scan with user-defined spacing on the sample [235]. When

the experimental protocol is described below, it should be understood that all scans and detector image acquisitions described there are carried out from within the SPEC environment.

For any SAXS or WAXD experiment, a critical factor is calibration of the X-ray beam, its position relative to the detector and the sample to detector distance. This is especially important for *in situ* experiments, because we are concerned with small shifts in peak positions due to externally applied load. However, changes in sample-to-detector distance, or in beam centre position, can also lead to shifts in peak position on the detector, and it is critical to separate these potential experimental artefacts from the physically meaningful changes arising from externally applied stimuli like load. Calibration of the sample to detector distance and beam centre is done by using silver behenate (commonly abbreviated AgBH) [236], a relatively unique crystalline material in that it has a repeat unit of the order of 10s of Angstroms (58 Angstroms), and dry rat tail tendon, which has a meridional D-period repeat of 65 nm arising from the fibrillar structure. We applied the AgBH calibration as the SAXS spectrum of AgBH gives a series of Debye rings which can be used to fit both the beam centre and sample-to-detector distance simultaneously. To carry out the calibration, the CALIBRANT routine in the community-standard software analysis package Fit2D was used. A final factor which is important for the quality of the SAXS image is the alignment of the beamstop. The beamstop is usually a small circular piece of a strongly X-ray absorbing material like lead, which is fixed onto a long glass capillary which is attached to a moveable stage near the detector. The beamstop is adjusted to block the direct beam from hitting the detector, which would damage the CCD sensor. However, the shape of the

beam is not perfectly cylindrical and some additional reflections of the X-rays may occur upstream of the main experimental hutch, which also need to be blocked by the beamstop. If the beamstop is adjusted to block the main beam but not these secondary reflections, these will show up as strong streaks of intensity around the beamstop and interfere with the physically meaningful reflections due to the D period especially at lower orders (i.e. small Bragg angle θ or low wavevector q). This adjustment must be done occasionally during the course of an experiment, when visual inspection shows the appearance of streaks around the beamstop, and is done by incrementally moving the beamstop in the horizontal and vertical directions until the image quality improves.

The wave-vector range chosen for the SAXS experiments is from 0.19 nm^{-1} to 0.54 nm^{-1}. This range was chosen because it includes the meridional peaks from the most intense 3rd and 5th order reflections of the collagen fibril, which are at $\sim 3 \times 2\pi/66$ nm $\sim$ 0.29 nm^{-1} and $\sim 5 \times 2\pi/66$ nm $\sim$ 0.48 nm^{-1}, as well as (in the equatorial direction) the diffuse peak arising from intermolecular spacing $d_m \sim 1.4$ nm at $q \sim 2\pi/1.4$ nm^{-1} = 4.5 nm^{-1}. While it would have been beneficial to have the 1st order collagen D-period reflection at $1 \times 2\pi/66$ nm $\sim$ 0.095 nm^{-1} as well, the size of the beamstop meant that the 1st order reflection was hidden under the beamstop. This limitation of lack of intensity at low wavevectors is a fundamental limitation to most microfocus synchrotron X-ray setups, where the divergence of the X-ray beam means a larger area of the region around $2\theta = 0$ (beam centre) must be blocked off to prevent the divergent direct beam from hitting the CCD detector directly. For an X-ray beam wavelength $\lambda \sim 1$ Å, the above wavevector range implies a sample to detector distance greater than

500 mm, which, due to the finite extent of most beamlines, corresponds to practical working distances of 500 – 1000 mm.

Specimens were placed onto the sample holder of the micro mechanical testing machine, centred with respect to the beam via a diode scan, and subject to a preloading cycle of 0.2N with a loading rate of 0.01 mm/s, to correct the misalignment during clamping. SAXS measurements were taken every 10% tissue strain increment with an external strain rate ~1%.s^{-1} for the loading increment, SAXS images were taken to the point of macroscopic tissue failure (which was ~ 160%).

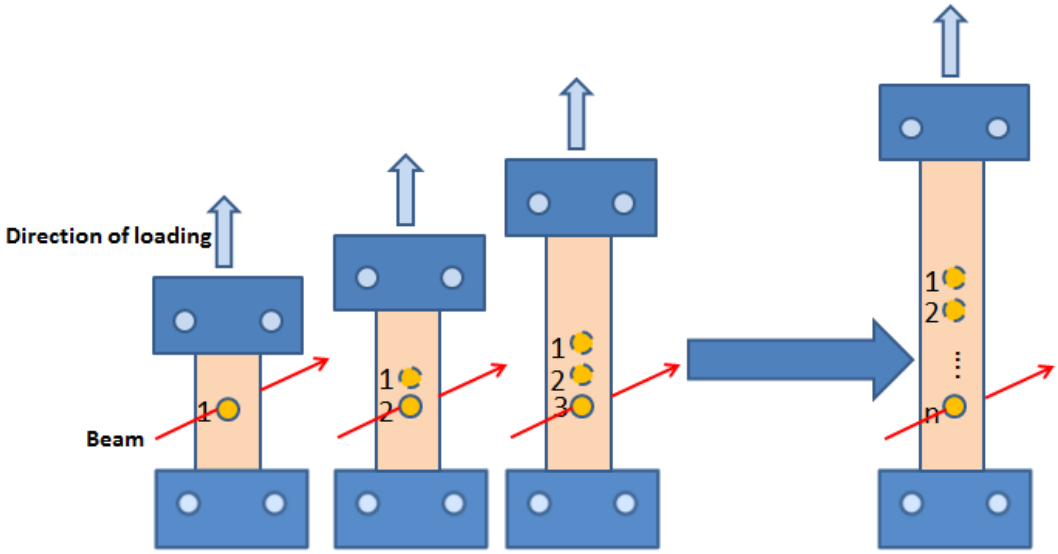

Figure 5.2 The schematic of constant strain rate to failure experimental protocol. *The position of beam is fixed, the circle with solid line is the actual area we are focusing.*

5.3.2.1 D period and fibril strain calculation

To calculate fibril strain, we need to measure the percentage shift in Bragg peaks of an axial diffraction pattern which was resulting from the 65-67 nm axial D-period of fibrils. The 5th order meridional collagen reflection was utilized for this data set. As described previously, the 2D SAXD spectra were radially integrated in a pie-shape sector (**Figure 5.3 (a)**) with an angular width of 40° (**Figure 5.3 (b)**). Subsequently, the selected 5th order peak was fitted by a Gaussian function (Equation 1) (**Figure 5.3 (c)**)

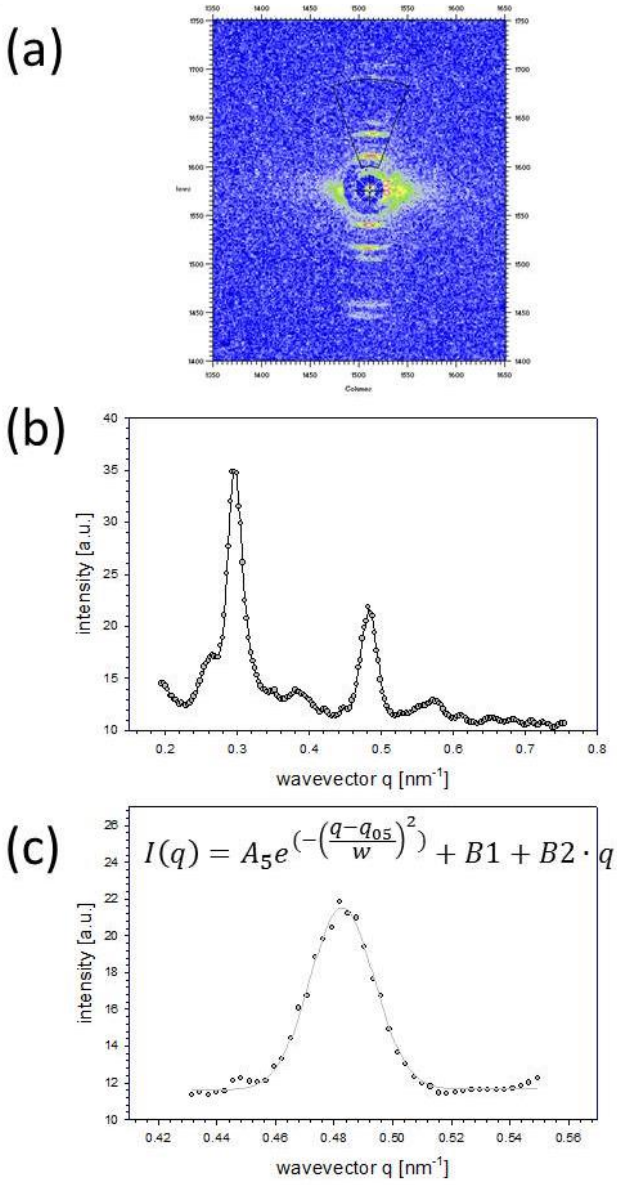

Figure 5.3 *(a) 2D SAXD pattern from stretched Holothuria edulis dermis with showing the discrete reflections arising from the collagen*

D period. (b)Averaged integrated intensity profile in the radial directions in the angular region shown in (a). (c)5th peak fitted by Gaussian function (solid line).

$$Y_{peak} = A_5 e^{\left(-\left(\frac{q-q_{05}}{w}\right)^2\right)} + B1 + B2 \cdot q \qquad \textbf{Equation 5.1}$$

Where A_5 q_{05}, w, q, represent the peak amplitude, peak position, meridional peak width and the modulus of the scattering vector respectively [232], B1 and B2 are parameters fits for the linear baseline. The D period was calculated from D = 5 × 2π/ q05. This method has been used extensively before for bone [231, 232, 237], mineralized tendon [238] , and tendon [239, 240].

The percentage changes in D value at non-zero external force (relative to the unstressed state) will provide a critical fibril strain parameter ε_F.

$$\varepsilon_F = \frac{D_{(\varepsilon_T)} - D_{(\varepsilon_{T=0})}}{D_{(\varepsilon_{T=0})}} = \frac{q_0(\varepsilon_{T=0})}{q_0(\varepsilon_T)} - 1 \qquad \textbf{Equation 5.2}$$

Where ε_T is tissue strain and and $\varepsilon_{T=0}$ represents the tissue strain when time equals 0.

5.2.3 Sample preparation

The species we used in this project is pink sea cucumber (species: *Holothuria edulis*), whose body wall is rich in collagenous tissue. Specimens of *Holothuria edulis* of medium size were collected from a commercial wholesaler (Tropical Marine Centre, Chorleywood, London). Sea cucumbers around 100 mm in length, and 20mm in width measured from the end to the tip, were chosen for the experiments (**Figure 5.4**). They were sacrificed humanely by placing in a -20 °C freezer, following which they were thawed out for sample preparation. Then the animals were cut longitudinally along the ventral surface using a razor blade. The viscera and muscle layers on the inside and the outer dermis of the body wall were removed by

forceps, leaving only the collagenous part. Razor blades were then used to cut standard-sized tissue pieces from the central dorsal area of the dermis along the longitudinal axis of animal. These specimens measured 12mm*1.8mm*1mm respectively. Specimens were stored in freezer (-20°C) until immediately prior to tensile testing. All studies were carried in accordance with the Animals (Scientific Procedures) Act 1986 of the UK, including revision 2013; invertebrates (except cephalopods) are not considered protected species under the Act.

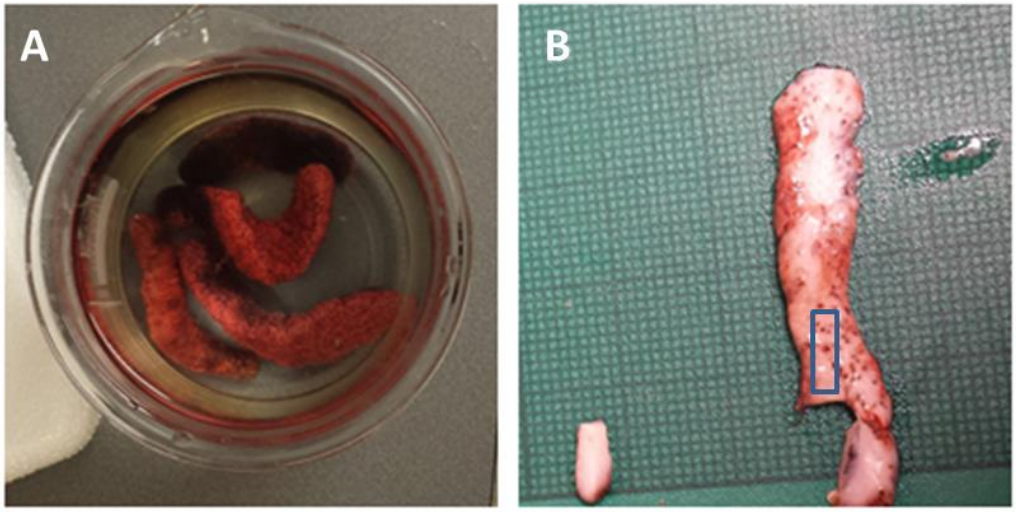

Figure 5.4 *Images showing the steps taken in sample preparation. (A) sea cucumber. (B)The sheet of sea cucumber body wall after the removal of inner and outer dermis, only the central part of dermis was left. Blue rectangle represents the dimension and orientation of the specimens.*

Tensile test clamps were machined for use in the mechanical test frame described previously. Sample gauge length was typically 4.5-6.5 mm. Three cycles of preloading with strain level of 3% were carried out in order to remove slack from sample before a tensile test begins. Sandpaper was glued onto the surface of the clamps, to increase adhesion between tissue and the clamp.

For all samples (which are 1 mm in width, relative to the beam size of 10-20 microns (or 0.01-0.02 mm), diode scans were used to ensure the beam was centred in the middle of the sample (horizontally) prior to the measurement. As a result, over the course of the test involving tensile deformation vertically, the beam is always well away from either edge of the sample. Further, feasibility tests with line scans across (horizontally) the samples showed a homogeneous SAXD pattern.

5.3 Results

5.3.1 SAXS Patterns of MCT

Figure 5.5 is the stress/strain curve of *Holothuria edulis* dermis with the SAXS patterns at different strain. Since the preloading is applied to the specimen, the toe region cannot be seen clearly from the Figure below. At the beginning of the test, we can observe that the stress increased with strain linearly. When the MCT specimen was further stretched, the tangent modulus changes and the plastic region started.

After that, MCT began to suffer destructive changes.

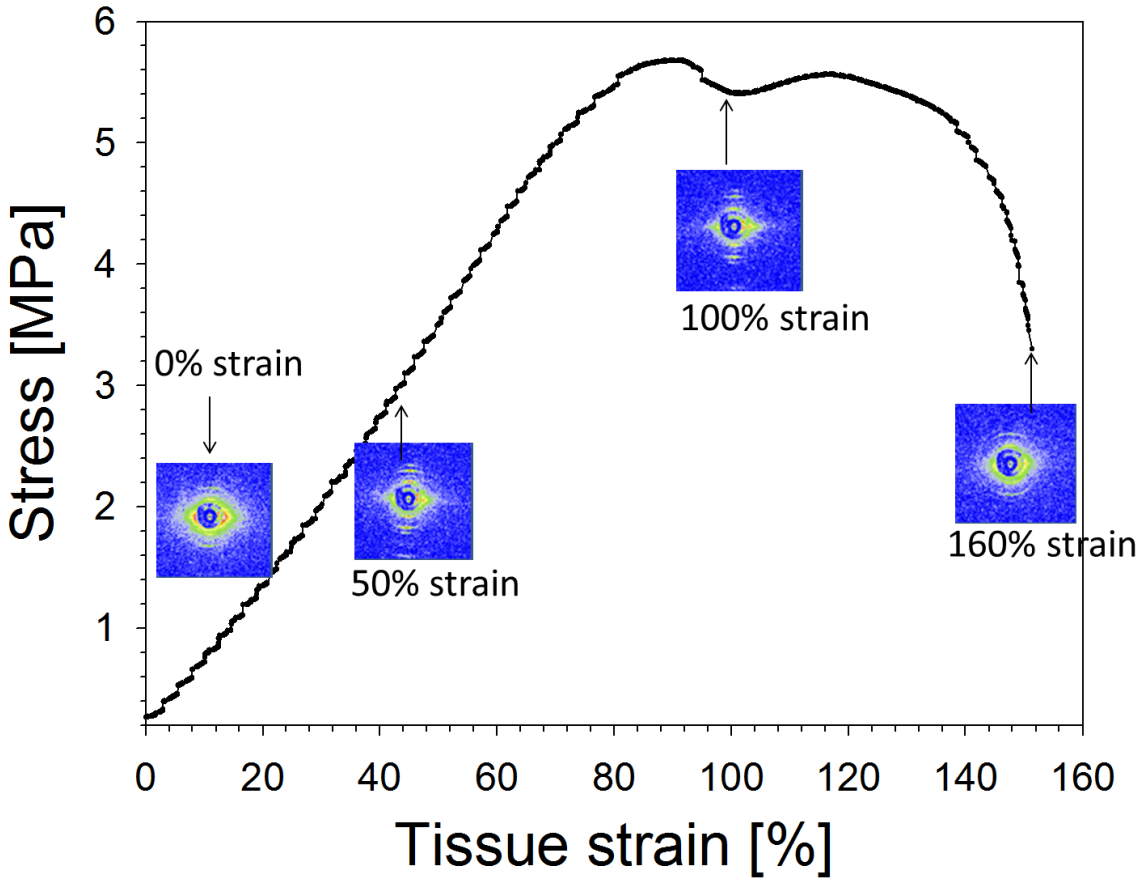

Figure 5.5 *The stress/strain curve of Holothuria edulis dermis under tensile force, with SAXS patterns corresponding to different strains, showing collagen fibril straightening, increase in SAXS peak intensities and reversion to unstressed type when tissue fails.*

Figure 5.6 below shows sample 2D SAXS patterns that were gained from sea cucumber. The first pattern (the upper left one) shows the spectra of MCT specimen at the original state (without stretching). Then as the specimen was applied to external force, more arc on the spectra are visible to us as the strain increasing. Finally, when the specimen is close to failure, the number of arcs decreased again. Also, it is observed that while stretching the sample, extent of arcing first

decreases and then increases.

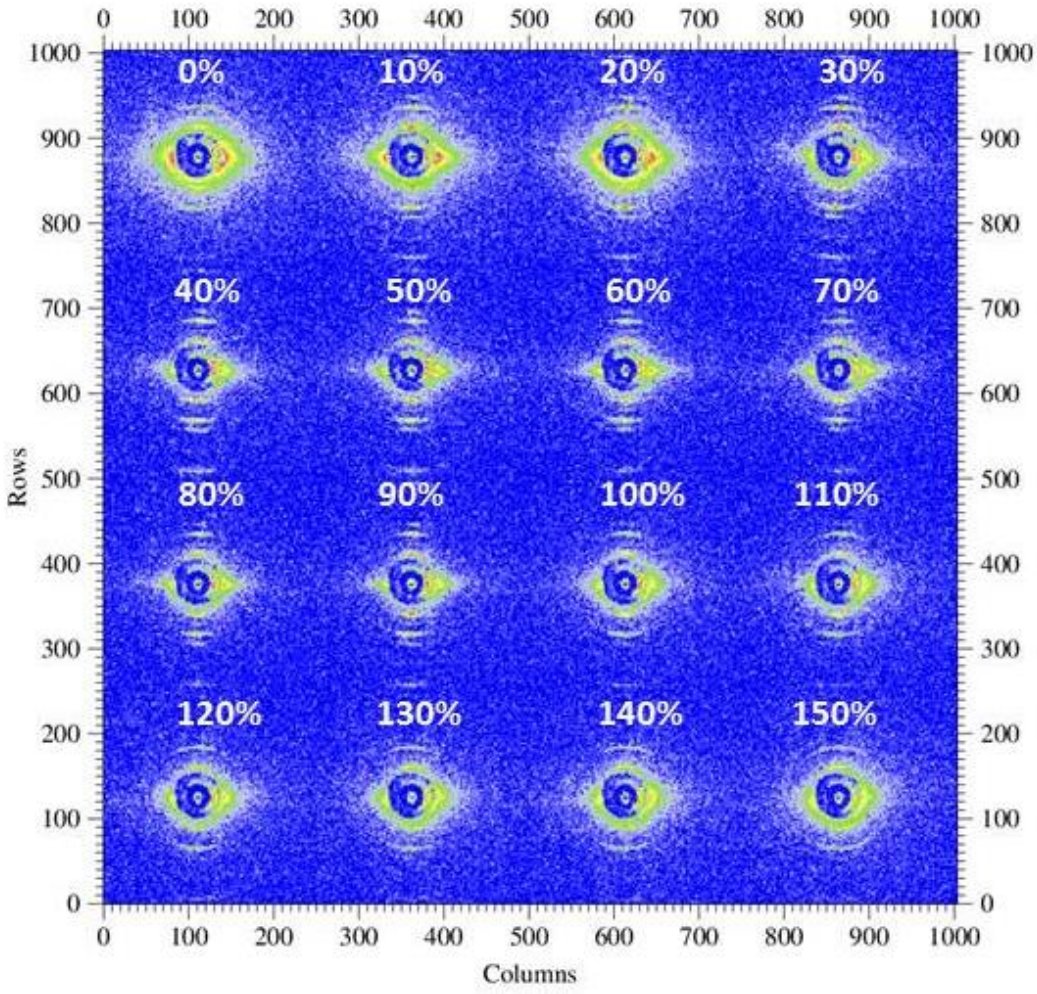

Figure 5.6 *2D SAXS pattern from stretched Holothuria edulis body wall, showing the discrete reflections arising from the collagen D period. From left to right, different patterns show the spectra of specimen, as the tissue strain increases from 0% to 160% with an increment of 10% (the strain values are indicated on the subplots).*

5.3.2 SAXD data evaluation

5.3.2.2 Changing of D period with applied stress

The evolution of collagen D period (that is, the strain at the fibrillar level) and the macroscopic motor strain is shown in **Figure 5.7**. From 0% to ~20-30%, the D spacing increases (by about ~1.1%) together with the stress, which increases in an approximate J-shaped curve (stress/strain curve concave up) to ~2-3 MPa. From ~30% to 60%, the D spacing increases much slower, in a plateau type region. Over this

same zone, the tissue stress does continue to increase, but close examination of the curve shows that the rate of increase has reduced, and the stress/strain curve is now concave-down. From 70% to 110%, the D-spacing rapidly decreases from its maximum value of ~65.2 nm to its starting value of ~64.4 nm. Over this same region, the macroscopic stress is now almost constant at ~5 MPa. For strain larger than 110% the D-spacing does not increase. Over the same strain-range, the tissue stress now drops rapidly from ~5 MPa to exhibit macroscopic failure.

These initial data point to an intriguing scenario where the increasing strains in the fibril contribute to the initial stiffening phase of the tissue stress (up to ~20-40%). For larger strains it appears that some form of interfibrillar debonding over 30-60% which leads to a plateauing of the fibril strain (which may be under a constant interfibrillar shearing stress of the type proposed for mineralized tissue by Gupta et al [241]. Surprisingly, the precise form of this debonding appears to be such that macroscopic drops in stress do not yet occur, rather the rate of increase of stress reduces. This suggest a possible scenario where the stress carrying ability is now transferred to shearing and elongating molecules in the interfibrillar matrix which carry the stress which has been lost by the fibrils. These interfibrillar matrix molecules could include fibrillin-rich microfibrils, proteoglycans, or the various mechanoeffector proteins like tensilin. As these are widely believed to be far less stiff than collagen, the reduced rate of increase of stress can be thereby understood. Clearly, for strains larger than ~60-70%, the ability of the connective tissue as a whole to bear the load starts reducing dramatically. This is clearly seen by the rapid decrease of the D period to its unstressed value over

the strain range of 70-100%. The reduction of the D-period implies a complete debonding of the fibrils from the extrafibrillar matrix and a consequent relaxation of the fibril to its unstrained state. In this zone, macroscopically the tissue starts to flow (that is, increase its length without increasing stress) as the other non-fibrillar components have possibly reached the limits of their deformability. For larger strains over 110%, the tissue fails, and there is no further change in the fibrillar strain.

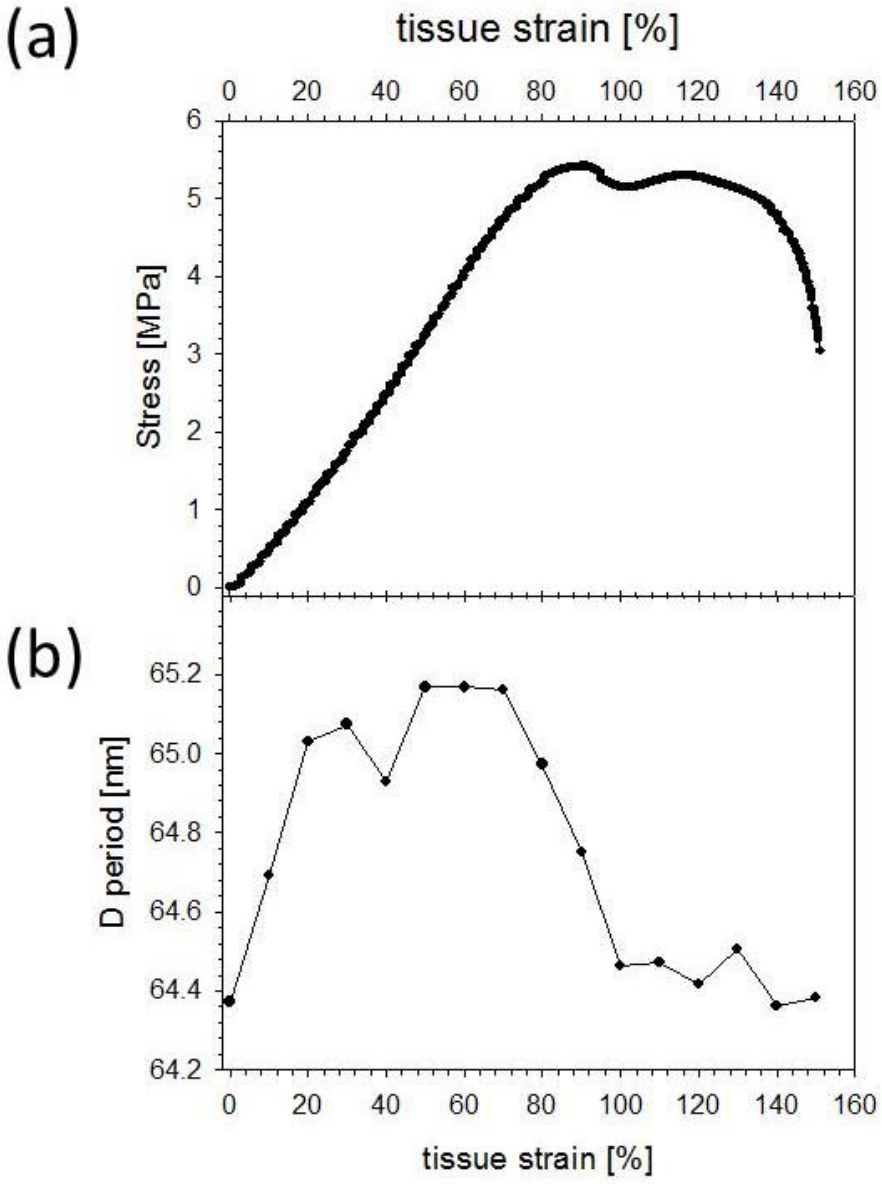

Figure 5.7 *(a) The applied stress-strain curve of MCT specimen; (b) The changing of D period obtained from 5th order peak as the increasing of motor strain*

From the changes of D period, the ε_F can be calculated using **Equation 5.2**. This is the first time that fibril strain in MCT was shown and it also shows that, in principle, MCT in various states of mechanical mutability could be analysed with SAXS pattern.

5.3.2.4 Intermolecular spacing dm calculation

The lateral spacing between tropocollagen molecules d_m, indicated schematically, is ~ 1.1 – 1.5 nm depending on the degree of hydration [242, 243] and mineralization. As a result, in the equatorial plane perpendicular to the fibril axis, there should arise a diffraction peak at $2\pi/d_m$. Because this lateral spacing is very irregular, the molecules are said to be arranged in a "liquid-like" manner [243, 244], so the peak is not sharp, but is a broad, diffuse peak. This peak can be detected in our SAXS pattern by taking a restricted angular CAKE sector perpendicular to the fibril axis, as indicated in **Figure 5.8** (a). As can be seen from the **Figure 5.8** (b), a broad peak centred at 15 Å (1.5 nm) is visible, and can be fitted in a similar manner as for the D period peak in the meridional spectrum. Note that this peak includes the background scatter from collagen fibril as well as empty beam.

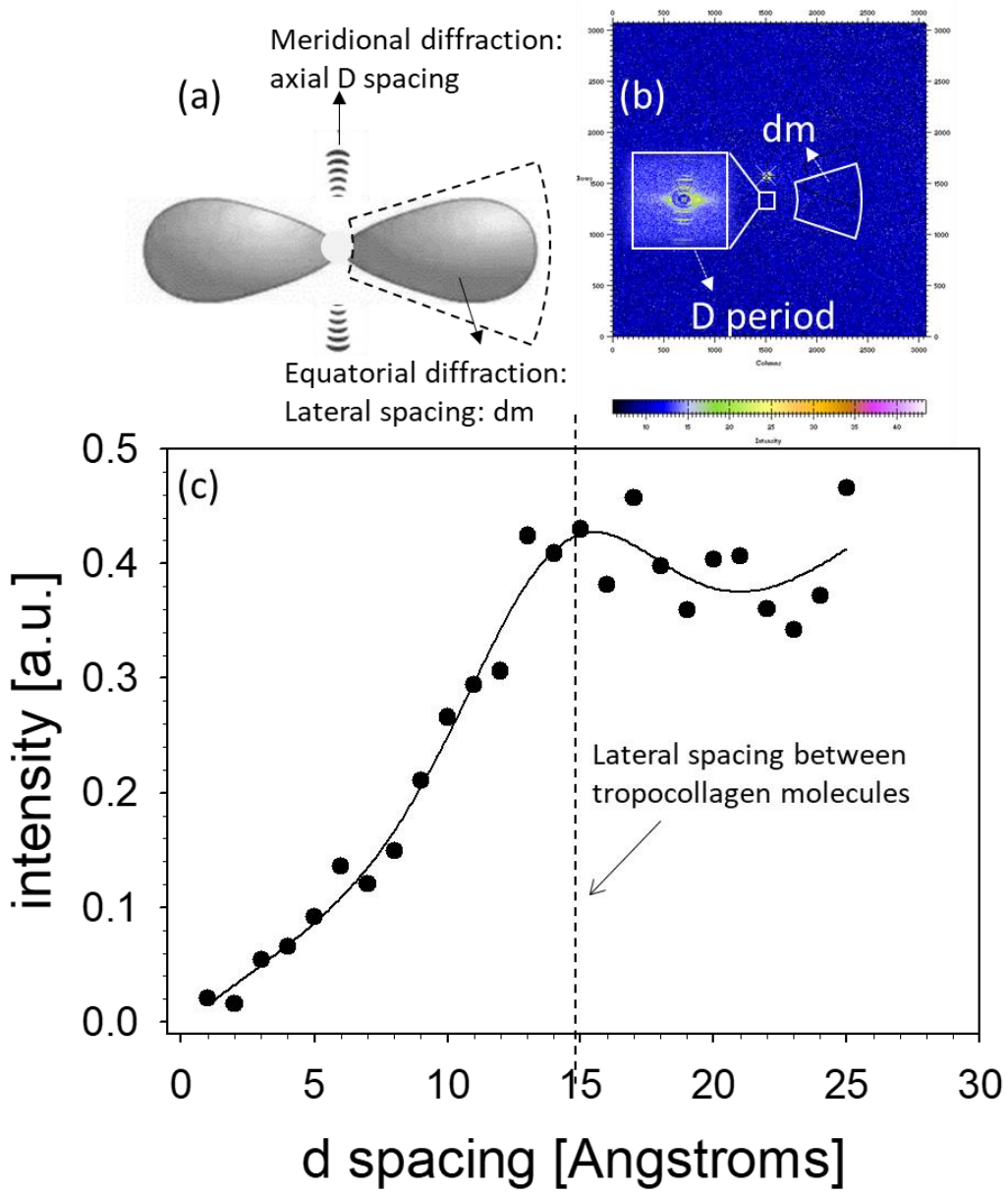

Figure 5.8 *(a) Schema of X-ray diffraction pattern, showing the position of meridional diffraction and equatorial scattering.(b) 2D SAXS pattern from a test specimen the integrated sector focused on the equatorial scattering coming from the lateral spacing of tropocollagen molecules. (c) Total integrated intensity profile of equatorial diffraction patterns. The solid line is the fitting curve of the real data.*

The physical significance of measuring the equatorial spacing during external deformation is that it provides a molecular-level probe of deformation transverse to the fibril axis. While increases in the *D*-

periodicity along the fibril axial measure the axial strain in the fibril in response to tensile stress, the transverse strain perpendicular to the fibril axis can be directly measured from the corresponding changes in d_m. **Figure 5.9** shows the changes of d_m when tensile forces were continuously applied to the specimen. From the **Figure 5.9** we can observe that the d_m shown a dropping trend in the first few frames. This revealed that the spaces between different tropocollagen molecules reduced and the lateral (equatorial) arrangement packed more compactly. Shortly before the specimen started to fail, the D-period suddenly went up. This is most probably the result of a partial stress release due to the failure of some collagen molecules in the assembly, which is consistent with the phenomenon of D period shifting back.

The changes of D period (along with the fibril axis) and d_m (perpendicular to the fibril axis) are consistent with the fact that this collagenous tissue has positive Poisson's ratio which we observed macroscopically from the real sample.

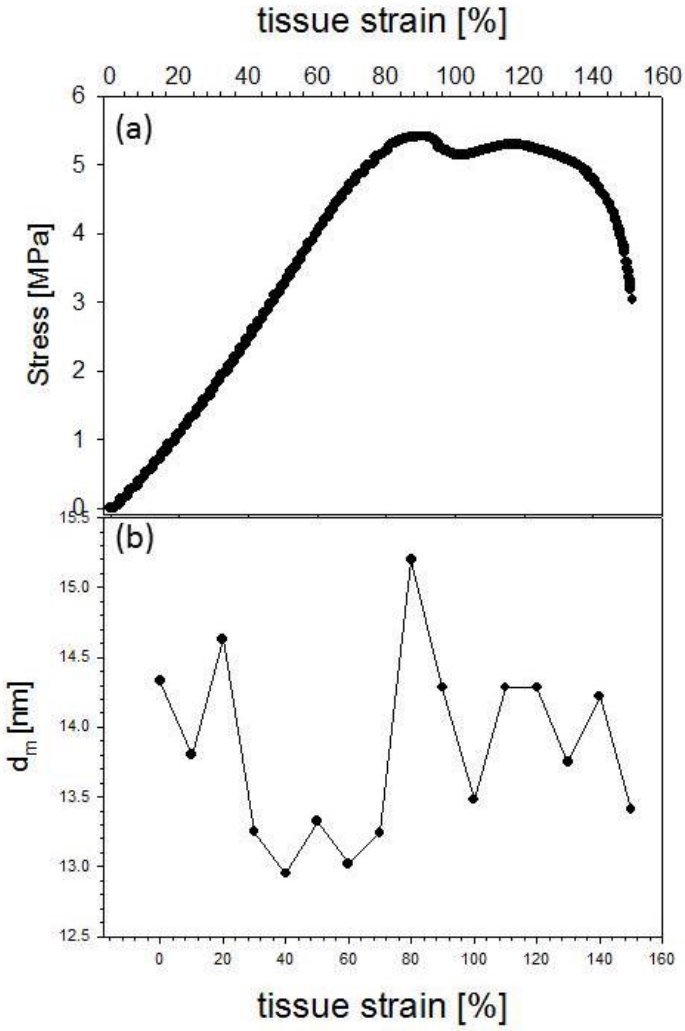

Figure 5.7 *(a) The applied stress-strain curve of MCT specimen. (b)The dm value from fitting results of the real data. The d_m first drop down with the applied forces and then went up suddenly when the specimen was closed to failure. Then it levelled out in the plastic deformation region.*

5.4 Conclusion

In conclusion, we have carried out the first SAXD measurements of the collagenous phase of echinoderm tissue, using the high brilliance synchrotron X-ray source. As viable MCT can change its mechanical states nearly instant (less than 1s) due to the neural cells activity, SAXD pattern will also change dynamically. While certain characteristics of the SAXD pattern in MCT show clear similarities with that of other collagenous tissues (meridional peaks with a strong 3rd order peak), the highest intensity in MCT is the 5th order, which is

not the case in other collagenous tissues like tendon, bone and cartilage [245]. These differences in the meridional SAXD pattern may arise from multiple factors, including the different noncollageneous molecules bound to the fibril surface (which include molecules like fibrosurfin in MCT [11]), and possibly altered biochemical structure of MCT tropocollagen chains compared to vertebrate collagen and altered hydration levels. Due to the limited biochemical data available on echinoderm fibrillar collagen, we cannot make definitive statements at this time. We can state, however, that the *in situ* X-ray methods used in tendon, bone and other collagenous tissue, when applied to MCT to determine the loading, leads to measurable fibril strain, reorientation and intermolecular spacing [16, 222]. The characteristic J-shaped curve associated with distinct changes in fibrillar SAXD pattern indicates that the fibrils – even in freeze-thawed MCT – play a mechanical role.

In this proof of concept experiment, we have thus validated the method of *in situ* SAXD on MCT-containing tissues, which allows us to apply it to viable tissue in the next stage. In terms of experimental improvements learned from these tests, the grip design will be changed, including a grooved slot for holding the samples in the clamps more stably in the centre. Secondly, to improve the fluid flow, we will clamp the ASW irrigation tubing (from the saline bag) stably onto the upper sample holder, in order to direct the fluid flow accurately to the sample and avoid any artefacts in the load reading due to the tubing brushing against the load cell during the experiment or sample mounting/dismounting.

Chapter 6 : Interfibrillar stiffening of echinoderm mutable collagenous tissue demonstrated at the nanoscale

6.1 Introduction

The mechanical properties of biological tissues are usually optimized to operate within specific physiological loading and strain ranges [12, 246]. With the exception of the common phenomenon of strain stiffening that occurs during mechanical loading [107], material-level changes in the overall mechanical properties of tissues typically occur slowly, driven by growth, remodelling or ageing [247]. The molecular level mechanisms underpinning these changes often involve permanent, irreversible changes, including covalent crosslinking *via* disulphide bridges in tendon [248], formation of metal-ion/protein complexes [249], or replacement of water with an inorganic phase as in biomineralization [250], although viscoelastic mechanical responses may involve transient cross-linking [251]. In contrast, changes in the mechanical properties of animal tissues that occur actively and reversibly within a few seconds are canonically mediated by ATP-dependent molecular motors, as in muscle [252]. A notable exception is the mutable collagenous tissue (MCT) of echinoderms (e.g. starfish, sea urchins, sea cucumbers), which undergoes rapid changes in stiffness under the control of the nervous system via ATP-independent mechanisms [11, 253, 254]. MCT is ubiquitous in echinoderms [11]; for example in the dermis (skin) of sea cucumbers [255, 256], the compass depressor ligament (CDL) of sea-urchins [133, 257, 258], and in the arms of feather stars [259]. The presence of MCT enables functionally diverse behaviours; for example in starfish, MCT enables body wall stiffening during feeding on prey and it also enables irreversible body wall softening prior to arm autotomy as a

defence against predation [11]. Thus, MCT represents an evolutionary adaptation of collagenous tissue to change mechanical properties dynamically, whilst in other phyla collagenous tissues largely act as passive mechanical springs. The benefits of MCT also include a much lower energy expenditure [260] compared with muscle tissue and the presence of MCT is considered to have been a major factor in the evolutionary success and ecological diversity of echinoderms (reviewed in Barbaglio et al [13]).

The initial identification of connective tissue of echinoderms as having mechanically unusual properties – illustrated by its denotation as "catch" connective tissue – was through the observed stiffening and softening response of such tissues to sea water of different ionic compositions, as well as neurotransmitters (e.g. acetylcholine) [256] and drugs (e.g. cocaine) [261]. Such chemical means to induce mutability in MCT remain a convenient and reproducible method to induce mechanically altered states [133, 262, 263]. Specifically, previous studies demonstrated that alteration of extracellular Ca^{2+} and K^{+} levels modulates the stiffness of living tissues in sea urchin spine ligaments [185, 256, 264-267], holothurian dermis [181, 255, 262, 268] and starfish [181]. Increased K^{+} concentration increases the stiffness of these examples of MCT, while decreased Ca^{2+} concentration lowers stiffness, when compared to artificial sea water (ASW) as a reference solution. The changes induced by these chemical methods are within the same order of magnitude as physiologically relevant mechanical changes occurring in MCT *in vivo*: under mechanical stimulation (pressing the tissue by hand), starfish body wall MCT stiffens by a factor of ~3.3 [181], while increasing K^{+} concentration leads to an increase of ~6.1 [181]. Conversely, the reduction of stiffness in

calcium free artificial sea water is considerable [191], which is comparable to the reduction to zero in the extreme case of limb autotomy where the tissue disintegrates structurally [269].

The unusual mechanical properties of MCT must arise from the micro- and ultrastructure of this tissue, which shows both commonalities with, as well as some clear differences from, the more familiar vertebrate collagenous tissues such as skin, tendon and bone. At the molecular level, the collagen of sea cucumber MCT is different from heterotrimeric vertebrate type I fibrillar collagen, consisting of homotrimers with three α_1 polypeptide chains [11]. These collagen molecules aggregate into discontinuous spindle-shaped collagen fibrils with a mean diameter of ~17 nm [270]. Proteoglycans are bound to the fibrillar surfaces, which along with non-collagenous proteins such as tensilin, stiparin and fibrosurfin comprise the interfibrillar matrix [189, 192, 271]. Together with fibrillin-rich microfibrils [192] the fibrillar collagen network comprises the bulk of the extracellular matrix (ECM) of MCT. Dispersed in this ECM are clusters of juxtaligamental cells (JLCs) [11, 260, 264, 267, 268] [133] (as seen from transmission-electron and light microscopy), which are MCT-effector cells that are under neural control [11, 133]. Furthermore, it is the innervation of MCT that is a key distinction between echinoderm and vertebrate collagenous tissues [133].

Initial hypotheses about the ultrastructural mechanism enabling the mechanical mutability described above focused on ion-mediated creation of physical crosslinks between fibrils and within the interfibrillar matrix in the ECM [254, 272]. Divalent calcium ions were proposed to be especially effective in increasing interfibrillar matrix stiffness, and their depletion in Ca^{2+}-free sea water solutions

was believed to be a major reason for the reduced stiffness. However, this hypothesis was disproved when cell-lysed MCT showed no mechanical mutability in the presence of such solutions [273]. It is therefore believed that the ionic treatments directly affect cellular secretion pathways in the JLCs, inducing release of proteins that alter interfibrillar binding, thus changing the stiffness of the tissue [11]. Several such proteins, including tensilin, softening and novel stiffening factor (NSF) have been identified [187, 189, 191, 192, 274]. It is believed that the JLCs secrete such effector proteins as a result of external stimuli (such as touch, aggressive attack, or alteration in the ionic strength of the sea water around the animal), thereby changing the stiffness of the tissue. Biochemical evidence to support this hypothesis includes the structural similarity of some of these proteins to the tissue inhibitors of matrix metalloproteinases (TIMPs) found in vertebrates [275]. Consistent with this notion, it has also been suggested that cysteine-rich sea urchin fibrillar domains (SURFs), found so far in the sea urchin collagen 2α and 5α N-propeptides, as well as fibrosurfin (an interfibrillar protein) [271, 276], play a role in enabling mutability. The 2α N-propeptides and fibrosurfin co-localise on collagen fibril surfaces in adult sea urchins. However, despite this considerable level of biochemical insight into MCT [11], the biophysical mechanisms by which the alteration in mechanics is mediated by the nanostructure – whether at the fibrillar or intrafibrillar level – are still not completely understood.

Techniques used to correlate ultrastructure with mechanics have been by necessity largely static and indirect, including imaging tissue after alteration of mechanical state with techniques like transmission electron microscopy [133]. These introduce unavoidable artefacts

from sample preparation and do not measure the changes as they occur in real-time. The use of *in situ* synchrotron X-ray diffraction to provide molecular- and supramolecular level images of the ultrastructural conformation during alteration of the mechanical state of MCT is a direct way to overcome these limitations [240, 241, 277, 278]. The axial periodicity of electron density along the long axis of collagen fibrils [279], with a repeat distance of D~65-67 nm, leads to Bragg diffraction peaks in X-ray scattering in the small-wavevector domain (< 5 nm^{-1}) characteristic of small angle X-ray diffraction (SAXD) [279]. Shifts in these peaks, as would be induced by mechanical loading or ionic treatments, are therefore a measure of the nanoscale fibril strain as demonstrated for vertebrate tissues [231, 240, 241, 277, 280]. By combining micromechanics with *in situ* small-angle X-ray scattering, it has been possible to shed light on the fundamental ultrastructural mechanisms enabling viscoelasticity, toughness and force generation in vertebrate tissues ranging from tendon [281], bone [231, 278], aorta [282] to muscle [283], as well as more unusual examples of biological optimization such as armoured fish scales [277]. Using SAXD, it was found that in cross-link deficient fibrils, increased molecular slippage led to larger fibril strains, compared to normal collagen fibrils [281], that high toughness of antler bone was due to inorganic/organic friction at the intrafibrillar level [241], and that fibrillar reorientation blunted crack propagation in skin [63], among other examples.

When combined with high-intensity synchrotron X-ray sources, time-resolved SAXD with *in situ* micromechanical loading could be employed to quantify the fibrillar deformation mechanisms of MCT in various states of mechanical mutability, thus clarifying the biophysical

mechanisms enabling this remarkable behaviour. Here, we apply these techniques to the sea cucumber dermis as a model system (Fig. 1). Understanding the molecular mechanisms enabling mutability may have applications in developing dynamic biomaterials, systems capable of changing their mechanical properties and the design of mechanically tuneable implants. The adaptive mechanical properties in MCT could, for example, provide insight into the repair of connective tissue pathologies in soft tissue, such as therapy in tendon or ligament weakening resulting from surgery or immobilisation [11], the design of implants capable of generating active forces, and in the area of neural implants where variable stiffness during insertion and implantation have been proposed [9].

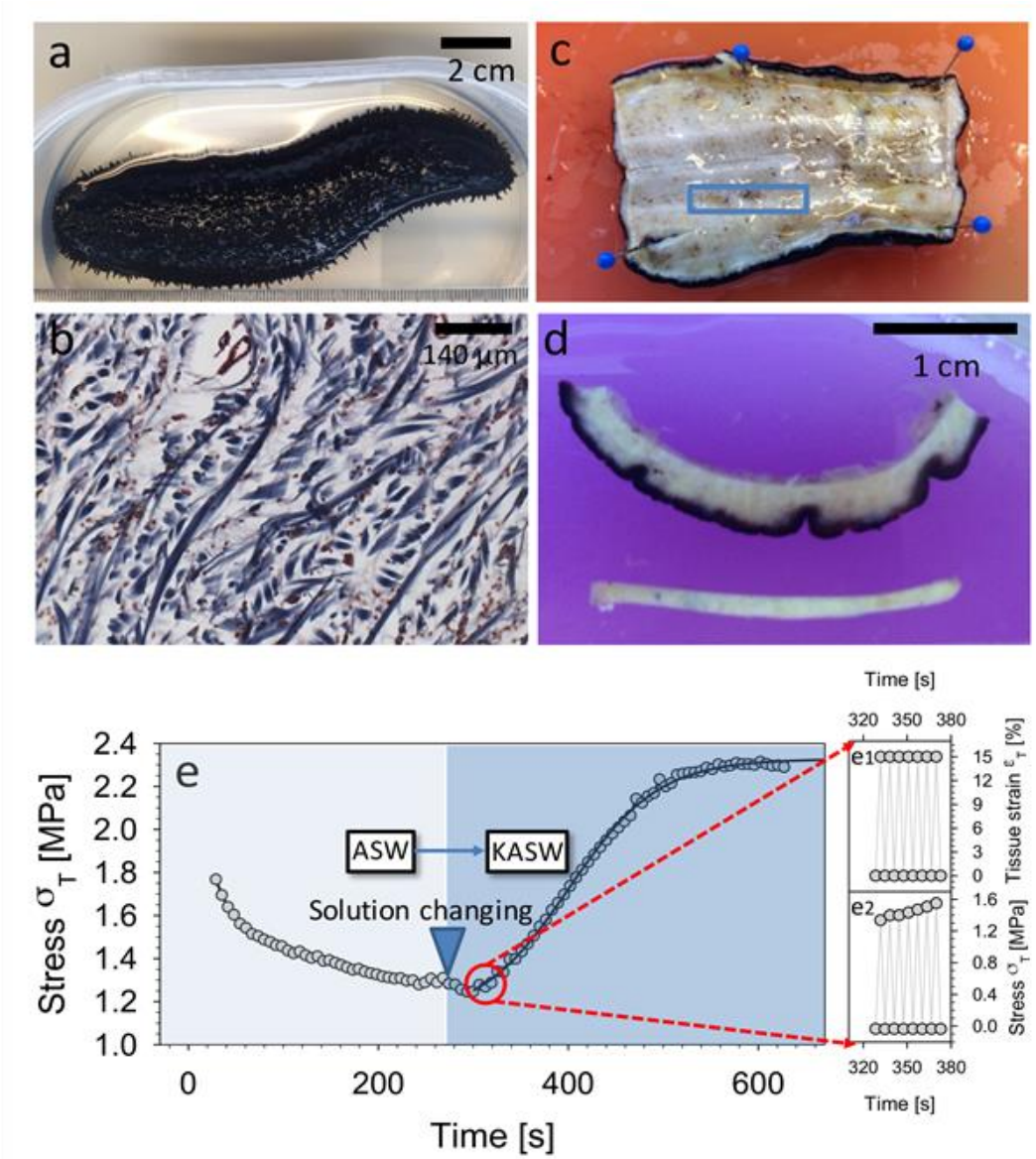

Figure 6.1 Sea cucumber body wall mutable collagenous tissue (MCT). *(a) Sea cucumber Holothuria leucospilota (b) Transverse section of sea cucumber body wall stained using Masson's Trichrome method; collagen fibrils appear blue (c) The sheet of body wall after animal was cut in half along the longitudinal plane. The blue rectangle indicates the dimensions and location of sectioned specimen, with the long dimension along the longitudinal axis. (d) View of sectioned sea cucumber dermis including dark outer dermis and inner layer, below is the tensile test specimen. Prior to testing, the dark-pigmented outer dermis as well as the inner layer was removed, leaving only the centre part of the specimen. (e) Time-dependent change in sea cucumber MCT mechanics induced via ionic treatment. The peak stress (per cycle) is plotted during strain-controlled cyclic loading of sea cucumber dermis at 0.3 Hz (to 15% tissue strain), with tissue immersed in ASW until ~290 s, followed by a change of the*

immersing solution to KASW (stiffening agent). A clear rise of peak stress (per cycle) is observed, fitted with a sigmoidal curve as a guide to the eye. Inset figures on the right show a magnified time-range over a few (seven) cycles, with both maximum and minimum stress and strain indicated.

6.2 Materials and methods

6.2.1 Dissection of sea cucumber body wall preparations

Specimens of the sea cucumbers (*Holothuria leucospilota*) were obtained from a commercial wholesaler (Marine Life, Paris, France), and delivered to the synchrotron SAXD beamline (in tanks of artificial sea water) a few hours prior to use. To prepare sea cucumber samples for the mechanical testing in different ionic solutions, we followed a protocol similar that used in previous studies of the mechanics of sea cucumber dermis [165, 260]. Specifically, after letting the sea cucumbers rest for 1 hour in sea water, samples from the white central part of the body wall dermis (**Figure 6.1**) were prepared. The attached viscera and muscle layers on the inside were pulled off with forceps, and the pigmented outer dermis was removed using razor blades, leaving only the collagenous part. Rectangular-shaped collagenous tissue pieces (10-20 mm×1.0mm×1.0mm) were cut out using a specialized construct with twin-razor blades fixed on either side of a 1 mm thick steel-section, to keep the thickness constantly close to 1 mm. As specimen are obtained from soft tissue, measurement with Vernier callipers would have deformed the tissue slightly. By estimating several degrees misalignment of the blades, the error of measurement is around 100 μm. The sectioning was done in the longitudinal direction of the body wall, used for tensile testing (**Figure 6.1 C-D**). While the total length of the sample varied between specimens, the gauge length was kept constant to 6 mm during the tensile testing (as described in the next section). Samples were rinsed in artificial

seawater (ASW) after sectioning. After the sections were prepared, and before mechanical testing, all samples were allowed to relax in ASW for 1 hour. Following this, specimens were incubated in ASW (control), high potassium concentration (stiff; high [K^+]) artificial seawater (KASW), or calcium-free artificial seawater (soft; CaF-ASW) for 1.5 hours. Compositions of these three solutions (ASW, KASW, and CaF-ASW) followed the protocol described previously by Motokawa [256]. As expected, this procedure resulted in relative elevation and reduction of stiffness for KASW and CaF-ASW treated dermis, consistent with other studies of chemically treated MCT [181].

6.2.2 *In situ* mechanical testing with SAXD

A compact micromechanical tester, designed by our group [241], specialized for holding biological tissues and capable of being fixed on the sample stage of a synchrotron SAXD beamline, was used. The tester contains a load cell (100 N rating), with attached amplifier (RDP Electronics Ltd, UK). Strain is applied by displacement of a DC-motor with encoder (M-126.DG, Physik Instrumente, Karlsruhe, Germany). A customized LabVIEW (National Instruments, UK) interface on a control-PC was used to control the applied tissue strain and strain rates. Adherence of the sample to the tensile tester grips was improved by using sandpaper of various grades between the tissue and the grip. The machine compliance of the tester was measured using a thick steel section. Compliance was found to be negligible compared to the stiffness of the sea cucumber body wall tissue under investigation. Engineering tissue strain (ε_{T0}) was calculated from the ratio of the displacement of the sample grips to the unstressed gauge length ~ 6 mm. As MCT is a soft tissue capable of considerable elongation, the engineering tissue strain (ε_{T0}) was converted into true

tissue strain (ε_T) using $\varepsilon_T = \ln(1+\varepsilon_{T0})$ [284] (See **Appendix**, section 3). Tissue stress σ was obtained by dividing force by cross-sectional sample area (1.0 mm^2). Rate of increase of stress with tissue strain (tangent modulus E_T [284]) was obtained from a linear regression between σ and ε_T with a moving window of $\Delta\varepsilon_T = 0.5\%$.

Combined microtensile deformation experiments with time-resolved acquisition of SAXD patterns were carried out at the High Brilliance ID02 beamline at the European Synchrotron Radiation Facility (ESRF, Grenoble, France). Body wall preparations were mounted in the microtensile tester immediately after incubation in test solutions. Samples with gauge length ~6 mm were stretched to failure at a constant velocity of 0.01 mm/s (corresponding to a strain rate of ~0.167%/s). Samples were kept hydrated by dropwise addition of the incubation solution during the test. SAXD patterns were acquired with a FReLoN CCD detector[285] with a 0.5 second exposure time, using a highly collimated synchrotron X-ray beam (beam size 20 (height) × 25 (width) μm at sample and detector positions, wavelength λ = 0.9951 Å (X-ray energy 12.46 keV) at a sample-to-detector distance of 1006.8 ± 1.0 mm determined with silver behenate at the sample position. Prior to the *in situ* deformation, 10 successive frames at the same sample position (with no deformation applied) and analysed the radial intensity profile of the 5th order Bragg peak. It was found that such successive exposures at the same point were identical, and only after the 10^{th} repeat was a reduction of peak intensity visible. Hence, possible radiation damage has no consequence for a single SAXS exposure at a previously unexposed point. Each SAXD pattern had a resolution of 2048×2048 pixels and a pixel area of 23.63×23.97 μm^2. SAXD patterns were collected continuously up to failure of the

specimen, with an interval between acquisitions of ~1.5% strain. Each SAXD pattern is therefore acquired on a tissue location which is ~6 mm × 0.015 = 90 μm shifted from the previous measurement. The beam diameter is much smaller (~1/5th of this shift) and there is thus no overlap of the beam onto tissue locations across SAXD measurements. As a result, radiation damage, due to multiple exposure of the beam to the same tissue location, is minimized. Radiation damage of protein assemblies and solutions occurs via combination of free radicals produced by water photolysis with free radicals from the proteins, leading to protein unfolding, aggregation, or breakage [286].Our strategy of continuous sample movement to avoid repeat exposures of the same point is one of several successful approaches to minimize radiation damage [286]. Other methods, including continuously replacing the sample (e.g. continuous flow in liquids) or adding radical scavengers to solutions (assuming no structural consequences) [286], are not applicable in the case of strain-stressed tissues considered here. Failure of the specimen usually occurred between 50 and 70% strain. As a result, typically about 40 patterns per sample (60%/1.5% = 40) were acquired.

6.2.3 Determination of fibril strain from SAXD

2D SAXD patterns of sea cucumber body wall collagen was obtained (Fig. 2(b)) and averaged azimuthally (in the angular plane of the X-ray detector) to obtain the Bragg peaks arising from the D-periodicity of SAXD fibrils. The azimuthal average of the intensity provides a 1D intensity profile $I(q)$ (q being the wavevector), which has characteristic Bragg peaks at integer multiples of $2\pi/D$. The software package Fit2D [287] was used, with the CAKE/INTEGRATE command, to carry out the integration. The 5th order peak was used for

fitting as it had the strongest peak intensity among the visible Bragg orders, enabling accurate peak fitting and determination of peak shifts (See **Appendix**, section 5). To centre the pattern around the clear 5th order peak at ~0.48 nm^{-1}, inner and outer wavevector limits of 0.45 nm^{-1} and 0.50 nm^{-1}, respectively, were used. Subsequently, the selected 5th order peak was fitted by a Gaussian function with a linear background term to account for the diffuse intensity scattering:

$$I(q) = I_{05} \exp\left(-\frac{1}{2}\left(\frac{q - q_{05}}{w} \right)^2 \right) + I_{00} + I'_{01}\, q \quad \textbf{Equation 6.1}$$

Here I_{05}, q_{05}, and w, represent the peak amplitude, peak position and meridional peak width, respectively (I_{00} and I'_{01} are diffuse background terms). The D-period was calculated from the relation D = 5 × 2π/ q_{05}. The percentage changes in D value at non-zero external force (relative to the unstressed state) provide the critical fibril strain parameter ε_F. The method described here has been used extensively by us for vertebrate collagenous tissues, specifically for bone and tendon [231, 240, 241, 288]:

$$\varepsilon_F = \frac{D(\varepsilon_T) - D(\varepsilon_T = 0)}{D(\varepsilon_T = 0)} = \frac{q_0(\varepsilon_T = 0)}{q_0(\varepsilon_T)} - 1 \quad \textbf{Equation 6.2}$$

To obtain the fibril strain ratio $\varepsilon_F/\varepsilon_T$ for each sample, a linear regression of fibril strain ε_F versus tissue strain ε_T was carried out (Sigma Plot, Systat Software), and the slope of the linear regression provided $\varepsilon_F/\varepsilon_T$ [231, 241, 278, 281]. The values of $\varepsilon_F/\varepsilon_T$ for each sample from the different treatment groups is given in a Table in **Appendix** section 4.

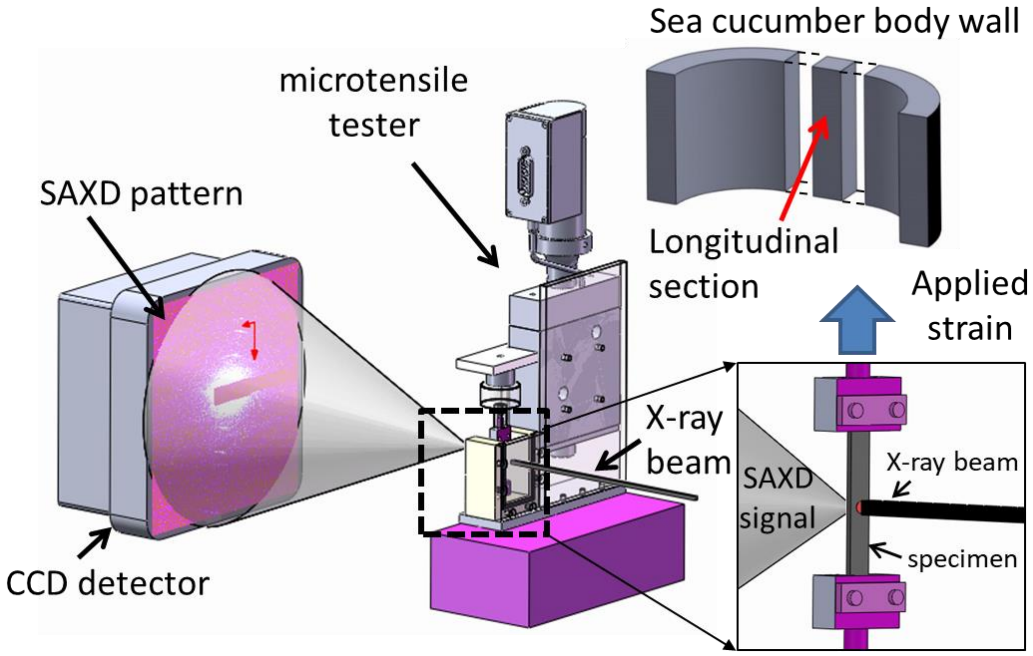

Figure 6.2 In situ nanomechanics with synchrotron small angle X-ray diffraction (SAXD): *Experimental configuration: Tensile tester (centre) with MCT specimen mounted along X-ray beam path in transmission geometry with CCD detector (left). Right inset: magnified view of sample in chamber, and incident X-ray beam (right) with SAXD scattering shown on left. The tensile strain is applied along the vertical direction. Upper right: Schematic of body wall of sea cucumber shown in Figure 6.1, with tensile test specimen sectioned with long axis parallel to the long axis of the animal.*

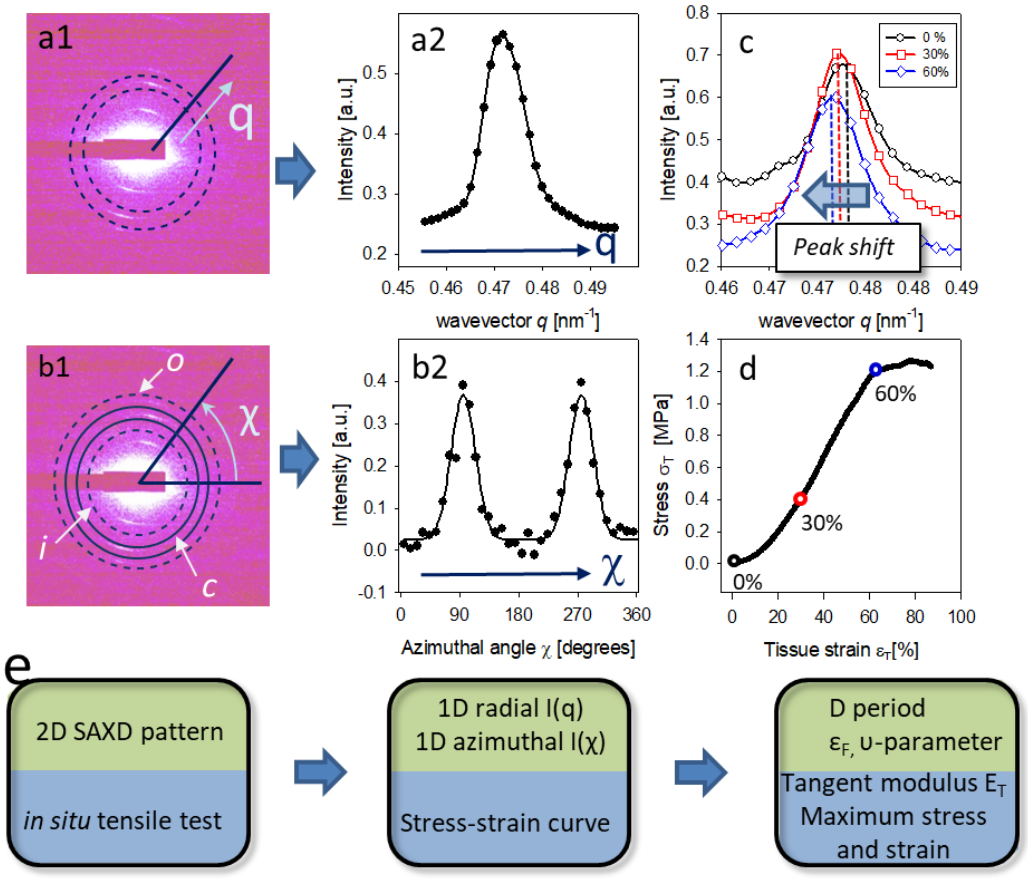

Figure 6.3 Data reduction pipeline: *(a1) a two-dimensional SAXD pattern from collagen fibrils in sea cucumber dermis MCT with predominant fibril orientation vertical; radial (q) direction indicated. Dotted lines denote the ring over which the azimuthal averaging of intensity is carried out. (a2) The azimuthally averaged radial intensity profile I(q) for the pattern in (a1). (b1) The same 2D SAXD pattern as (a1), with the inner, outer and central rings (i, o and c respectively on the figure) shown schematically, over which radial averaging of intensity is carried out; azimuthal (χ) direction indicated. (b2) The radially averaged intensity profile I (χ). In (a2) and (b2) both experimental data (open circles) and fits to model functions (solid lines) are shown. (c) Radial intensity profile I(q) for three levels of applied tissue strain ε_T = 0% (circles), 30% (squares) and 60% (diamonds), showing the shift of peak position to lower wavevector with increasing strain. (d) Tissue stress-tissue strain plot for sea cucumber dermis in tension, with circles (black: 0%; red: 30%; blue: 60% (colour online)) indicating the points from which the I(q) plots in (d) are shown. (e) Flowchart corresponding to the data reduction steps in (a1-b2) above, with parameters obtained at each step indicated.*

6.2.4 Determination of fibril orientation measured from SAXD

In a complementary manner to fibril strain, the angular fibril distribution was calculated from the azimuthal intensity profile $I_5(q)$ of the 5th order Bragg reflection of the collagen D-spacing. The azimuthal profile was calculated by first integrating (using the Fit2D/CAKE command) the 2D intensity pattern radially in a narrow band of wave-vectors around the peak position q_{05} ~ 0.48 nm^{-1} of the 5th order reflection, i.e. over the wavevector range 0.45 – 0.50 nm^{-1}. The background-corrected azimuthal intensity distribution $I_{\text{corrected}}(\chi)$ was calculated by first averaging the azimuthal intensity profiles in two rings around the 5th order peak position, and subtracting the averaged intensity from the centre (peak) ring, as described earlier for bone [289], and is shown in **Figure 6.3 (b1)**.

$$I_{corrected}(\chi) = I_{original}(\chi) - \frac{1}{2}(I_{outer}(\chi) + I_{inner}(\chi)) \quad \textbf{Equation 6.3}$$

To ensure the full azimuthal width of the peaks was captured, the intensity profile was calculated over the full circle (0 to 360º). Angular coordinates corresponding to high values of $I_{\text{corrected}}(\chi)$ denote a greater proportion of fibrils along the specified azimuthal angle. The profile $I_{\text{corrected}}(\chi)$ was then fitted to a function with two Gaussian peak profiles, separated by 180 degrees.

$$I_{corrected}(\chi) = I_{0\chi}\left(\exp\left(-\frac{1}{2}\left(\frac{\chi-\chi_0}{\Delta\chi_0}\right)^2\right) + \exp\left(-\frac{1}{2}\left(\frac{\chi-\chi_0-\pi}{\Delta\chi_0}\right)^2\right)\right) \quad \textbf{Equation 6.4}$$

The parameter χ_0 defines the main direction of orientation of the fibrils, while $\Delta\chi_0$ is a parameter characterising the width of the distribution and $I_{0\chi}$ is an amplitude term proportional to the total SAXD intensity of the 5th order reflection. It is noted that whilst applied forces will induce shifts in q_{05} over the course of the test, these will turn out to be

sufficiently small such that the same narrow band around the initial peak position can be used over the entire test.

A collagen fibril distribution with a narrow angular width (corresponding to well-oriented fibrils) is characterized by a low value $\Delta\chi_0$ and twin sharp peaks in $I_{corrected}(\chi)$ above a low baseline intensity, while a distribution with a wide angular dispersion in fibril orientation is characterized by high $\Delta\chi_0$ and a nearly constant $I_{corrected}(\chi)$. We define a dimensionless parameter υ, derived from $I_{corrected}(\chi)$, which can be used to determine if the fibril distribution is narrow or broad.

υ = Std. Dev.($I_{corrected}(\chi)$) / Mean($I_{corrected}(\chi)$) **Equation 6.5**

It can be seen that an isotropic (wide) fibril angular distribution, corresponding to a nearly constant $I_{corrected}(\chi)$, will have $\upsilon \sim 0$, while υ will increase as the angular width reduces.

6.3 Results

Synchrotron SAXD measurements of fibrillar strain in MCT from sea cucumber dermal tissue were carried out at beamline ID02 at the European Synchrotron Radiation Facility (Grenoble, France) as shown in **Figure 6.2**. Prior to testing, tissue specimens were chemically incubated in artificial sea water (ASW) and two ionically modified solutions of ASW (potassium rich ASW (KASW) and calcium free ASW (CaF-ASW)) which are known to induce standard state, stiffening and softening of sea cucumber dermis respectively [262, 272] (for details see *Materials and Methods*). The fibril strain ε_F is the fractional increase in fibril length (as measured from the shifts in the meridional Bragg peaks in the SAXD pattern of MCT collagen fibrils), while tissue strain ε_T is the fractional increase in MCT sample length and tissue stress σ_T is the force divided by sample area. Considering

the fibrillar-level strain ε_F and tissue stress developed in MCT during stretch to failure tests, it is observed (**Figure 6.4(a)**) that fibrils in tissues with different chemical stimulation - CaF-ASW, ASW and KASW - show a differing extent of elongation at the same tissue strain ε_T. At a given tissue strain, the amount of fibril strain is proportional to the stress taken up by the fibrils. At a tissue strain ε_T around 10%, fibrils in KASW-tissue have a much higher extension of ~0.5% compared to ASW (0.07%). Likewise, the fibril strain for CaF-ASW is much lower (~0.001%), indicating mainly interfibrillar sliding. The maximum fibril strain developed in KASW is much larger than in CaF-ASW, and the fibril strain in ASW is in between that of KASW and CaF-ASW. **Figure 6.4(b)** shows corresponding averaged mean strain-stress curves for body wall tissue in KASW (red), ASW (black) and CaF-ASW (blue). The averaged macroscopic stress σ_T with tissue strain ε_T at 40% for KASW-treated (4.08 MPa) specimens is significantly higher than CaF-ASW (0.13 MPa), while the ASW-treated (0.77 MPa) specimens are in between these extremes. We note that the increase of fibril strain with applied tissue strain is not completely smooth in all cases, as evidenced by the error bars. This is most noticeable in the case of KASW-treated tissue, where there are clear local peaks at ~10 and 30% strain followed by dips. The structural reasons for this behaviour will be considered further when the model to explain fibrillar deformation is developed in the Discussion. Further, the variation of the macroscopic tensile stress (at the tissue-level) for the whole specimen for all treatments (KASW, ASW and CaF-ASW) is much greater compared to the strain developed at the fibril-level (**Figure 6.4a**), indicating that interfibrillar components of the extracellular matrix are important in mechanisms of MCT.

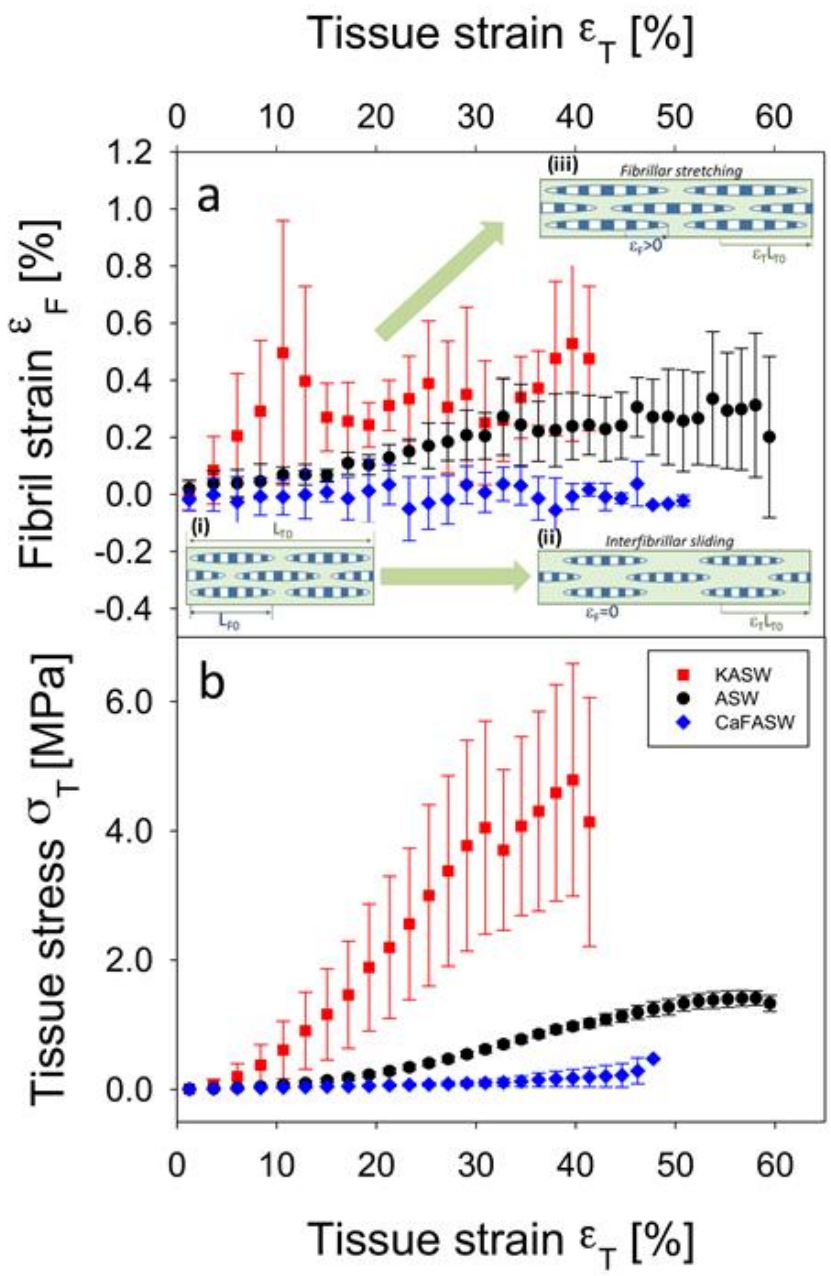

Figure 6.4 Altered fibrillar stress- and strain take-up in ionically-treated MCT. *(a) Fibril strain versus applied tissue strain from ionically treated sections of MCT dermis, measured from the peak shifts of the 5th order collagen reflections in the SAXD pattern. The rate of increase of fibril strain with tissue strain ($\varepsilon_F/\varepsilon_T$) is proportional to the amount of stress taken up by the collagen fibrils. Data from control (ASW): black circles, n=4; stiffened (KASW): red squares, n=4; and softened (CaF-ASW): blue diamonds, n=3. All samples in*

each group are binned according to tissue strain with bin widths of 2.0%; error bars are standard deviations. Stiffened MCT exhibits a higher rate of increase of fibril strain compared to control, whilst softened MCT shows essentially no increase in fibril strain. Inset schematics (i) Fibrils (striated ellipsoids; length LF0) separated by interfibrillar matrix, in unloaded MCT of length LT0. (ii) In softened MCT (CaF-ASW treated), while the tissue elongates ($\varepsilon_T>0$), the fibrils do not stretch, but slide in the interfibrillar matrix ($\varepsilon_F=0$). (iii) In stiffened MCT (KASW treated), there is increased stress transfer to the fibrils, leading to fibrillar stretching ($\varepsilon_F>0$). (b) Corresponding macroscopic tensile stress/strain curves for the control, stiffened and softened groups, binned according to tissue strain (error bars: standard deviations), showing clear differences in tangent modulus and maximum stress achieved.

The differences in Ca^{2+} or K^+ concentrations in CaF-ASW, ASW and KASW led to changes of maximum tangent modulus and maximum tissue stress (**Figure 6.5**). Ca-FASW-treated (0.69±0.59 MPa) samples had ~80% lower maximum tangent modulus compared to ASW (3.23±0.40 MPa), while the maximum tangent modulus for KASW-treated samples (17.27 ±6.70 MPa) was 4 times larger. Concurrently, the maximum stress of each state is very different, with the loads borne by CaF-ASW-treated tissue (0.30 ± 0.32 MPa) being much less (~80 %) compared to ASW-tissue (1.30 ± 0.20 MPa) while KASW-tissue (6.39 ± 0.44 MPa) had maximum stress 4 times higher than the control. Similarly, nanoscale parameters like fibril strain also show clear differences between treatments (**Figure 6.5(c) and (d)**). Compared to maximum fibril extension (**Figure 6.5(c)**) developed in KASW (0.94%), fibrils in CaF-ASW (0.09%) and ASW (0.35%) had a reduced elongation, with ~95% and 80% less strain respectively. Fig. 4(d) shows the ratio of fibril strain to tissue strain ($\varepsilon_F/\varepsilon_T$) for the three states, which is observed to be consistent with **Figure 6.5(c)**, showing that stiffened tissue sections have ($\varepsilon_F/\varepsilon_T$) of 0.044, larger than control

specimens, whilst softened tissue sections have almost negligible fibril strain take-up ($\varepsilon_F/\varepsilon_T \sim 0$). The parameter $\varepsilon_F/\varepsilon_T$ will be used to confirm the modelling results, which will be illustrated later.

To test whether these mechanical and ultrastructural parameters are statistically different, pairwise *t*-tests were performed (Sigma Plot v10, SyStat Software), with results summarized in **Table 6.1**. At the tissue level, the maximum tangent modulus of ASW was significantly higher than that of CaFASW ($p<0.001$). There is a statistically significant difference ($p<0.01$) of maximum tangent modulus between ASW vs. KASW and CaFASW vs. KASW. The maximum stress was lower in CaFASW compared to both ASW and KASW ($p<0.01$), and there is also a significant difference between KASW and ASW. At the fibrillar level, statistical analysis shows that there is no significant difference for maximum ε_F and mean $\varepsilon_F/\ \varepsilon_T$ across different treatments, except for the maximum fibril strain ε_F between the stiffest (KASW) and least stiff (CaFASW) states ($p<0.05$).

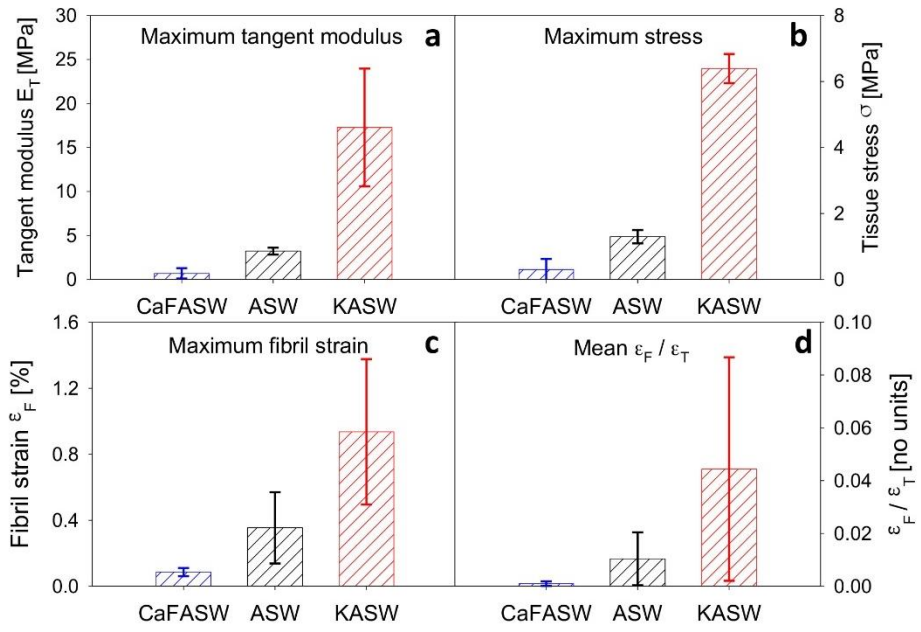

Figure 6.5 Quantified MCT mechanics. *(a) Averaged maximum tangent modulus and (b) maximum stress for control (ASW; black; n=4), stiffened (KASW; red; n=4) and softened (CaF-ASW; blue; n=3) specimens from MCT dermis; error bars are standard deviations. n denotes the number of samples in each treatment group. At the tissue level, stiffened MCT always exhibits remarkably higher mechanical properties compared to the control group, and for the softened one, the binned maximum tangent modulus and the maximum stress is almost negligible. At the fibrillar level, the fibril strain (c) and the ratio of the fibril strain to tissue strain ((d); the fraction of the deformation taken up at the fibril level) for the stiffened, control and softened MCT follows the same trend with properties at the tissue level.*

Table 6.1 Statistic analysis of Maximum E_T, Maximum σ, Maximum ε_F, Mean $\varepsilon_F/\ \varepsilon_T$ across different treatment

P value	Maximum E_T	Maximum σ	Maximum ε_F	Mean $\varepsilon_{F/}\ \varepsilon_T$
ASW vs CaFASW	0.00098	0.00297	0.0920	0.1240
KASW vs ASW	0.00577	0.00515	0.0816	0.2318
KASW vs CaFASW	0.0086	0.00615	0.0364	0.2713

We believe this lack of significance may arise due to a combination of the limited number of samples measurable at the synchrotron (maximum 4 per group) and the relatively weak SAXD scattering signal of MCT and associated noise in the fit parameters.

In a complementary manner, we consider the alterations in the fibril orientation distribution on application of external load. The υ-parameter, derived from the angular distribution of the SAXD intensity, is a dimensionless number which is zero when fibrils are distributed at all angles with equal likelihood, and positive when fibrils are aligned either along one or a couple of principal directions. A representative plot of the υ parameter as a function of tissue strain (**Figure 6.6(a)**) exhibits an initially high value of ~1.3 (corresponding to two main fibril directions equidistant (azimuthally) from the

vertical direction) that is followed by a decrease to a minimum around 20% tissue strain. The initial two directions correspond to two principal helical fibre pitches along the long axis of the animal. The initial reduction in the υ parameter corresponds to a more random fibril orientation, as indicated schematically by the insets in **Figure 6.6 (a-c)**, and represents the stress-induced breakdown of the two main fibril directions into a single broad distribution centred on the (vertical) direction of applied tensile load. For tissue strains larger than 20%, the υ parameter increases monotonically with increasing tissue strain, before levelling off near tissue strains of ~40-50% close to macroscopic failure. The increase of the υ parameter represents a narrowing of the azimuthal width of the initial broad fibril distribution around the direction of applied load. The tissue strain at the transition between the reduction of the υ parameter and the subsequent increase is denoted by ε_{Tr}. The analysis of mean ε_{Tr} across three groups of specimens is shown in **Figure 6.7(a)**. The results indicate that soft (CaF-ASW) samples always have a higher ε_{Tr}, relative to the control (ASW) and stiffened (KASW) samples, which implies that the rate of reorientation (from the initial distribution with two main directions to a random and then highly oriented distribution) is slower for the softened MCT.

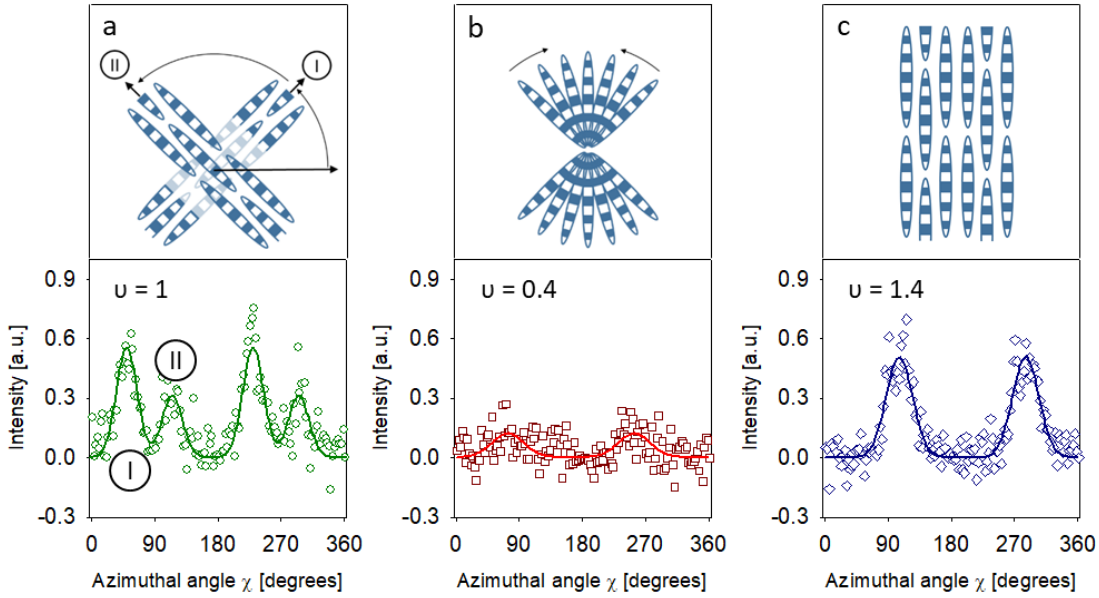

Figure 6.6 Strain-induced fibril alignment of MCT in stiffened, control and softened states*: (a)-(c) Top row: schematic illustration of fibril distribution at increasing tissue strain levels; Bottom row: corresponding I(χ) plots for a control (ASW) sample with corresponding υ-parameter. (a) (0% strain) shows bimodal distribution due to two groups of fibres (I and II) inclined to the direction of tensile load at two principle fibre directions (arrows). In the below I (χ) profile, the two sets of peaks are arising from two groups of fibril bundles labelled I and II. (b) (20% strain) shows a wider range of orientations due to fibrils progressively reorienting toward the tensile axis (low υ) and (c) (55% strain) shows highly aligned fibres along the vertical direction (higher υ)*

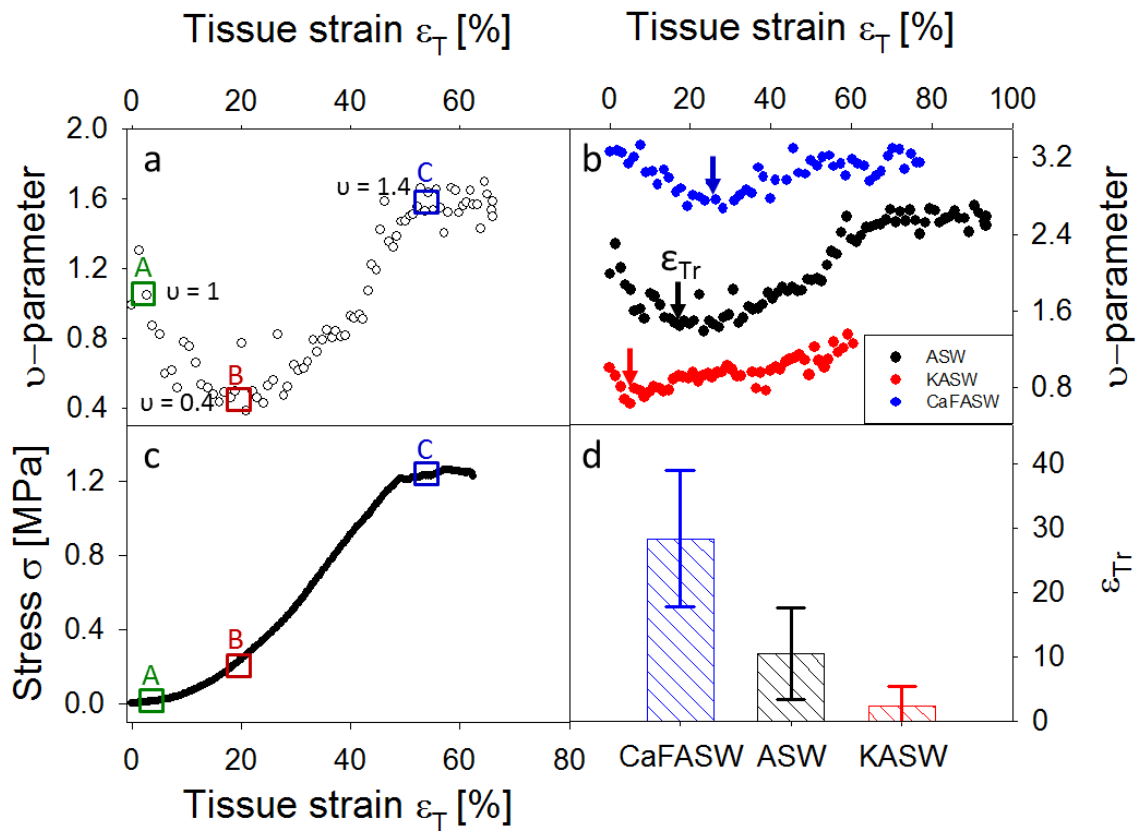

Figure 6.7 *(a) Initial decrease followed by increase of υ-parameter with increase tissue strain, for control (ASW) MCT, exhibiting an initial decrease, a local minimum at tissue strain ~ 20%, followed by an increase. (b) A typical stress-strain curve for ASW-treated MCT. In (a) and (b), rectangles indicate strain locations corresponding to* ***Figure 6.6*** *(a)-(c). (c) Variation of the strain-induced changes in the υ-parameter as a function of the mechanical state of MCT due to ionic treatment. Data from one representative MCT specimen in each state is shown. The tissue strain corresponding to the local minimum in υ is indicated by a vertical arrow, denoted εTr, and is lowest for the stiffened and highest for the softened specimen. (d) Averaged εTr across the three treatments (control (ASW; black; n=4), stiffened (KASW; red; n=4) and softened (CaF-ASW; blue; n=3)); error bars are standard deviations.*

6.4 Model and Discussion

These experimental results, showing clear alterations in the deformation at the fibrillar level when MCT is stimulated into its stiff and soft states, can be used to build a simple model that sheds light on the key biophysical mechanisms enabling mutability [187, 189, 191,

192, 274]. Prior research has proposed, but not directly demonstrated, that certain proteins secreted by JLCs including tensilin [273, 274], stiparin [192] and NSF [191] act to cross-link the fibrils. A complete ultrastructural mechanism for MCT mutability has not, however, been quantitatively established, and each protein appears to only be involved in a specific subset of the mechanical response, such as in stiffening a compliant specimen back to the reference state (as is the case for tensilin [273, 274]). At the ultrastructural level, the parallel-packed fibrils and interfibrillar matrix of MCT can be represented as shown in **Figure 6.7(a)**. The covalently cross-linked $(\alpha 1)_3$ collagen fibrils are expected to have much greater stiffness (~0.5-2 GPa [290]) than the interfibrillar matrix (which can be considered a negatively charged hydrated gel [291]), although precise values for the interfibrillar matrix modulus are unknown. Under tensile loading, the highly anisotropic fibrillar structure together with the expected stiffness mismatch between the fibrils and the interfibrillar matrix will lead to a characteristic inhomogeneous deformation field at the nanoscale. In this deformation field, tensile forces develop in the fibrils and matrix, and significant shear occurs in the interfibrillar matrix connecting fibrils [292]. The shearing force lines are shown in the insets in **Figure 6.7(b)**, and can be considered as representations of the cross-linking between fibrils proposed previously [11]. Consequently, the fibril strain is only a fraction of the total strain (due to the remaining shearing strain in the interfibrillar matrix).

In order to keep the model analytically simple we consider a unidirectional fibre composite; whilst the initial unstrained MCT shows two main fibril directions around the direction of stretch (**Figure 6.6(b)**), it is observed that for tissue strains larger than ~20%

the fibrils are highly aligned to the direction of applied stress and the uniaxial fibril arrangement is expected to be a good approximation for this region at least. This type of model, denoted a staggered model, has been proposed before, by us [241] and others [292, 293] for deformation of the ultrastructure of bone mineralized fibrils, tendon, enamel and dentine [231, 294], where a similar high stiffness element in tension (e.g. mineral platelet) is effectively in serial-loading with a low stiffness element loaded in shear (e.g. collagen fibrils). The deformation of the fibril ε_F, shear of the interfibrillar matrix γ_{IF}, and tissue level stress σ_T, among other quantities, have been calculated from load-balance equations at the nanoscale [241]. These lead to expressions for the fibril to tissue strain ratio, and the tissue modulus E_T, in terms of the structural and constitutive parameters:

$$\frac{\varepsilon_T}{\varepsilon_F} = 1 + \frac{4}{\rho_1^2}\frac{1-\Phi_1}{\Phi_1}\frac{E_F}{\gamma_{IF}E_{IF}} \qquad \textbf{Equation 6.6}$$

$$E_T = \Phi_1 E_F \frac{\varepsilon_F}{\varepsilon_T} + (1-\Phi_1)E_{IF} = \frac{\Phi_1 E_F}{1 + \frac{4}{\rho_1^2}\frac{1-\Phi_1}{\Phi_1}\frac{E_F}{\gamma_{IF}E_{IF}}} + (1-\Phi_1)E_{IF} \quad \textbf{Equation 6.7}$$

In the equations above, Φ_1 denotes the fibril volume fraction, ρ_1 the fibril aspect ratio, E_F the fibril elastic modulus, E_{IF} the interfibrillar modulus, and γ_{IF}~0.40 is the ratio between shear (G_{IF}) and tensile (E_{IF}) modulus of the interfibrillar matrix ($G_{IF}=\gamma_{IF}E_{IF}$)[241]; other terms have been defined earlier in the text. As our scheme enables measurement of deformation at the fibrillar level concurrently with tissue-level mechanical stress and strain, a parametric variation of fibril strain and tissue modulus may now be carried out and compared to the experimental results reported earlier in **Figure 6.5** and **6.6**. These results are shown in **Figure 6.8(b)** and discussed below.

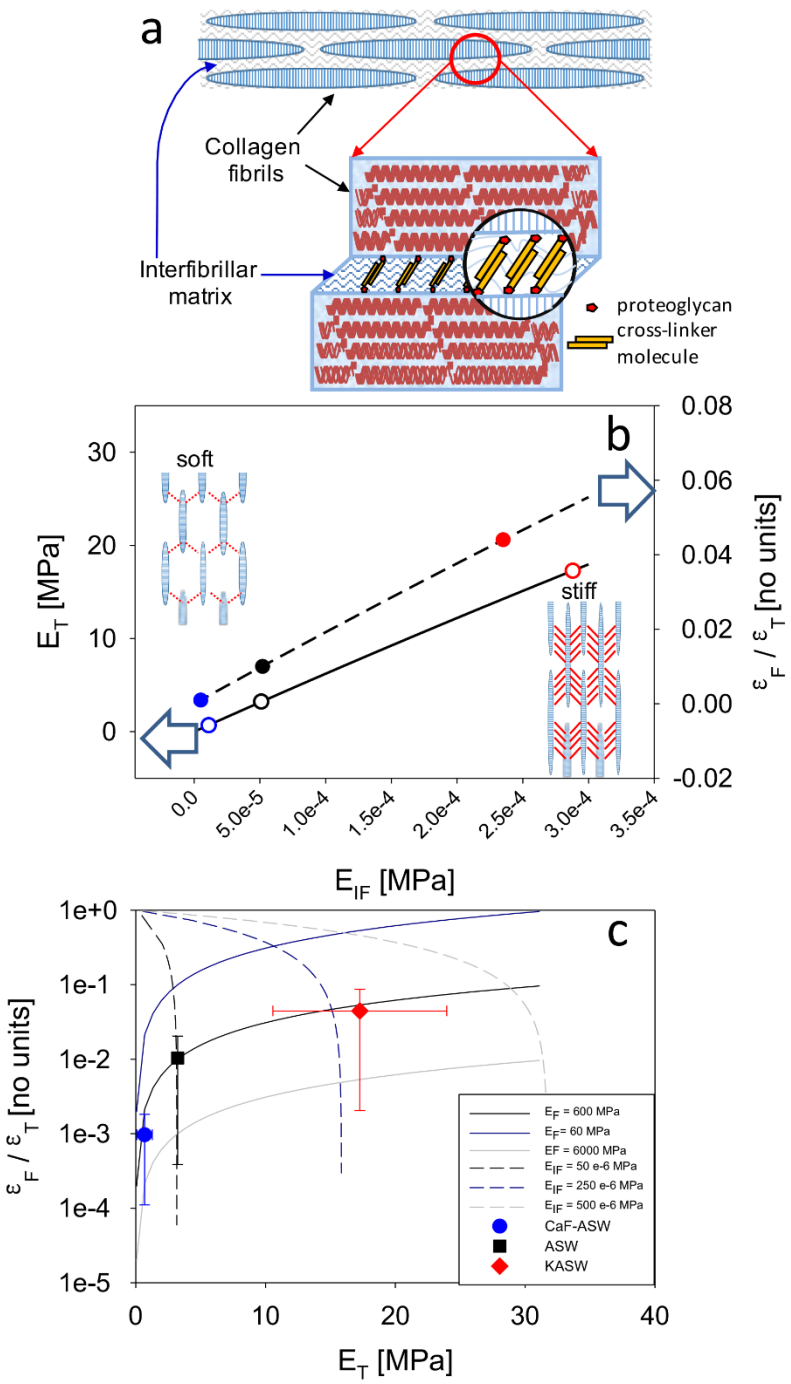

Figure 6.8 Staggered model of MCT nanomechanics. *(a) Staggered model for MCT: discontinuous, spindle-shaped collagen fibrils aggregating in parallel. The attached PGs serve as a binding site for interfibrillar cohesion mediated by cross-linker molecules[11]. (b) Elevation of interfibrillar stiffness E_{IF} leads to a corresponding increase in both tissue modulus E_T (left hand ordinate; solid line:*

staggered model prediction) and fibril-to-tissue strain ratio ($\varepsilon_F/\varepsilon_T$) (right hand ordinate; dashed line: staggered model prediction). Symbols show experimental values for each tissue group with E_{IF} calculated from the staggered model equations (filled symbols: from ***Equation 6.6****; open symbols: from* ***Equation 6.7****. Open arrows indicate the ordinate each line belongs to. The inset schematics show the shear transfer, and consequent stress take-up, between fibrils in softened (left) and stiffened (right) states. Increased shear stress in the stiffened interfibrillar matrix is shown qualitatively by a larger number of interfibrillar shear lines. (c) Positive correlation between $\varepsilon_F/\varepsilon_T$ and E_T demonstrates that interfibrillar stiffening is the mechanism for alteration of MCT mechanics. The staggered-model relations between ($\varepsilon_F/\varepsilon_T$) and E_T* ***(Equation 6.8****) are shown via solid curves (with a positive gradient) for varying E_{IF} and three fixed levels of E_F (blue: 60 MPa, black: 600 MPa, and grey: 6000 MPa). Likewise, dashed lines show staggered-model predictions for ($\varepsilon_F/\varepsilon_T$) vs. E_T for varying E_F and three fixed levels of E_{IF} (black: 50×10^{-6} MPa, dark blue: 250×10^{-6} MPa, and grey: 500×10^{-6} MPa). Symbols show experimental ($\varepsilon_F/\varepsilon_T$) and E_T, which show a clear positive correlation, indicating interfibrillar stiffening (blue: CaF-ASW, black: ASW and red: KASW; error bars are standard deviations).*

Considering, for the moment, that the collagen fibrils have a constant elastic modulus E_F, we first examine the effects of altering the interfibrillar modulus on the change in tissue stiffness. Such a scenario corresponds to an alteration in cohesion due to secretion of stiffening factors such as tensilin, stiparin and NSF. As seen in **Equation 6.7**, the increase in tissue stiffness arises due to both the increased load borne by the interfibrillar matrix (second term on the right-hand side in **Equation 6.7** as well as – much more significantly – the increased stress borne by the collagen fibril due to the larger shear stress transferred by the interfibrillar matrix (first term on the right-hand side). The stress borne by the collagen fibril is large due to the large contact surface area between the fibrils and the interfibrillar matrix due, in turn, to the large fibril aspect ratio ρ_1. Concurrently with the increase in tissue stiffness, the fibril strain increases as a fraction of

the tissue strain, as larger tensile forces are transferred to the elastic fibrils with increased fibril strain.

In order to compare the model predictions with experimental data (**Figure 6.8(b) and (c)**), initial estimates of some of the unknown parameters need to be made. The length and fibril diameter distributions for echinoderm collagen fibrils have been estimated previously [198, 270]. While the maximum and minimum values span a wide range, a constant spindle shaped morphology was reported [270]. The most frequent value (mode) in the diameter distribution was ~100 nm [198], and the length ranged from 50 μm to 1 mm. Using the constant shape of the collagen fibrils reported previously [270] and the diameter distribution shown in [198] , these values can be used to estimate the maximal length to be ~120 μm. These lead to an aspect ratio of ~1000. The fibril modulus for individual sea cucumber fibrils isolated from the tissue was measured to be ~ 500 MPa [290]. As described in the **Appendix**, these values can be used, together with the experimentally determined values of $\varepsilon_F/\varepsilon_T$ and E_T, to obtain estimates of fibril volume fraction $\Phi_1 \sim 0.54$ and the interfibrillar modulus $E_{IF} \sim 50 \times 10^{-6}$ MPa (in the ASW-case). The fibril volume fraction will not vary across treatments, but the interfibrillar modulus will change. With these numerical values, the two trends described above – increase in both tissue stiffness (E_T) as well as in fibril strain ratio $\varepsilon_F/\varepsilon_T$ with increasing E_{IF} – are plotted in **Figure 6,8(b)**, together with the experimentally measured values for the softened, control and stiffened groups. **Equation 6.6** is used to calculate interfibrillar matrix stiffness E_{IF} for each tissue group from measured $\varepsilon_F/\varepsilon_T$, which are then plotted (symbols) together with model curves (lines). In a similar manner, **Equation 6.7** is used to obtain E_{IF}

from measured tissue moduli E_T for each group. For consistency of the model, the two calculated sets of E_{IF} should match, and indeed, it is observed that both methods give similar values for E_{IF} across the tissue groups.

In principle, however, there are two distinct ways in which the stiffness of MCT can be modified: either by the interfibrillar matrix stiffening (as considered above) or by alterations of the mechanics of the collagen fibrils, possibly by modulation of intrafibrillar cohesion. These two scenarios – fibrillar versus interfibrillar stiffening – lead to different behaviours at the fibrillar level. In the fibrillar stiffening case, the fibrillar strain (as a fraction of tissue strain) will reduce as the tissue stiffens, whilst in the interfibrillar stiffening case, the fibrillar strain will increase as the tissue stiffens, as can be seen by combining **Equations 6.6** and **6.7** to obtain parametric plots of $\varepsilon_F/\varepsilon_T$ and E_T as functions of E_{IF} and E_F.

$$\frac{\varepsilon_F}{\varepsilon_T} = \frac{E_T - (1-\Phi_1)E_{IF}}{\Phi_1 E_F} \quad \textbf{Equation 6.8}$$

In the model, changing the aspect ratio by ±10% leads to a variation of 20 % in both ε_F / ε_T and E_T (Appendix, section 2). In order to conclusively demonstrate interfibrillar stiffening, and exclude fibrillar stiffening as the key mechanism for mechanical changes in MCT, the experimental data for $\varepsilon_F/\varepsilon_T$ and E_T are plotted in **Figure 6.8(c)** together with two sets of three predictive curves from the model. The first set of three curves (solid lines) corresponds to a continuous increase in interfibrillar modulus (for several discrete values of fibrillar stiffness), while the second set (dashed lines) corresponds to continuously increasing fibrillar stiffness for several values of

interfibrillar stiffness. It is clearly seen that the experimental data show an increase in $\varepsilon_F/\varepsilon_T$ with E_T, corresponding to the case of interfibrillar matrix stiffening. Further, it is apparent that the mean values lie along the predicted curve for a collagen fibril modulus E_F = 600 MPa, which is close to the value of 500 MPa reported by Eppell et al [290]. This finding provides evidence in support of the long-held, but not directly demonstrated, hypothesis that the alteration of MCT mechanical properties arises due to changes in interactions between fibrils (through changes in the interfibrillar matrix) rather than alterations in the mechanical properties of the fibrils themselves [11].

From the variation of interfibrillar matrix stiffness certain observations can be made. In MCT, E_{IF} is, even in the stiffest state, ~0.25 kPa - at least 6 orders of magnitude lower than the stiffness of the fibril ~0.6 GPa. In the state of least stiffness, there is a factor of ~100 reduction in E_{IF} relative to the already low value of 0.25 kPa, to ~5-10 Pa, and the matrix can be considered a fluid. However, the increased stiffness of MCT in the stiffened state (necessary for its physiological maintenance of posture or locomotion [11]) is almost entirely due to the increased fibrillar recruitment to bear stress, and not due to the stress carried in the interfibrillar matrix. The ratio of the stress in the interfibrillar matrix to that in the fibril can be calculated from:

$$\frac{\sigma_{IF}}{\sigma_F} \approx \left(\frac{1-\Phi_1}{\Phi_1}\right)\left(\frac{E_{IF}}{E_F}\right)\left(\frac{\varepsilon_T}{\varepsilon_F}\right) = \left(\frac{0.46}{0.54}\right)\left(\frac{50\times10^{-6}}{0.6}\right)\left(\frac{1}{0.01}\right) = 7.1\times10^{-3}$$

i.e. only ~0.7% of the total stress is borne by the interfibrillar matrix. Under alteration of mechanical state, the relative increase in fibril stress can be calculated from the change in fibril strain ratio, *via*

$$\sigma_F = \Phi_1 E_F \frac{\varepsilon_F}{\varepsilon_T}$$

We observe that fibril stress increases by a factor of ~4 (**Figure 6.5(d)**) in the stiff state compared to the standard state. Conversely, in the softened state, the fibril stress decreased by a factor of ~10 relative to the standard state. We also note that we have (for simplicity) considered the interfibrillar matrix to stiffen homogeneously. In practice, there can be local heterogeneities (both temporal and spatial) in stiffness, possibly due to conformational changes in the non-collagenous proteins, local entanglements and other phenomena. Such heterogeneities would lead to local increases (or decreases) in interfibrillar stiffness, which would increase (or decrease) stress transfer between fibrils. Such alterations in stress transfer would explain the local maxima and minima in the fibril strain measured in stiffened KASW-treated MCT observed in **Figure 6.4(a)**. In this regard, the recent finding of collagen molecular shortening – due to water content changes – leading to large tensile stresses in tendon may be of relevance [295].

These findings shed light on the synergistic action at the nanoscale enabling mutability in MCT. By itself, the stress in the stiffened (or softened) interfibrillar matrix is by no means sufficient to account for the change in tissue stiffness. However, due to the large anisotropy and surface to volume ratio of the fibrils, considerable contact area exists for binding of the interfibrillar proteins and glycosaminoglycans to the fibrils. Such binding is likely to occur at the gap-zones (separated by D~65-67 nm) identified previously as putative binding sites for proteoglycans in collagens [296]. As a result, the total stress transferred to the collagen fibrils is effectively amplified by the aspect ratio ρ~1000. Small changes in the mechanical properties of the

interfibrillar matrix are thus amplified to apply considerable stress to the elastic fibrils, as a consequence of which the fibrils are more effectively recruited to bear load. Prior biochemical evidence suggests the involvement of proteins like tensilin and NSF in the stiffening of the matrix [191, 273, 274]. It is probable that these proteins physically cross-link to the existing glycosaminoglycans and proteoglycans, which in turn are bound to the gap-zones in collagen fibrils. It is conjectured that these proteins are acting like a bridge binding the proteoglycan/GAG sites of two adjacent fibrils together [11, 268]. In this manner, increased matrix stiffening combined with effective shear load transfer to the fibrils enables MCT to undergo considerable (by a factor of ~25; **Figure 6.8(b)**) changes in tissue stiffness. The physical cross-linking process shows time-dependent property, most likely due to diffusion of proteins secreted by the JLCs in between the collagen fibrils, combined with progressive occupation of binding sites for these proteins in the interfibrillar matrix. This process of increased interfibrillar stiffening, enabling alteration of mechanical behaviour, is likely to be a general property of MCT in echinoderms.

It is worth noting that possible changes in D-period that could also result from molecular/microfibrillar rotation during stretching. Collagen molecules from different tissues have 5°-17° tilt with respect to their fibril axis, with tendon showing low tilt angles and corneal collagen large tilt angles [297]. To uncouple the influence of intermolecular changes in MCT, a follow-up study using wide angle x-ray scattering as in [298] can be carried out to understand whether such rotation plays a role in MCT.

6.5 Conclusion

In this first direct measurement of the nanoscale fibrillar deformation mechanisms of freeze – thawed MCT, we have demonstrated that the use of *in situ* X-ray methods together with mechanical testing is capable of quantifying both the material-level mechanisms by measuring the percentage shifts in the 67-nm meridional periodicity of the collagen fibrils.

The approach opens up several promising further avenues of investigation, e.g. alterations in the molecular level diffraction patterns would provide combined molecular as well as fibrillar real-time structural information, the use of the stiffening or softening agents in MCT could be tested *in situ* for efficacy [299].

Chapter 7 : An experimental study of the ability to change viscoelastic state

7.1 Introduction

In the previous chapter, we evaluated the fibril strain changes in response to the mechanical and chemical stimulation of MCT containing tissue, by considering both the collagen fibrils and the interfibrillar matrix as elastic components. However, it is well-known that MCT (like many soft collagenous tissues [284]) is viscoelastic, i.e. the mechanical properties are time-dependent, including the change of mechanical state. The viscoelastic properties of sea cucumber body-wall had been previously quantified and examined by means of macroscopic mechanical tests, for example, creep [142, 189, 300, 301], tensile [139, 176], stress relaxation [177, 302, 303] and dynamic tests [145, 302]. To compare the mutability in a controlled manned, a common method was applied to this tissue with several types of treatments which is capable of inducing standard, softened or stiffed mechanical states with either intermediate, minimum or maximum of viscosity and stiffness. For example, in the stress relaxation tests performed by Greenberg in 1984, it was found that the relaxation time of sea cucumber dermis increased dramatically when the stiffening agent was introduced to the system [303]. In accord with experiment, the change in viscosity of ligament from echinoid (species: *Diadema setosum*) has been investigated via creep test, in which the elongation of specimens were recorded under the constant load, by showing viscosity increased when a stiffening agent, acetylcholine (ACh) and K^+ was introduced to the bathing solution [142].

The origins of *time-dependent* mechanics in MCT at the nanoscale is essential to an understanding of the dynamics of active force generation in the organs containing MCT. Specifically, the time-scales at which organs or their components can straighten, bend or articulate (via changes in MCT-state) depends crucially on the rate of change of the mechanical state of the interfibrillar matrix and fibrils. Understanding how rapidly such changes of state can occur is also important in potential translation of MCT-like tissues into components of dynamic biomedical devices or soft robotic applications [304]. However, such a material-level understanding corresponds exactly to a viscoelastic modelling and characterization of MCT-tissue at the nanoscale. We report the first such attempts in this chapter.

To understand the technical issues here, we recall that at the nanoscale MCT-tissue is effectively a fibrillar composite with semicrystalline collagen fibrils in an amorphous biopolymer matrix containing, most likely, mechanoeffector molecules like tensilin [62, 165]. During mechanical stimulation, both the fibril phase and the matrix phase are expected to be viscoelastic and change their properties with time. Moreover, our recent work [123] (also reported in **Chapter 6**) showed clearly that changes in the interfibrillar matrix, rather than the fibril, should be the focus of attention when considering changes in MCT-mechanical state. However, it is not equally easy to measure each phase. While single-fibril testing using technically sophisticated MEMS-type devices have determined the stress relaxation curve of collagen fibrils [93], the direct measurement of the dynamic mechanical properties of the thin layers of interfibrillar matrix is much more difficult, owing to the small volume (length scale: sub-micron to nanometre) of the nanoconfined layers of matrix in MCT. Moreover,

unlike collagen fibril staggering (with meridional peaks arising from the D period), the non-collagenous matrix is amorphous, making it impossible to get direct structural information via changes in the X-ray diffraction signal. It is also difficult to model the intrinsic time-dependent properties of the matrix.

In the current chapter, we combined macro-mechanical stress relaxation with *in situ* SAXD to demonstrate the time-dependent mechanical properties of MCT from macroscopic- down to fibrillar length scales, with the fibrillar stress relaxation behaviour determined *in-situ* in different mechanical states. We incorporate stress relaxation data at macroscopic level and fibrillar level into a model which will provide the time-dependent mechanical behaviour of both the interfibrillar matrix as well as collagen fibrils. The model advances current knowledge by going beyond macro- and micro-scale phenomenological spring-dashpot models by combining the spring with linear elasticity and the dash-pot with linear viscosity, which have hitherto been used to investigated the time-dependent behaviour of MCT [145]. Methods derived from Materials Science for composite materials [305, 306] are used to predict both static- and time-dependent properties of MCT. A similar chemical protocol to that used in **Chapter 6**, for inducing stiffening/softening effects of mechanical properties is used.

7.2 Materials and methods

7.2.1 Sample preparation

The species we used in this project is black sea cucumber (species: *Holothuria altra*), whose body wall is rich in collagenous tissue. Specimens of *Holothuria altra* of medium size were collected from a

commercial wholesaler (Tropical Marine Centre, Chorleywood, London). Sea cucumbers around 100 mm in length, and 20mm in width measured from the end to the tip. This species has a thick body wall (~5 mm), which was largely composed by collagenous tissue. To prepared stiffened, standard and compliant state of MCT containing specimens for the stress relaxation tests, same protocol used in **Chapter 6** had been followed.

7.2.2 Synchrotron stress relaxation testing combined with *in situ* SAXD

Prepared *Holothuria altra* specimens were mounted in the customized microtensile tester at the Noncrystalline Diffraction beamline I22, Diamond Light Source (Oxfordshire, UK). A wavelength of 0.08857 nm and a beam-size of 15 μm was used for SAXD spectra acquisition. The sample to detector distance was 997.17 mm ± 1 mm, which was calculated from the standard sample AgBH using the POWDER DIFFRACTION → CALIBRANT routine in Fit2D. SAXD images were acquired with a PILATUS-2M detector with a 0.5 second exposure time.

The SR experimental protocols are shown schematically in **Figure 7.1(C1, C2)**. During the mechanical tests, samples (KASW-treated n=4, CaFASW-treated n=4 and ASW treated n =3) were stretched to a fixed strain of 50% at a constant velocity of 0.01 mm/s (~0.167%/s); **Figure 7.1 (B1)**). The first SAXD measurement of each test was taken at 0%, followed by 35 SAXD measurements acquired, with a time interval of 10 seconds between each measurement, during the relaxation phase.

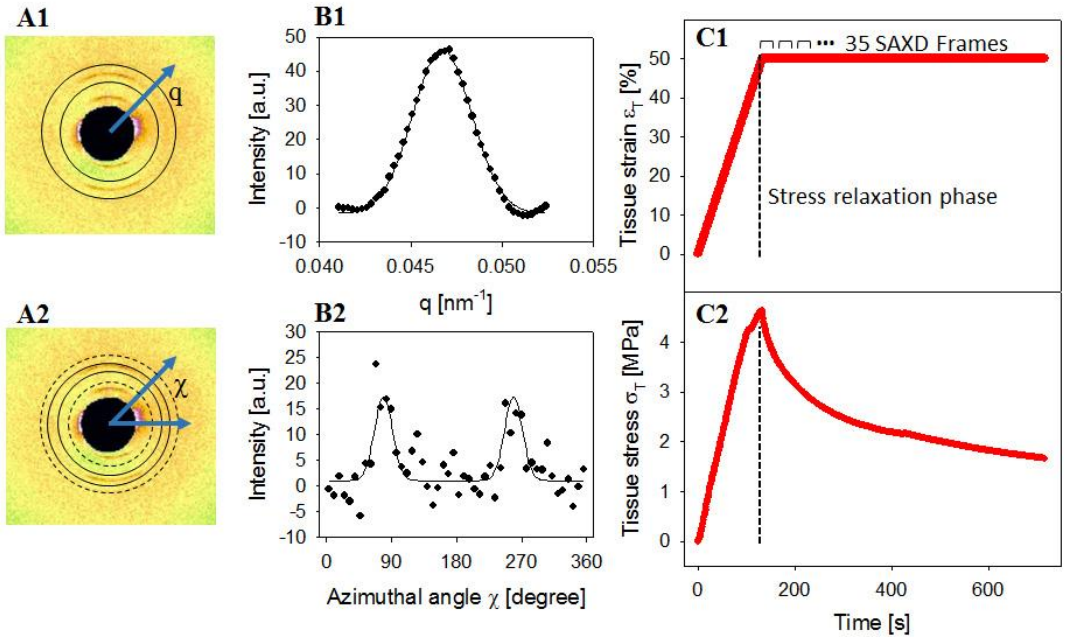

Figure 7.1 Macro to micro mechanics with small angle X-ray diffraction. *(A1) SAXD pattern obtained from sea cucumber dermis (MCT), the diffraction peaks arising from centre is corresponding to the lattice made by axial electron density periodicity of fibrils in MCT. Solid line indicates the area where the azimuthal averaging was carried out. (A2) The same SAXD pattern shown in (A1), with a centre, outer and inner ring presented as a guideline showing the area where radial averaging was carried out and the two narrow circles using for intensity correction. (B1, B2) The one-dimensional azimuthal averaging I(q) profile and radial averaging profile I(χ) obtained from the two-dimensional SAXD pattern. (C1) Tissue strain-time plot from MCT. The first SAXD pattern was acquire at the 0 strain, then series of data were recorded during the relaxation phase. (B2) The corresponding tissue stress-time plot.*

7.2.3 SAXD data analysis

7.2.3.1 Fibril strain calculation and fibril orientation

2D SAXD spectra of sea cucumber body wall was integrated azimuthally across a full circle of 360° sector with a wavevector q ranging from 0.42 -0.52 nm^{-1} (the analysis of fibril orientation and peak intensity will be illustrated later). The 5^{th} Bragg peak arising from meridional stagger D of collagen molecules in fibril was observed from the position expected (**Figure 7.1 (B1)**). For the fibril

strain and fibril orientation determination, a similar protocol described in **Chapter 5** had been followed.

7.2.3.2 Determination of meridional peak intensities

The azimuthally integrated SAXD $I(q)$ profile, with a larger range of wavevectors (compared to **Figure 7.1 B1**) is presented in **Figure 7.2**. We can see that not all meridional diffraction peak orders have the same intensity. The strongly nonlinear background is arising from the pure SAXS scattering from the fibril and possibly some of the hydrated interfibrillar matrix. To separate the background and determine the diffraction peak intensity of the meridional pattern, over short wavevector ranges of ~ 0.1 nm^{-1} (comparable to the spacing between adjacent Bragg orders), the diffuse scattering was assumed as a linear baseline around the peak, and was subtracted from the total intensity. This background baseline was calculated by a linear regression by taking 3 points from both the left and right sides of the peak. The peak profile after linear background subtraction of I_3 (symbol: pink) and I_5 (symbol: green), with fitted line as a guide to the eye, in shown in the inset of **Figure 7.2**. The peak intensities will be used in calculating the intrafibrillar axial organization and gap/overlap ratio in the fibril, and possible changes during stress relaxation.

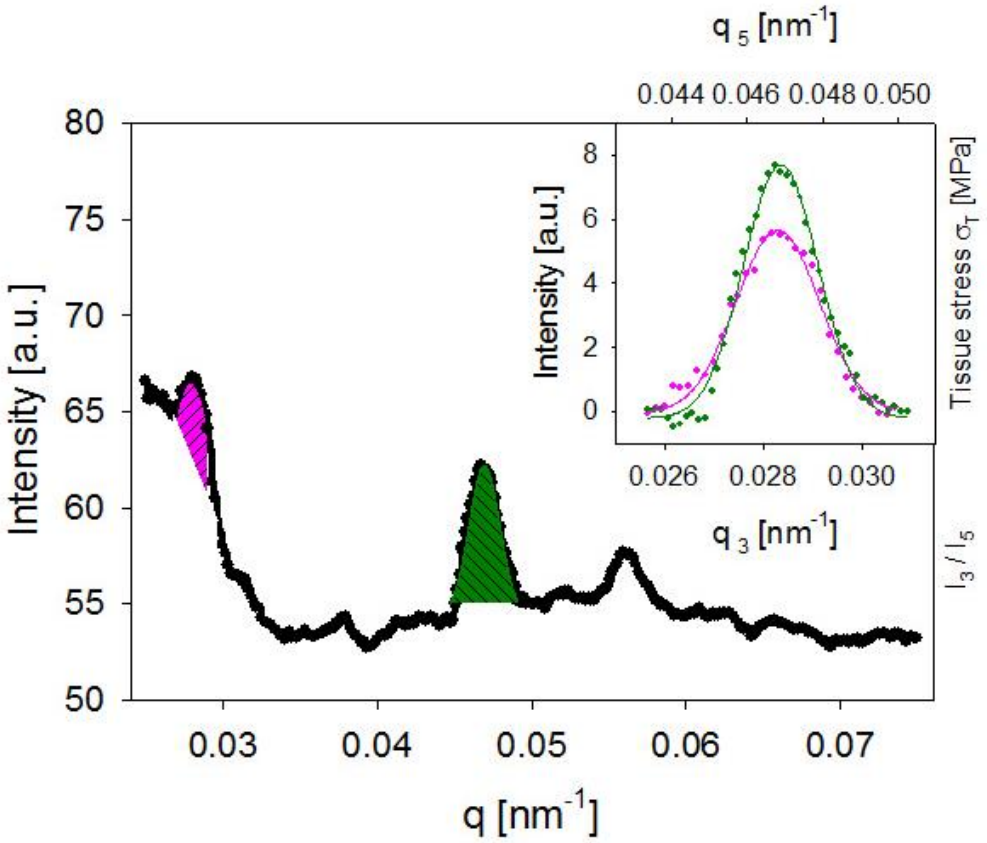

Figure 7. 2 *Averaged integrated intensity profile in the radial directions, the 3rd and 5th order Bragg peaks were denoted as pink and green, respectively. Inset shown the 3rd and 5th intensity profile after linear background subtraction*

7.2.3.3 Determination of the overlap and gap ratio

The gap/overlap ratio G/O, characterizing the intrafibrillar arrangement of tropocollagen molecules, can be extracted from the relative peak intensities of the I(q) plots. Such a treatment has been reported for uniaxially ordered tendon collagen before [88] and is a straightforward result in small X-ray diffraction of ordered fibrous crystals.

The structural model assumes a uniaxial periodicity of electron density linked to the D-period. Specifically, assume the gap zone inside the fibril to have a length G and the overlap zone to have a length O and a uniform electron density in each zone, with O + G = D,

then it will be shown below (see also [307]) that the ratio of the peak intensities of the n_1^{th} peak to that of the n_2^{th} peak is:

$$\frac{I_{n_1}}{I_{n_2}} = \left(\frac{n_2}{n_1}\right)^2 \left(\frac{sin\left(\pi n_1 \frac{O}{D}\right)}{sin\left(\pi n_2 \frac{O}{D}\right)}\right) \quad \textbf{Equation 7.1}$$

The two most prominent peaks in the radial profile I(q) were the 3rd and 5th order. Hence, from the ratio of the intensities of the $n_1 = 5^{th}$ order peak to the $n_2 = 3^{rd}$ order peak (I_{q3}/I_{q5}) the ratio O/D was determined by numerically solving the above equation for O/D, given an experimentally measured intensity ratio. It is noted that the assumption of a constant electron density is likely not strictly accurate, as has been found in vertebrate collagen types [308], but in the absence of a detailed information on the amino acid sequences and structure of collagen in starfish body wall, we use it as an approximation.

The physical background behind plotting the relative intensities is that the SAXD spectrum does not only provide the dimensions of the repeating unit cell (*D*) but also information on its internal structure (specifically the fraction *f* of dense (overlap) and less-dense molecular packing inside the unit cell). In this sense, it is akin to the structure factor in conventional powder X-ray diffraction[201] which provides information on internal structure in the (atomic) unit cell[309].To derive the result shown above, if O/(O+G=D) is denoted as the fraction *f*, $0 < f < 1$, then the electron densities in the two zones are different, with the electron density in the overlap region $\rho_O > \rho_G$. We assume that the fibril is oriented with its long axis along the vertical (*z*-) axis. From the basic equation of X-ray scattering from a material with varying electron density $\rho(\mathbf{x})$, we have

$$I(\boldsymbol{q}) = \left|\iiint \rho(\boldsymbol{x})\, e^{-i\boldsymbol{q}.\boldsymbol{x}} d\boldsymbol{x}\right|^2 =$$

$$\left|\iint dx\, dy e^{-i(q_x x + q_y y)} \int dz\, \rho(z) e^{-iq_z.z}\right|^2 \quad \textbf{Equation 7.2}$$

The electron density $\rho(z)$ is periodic in z with a period D, and the X-ray scattering intensity is a function of the difference in electron densities between the gap and overlap zones. We can write the electron density difference $\rho_{O\text{-}G}(z)$ as a sum over the difference in electron densities in all the repeating D-period unit lattices

$$\rho_{O-G}(z) = \sum_{k=-M}^{M} \rho_{o;O-G}(z + kD)$$

with $\rho_0(z)$ is the electron density in a single D-periodic unit cell, and (2M+1) >>1 is the (large) number of repeating D-periodic units inside the fibril. The electron density can be written as

$$\rho(z) = \begin{cases} \rho_0 & 0 < z \leq fD \\ 0 & fD < z \leq D \end{cases}$$

With this change, by summing the resulting geometric series in $\exp(iq_zD)$ that the intensity $I(q_z)$ as a function of the q_z component of the reciprocal lattice vector is

$$I(q_z) = \left(\frac{2\rho_0}{q} \cdot \frac{\sin\left(\frac{qfD}{2}\right)}{\sin\left(\frac{qD}{2}\right)} \cdot \sin\frac{qD}{2} \cdot (2M+1)\right)^2 \quad \textbf{Equation 7.3}$$

As M $\rightarrow \infty$ (i.e. the number of repeating D-periodic unit cells inside the scattering volume is very large), then the second term in the equation is the well-known Laue function $\sin^2((2M+1)x)/\sin^2(x)$ [202], which is nonzero only for $x = k\pi$ where k is an integer. As a result, the intensity function is nonzero only near q_z values given by the relation

$$q_z D = 2k\pi \Rightarrow q_z^k = \frac{2k\pi}{D}$$

which is the expected result for a 1-D crystal with a repeating period of *D* along its axis. Further, the intensity of the k^{th} peak is

$$I_k = \left(\frac{D\rho_0}{k\pi}\right)^2 (\sin(\pi k f)(2M+1))^2 \quad \textbf{Equation 7.4}$$

From this result, a few general observations can be made. First, if the overlap/D ratio f = ½, then the peak intensities of all even orders k = 2m (2, 4, 6, …) are identically zero as sin($m\pi$)=0 for any integer m. We can calculate the ratio of the n^{th} to the m^{th} peak orders as a function of f:

$$\frac{I_n}{I_m}(f) = \left(\frac{m}{n}\right)^2 \left(\frac{\sin n\pi f}{\sin m\pi f}\right)^2 \quad \textbf{Equation 7.5}$$

By choosing (m, n) pairs appropriately, we can graph the predicted intensity versus the actual intensity for various order-combinations in $I(q)$, in order to estimate f in the framework of this one-dimensional model and compare these to measured values of the peak intensity ratios [88].

The physical relevance of the overlap/D ratio f is for nanoscale deformation arises because intrafibrillar gliding of tropocollagen molecules could, for example, lead to an increase in the gap zone (hence a reduction in f), together with an increase in D. However, it is clear that in such a case, it would be misleading to consider the intrafibrillar components as stretching even though the effective fibril strain (from changes in D) would be increasing. Conversely, if the tropocollagen molecules in the gap- and overlap-zones both stretch

exactly the same amount, *f* will remain unchanged but both the fibril- and molecular strain will have increased.

7.3 Results

7.3.1 Interfibrillar kinetics during stress relaxation

The data reduction results of SAXD pattern collected during time course of the relaxation phase of the mechanical test on MCT-containing tissue and the corresponding macroscopic stress-time plots were shown in **Figure 7.3,** in order to compare the time-dependent behaviour of MCT from macro- down to nano-level. From **Figure 7.3**, we observed that, at the same tissue strain, the maxima of fibril elongation in KASW (n=4) is much larger than the case in CaF-ASW (n=4), with ASW (n=3) sitting in between that of KASW and CaF-ASW, which is consistent with the phenomenon we found in the prior set of stress-to-failure experiments (**Chapter 6**). At the starting point of relaxation phase (tissue strain: 50%), fibril in KASW has a much higher extension of 1.62% in contrast to ASW (0.65%) and CaF-ASW (0.26%). The corresponding tissue stress at this strain level of KASW-treated specimen (5.23 MPa) is significantly larger than that of ASW (1.31 MPa) and CaF-ASW (0.16 MPa). The trend of stress at tissue level (σ_T) (**Figure 7.3 (B)**), and the strain at fibrillar level (ε_F) (**Figure 7.3 (B)**) shown similar behaviour of decreasing: change rapidly initially and then change slowly. Considering the fibril strain and the tissue stress(σ_T) evolved in MCT during stress relaxation, it is shown that collagen fibrils with at different mechanical states (treated by CaF-ASW, ASW and KASW) has different rate of decrease for collagen fibril D period. We also noted that at the end of the relaxation phase, the residual fibril strain in stiffened state (1.03%) is greatly higher than the standard state (0.22%), whilst in the softened state,

fibril almost slide out completely with a fibril strain close to 0%. Likewise, fibril in stiffened state retains large residual tissue stress (2.69 MPa) compare to softened state (~ 0 MPa) whilst standard state (0.5 MPa) is in the middle of these two extremes. The fact that the stiffened state retains a residual fibril strain which is much greater compare the other two groups suggests that the additional stiffening force does not relax away instantly. Lastly, it is also observed that tissue stress decays even when the fibril strain is a constant in the KASW-case, suggesting that the fibril is viscoelastic and which relaxes at a fixed macroscopic strain. The differences for maximum fibril strain and the fibril strain residue are clear and significant among treatments.

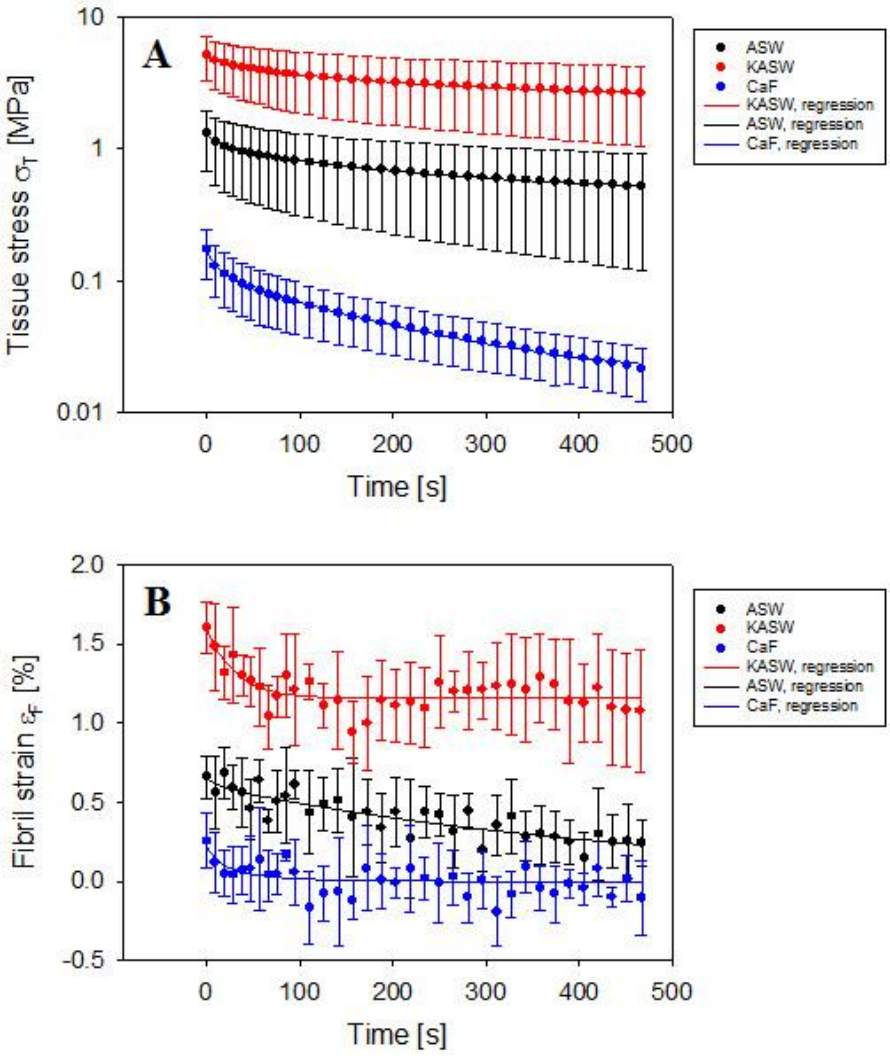

Figure 7.3 The interfibrillar kinetic of the stress relaxation mechanisms from macroscopic to nano length scale. *(A) The macroscopic stress relaxation behaviour of ionically treated specimens, binned across treatments, showing a clear difference in maximum stress achieved and the stress residue remained. (B) The corresponding nanoscale fibril strain-time plots of MCT dermis, measured from the peak shifts of SAXD pattern.*

The solid fit-lines in **Figure 7.3** are double exponential fits $\varepsilon_F = \Delta\varepsilon_{1,F} e^{\left(\frac{-t}{\tau_{1,F}}\right)} + \Delta\varepsilon_{2,F} e^{\left(\frac{-t}{\tau_{2,F}}\right)} + \varepsilon_{0,F}$ to the data. A double exponential curve is used to accommodate the fact that here, as in other tissues like tendon [16, 240], a rapid initial change in strain (and stress), over timescales $\tau_{1,F}$, is accompanied by a much longer time-scale reduction over $\tau_{2,F}$,. To minimize the degree of freedom enabled by multiple

parameters, and to demonstrate the link between macroscale mechanical change and nanoscale structural change, the fits were first carried out for the stress relaxation data at the tissue level (**Figure 7.3 (A)**). Following this step, the same $\tau_{1,2}$ was used for the fitting of measured strain at the fibrillar level (**Figure 7.3 (B)**) in order to constrain the fitting results. We observed that the CaF-ASW, ASW and KASW resulted in changes of the short time-scale parameter τ_1 and long-time scale parameter τ_2 (**Figure 7.4**). **Figure 7.4 (A)** shown the nanoscale parameters: the CaF-ASW stimulated specimens (τ_1: 11.7 s) has a ~ 42.4% lower than that of KASW (τ_1: 20.3s), whilst τ_1 (13.5s) for ASW is in between of KASW and CaF-ASW. Similarly, the results of τ_2 also shown differing values between treatments **Figure 7.4 (A)**.

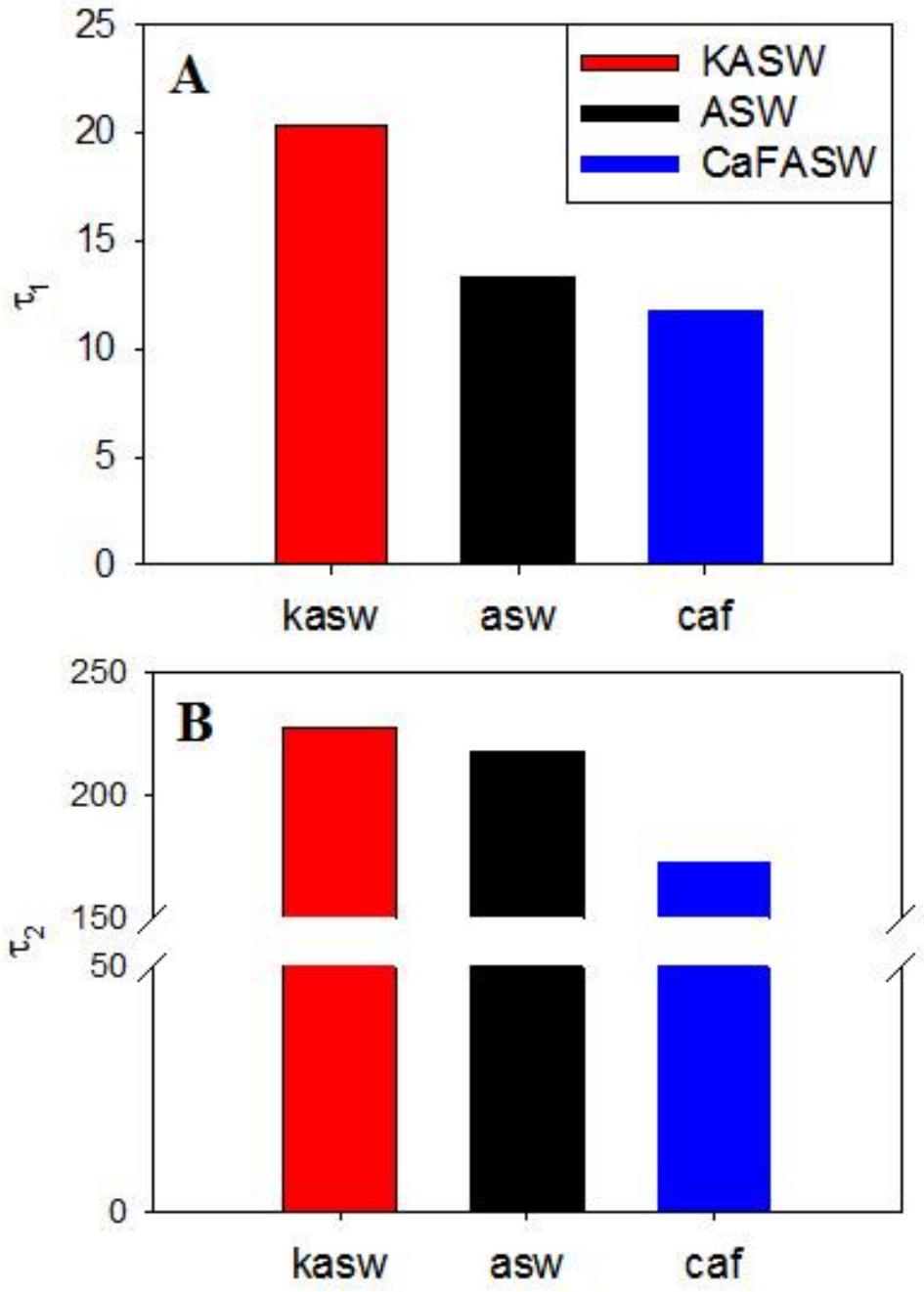

Figure 7.4 *Bar plot comparing the time constant τ_1 and τ_2 for ASW, CaF-ASW and KASW at the fibrillar level (from binned data).*

To do statistical analysis on the difference in time constants between the groups, pairwise *t*-tests were carried out (ASW vs CaFASW, ASW vs KASW and CaFASW vs KASW groups; Sigma Plot v10, SyStat Software). Specifically, for each individual (not group-binned) sample,

the stress-time and fibril strain-time behaviour was fitted to the two-exponential model, and the fitted time-constants τ_1 and τ_2 were compared (**Table 7.1**). Note that at the fibril level, only two extremes - KASW and CaFASW- were compared due to the relatively noisy data from ASW leading to failure to fit. Note, however, that the time-constants for the stress-time behaviour (which fit well) are sufficient to discriminate between groups. At the tissue level, there is a statistically significant differences ($p<0.05$) of the short time constant τ_{T1} between the stiffest state (KASW) and the two other states (ASW and CaFASW). The long-time constant τ_{T2} shows the opposite behaviour: the least stiff state (CaFASW) is significantly ($p<0.05$) different from the other two (ASW and KASW). For the fibrillar time constants to individual curves (rather than binned), comparisons with ASW are not possible for $\tau_{F1,2}$, and for KASW vs CaFASW, the differences are not significant.

Table 7.1 *Statistical analysis for time constants at fibril level τ_{F1} and τ_{F2}, tissue level τ_{T1} and τ_{T2} across different treatments*

P value	KASW vs CAFASW	KASW vs ASW	ASW vs CaFASW
τ_{F1}	0.1814	n/a	n/a
τ_{F2}	0.0847	n/a	n/a
τ_{T1}	3.0161e-3	9.8898e-3	0.7097
τ_{T2}	0.0148	0.6854	0.0156

For completeness, the fibril orientation during stress relaxation was also considered. **Figure 7.5** shows a typical representative angular distribution of X-ray intensity (5^{th} order) for the first 8 frames in initial rapid changing regime during the relaxation phase. A small amount of shift from 90.62° (dash line) to smaller angle centred in ~ 85° (solid line) is observed, indicating there is a small change of fibril orientation between the first frame and the subsequent frames.

However, there is no discernible time-dependent collagen fibril reorientation during relaxation phase, as the systematic difference for the peak position of frame 2-8 is not apparent.

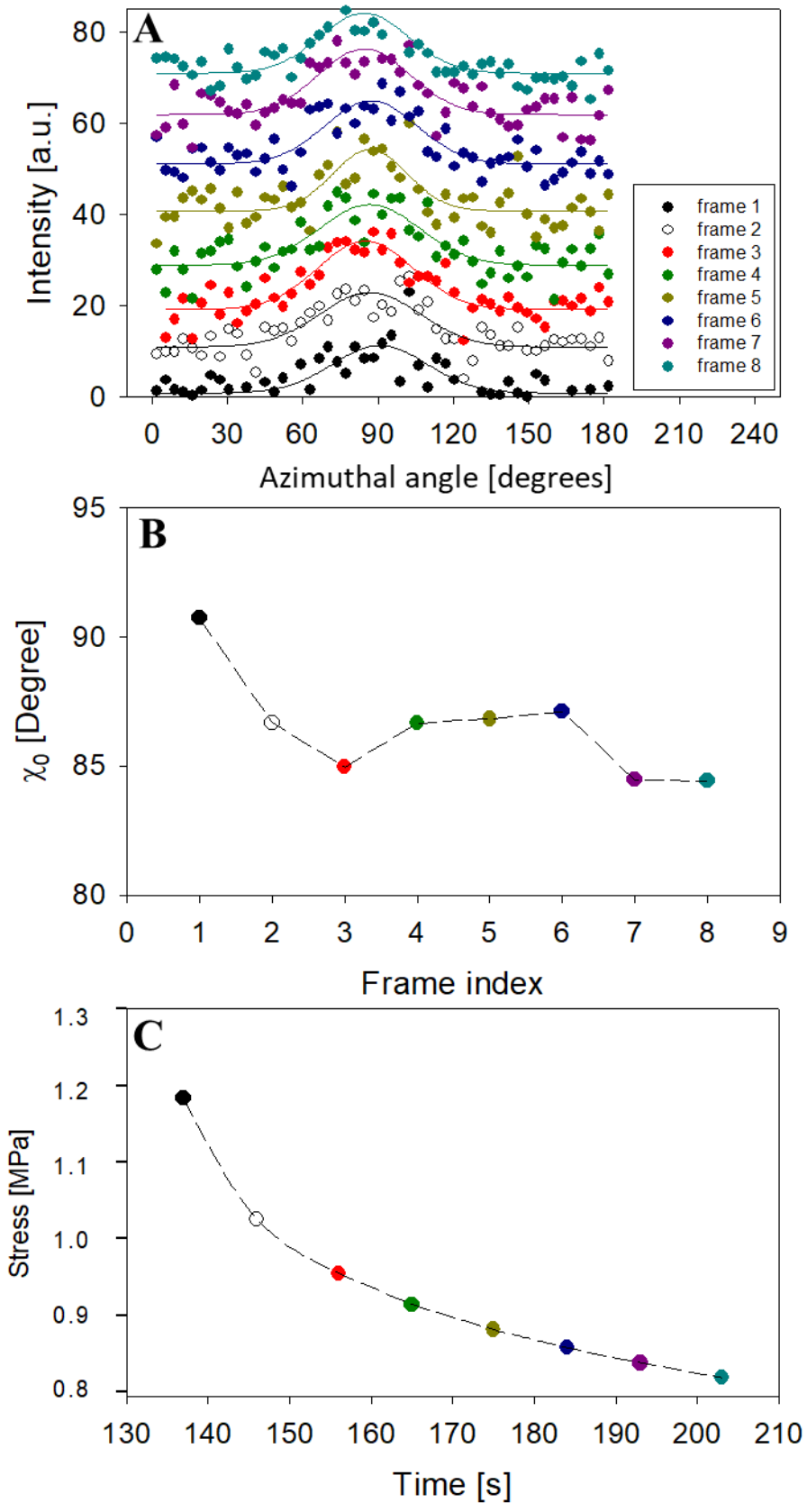

Figure 7.5 *(A)The radial integrated intensity profiles I(χ) from series of SAXD time frames for MCT. For simplicity, only 0-180° has been*

presented here. For comparison, successive I(χ) profiles were shifted vertically by sequence. The angular distribution intensity for these time frames are similar.(B) The fitted peak position χ_0 of each frame. (C) Stress-time plot showing time point when the series SAXD frames were taken.

7.3.2 Intrafibrillar kinetics during stress relaxation

The relative Bragg's peak intensity differences are related to the structural gap/overlap packing at the collagen molecular level, as discussed in the previous section. The step function prediction (**Equation 7.1**) of O/D overlap ratios when n=3 and m=5 is shown in **Figure 7.6**. A. Region within green solid lines is the intensity ratio of 3^{rd} and 5^{th} Bragg's peak ($I_3/I_{5)}$ calculated from experimental data (ASW, CaF-ASW and KASW), showing that the corresponding O/D overlap ratio variants from 0.364 to 0.366. The O/D ratios for ASW, CaF-ASW and KASW during the relaxation is presented **Figure 7.6 B**. The changes in the course of time were seen across three stimulated states is not evident, hence there is no evidence suggesting collagen molecules rearrange internally inside the fibril during relaxation; collagen fibrils contracted isomorphically during relaxation.

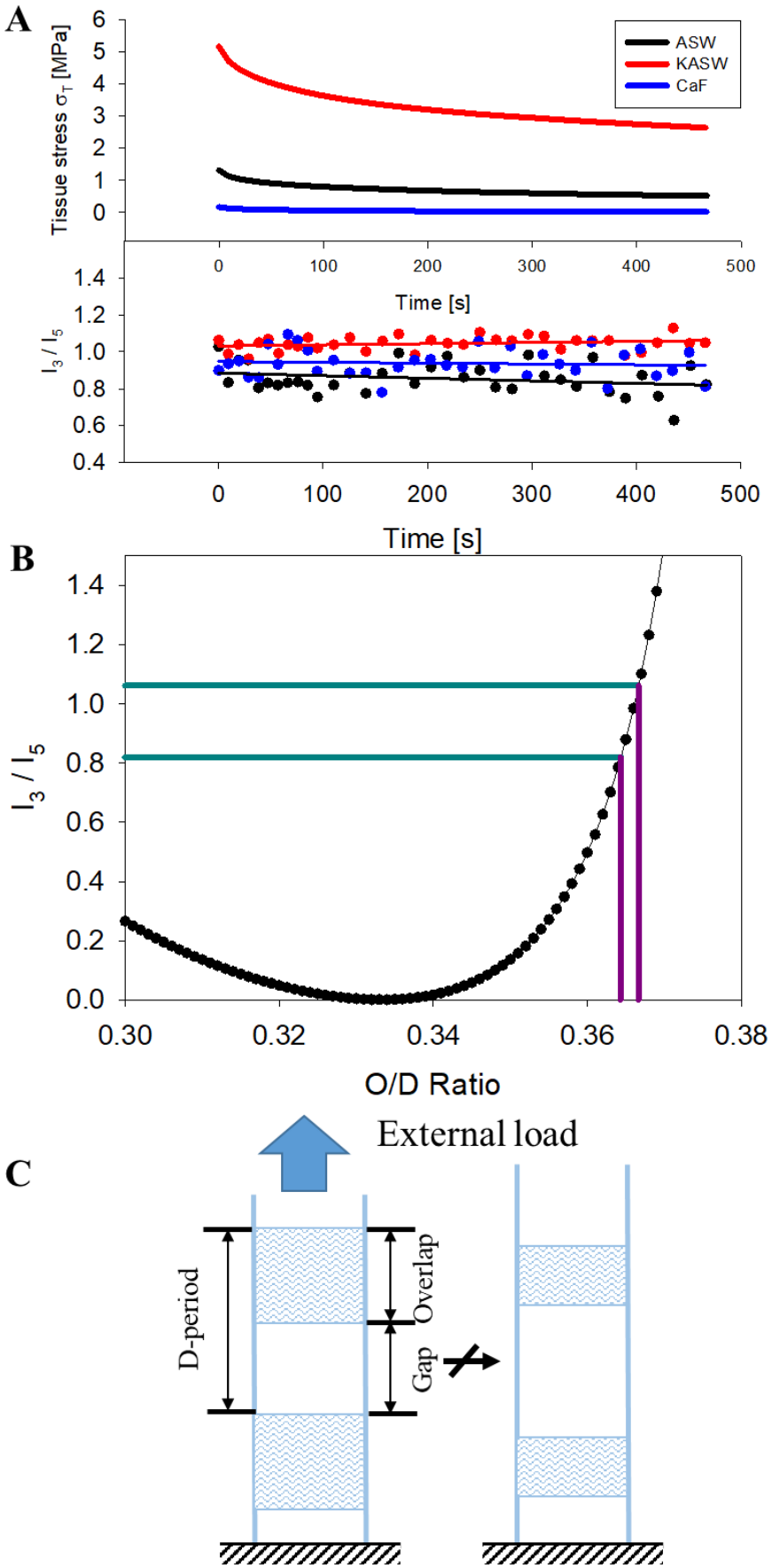

Figure 7.6 The intrafibrillar kinetics of the stress relaxation

mechanisms from macroscopic to nano length scale. *(A) Upper: The stress-relaxation curves for ASW, KASW and CaFASW. Lower: the typical tissue stress- time plots of ASW, KASW and CaF-ASW treated specimen and the corresponding I3/I5 ratio – time plots and the linear fitted solid line for each treatment. (B) The step function prediction (**Equation 7.5**) of I_3/I_5 as a function of O/D ratio. The experimental calculated I_3/I_5, ranging from 0.63 to 1.1, are represented by the two green solid lines, with the corresponding O/D ratio shown in two purple solid lines. (C) No change in Overlap/ D-period ratio shows that intrafibrillar sliding of tropocollagen molecules is not the main component during the stress relaxation.*

7.3.3 Model prediction

The experimental data, demonstrating a clear difference in the time-dependent behaviour at the nanoscale with differing chemical stimulation. A model, which could predict the load bearing by fibril and the matrix, was built by Dr. Ettore Barbieri using the self-consistent method for composites [305] and its generalization to viscoelastic creep [306].

At the fibrillar level, tissue was constituted by collagen fibril and interfibrillar matrix. In the strain-controlled stress relaxation experiment, the tissue strain ε_T = constant, the tissue stress σ_T and fibril strain ε_F are known quantities. Both σ_T and ε_F exhibit a viscoelasticity characterised by an exponential decay.

The known quantity σ_T was given by:

$$\sigma_T = (1-\phi)\sigma_M(t) + \phi\sigma_F t \quad \textbf{Equation 7.6}$$

Where σ_M and σ_F are unknown quantities we wish to estimate, ϕ, the volume fraction of fibril, is a known constant of 0.56.

From **Equation 7.6**, the expression of can be σ_M obtained.

$$\sigma_M(t) = \frac{1}{(1-\phi)}(\sigma_T(t) - \phi\sigma_F t) \quad \textbf{Equation 7.7}$$

We need to estimate σ_F first if we wish to estimate the load bearing by matrix (σ_M).

Owing to the effect of stress-strain history on viscoelastic behaviour of fibril, the σ_F can be expressed as:

$$\sigma_F(t) = \frac{1}{1-\nu_F^2}\int_{\infty}^{t} E_F(t-\tau)\frac{d\varepsilon_F}{d\tau}d\tau = E_F(t) * \varepsilon_F(t) \quad \textbf{Equation 7.8}$$

Where $E_F(t)$ is the relaxation modulus of fibril, σ_F is considered to be a convolution between $E_F(t)$ and $d\varepsilon_F/dt$ (t), which denoted as $*$.

The only unknown quantity is $E_F(t)$, which could be estimated from self-consistent method of composites, using Laplace transform:

$$S_F(s) = sE_F(s)\epsilon_F(s) \quad \textbf{Equation 7.9}$$

$$\boldsymbol{\epsilon}_F(s) = A_F(s)\boldsymbol{\epsilon}_T(s) \quad \textbf{Equation 7.10}$$

where $\boldsymbol{\varepsilon}_T(s)$ and $\boldsymbol{\varepsilon}_F(s)$ are second order strain tensor and $A_F(s)$ is a fourth tensor (strain concentration tensor), which can be expressed as:

$$A_F(s) = [\boldsymbol{L} + \boldsymbol{S}(s)M_F\big(l_F(s) - l_T(s)\big)]^{-1} \quad \textbf{Equation 7.11}$$

where $\boldsymbol{L}$ is a fourth-order identity tensor, $\boldsymbol{S}$ is a fourth-order Eshelby tensor [310] for fibril, $M(\cdot)$ is the fourth-order compliant tensor in Laplace domain, $l(\cdot)$ is the fourth-order stiffness tensor in Laplace domain.

From the experimental data,

$$\boldsymbol{\varepsilon}_T = const. \forall \geq 0 = \boldsymbol{\varepsilon}_T^0 H(t) \rightarrow \boldsymbol{\epsilon}_T(s) = \frac{\boldsymbol{\varepsilon}_T^0}{s} \quad \textbf{Equation 7.12}$$

where $H(t)$ is the Heaviside function defined as:

$$H(t) = \begin{cases} 0 \; if \; t < 0 \\ 1 \; if \; t \geq 0 \end{cases}$$

The stress relaxation can be fitted using two-time constant exponential function:

$$\sigma_T(t) = \sigma_T^0 H(t) + \sigma_T^{(1)} e^{-t/t_{T1}} + \sigma_T^{(2)} e^{-t/t_{T2}}$$ **Equation 7.13**

Therefore, in the Laplace domain, Equation 8 can be written as,

$$S_T(s) = \frac{\sigma_T^0}{s} + \frac{\sigma_T^{(1)}}{s+1/t_{T1}} + \frac{\sigma_T^{(2)}}{s+1/t_{T2}}$$ **Equation 7.14**

Therefore,

$$E_T(s) = \frac{1}{s}\frac{S_{T(s)}}{\epsilon_{T(s)}}$$ **Equation 7.15**

In fact,

$$\epsilon_F(s) = \frac{\varepsilon_F^0}{s} + \frac{\varepsilon_F^{(1)}}{s+1/t_{F1}} + \frac{\varepsilon_F^{(2)}}{s+1/t_{F2}}$$ **Equation 7.16**

Substituting **Equations 7.11** and **7.15** into Equation **7.9**, leads to an equation of E_F that can be solved explicitly.

$$E_F(s) = E_F(s, \varepsilon_T^0, \sigma_T^{(1)}, \sigma_T^{(2)}, t_{T1}, t_{T2}, \nu_T, \varepsilon_F^0, \varepsilon_F^1, \varepsilon_{F,}^2 t_{F1}, t_{F2}, \nu_T)$$
Equation 7.16

Equation 7.16 is a function with all parameters known by experimental data.

Substituting **Equation 7.16** into **Equation 7.9**, now the Laplace transform of the fibril stress can be inverted numerically:

$$\sigma_F(t) = l^{-1}\{S_F(s)\}$$ **Equation 7.17**

The model prediction for the stress taken by collagen fibril σ_F and the interfibrillar matrix σ_M under different chemical stimulation state (CaF-ASW (softened), ASW (standard) and KASW (stiff)) is shown in **Figure 7.7**.

The blue solid line in **Figure 7.7** (A, B and C) show corresponding stress-time curves for body wall tissue in CaF-ASW (A), ASW (B) and KASW (C). The averaged macroscopic stress σ_T with tissue strain

ε_T at the beginning of relaxation phase for KASW-treated (5.11 MPa) specimens is significantly higher than CaF-ASW (0.17 MPa), while the ASW-treated (1.3 MPa) specimens are in between these extremes.

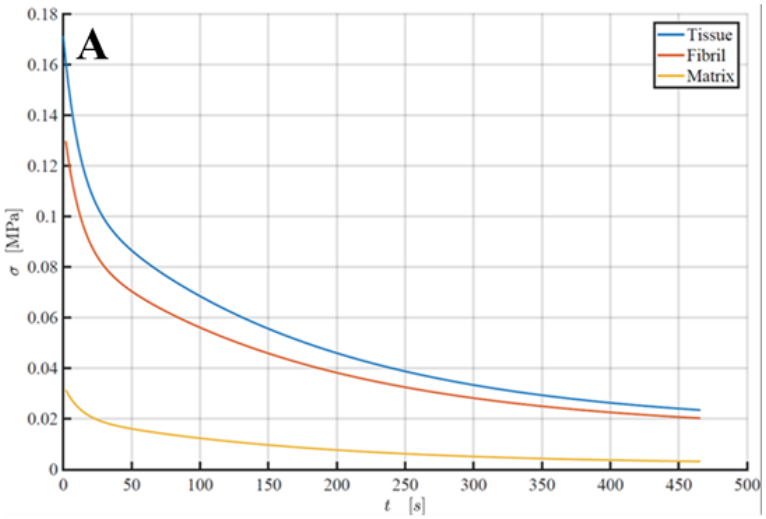

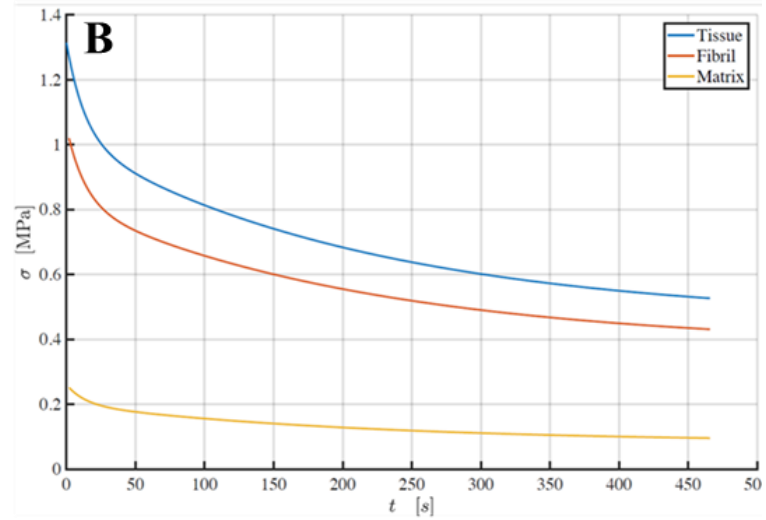

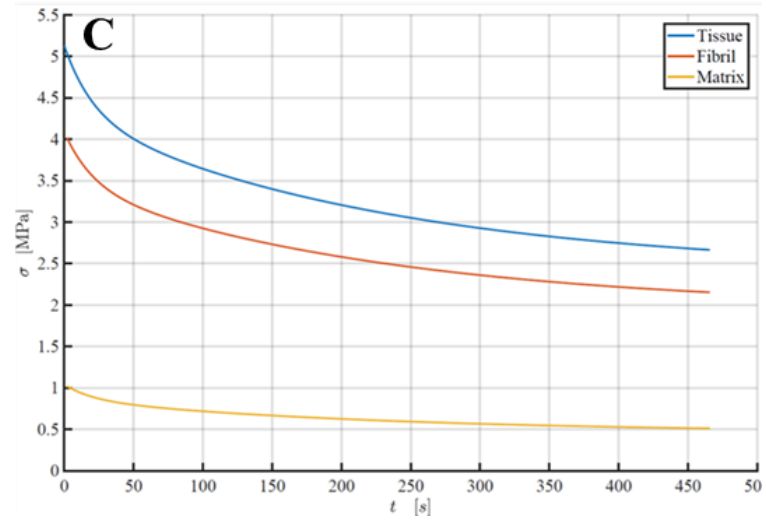

Figure 7.7 *Model prediction for MCT time-dependent mechanism for (A) Softening state induced by CaF-ASW, (B) Standard state induced by ASW and (C) Stiffening state induced by KASW*

7.4 Discussion and Conclusion

The phenomenon of viscoelasticity of passive vertebrate collagenous tissues has been extensively investigated experimentally and theoretically [16, 74, 311]. Nevertheless, structural mechanisms (rather than phenomenological models) are relatively scarce, with the most widely known model (the quasi-linear viscoelastic model of Fung [107]) not having a direct structural interpretation. Models of varying degree of complexity – from the simple spring-dashpot model to constitutive finite-element models – have been used to explored the viscoelasticity of collagenous tissues [281, 312, 313]. In spring-dashpot models, the system is modelled as an elastic spring (collagen fibril) in parallel with a viscous element (the extrafibrillar matrix) [281].

The most common soft collagenous tissue where viscoelasticity has been studied experimentally is tendon, a well-documented parallel-fibred collagenous tissue with a hierarchical structure assembled from fibril (nm), fibre (μm) and then fascicle (~mm), with non-collagenous matrices between each component which facilitating load shearing and transferring units [23] (see also **Chapter 6**). In tendons, the role of fascicles (~hundreds of microns in diameter), bound together by interfascicular matrix, as well as fibrils has been considered. Fascicles are crucial to the overall functionality by allowing the tendon to deform via interfascicular matrix sliding [60, 314, 315]. At the smaller (nanometre) scale, fibril stress relaxation experiments combined with

in situ synchrotron SAXD [16, 240] have shown the existence of a serially-coupled viscoelastic system at the fibrillar level (a Voigt model and a Maxwell model in series), with each viscoelastic model representing the fibril and the interfibrillar matrix, respectively. In other tissues like skin with multiple orientations of fibrils, the fibrillar reorientation – rather than elongation – has been proposed as the dominant mechanism of structural change during stress relaxation [245].

Structurally, the sea cucumber MCT-dermis is more similar to skin than tendon, due to its wider fibril distribution. It is therefore interesting, and not immediately obvious, what the nanoscale structural deformation mechanisms during transient viscoelastic loading in stress relaxation will be. While the fibrillar components have viscoelastic behaviour [93], we were motivated by the prior experimental work on tendon, where the interfascicular matrix has a known influence on the tissue mechanics, to see if the interfibrillar matrix might have a similar effect in MCT. Interestingly, by comparing the stress relaxation experiments of MCT with tendon, we find that the time constant τ_1 and τ_2 of stiffened, standard and softened MCT in both tissue level and fibrillar level are larger than that of tendon [316].

By using a multiscale model where the contribution of the different components – interfibrillar matrix and fibrils – can be combined to give tissue-level structural and mechanical response, it is possible to extract the time-dependent mechanical behaviour in the interfibrillar matrix (**Figure 7.7**, yellow curves). The extraction of the mechanics of this amorphous, GAG-rich matrix is relevant for two reasons. **First,** while the tissue-level mechanics is obtained from macroscale

mechanics, and the fibrillar-level deformation is measurable from SAXD, the unstructured, amorphous nature of the interfibrillar matrix makes it difficult to obtain its mechanical response *in situ*. The combination of ultrastructural SAXD probes with mechanical modelling, as described here, circumvents this problem. **Secondly** – and following from the first point – the time-dependent changes in the interfibrillar matrix are (as shown in **Chapter 6**) the main mechanism driving changes in viable MCT tissue, via active-force generation. It is this aspect of MCT, facilitating the ability to switch the state of the whole tissue actively, to which we now turn in the following **Chapter 8.**

Chapter 8 : *In situ* imaging of active force generation in MCT

8.1 Introduction

The previous two chapters have reported results about the nanomechanics of mutable collagenous tissue (MCT)[11, 12], the only collagenous tissue capable of active force generation [13]. The mechanism of crosslink-induced interfibrillar stiffening had been demonstrated in **Chapter6**, and the time-dependent changes in this interfibrillar matrix in different states of mutability in **Chapter 7**. To develop a fully mechanistic understanding of the processes of MCT using *in situ* X-ray nanomechanics, however, three main areas need to be developed (a) to understand changes in mechanics during physiological stiffening rather than through indirect chemically induced action on the cells (b) to link the intracellular activity to release of mechano-effector cross-linker molecules and (c) to be able to experimentally measure the nanoscale changes *during* such change of mechanical state, rather than before and after, as was the case for incubated tissue of the type studied in **Chapters 6** and **7**. In this **Chapter 8**, we take a step toward these goals by addressing the last point (c), which is the most immediately accessible, via designing a dual-syringe-pump system which can controllably change the immersing solution in which MCT-tissue is placed, thus enabling generation of force *in situ*. Our goal is to study the kinetics of fibrillar change during alteration of mechanical state.

The need for understanding the kinetics (rather than only the static states) is relevant both biologically and in terms of potential applications. Considering the biological angle, with sufficient and rapid stimulation, echinoderms can undergo drastic change of stiffness rapidly and reversibly. An extreme case of a stiffness change is the autotomy of body parts of echinoderms: when brittle star loses one of it's arms at the location away from the stimulation point, the stiffness of the ligament at the autotomising location decreases to < ~0.1 % of its normal value within seconds [317],. Such changes of stiffness could also be duplicated experimentally with treatment of neuro-active agents for example, K^+ and Ca^{2+} enriched sea water, or some other appropriate neuropeptides via different type of mechanical tests, including creep [143, 167, 178], stress relaxation [184] and cyclic loading [132, 146, 167].

In terms of applications, understanding the time scale of active force generation quantitatively by controlling changed stiffness of tissue with time will help in the engineering design of novel bioinspired materials and devices inspired by MCT [12]. Such adaptable biomaterials would have applications from implants in structural soft tissues where dynamic force-generation is needed (e.g. in pacemakers) and components for biomimetic "soft robots" [318], which respond to external stimuli in a controlled way [319-323]. In this regard, collagen-based MCT is an ideal biological model of a stimuli-responsive system, from a mechanical point of view (stiffness changes from 0.1 to 10 MPa over two orders of magnitude) (**Figure 8.1 (B)**). Since the stiffening or de-stiffening processes are expected to be a kinetic process (**Figure 8.1 (C)**), in which the molecules are binding or de-associating from interfibrillar matrix within a certain rate, the

challenge is to understand details of the binding rates, and (possibly in conjunction with other methods like spectroscopy and molecular modelling) develop a supramolecular model for the process. **Here, we develop an experimental system to quantify the generation of active forces and conformational changes**.

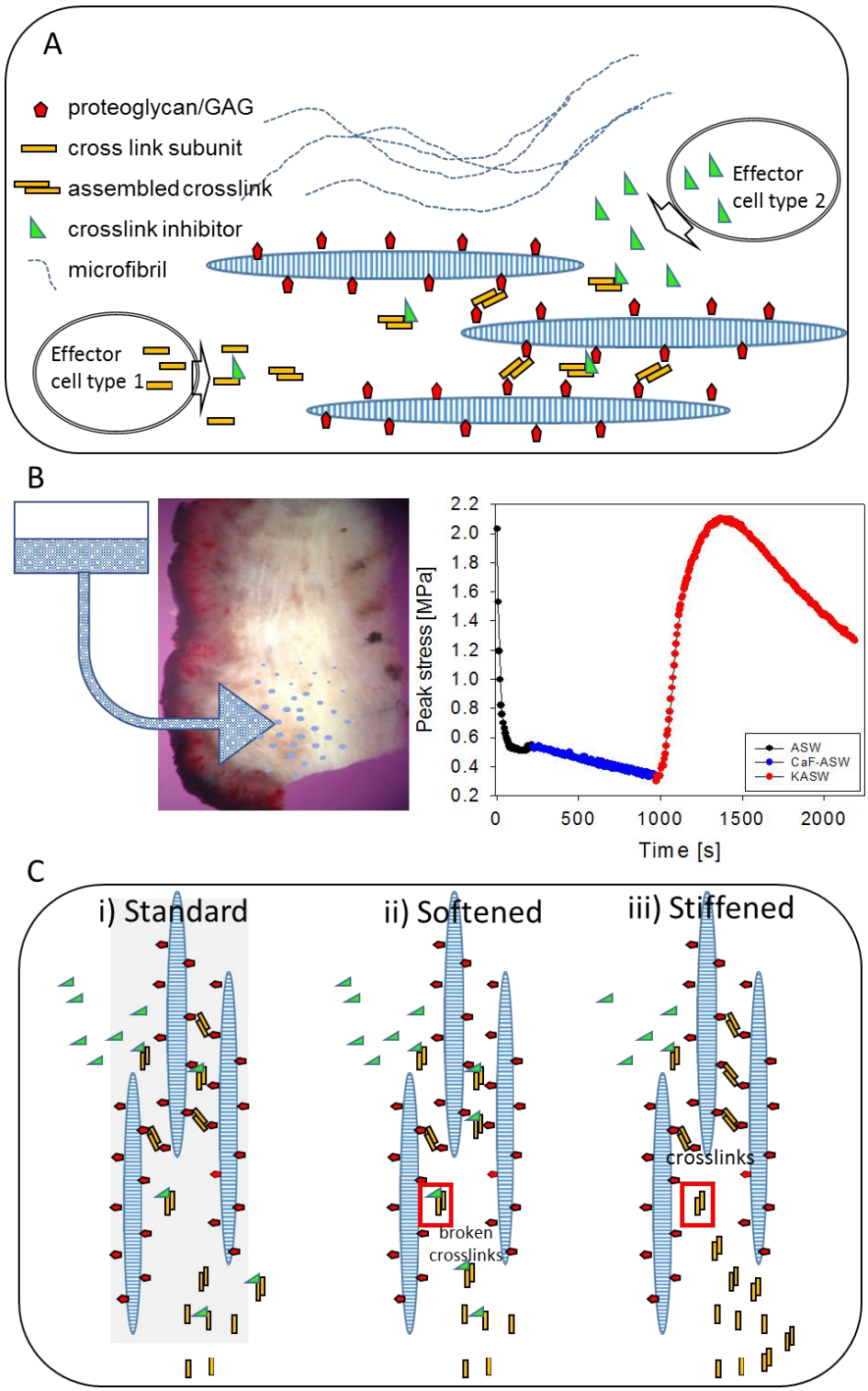

Figure 8.1 Mechanics of MCT (A) Model representation of MCT structure at the nanoscale. *The softening effects results from the release of softening molecules (crosslink inhibitor) from a specific effector cell type 2, which will cleave interfibrillar crosslinks from the GAGs-binding sites and finally leads to interfibrillar sliding as the amount of crosslinks decreases. The reversible effect, re-stiffening can*

be achieved by the release of crosslinks subunits from another effector cell type 1. (B) Upper: Strip of dissected sea cucumber dermis includes a pigmented outer layer and a thin inner layer. MCT-containing tissue will response to external stimuli for example chemical stimulation by exchanging incubated environment. Bottom: Active force generation mechanism of MCT induced by softening agent (CaF-ASW) and stiffening agent (KASW). (C) Schematic representation showing how the mechanical state is changed from soften to stiffened.

8.2 Materials and Method

8.2.1 Dissection of Sea Cucumber Body Wall Preparations

Black Sea cucumbers (*Holothuria Altra*) were collected from a commercial wholesaler (Tropical Marine Centre, Chorleywood, London). Similar chemical stimulation protocol of **Chapter 6** was followed.

8.2.2 Design of *in situ* fluidic injection setup in combination with synchrotron X-ray nanomechanics

To test the dynamics of interfibrillar crosslinks forming or breaking at the nanoscale, it is necessary to controllably change the solution in which the sea cucumber dermis tissue is immersed, over timescales of a few seconds. Various options to carry this out were considered, including

a) the use of an automated injection via a microneedle inserted into the tissue of the solution
b) the use of motorized syringe pumps to exchange fluids in the chamber and
c) the use of peristaltic pumps for a similar purpose as in b).

After discussion a) was rejected as too complex, and possibly inducing additional mechanical perturbation to the tissue, c) as not

precise enough in fluid dispensing (ml or less) and b) was therefore chosen.

A constraint of the design was that it should involve minimal expenditure on equipment, as such funds were not available, keeping to within the £100-200 GBP allowed for a student project (with which this was combined). Commercial multi-channel syringe pumps (~£2000-£5000 at the time of the project) were hence excluded. The use of open-source hardware, as exemplified by sites such as Appropedia (http://www.appropedia.org/) was therefore considered. Such open source hardware depends on the use of 3D printing, RepRap printer technology, open-source design files, and low-cost individual components such as stepper motors, and controllers like Arduino, Raspberry Pi or Beaglebone PC. From the Open Source Syringe Pump, available on the Appropedia website (http://www.appropedia.org/Open-source_syringe_pump), design STL files were obtained, which were then adapted with minor modifications (via 3D modelling software like Sketchup Pro; www.sketchup.com) to a final syringe-pump assembly.

The LabVIEW control interface developed in the previous chapters was modified to integrate the syringe-pump control into the program, jointly by myself (J. Mo) and the SEMS electronics/programming technician Jun Ma. A schematic of the experimental procedure is shown below (**Figure 8.2**). Briefly, the goal is to load the MCT tissue cyclically with a fixed strain amplitude of ~15% tissue strain, whilst obtaining a series of SAXD measurements precisely at the positions of peak- and minimum strain. This controlled acquisition is different from the continuous acquisition described in **Chapters 6** and **7**, and needs to integrate the delivery of an output TTL-type (Transistor-

Transistor Logic) pulse which will trigger the X-ray detector at the SAXD beamlines at the precise points of peak strain. The data acquisition board (DAQ device) was connected to the control laptop and will be responsible for translating the analog signal, which was generated from control laptop at the at the precise points of peak strain, into series of TTL pulses, which then be delivered control system of beamline and will trigger the SAXD acquisition. The combined setup, shown in **Figure 8.2 (B)**), was built. The interface enabled fluid-exchange, driven by two separate syringe pumps controlled by NEMA-17 type stepper motors of the type used for 3D-printers or DIY CNC machines. The fluid exchange was applied during the mechanical test to introduce the softening/stiffening agent (like KASW or CaF-ASW) into the system (**Figure 8.2 (A)**).

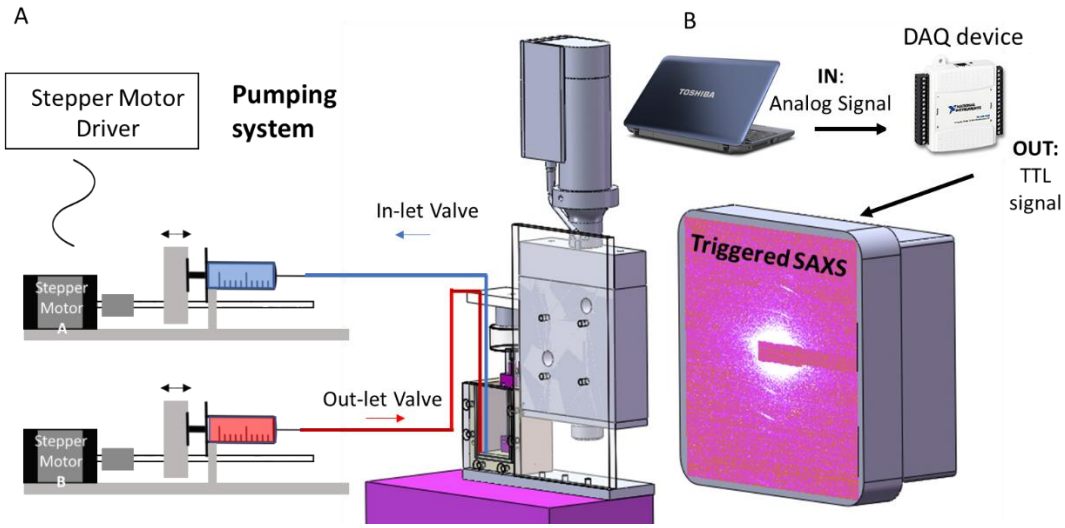

Figure 8.2 Experimental configuration. *(A) Micromechanical test device (Centre) with MCT specimen mounted. (A) Syringe pumping systems, enabling fluidic inject during the test. (B) Continuous SAXD measurement triggered by series of TTL signal sending from external device.*

8.2.2.1 Subsystem 1: Pumping Hardware and Fluid exchanging system

The primary component for pumping system are two plastic syringes (20 ml; Fisher Scientific) together with two stepper motors (Model

201.SMA.150.050PS; Williamson Pumps Ltd). Other hardware for supporting this system includes two M5 threaded rods with eight M5 nuts, two rod couplers, two plastic tubes for in-flow and out-flow of fluid, connected to the fluid chamber. The hardware is then assembled with the structural elements (**Figure 8.3**). The structural elements of this two-pump fluid exchange system is designed by Michigan Tech's Open Sustainability Technology Lab, available as stereolithography (STL) files, and are shown in **Figure 8.3** [324]. These were printed at the SEMS mechanical workshop on a Stratasys FDM printer (Model: FDM 360 mc). Most other elements were purchased on eBay with a minimal expenditure, keeping the costs to within manageable levels. To send commands to motors that drive syringe pumps, a stepper motor driver (DAQ device) is needed for translating LabVIEW commands to drive the pump motors. Prior to the cyclic loading test, two syringes, one empty, designing for suction of the fluid existing in the chamber (initially ASW) and the other, for refilling with either KASW or CaF-ASW, were prepared and connected to the micromechanical system.

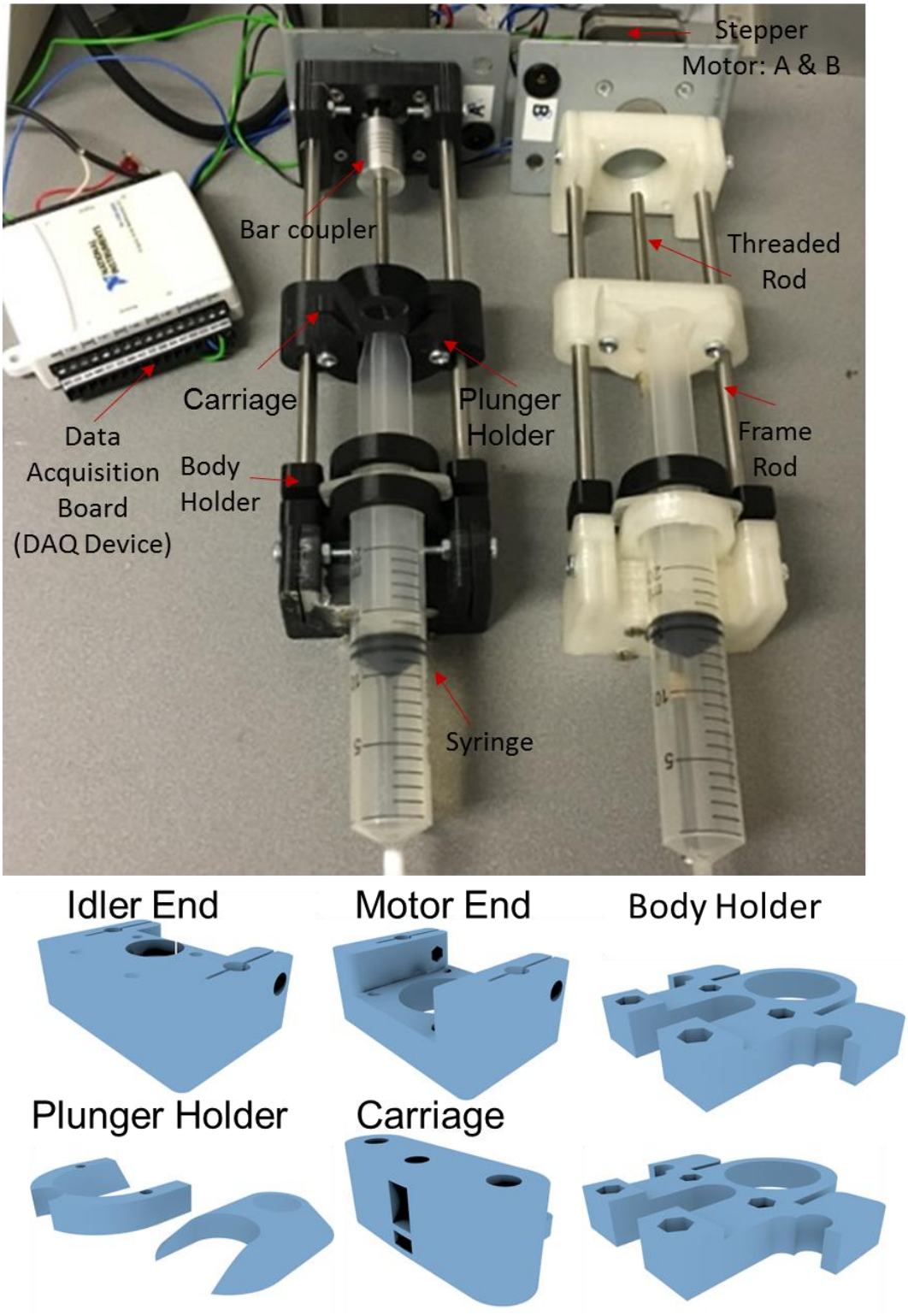

Figure 8.3 *The assembled pumping system. 3D drawing at the bottom shows the structural elements, including one idler end, one motor end, one plunger holder, one carriage and two body holders.*

8.2.2.2 Subsystem 2: Micromechanical Testing Devices with SAXD measurement triggering signal

The micromechanical deformation device, described previously in Chapters 3-4 in detail, was used. The cyclic loading experiments with *in situ* SAXD was carried out at the Noncrystalline Diffraction (NCD) beamline I22 (microfocus setup), at Diamond Light Source (DLS). All specimens (prepared and incubated in ASW-solution as described in **Chapters 6**) were mounted in the fluid chamber, with a gauge-length ~6 mm, at the beginning of the tests. For the cyclic loading test, specimens were periodically stretched to 15% strain and relaxed to its original position at a constant rate of 0.3 HZ, along the vertical direction. To acquire series of SAXD patterns at the peak of the displacement, the triggered SAXD measurements were set up prior to the experiment (**Figure 8.3 (B)**): The data acquisition device, connected to the mechanical tests laptop, were programmed and adjusted to output a ~3.8V pulse (TTL) at the peak of the displacement. Then these series of TTL pulses, will be transfer through the cable (10 m) to trigger a single SAXS measurement each cycle through TFG (Time Frame Generator). The other end of cable was an electrical connector (LEMO FFA 00), which needed to be able to connect to the plug-patch panel at the I22 control-cabin, enabling the TTL pulse of 3.8V was detected by GDA, the control system of beamline, and trigger the SAXD data acquisition **(Figure 8.4)**.

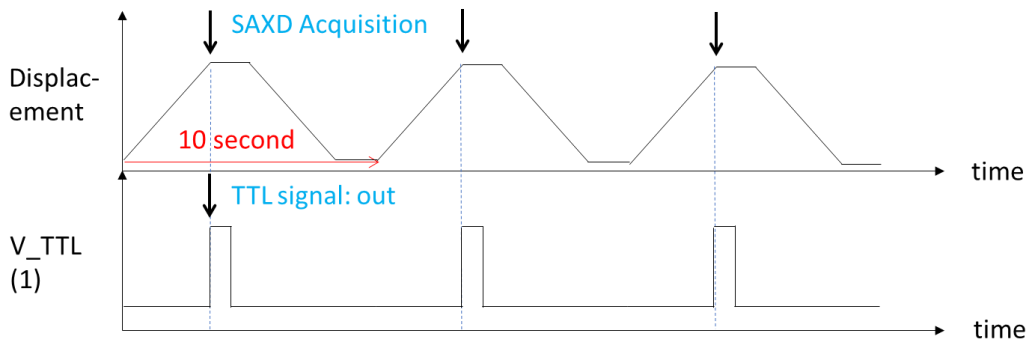

Figure 8.4 Triggered SAXD measurements. *Upper: the displacement of DC motor over time, arrow indicates the triggered SAXD measurement. Bottom: the oscillographic display showing the series of TTL pulses, which will be transmitted and triggered SAXD acquisition.*

8.2.2.3 Subsystem 3: LabVIEW-control Interface

The control system for two-pump fluid exchange system comprised two main parts: The stepper-motor driver and the LabVIEW-based control interface (**Figure 8.5**). The commands are input to the LabVIEW panel, and drive the stepper motor in forward or backward motions at specific rates, to control injection or refill of syringe. wean internal calibration function converts the rate of stepper-motor movement to the flow rate of fluid.

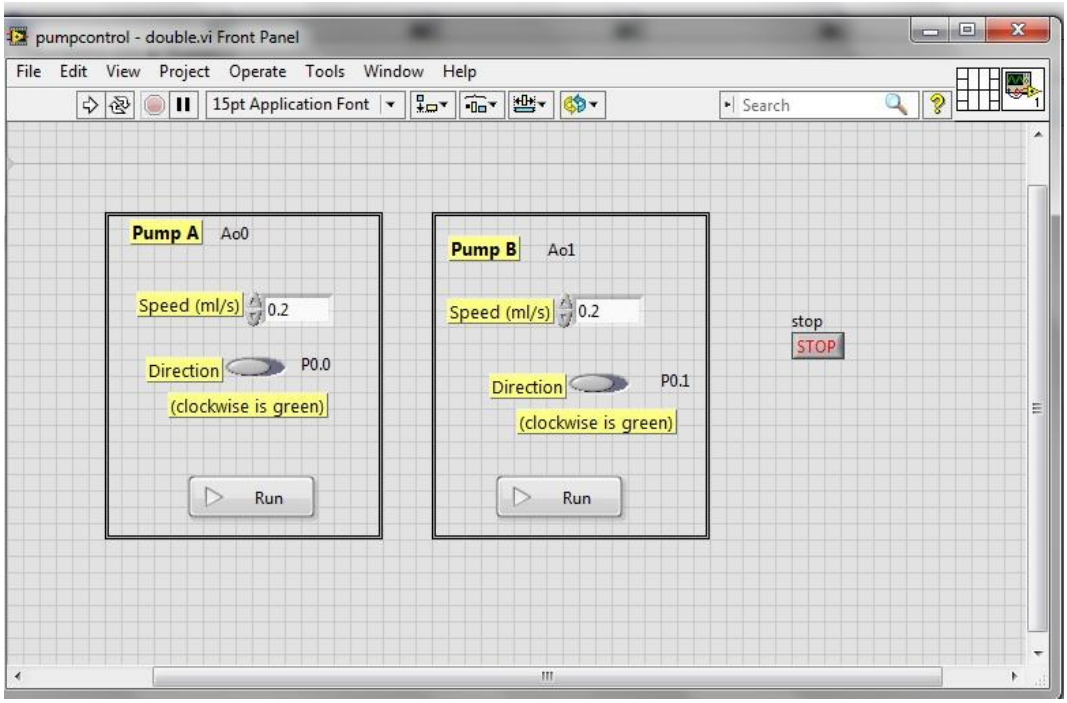

Figure 8.5 LabVIEW-based control interface for syringe pumping system. *The microfluidic pumping system for experiments includes two*

pumps, A and B. The in-let and out-let of fluid flux in control by the direction of stepper motor rotation.

In developing the control system for cyclic loading tests (**Figure 8.6**), we need to acquire the SAXD frame precisely at peak stress in each cycle, which is impossible to do manually. Therefore, an electronically triggered SAXD measurement is necessary(**Figure 8.2**), where we used a National Instruments DAQ system (controlled by the laptop running the mechanical test software), to sending a ~3.8V pulse (TTL) to the SAXD detector when the peak stress is reached. By setting the detector to acquire a SAXD frame on an external trigger pulse, the synchronized acquisition of fibrillar information (via SAXD) at peak stress-points during cyclic loading was achieved.

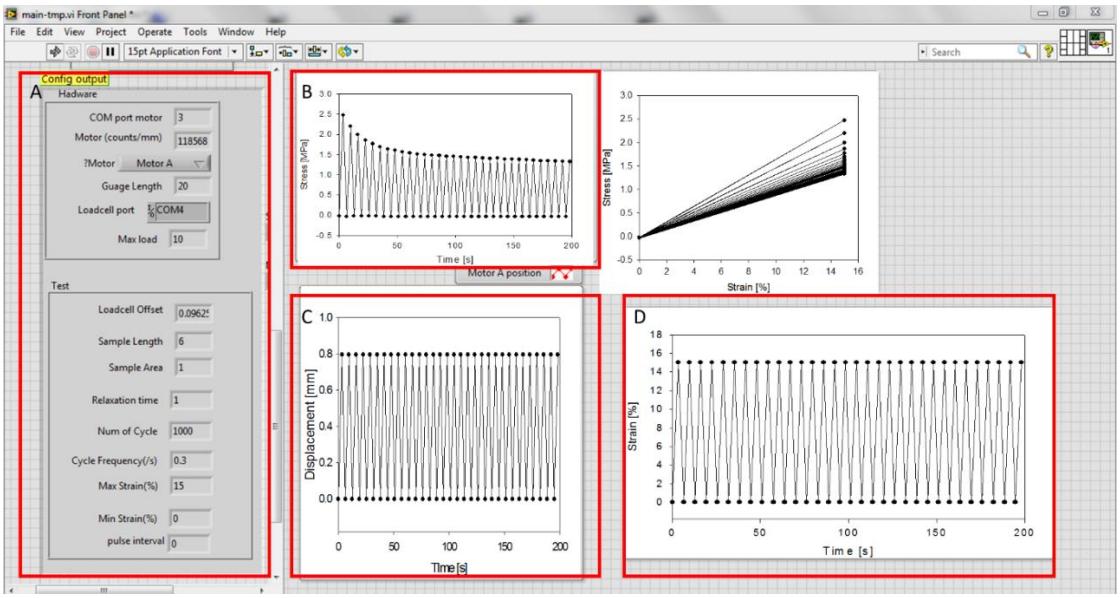

Figure 8.6 LabVIEW-based control system for triggered SAXD measurements with cyclic loading. *(A) The input parameters for experimental configuration. The frequency (0.3 HZ), maximum strains (15%) and number of cycles (1000) was pre-defined prior to the tests. (B, C, D) magnified time range over several cycles, demonstrating the peak stress, strain and displacement of DC motor.*

8.3 Results

8.3.1 In-house Cyclic Loading Tests

Before the synchrotron experiments, we carried out lab-based cyclic loading tests to validate the setup and quantify macroscopic changes in mechanical properties. **Figure 8.7** shows three peak stress- time curves for KASW, a stiffening agent. The peak stress of each cycle is plotted against time during fixed strain (15% tissue strain) cyclic loading of MCT at frequency of 0.3HZ, with immersing in ASW in the fluid chamber until 246 ± 30 s, following by an exchange of the bathing solution from ASW to KASW. The KASW-case had a stiffening effect, whereby the effect could be observed within several seconds. In the cyclic loading tests, specimen developed peak stress which was almost constant without chemical stimulation. When KASW (stiffening agent) was introduced to the system, peak stress increased by 79.34%, 80.85%, 113.36%, indicating an increase of stiffness resulting from this chemical.

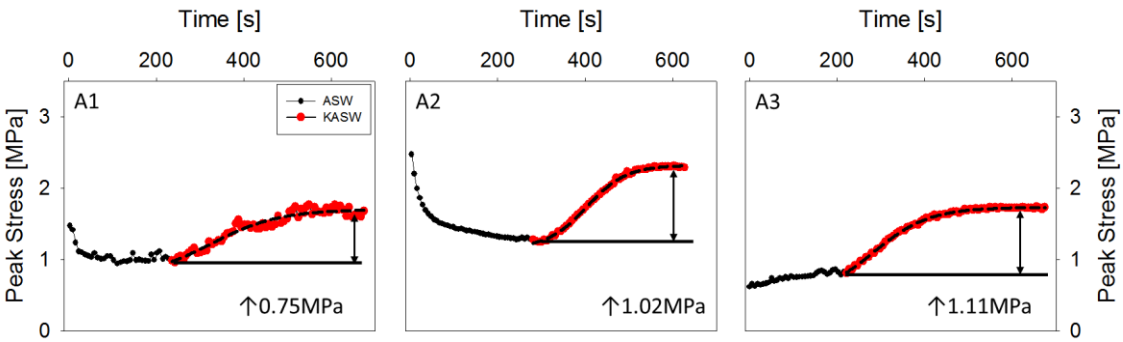

Figure 8.7 The effect of KASW on stiffness of MCT-containing specimens in the cyclic loading tests. *(A1, A2, A3). The peak stress of each cycle progressively increased after the KASW (~200 s) was introduced to the system. The region which denoted in black is the ASW-immersing specimen, followed by a bathing solution exchange from ASW to KASW, which was denoted in red. The stiffening region was fitted with a sigmoidal curve (f= y0+a/(1+exp(-(x-x0)/b)) as guideline to eyes. Stress number in each panel corresponds to the*

magnitude of the bidirectional arrow showing the stress increase relative to the unstimulated stabilized value

8.3.2 Comparison of mechanical behaviour in lab and synchrotron experiments

The comparison of mechanics between lab cyclic loading data with synchrotron cyclic loading data in which MCT specimens were exposed to high-dosage of X-ray beam is presented in **Figure 8.9**. The increase of peak stress tested in lab (denoted in red) shows that the stiffening effect was observed almost instantly after the KASW was injected, followed by peak stress dramatically increase from 1.24 MPa to 2.31 MPa. The example cyclic data collected in synchrotron was denoted in pink using the same mechanical testing protocol, and the peak stress was increased from 0.75 MPa to 0.81 MPa. The percentage changes of peak stress of these two tests was 86.3% and 7.4% without or with X-ray. Another unambiguous evidence of radiation damage is the splitting peak from I (q) profile (**Figure 8.10**), which results from unfolding, aggregation, or breakage of protein.

Although the specimens were damaged by X-ray beam, there was still some trends of interfibrillar stiffening effect induced by KASW at the nanoscale, which will be discussed in the next subsection.

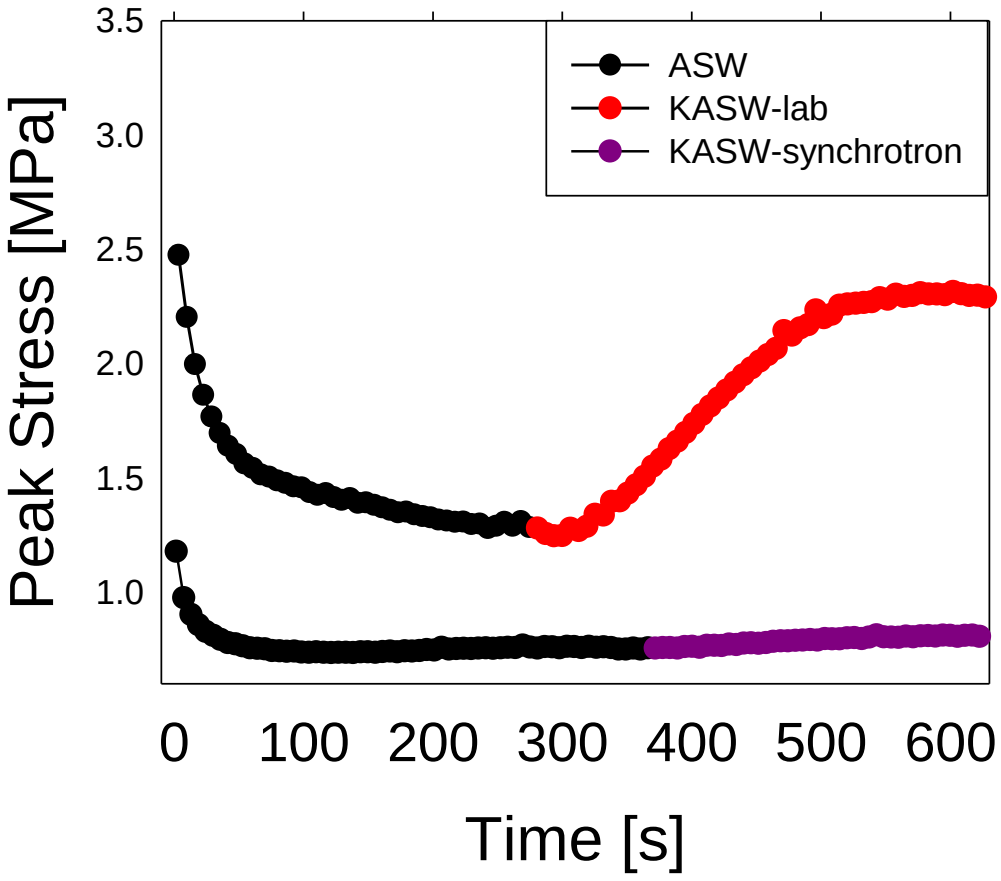

Figure 8.9 *Time-dependent change in MCT mutability induced via ionic treatment in different environment, with (denoted in pink) or without exposure (denoted in red) to X-ray. The peak stress (per cycle) is plotted with time during cyclic loading tests, showing a clear difference of peak stress (per cycle) is observed in differing condition.*

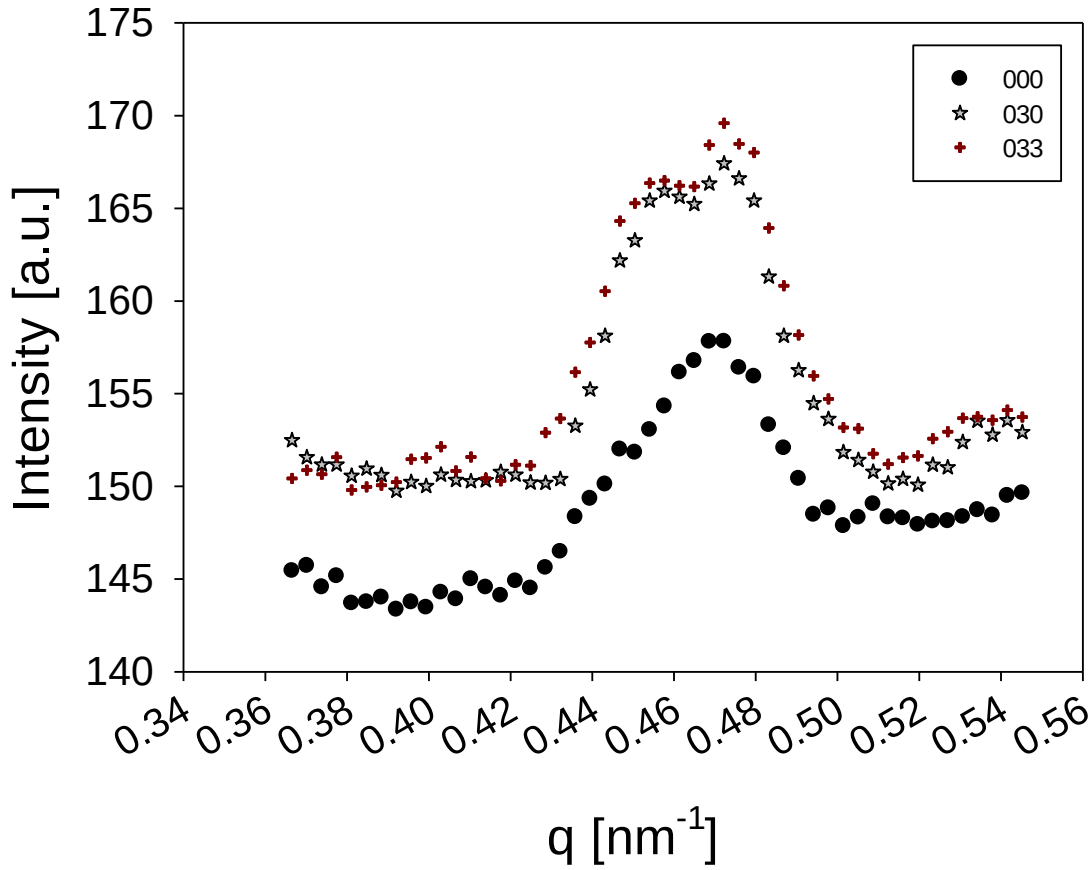

Figure 8.10 *Intensity profile integrated radially, with 5th order Bragg peak at ~0.475 nm^{-1}. Black filled circle is the scan at start of SAXS measurements. Grey star and red cross are the 31st and 34th scans where a split 5th order peak pattern in the SAXD profile appears, indicating nanostructural change due to radiation damage.*

8.3.3 Synchrotron SAXD data evaluation

The peak stress at the tissue level was recorded together with fibril strain ε_f (derived from SAXD pattern) during the cyclic loading. **Figure 8.11 (A)** shows the fibril strain ε_f as a function of the time of specimens. The range of fibril strain developed in KASW (~0 – 0.5%)is much larger than the range for ASW (~0 – 0.2%). Fibrils in different treatments, KASW and ASW shown a clear difference of fibril elongation. After the application of KASW, the macroscopic peak stress increases together with fibril strain developed at the fibrillar level.

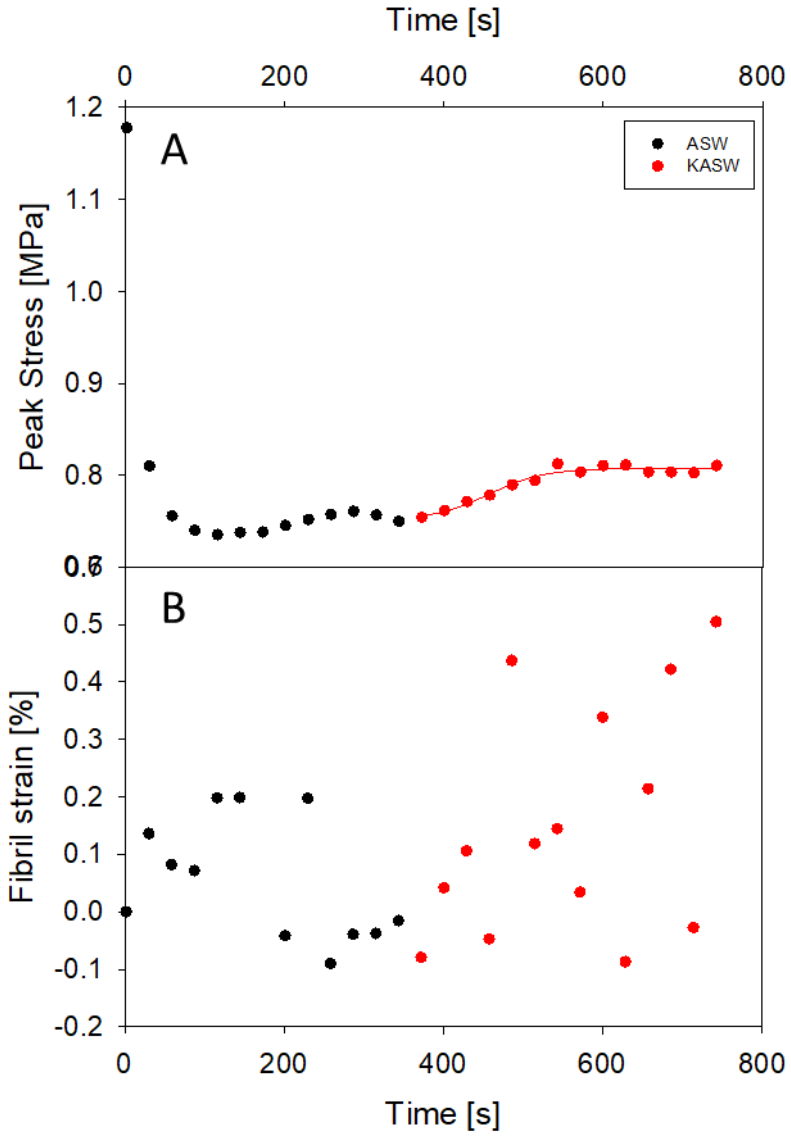

Figure 8.11 *Fibrillar stress increase with ionically KASW treated MCT. An increase of peak stress and fibril strain (per cycle) is observed*

8.4 Discussion and Conclusion

A process of identifying technical problem for equipment designing and manufacturing, control system coding and building is presented in this chapter. Customized 3D printing syringe pumps was made for long-term solution exchanging within introducing chemical stimulation into the system. Syringe pump system was comprised by hardware the structural elements, syringes and software, the control system. Here the frameworks of structural elements were designed by Michigan Tech's Open Sustainability Technology Lab [324]. Other components including stepper motor, syringe and tubing system was bought from commercial company. A USB-host DAQ device was connected to PC, which will then be controlled by LabVIEW-based control program. To acquire continuous SAXD measurement at the peak stress position, LabVIEW-based cyclic loading program which could be able to generate series TTL pulse via DAQ device was built.

However, synchrotron tests showed that the repeated exposures of the tissue led to radiation damage. We initially planned on using the strategy of moving the specimen continuously under the beam to avoid overexposures and excess radiation dosage at one point, which worked well for prior uniaxial stretch-to-failure and stress relaxation (**Chapters 6** and **7**). Further, by using in this case a fully immersed fluid chamber (water bath) in which specimens were immersed also led to X-ray absorption and attenuation, thus reducing dosage. Nevertheless, while lab-tests of the setup confirmed a dramatic change in mechanical properties on altering the bathing solution, there is still a gap between lab- and synchrotron mechanical data. We therefore

conclude that this change arises from the radiation damage effect, which results in protein unfolding, aggregation, or breakage. Despite these issues affecting our original experimental plan, we have one good data set which shows some evidence of fibril strain increase, which requiring validation in future studies to confirm the interfibrillar stiffening effect occurring in real-time.

Chapter 9 : Summary and Future Work

9.1 Summary

This PhD project has shed new light, using advanced X-ray characterization techniques, on the structural mechanisms enabling dynamic mechanical properties in mutable collagenous tissue (MCT). As the first work of its kind (that we are aware of), we proceeded in a stepwise manner to understand the role of the fibrillar and nonfibrillar matrix during deformation. In **Chapter 5**, as a proof of concept, SAXD measurements were collected on freeze-thawed MCT specimen. Then, in **Chapter 6**, we carried out *in situ* SAXD combing with quasi-static micromechanical deformation to study MCT structure-function relations in response to variable stimuli at the nanoscale. The stiffening and destiffening mechanisms leading to their remarkable mutability was found to be controlled by the change of the properties of the interfibrillar matrix between the fibril instead of changing the properties of collagen fibrils. A staggered fibril model was built to explain the nanoscale interfibrillar shear transfer validating by interfibrillar crosslink quantitatively. These findings suggest that future research focus on the interaction of the interfibrillar matrix molecules with collagen, specifically, to be able to control MCT properties and devise mimics.

In the next stage (**chapter 7**), we moved beyond static mechanical properties to investigate the transient viscoelastic response, carrying out the stress relaxation tests on MCT with different stimulation states, to determine the time-dependent response of interfibrillar matrix and fibril of MCT-containing tissue. By fitting the stress relaxation data at both tissue level and fibrillar level, we established that the time-

dependence of macroscale mechanics arose from the fibrillar-interfibrillar matrix interactions, due to the similar time constants between both processes. We also found that the stiffened state of MCT corresponds to a near-permanent "set" of the fibrils, which augurs well for its ability to be used in applications where longer-term load bearing is needed. A mathematical model which can use the experimental data to extract the response of the amorphous interfibrillar matrix, was applied to extract the viscoelastic behaviour of the interfibrillar matrix.

In the last research chapter (**chapter 8**), we investigated the kinetics of the change of state between mechanically softened, standard and stiff states, to understand how active force is generated in MCT. We used cyclic loading tests when the different chemical stimulating agents was applied via a new fluidic system (CaF-ASW: softening agent; KASW: stiffening agent), during *in situ* synchrotron SAXD. Technical issues including the customized fluidic system for stimuli-agent injection and the control system set-up for triggering SAXD acquisitions precisely at the maximum displacement position, were solved. However, radiation damage issues related to variability in beam quality made acquisition of reliable SAXD data difficult in the single beam-time we had to test the final setup. Nevertheless, a few SAXD measurements, showing the change of collagen fibril elongation in response to stimulating agents, were obtained.

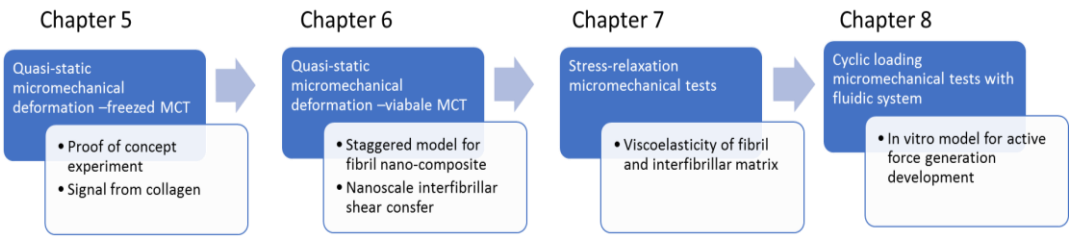

Figure 9 1 Flowchart showing the progression of research

9.2 Future work

Firstly, for completeness, to develop an *in vitro* model for understanding the rate and extent of force generation, further synchrotron experiments are needed for quantifying the nanoscale mechanisms of force generation, as the real-time measurements using synchrotron X-ray scattering during stimuli agent induced stiffening and softening are insufficient. SAXD data collected during the first time of cyclic loading test at synchrotron suffered from radiation damage, which both affected the fibrillar information, as well as the overall stimuli-responsive ability of MCT-containing tissue. To minimize the radiation damage, methods including changed step size, less frequent acquisition between scans, and use of ESRF (rather than DLS) for better SAXD pattern quality with lower exposure time (and hence lower damage) should be considered and applied to future experiments. Further measurements, reducing radiation damage, are needed to complete the dataset, and to build up a robust *in vitro* model for active force generation, possibly including injection of peptides and proteins proposed to have mechano-effector properties in MCT. As stated in **Chapter 6**, combined SAXS/WAXD studies to decouple the effects of fibrillar and molecular elongation versus molecular rotation [298] would also be very useful.

Secondly, to progress the development of MCT-like tissue, dissolution and reconstitution of MCT tissue, combined with mechano-effector molecules, could be a promising approach. Protocols exist to extract collagen from sea cucumber dermis [267, 325]. The mechanical behaviour of these reconstituted SC dermis strips could be firstly

studied in lab with quasi-static deformation, stress relaxation and cyclic loading to examine their mechanical properties as well as the stimuli-responsive capacity. Following this, proof-of-concept synchrotron experiments with nanomechanical deformation on these synthesized reconstituted MCT strips, combining tissue with addition of possible mechano-effector molecules, using similar set-ups to those described in **chapters 5-8**.

These studies will, in the long term, advance the understanding of the design principles of biomimetic “soft robots” and help develop a new echinoderm-inspired fibre-based material with the capacity of active force generation.

Reference

1. Roy, D., J.N. Cambre, and B.S. Sumerlin, *Future perspectives and recent advances in stimuli-responsive materials.* Progress in Polymer Science, 2010. **35**(1): p. 278-301.
2. El-Sherbiny, I.M. and M.H. Yacoub, *Hydrogel scaffolds for tissue engineering: Progress and challenges.* Global Cardiology Science and Practice, 2013: p. 38.
3. Liu, J., *Oligonucleotide-functionalized hydrogels as stimuli responsive materials and biosensors.* Soft Matter, 2011. **7**(15): p. 6757-6767.
4. Gupta, P., K. Vermani, and S. Garg, *Hydrogels: from controlled release to pH-responsive drug delivery.* Drug discovery today, 2002. **7**(10): p. 569-579.
5. Mura, S., J. Nicolas, and P. Couvreur, *Stimuli-responsive nanocarriers for drug delivery.* Nature materials, 2013. **12**(11): p. 991.
6. De las Heras Alarcón, C., S. Pennadam, and C. Alexander, *Stimuli responsive polymers for biomedical applications.* Chemical Society Reviews, 2005. **34**(3): p. 276-285.
7. Cole, M.A., et al., *Stimuli-responsive interfaces and systems for the control of protein–surface and cell–surface interactions.* Biomaterials, 2009. **30**(9): p. 1827-1850.
8. Bar-Cohen, Y., *Electroactive polymer (EAP) actuators as artificial muscles: reality, potential, and challenges*. Vol. 136. 2004: SPIE press.
9. Capadona, J.R., et al., *Stimuli-responsive polymer nanocomposites inspired by the sea cucumber dermis.* Science, 2008. **319**(5868): p. 1370-4.
10. Xia, F. and L. Jiang, *Bio‐inspired, smart, multiscale interfacial materials.* Advanced materials, 2008. **20**(15): p. 2842-2858.
11. Wilkie, I., *Mutable collagenous tissue: overview and biotechnological perspective*, in *Echinodermata*. 2005, Springer. p. 221-250.
12. Egan, P., et al., *The role of mechanics in biological and bio-inspired systems.* Nature Communications, 2015. **6**: p. 1–12.
13. Barbaglio, A., et al., *The mechanically adaptive connective tissue of echinoderms: its potential for bio-innovation in applied technology and ecology.* Mar Environ Res, 2012. **76**: p. 108-13.
14. Karunaratne, A., et al., *Significant Deterioration in Nanomechanical Quality Occurs Through Incomplete Extrafibrillar Mineralization in Rachitic Bone: Evidence From In-Situ Synchrotron X-ray Scattering and Backscattered Electron Imaging.* Journal of Bone and Mineral Research, 2012. **27**(4): p. 876-890.
15. Screen, H.R.C., et al., *Extrafibrillar diffusion and intrafibrillar swelling at the nanoscale are associated with stress relaxation in the soft collagenous matrix tissue of tendons.* Soft Matter, 2011. **7**(23): p. 11243-11251.
16. Gupta, H.S., et al., *In situ multi-level analysis of viscoelastic deformation mechanisms in tendon collagen.* Journal of Structural Biology, 2010. **169**(2): p. 183-191.
17. Gupta, H.S., et al., *Cooperative deformation of mineral and collagen in bone at the nanoscale.* Proceedings of the National Academy of Sciences of the United States of America, 2006. **103**(47): p. 17741-17746.
18. Gupta, H.S., et al., *Nanoscale deformation mechanisms in bone.* Nano Letters, 2005. **5**(10): p. 2108-2111.
19. Dobbie, J.W., J.K. Lloyd, and C.A. Gall, *Categorization of Ultrastructural-Changes in Peritoneal Mesothelium, Stroma and Blood-Vessels in Uremia and Capd Patients.* Advances in Peritoneal Dialysis, Vol 6, 1990. **6**: p. 3-12.

20. Elliott, D., *Structure and function of mammalian tendon.* Biological Reviews, 1965. **40**(3): p. 392-421.
21. Cen, L., et al., *Collagen tissue engineering: Development of novel biomaterials and applications.* Pediatric Research, 2008. **63**(5): p. 492-496.
22. Rizzo, D.C., *Fundamentals of anatomy and physiology*. 2015: Cengage Learning.
23. Fratzl, P., *Collagen: structure and mechanics*. 2008: Springer Science & Business Media.
24. Kannus, P., *Structure of the tendon connective tissue.* Scandinavian Journal of Medicine & Science in Sports, 2000. **10**(6): p. 312-320.
25. Fratzl, P. and R. Weinkamer, *Nature's hierarchical materials.* Progress in Materials Science, 2007. **52**(8): p. 1263-1334.
26. Weiner, S. and H.D. Wagner, *The material bone: Structure mechanical function relations.* Annual Review of Materials Science, 1998. **28**: p. 271-298.
27. Rho, J.Y., L. Kuhn-Spearing, and P. Zioupos, *Mechanical properties and the hierarchical structure of bone.* Medical Engineering & Physics, 1998. **20**(2): p. 92-102.
28. Fratzl, P., et al., *Structure and mechanical quality of the collagen-mineral nano-composite in bone.* Journal of Materials Chemistry, 2004. **14**(14): p. 2115-2123.
29. Silver, F.H., J.W. Freeman, and D. DeVore, *Viscoelastic properties of human skin and processed dermis.* Skin Res Technol, 2001. **7**(1): p. 18-23.
30. Holzapfel, G.A., T.C. Gasser, and R.W. Ogden, *A new constitutive framework for arterial wall mechanics and a comparative study of material models.* Journal of Elasticity, 2000. **61**(1-3): p. 1-48.
31. Frantz, C., K.M. Stewart, and V.M. Weaver, *The extracellular matrix at a glance.* Journal of Cell Science, 2010. **123**(24): p. 4195-4200.
32. Berg, R.A. and D.J. Prockop, *Thermal Transition of a Non-Hydroxylated Form of Collagen - Evidence for a Role for Hydroxyproline in Stabilizing Triple-Helix of Collagen.* Biochemical and Biophysical Research Communications, 1973. **52**(1): p. 115-120.
33. Heidemann, E. and W. Roth, *Synthesis and Investigation of Collagen Model Peptides.* Advances in Polymer Science, 1982. **43**: p. 143-203.
34. Kjellen, L. and U. Lindahl, *Proteoglycans - Structures and Interactions.* Annual Review of Biochemistry, 1991. **60**: p. 443-475.
35. Scott, J.E. and A.M. Thomlinson, *The structure of interfibrillar proteoglycan bridges ('shape modules') in extracellular matrix of fibrous connective tissues and their stability in various chemical environments.* Journal of Anatomy, 1998. **192**: p. 391-405.
36. Kadler, K.E., et al., *Collagens at a glance.* Journal of Cell Science, 2007. **120**(12): p. 1955-1958.
37. Brodsky, B. and J.A.M. Ramshaw, *The collagen triple-helix structure.* Matrix Biology, 1997. **15**(8-9): p. 545-554.
38. Brodsky, B. and N.K. Shah, *Protein motifs .8. The triple-helix motif in proteins.* Faseb Journal, 1995. **9**(15): p. 1537-1546.
39. Kielty, C.M. and M.E. Grant, *The collagen family: structure, assembly, and organization in the extracellular matrix.* Connective Tissue and Its Heritable Disorders: Molecular, Genetic, and Medical Aspects, Second Edition, 2003: p. 159-221.
40. Reilly, D.T., A.H. Burstein, and V.H. Frankel, *The elastic modulus for bone.* J Biomech, 1974. **7**(3): p. 271-5.
41. Dublet, B., et al., *The Structure of Avian Type-Xii Collagen - Alpha-1(Xii) Chains Contain 190-Kda Non-Triple Helical Amino-Terminal Domains and Form*

Homotrimeric Molecules. Journal of Biological Chemistry, 1989. **264**(22): p. 13150-13156.
42. Koch, M., et al., *Collagen XXIV, a vertebrate fibrillar collagen with structural features of invertebrate collagens - Selective expression in developing cornea and bone.* Journal of Biological Chemistry, 2003. **278**(44): p. 43236-43244.
43. Burgeson, R.E., *New Collagens, New Concepts.* Annual Review of Cell Biology, 1988. **4**: p. 551-577.
44. Sutmuller, M., J.A. Bruijn, and E. deHeer, *Collagen types VIII and X, two non-fibrillar, short-chain collagens. Structure homologies, functions and involvement in pathology.* Histology and Histopathology, 1997. **12**(2): p. 557-566.
45. Fukai, N., S.S. Apte, and B.R. Olsen, *Nonfibrillar Collagens.* Extracellular Matrix Components, 1994. **245**: p. 3-28.
46. Inoguchi, K., et al., *The Messenger-Rna for Alpha-1(Xix)-Collagen Chain, a New Member of Facits, Contains a Long Unusual 3'-Untranslated Region and Displays Many Unique Splicing Variants.* Journal of Biochemistry, 1995. **117**(1): p. 137-146.
47. Khoshnoodi, J., et al., *Molecular recognition in the assembly of collagens: Terminal noncollagenous domains are key recognition modules in the formation of triple helical protomers.* Journal of Biological Chemistry, 2006. **281**(50): p. 38117-38121.
48. Franzke, C.W., P. Bruckner, and L. Bruckner-Tuderman, *Collagenous transmembrane proteins: Recent insights into biology and pathology.* Journal of Biological Chemistry, 2005. **280**(6): p. 4005-4008.
49. Than, M.E., et al., *The 1.9-angstrom crystal structure of the noncollagenous (NC1) domain of human placenta collagen IV shows stabilization via a novel type of covalent Met-Lys cross-link.* Proceedings of the National Academy of Sciences of the United States of America, 2002. **99**(10): p. 6607-6612.
50. Ricard-Blum, S., *The Collagen Family.* Cold Spring Harbor Perspectives in Biology, 2011. **3**(1).
51. Sawada, H., H. Konomi, and K. Hirosawa, *Characterization of the collagen in the hexagonal lattice of Descemet's membrane: its relation to type VIII collagen.* J Cell Biol, 1990. **110**(1): p. 219-27.
52. Stephan, S., et al., *Expression and supramolecular assembly of recombinant alpha 1(VIII) and alpha 2(VIII) collagen homotrimers.* Journal of Biological Chemistry, 2004. **279**(20): p. 21469-21477.
53. Hashimoto, T., et al., *CLAC: a novel Alzheimer amyloid plaque component derived from a transmembrane precursor, CLAC-P/collagen type XXV.* Embo Journal, 2002. **21**(7): p. 1524-1534.
54. Verdier, Y. and B. Penke, *Binding sites of amyloid beta-peptide in cell plasma membrane and implications for Alzheimer's disease.* Current Protein & Peptide Science, 2004. **5**(1): p. 19-31.
55. Felbor, U., et al., *Secreted cathepsin L generates endostatin from collagen XVIII.* Embo Journal, 2000. **19**(6): p. 1187-1194.
56. Homandberg, G.A., et al., *Heparin-Binding Fragments of Fibronectin Are Potent Inhibitors of Endothelial-Cell Growth.* American Journal of Pathology, 1985. **120**(3): p. 327-332.
57. O'Reilly, M.S., et al., *Antiangiogenic activity of the cleaved conformation of the serpin antithrombin.* Science, 1999. **285**(5435): p. 1926-1928.
58. Keene, D.R., E. Engvall, and R.W. Glanville, *Ultrastructure of Type-Vi Collagen in Human-Skin and Cartilage Suggests an Anchoring Function for This Filamentous Network.* Journal of Cell Biology, 1988. **107**(5): p. 1995-2006.

59. Petruska, J.A. and A.J. Hodge, *A Subunit Model for the Tropocollagen Macromolecule.* Proc Natl Acad Sci U S A, 1964. **51**: p. 871-6.
60. Thorpe, C.T., et al., *Fascicles and the interfascicular matrix show adaptation for fatigue resistance in energy storing tendons.* Acta biomaterialia, 2016. **42**: p. 308-315.
61. Silver, F.H., J.W. Freeman, and G.P. Seehra, *Collagen self-assembly and the development of tendon mechanical properties.* Journal of Biomechanics, 2003. **36**(10): p. 1529-1553.
62. Wilkie, I.C., *Mutable collagenous tissue: overview and biotechnological perspective.* Prog Mol Subcell Biol, 2005. **39**: p. 221-50.
63. Yang, W., et al., *On the tear resistance of skin.* Nature Communications, 2015. **6**.
64. Cribb, A.M. and J.E. Scott, *Tendon Response to Tensile-Stress - an Ultrastructural Investigation of Collagen - Proteoglycan Interactions in Stressed Tendon.* Journal of Anatomy, 1995. **187**: p. 423-428.
65. Puxkandl, R., et al., *Viscoelastic properties of collagen: synchrotron radiation investigations and structural model.* Philosophical Transactions of the Royal Society of London Series B-Biological Sciences, 2002. **357**(1418): p. 191-197.
66. Pradas, M.M. and R.D. Calleja, *Nonlinear Viscoelastic Behavior of the Flexor Tendon of the Human Hand.* Journal of Biomechanics, 1990. **23**(8): p. 773-781.
67. Haut, T.L. and R.C. Haut, *The state of tissue hydration determines the strain-rate-sensitive stiffness of human patellar tendon.* Journal of Biomechanics, 1997. **30**(1): p. 79-81.
68. Robinson, P.S., et al., *Strain-rate sensitive mechanical properties of tendon fascicles from mice with genetically engineered alterations in collagen and decorin.* Journal of Biomechanical Engineering-Transactions of the Asme, 2004. **126**(2): p. 252-257.
69. Wu, J.J., *Quantitative constitutive behaviour and viscoelastic properties of fresh flexor tendons.* International Journal of Artificial Organs, 2006. **29**(9): p. 852-857.
70. Lynch, H.A., et al., *Effect of fiber orientation and strain rate on the nonlinear uniaxial tensile material properties of tendon.* Journal of Biomechanical Engineering-Transactions of the Asme, 2003. **125**(5): p. 726-731.
71. Wu, J.Z., et al., *Estimation of the viscous properties of skin and subcutaneous tissue in uniaxial stress relaxation tests.* Bio-Medical Materials and Engineering, 2006. **16**(1): p. 53-66.
72. Usha, R., V. Subramanian, and T. Ramasami, *Role of secondary structure on the stress relaxation processes in rat tail tendon (RTT) collagen fibre.* Macromolecular Bioscience, 2001. **1**(3): p. 100-107.
73. Silver, F.H., et al., *Transition from viscous to elastic-based dependency of mechanical properties of self-assembled type I collagen fibers.* Journal of Applied Polymer Science, 2001. **79**(1): p. 134-142.
74. Screen, H.R.C., et al., *An investigation into the effects of the hierarchical structure of tendon fascicles on micromechanical properties.* Proceedings of the Institution of Mechanical Engineers Part H-Journal of Engineering in Medicine, 2004. **218**(H2): p. 109-119.
75. Provenzano, P.P. and R. Vanderby, *Collagen fibril morphology and organization: Implications for force transmission in ligament and tendon.* Matrix Biology, 2006. **25**(2): p. 71-84.
76. Screen, H.R.C., et al., *Local strain measurement within tendon.* Strain, 2004. **40**(4): p. 157-163.
77. Screen, H.R.C., et al., *Development of a technique to determine strains in tendons using the cell nuclei.* Biorheology, 2003. **40**(1-3): p. 361-368.

78. Screen, H.R.C., et al., *Cyclic tensile strain upregulates collagen synthesis in isolated tendon fascicles.* Biochemical and Biophysical Research Communications, 2005. **336**(2): p. 424-429.
79. Screen, H.R.C., et al., *Cyclic tensile strain upregulates collagen production in isolated tendon fascicles.* International Journal of Experimental Pathology, 2005. **86**(3): p. A8-A9.
80. Screen, H.R.C., et al., *The influence of noncollagenous matrix components on the micromechanical environment of tendon fascicles.* Annals of Biomedical Engineering, 2005. **33**(8): p. 1090-1099.
81. Screen, H.R., et al., *The influence of noncollagenous matrix components on the micromechanical environment of tendon fascicles.* Ann Biomed Eng, 2005. **33**(8): p. 1090-9.
82. Marks, M.H., R.S. Bear, and C.H. Blake, *X-ray diffraction evidence of collagen-type protein fibers in the Echinodermata, Coelenterata and Porifera.* J Exp Zool, 1949. **111**(1): p. 55-78.
83. North, A.C., P.M. Cowan, and J.T. Randall, *Structural units in collagen fibrils.* Nature, 1954. **174**(4442): p. 1142-3.
84. Miller, A. and J.S. Wray, *Molecular packing in collagen.* Nature, 1971. **230**(5294): p. 437-9.
85. Folkhard, W., et al., *Structural Dynamic of Native Tendon Collagen.* Journal of Molecular Biology, 1987. **193**(2): p. 405-407.
86. Folkhard, W., et al., *Quantitative-Analysis of the Molecular Sliding Mechanism in Native Tendon Collagen - Time-Resolved Dynamic Studies Using Synchrotron Radiation.* International Journal of Biological Macromolecules, 1987. **9**(3): p. 169-175.
87. Mosler, E., et al., *Stress-Induced Molecular Rearrangement in Tendon Collagen.* Journal of Molecular Biology, 1985. **182**(4): p. 589-596.
88. Sasaki, N. and S. Odajima, *Elongation mechanism of collagen fibrils and force-strain relations of tendon at each level of structural hierarchy.* Journal of Biomechanics, 1996. **29**(9): p. 1131-1136.
89. Rinnerthaler, S., et al., *Scanning small angle X-ray scattering analysis of human bone sections.* Calcif Tissue Int, 1999. **64**(5): p. 422-9.
90. Fratzl, P., et al., *Nucleation and growth of mineral crystals in bone studied by small-angle X-ray scattering.* Calcif Tissue Int, 1991. **48**(6): p. 407-13.
91. Fratzl, P., et al., *Mineral crystals in calcified tissues: a comparative study by SAXS.* J Bone Miner Res, 1992. **7**(3): p. 329-34.
92. Paris, O., et al., *Analysis of the hierarchical structure of biological tissues by scanning X-ray scattering using a micro-beam.* Cellular and Molecular Biology, 2000. **46**(5): p. 993-1004.
93. Shen, Z.L., et al., *Viscoelastic properties of isolated collagen fibrils.* Biophys J, 2011. **100**(12): p. 3008-15.
94. Graham, J.S., et al., *Structural changes in human type I collagen fibrils investigated by force spectroscopy.* Experimental cell research, 2004. **299**(2): p. 335-342.
95. Eppell, S., et al., *Nano measurements with micro-devices: mechanical properties of hydrated collagen fibrils.* Journal of the Royal Society Interface, 2006. **3**(6): p. 117-121.
96. Wenger, M.P., et al., *Mechanical properties of collagen fibrils.* Biophysical journal, 2007. **93**(4): p. 1255-1263.

97. Sasaki, N. and S. Odajima, *Stress-strain curve and Young's modulus of a collagen molecule as determined by the X-ray diffraction technique.* Journal of Biomechanics, 1996. **29**(5): p. 655-658.
98. Goh, K.L., et al., *Ageing changes in the tensile properties of tendons: influence of collagen fibril volume fraction.* J Biomech Eng, 2008. **130**(2): p. 021011.
99. Cohen, N.P., R.J. Foster, and V.C. Mow, *Composition and dynamics of articular cartilage: structure, function, and maintaining healthy state.* Journal of Orthopaedic & Sports Physical Therapy, 1998. **28**(4): p. 203-215.
100. Lai, W.M., J. Hou, and V.C. Mow, *A triphasic theory for the swelling and deformation behaviors of articular cartilage.* J Biomech Eng, 1991. **113**(3): p. 245-258.
101. Mow, V.C., et al., *Biphasic creep and stress relaxation of articular cartilage in compression: theory and experiments.* J Biomech Eng, 1980. **102**(1): p. 73-84.
102. Sophia Fox, A.J., A. Bedi, and S.A. Rodeo, *The basic science of articular cartilage: structure, composition, and function.* Sports health, 2009. **1**(6): p. 461-468.
103. Annaidh, A.N., et al., *Characterization of the anisotropic mechanical properties of excised human skin.* Journal of the Mechanical Behavior of Biomedical Materials, 2012. **5**(1): p. 139-148.
104. Silver, F.H., L.M. Siperko, and G.P. Seehra, *Mechanobiology of force transduction in dermal tissue.* Skin Research and Technology, 2003. **9**(1): p. 3-23.
105. Hussain, S.H., B. Limthongkul, and T.R. Humphreys, *The Biomechanical Properties of the Skin.* Dermatologic Surgery, 2013. **39**(2): p. 193-203.
106. Cheng, W., et al., *The content and ratio of type I and III collagen in skin differ with age and injury.* African Journal of Biotechnology, 2011. **10**(13): p. 2524-2529.
107. Fung, Y.-c., *Biomechanics: mechanical properties of living tissues*. 2013: Springer Science & Business Media.
108. Manschot, J. and A. Brakkee, *The measurement and modelling of the mechanical properties of human skin in vivo—I. The measurement.* Journal of Biomechanics, 1986. **19**(7): p. 511-515.
109. Diridollou, S., et al., *In vivo model of the mechanical properties of the human skin under suction.* Skin Research and technology, 2000. **6**(4): p. 214-221.
110. Hendriks, F., et al., *A numerical‐experimental method to characterize the non‐linear mechanical behaviour of human skin.* Skin research and technology, 2003. **9**(3): p. 274-283.
111. Sanders, R., *Torsional elasticity of human skin in vivo.* Pflügers Archiv European Journal of Physiology, 1973. **342**(3): p. 255-260.
112. Berardesca, E., et al., *In vivo biophysical characterization of skin physiological differences in races.* Dermatology, 1991. **182**(2): p. 89-93.
113. Agache, P., et al., *Mechanical properties and Young's modulus of human skin in vivo.* Archives of dermatological research, 1980. **269**(3): p. 221-232.
114. Gong, J., J. Arnold, and S. Cohn, *Composition of trabecular and cortical bone.* The Anatomical Record, 1964. **149**(3): p. 325-331.
115. Wainwright, S.A., *Mechanical design in organisms*. 1982: Princeton University Press.
116. Fratzl, P., I. Burgert, and H.S. Gupta, *On the role of interface polymers for the mechanics of natural polymeric composites.* Physical Chemistry Chemical Physics, 2004. **6**(24): p. 5575-5579.
117. Cowin, S.C. and S.B. Doty, *Tissue mechanics*. 2007: Springer Science & Business Media.
118. Wang, J.H., *Mechanobiology of tendon.* J Biomech, 2006. **39**(9): p. 1563-82.

119. Woo, S.L.Y., *Mechanical-Properties of Tendons and Ligaments .1. Quasi-Static and Non-Linear Viscoelastic Properties.* Biorheology, 1982. **19**(3): p. 385-396.
120. Shadwick, R.E., *Elastic Energy-Storage in Tendons - Mechanical Differences Related to Function and Age.* Journal of Applied Physiology, 1990. **68**(3): p. 1033-1040.
121. Bennett, M.B., et al., *Mechanical-Properties of Various Mammalian Tendons.* Journal of Zoology, 1986. **209**: p. 537-548.
122. Jordan, H., *Uber "reflexarme" Tiere. IV. Die Holothurien. 1 Mitteilung. Die Holothurien als hohlorganartige Tiere und die Tonusfunktion ihrer Muskulatur. .* Zool. Jahrb. Abt., 1914. **3**(34): p. 365- 436
123. Mo, J., et al., *Interfibrillar stiffening of echinoderm mutable collagenous tissue demonstrated at the nanoscale.* Proceedings of the National Academy of Sciences, 2016: p. 201609341.
124. Haut, R., *Age-dependent influence of strain rate on the tensile failure of rat-tail tendon.* J Biomech Eng, 1983. **105**(3): p. 296-9.
125. von Uexküll, J., *Die physiologie des Seeigelstachels*. 1900.
126. Wilkie, I., *Mutable collagenous tissues: extracellular matrix as mechano-effector.* Echinoderm studies, 1996. **5**: p. 61-102.
127. Wilkie, I., *Is muscle involved in the mechanical adaptability of echinoderm mutable collagenous tissue?* Journal of experimental biology, 2002. **205**(2): p. 159-165.
128. Takemae, N. and T. Motokawa, *Mechanical properties of the isolated catch apparatus of the sea urchin spine joint: muscle fibers do not contribute to passive stiffness changes.* The Biological Bulletin, 2005. **208**(1): p. 29-35.
129. Birenheide, R., K. Yokoyama, and T. Motokawa, *Cirri of the stalked crinoid Metacrinus rotundus: neural elements and the effect of cholinergic agonists on mechanical properties.* Proceedings of the Royal Society of London B: Biological Sciences, 2000. **267**(1438): p. 7-16.
130. Trotter, J., et al., *Towards a fibrous composite with dynamically controlled stiffness: lessons from echinoderms.* Biochemical Society Transactions, 1999. **28**(4): p. 357-362.
131. Wilkie, I.C., et al., *Mechanical properties of the collagenous mesohyl of Chondrosia reniformis: evidence for physiological control.* Boll. Mus. Ist. Biol. Univ. Genova, 2004. **68**: p. 665-672.
132. Motokawa, T. and A. Tsuchi, *Dynamic mechanical properties of body-wall dermis in various mechanical states and their implications for the behavior of sea cucumbers.* The Biological Bulletin, 2003. **205**(3): p. 261-275.
133. Ribeiro, A.R., et al., *New insights into mutable collagenous tissue: correlations between the microstructure and mechanical state of a sea-urchin ligament.* PLoS one, 2011. **6**(9): p. e24822.
134. Ribeiro, A.R., et al., *Matrix metalloproteinases in a sea urchin ligament with adaptable mechanical properties.* PLoS One, 2012. **7**(11): p. e49016.
135. Birenheide, R. and T. Motokawa, *To be stiff or to be soft - The dilemma of the echinoid tooth ligament .1. Morphology.* Biological Bulletin, 1996. **190**(2): p. 218-230.
136. Takemae, N. and T. Motokawa, *Mechanical properties of the isolated catch apparatus of the sea urchin spine joint: Muscle fibers do not contribute to passive stiffness changes.* Biological Bulletin, 2005. **208**(1): p. 29-35.
137. Birenheide, R., A. Tsuchi, and T. Motokawa, *To be stiff or to be soft - The dilemma of the echinoid tooth ligament. II. Mechanical properties.* Biological Bulletin, 1996. **190**(2): p. 231-236.

138. Motokawa, T. and A. Tsuchi, *Dynamic mechanical properties of body-wall dermis in various mechanical states and their implications for the behavior of sea cucumbers.* Biol Bull, 2003. **205**(3): p. 261-75.
139. Motokawa, T., *Mechanical mutability in connective tissue of starfish body wall.* Biol Bull, 2011. **221**(3): p. 280-9.
140. O'Neill, P., *Structure and mechanics of starfish body wall.* J Exp Biol, 1989. **147**: p. 53-89.
141. Wilkie, I.C., et al., *Mechanical properties of the compass depressors of the sea-urchin Paracentrotus lividus (Echinodermata, Echinoidea) and the effects of enzymes, neurotransmitters and synthetic tensilin-like protein.* PloS one, 2015. **10**(3): p. e0120339.
142. Birenheide, R., A. Tsuchi, and T. Motokawa, *To be stiff or to be soft--the dilemma of the echinoid tooth ligament. II. Mechanical properties.* The Biological Bulletin, 1996. **190**(2): p. 231-236.
143. Wilkie, I., C. Carnevali, and F. Bonasoro. *Evidence for the'cellular calcium regulation hypothesis' from'simple'mutable collagenous structure: the brachial and cirral syzygial ligaments of Antedon mediterranea (Lam.)*. in *European Conference on Echinoderms*. 1999. Balkema.
144. Ellers, O. and M. Telford, *Advancement mechanics of growing teeth in sand dollars (Echinodermata, Echinoidea): a role for mutable collagenous tissue.* Proceedings of the Royal Society of London B: Biological Sciences, 1996. **263**(1366): p. 39-44.
145. Szulgit, G.K. and R.E. Shadwick, *Dynamic mechanical characterization of a mutable collagenous tissue: response of sea cucumber dermis to cell lysis and dermal extracts.* Journal of Experimental Biology, 2000. **203**(10): p. 1539-1550.
146. Birenheide, R., et al., *Peptides controlling stiffness of connective tissue in sea cucumbers.* The Biological Bulletin, 1998. **194**(3): p. 253-259.
147. Ribeiro, A.R., et al., *New Insights into Mutable Collagenous Tissue: Correlations between the Microstructure and Mechanical State of a Sea-Urchin Ligament.* Plos One, 2011. **6**(9).
148. Ovaska, M., et al., *Deformation and fracture of echinoderm collagen networks.* Journal of the mechanical behavior of biomedical materials, 2017. **65**: p. 42-52.
149. Charlina, N.A., I.Y. Dolmatov, and I.C. Wilkie, *Juxtaligamental system of the disc and oral frame of the ophiuroid Amphipholis kochii (Echinodermata: Ophiuroidea) and its role in autotomy.* Invertebrate biology, 2009. **128**(2): p. 145-156.
150. Trotter, J.A., F.A. Thurmond, and T.J. Koob, *Molecular structure and functional morphology of echinoderm collagen fibrils.* Cell and tissue research, 1994. **275**(3): p. 451-458.
151. Thurmond, F.A. and J.A. Trotter, *Native collagen fibrils from echinoderms are molecularly bipolar.* J Mol Biol, 1994. **235**(1): p. 73-9.
152. Trotter, J.A., F.A. Thurmond, and T.J. Koob, *Molecular structure and functional morphology of echinoderm collagen fibrils.* Cell Tissue Res, 1994. **275**(3): p. 451-8.
153. Barbaglio, A., et al., *Ultrastructural and biochemical characterization of mechanically adaptable collagenous structures in the edible sea urchin Paracentrotus lividus.* Zoology (Jena), 2015. **118**(3): p. 147-60.
154. Ferrario, C., et al., *Marine-derived collagen biomaterials from echinoderm connective tissues.* Mar Environ Res, 2016.
155. Cluzel, C., et al., *Sea urchin fibrillar collagen 2 alpha chain participates in heterotrimeric molecules of (1 alpha)(2)2 alpha stoichiometry.* Matrix Biology, 2000. **19**(6): p. 545-547.

156. Trotter, J.A.a.K., T. J., *Evidence that calcium-dependent cellular processes are involved in the stiffening response of holohutrian dermis and that dermal cells contain an organic stiffening factor.* The Journal of Experimental Biology, 1995. **198**: p. 1951–1961.
157. Kimura, S., et al., *Molecular characterization of fibrillar collagen from the body wall of starfish Asterias amurensis.* Comparative Biochemistry and Physiology Part B: Comparative Biochemistry, 1993. **104**(4): p. 663-668.
158. Trotter, J.A., et al., *Covalent composition of collagen fibrils from the dermis of the sea cucumber, Cucumaria frondosa, a tissue with mutable mechanical properties.* Comparative Biochemistry and Physiology Part A: Physiology, 1995. **112**(3): p. 463-478.
159. Trotter, J., et al., *Towards a fibrous composite with dynamically controlled stiffness: lessons from echinoderms*. 2000, Portland Press Limited.
160. Esko, J.D., K. Kimata, and U. Lindahl, *Proteoglycans and sulfated glycosaminoglycans.* 2009.
161. Ribeiro, A.R., et al., *Correlations between the biochemistry and mechanical states of a sea-urchin ligament: a mutable collagenous structure.* Biointerphases, 2012. **7**(1-4): p. 38.
162. Bjornsson, S., *Quantitation of proteoglycans as glycosaminoglycans in biological fluids using an alcian blue dot blot analysis.* Analytical Biochemistry, 1998. **256**(2): p. 229-237.
163. Takehana, Y., et al., *Softenin, a novel protein that softens the connective tissue of sea cucumbers through inhibiting interaction between collagen fibrils.* PloS one, 2014. **9**(1): p. e85644.
164. Szulgit, G., *The echinoderm collagen fibril: a hero in the connective tissue research of the 1990s.* Bioessays, 2007. **29**(7): p. 645-653.
165. Tamori, M., et al., *Tensilin-like stiffening protein from Holothuria leucospilota does not induce the stiffest state of catch connective tissue.* Journal of experimental biology, 2006. **209**(9): p. 1594-1602.
166. Mashanov, V., et al., *Juxtaligamental cells in the arm of the brittlestar Amphipholis kochii Lütken, 1872 (Echinodermata: Ophiuroidea).* Russian Journal of Marine Biology, 2007. **33**(2): p. 110-117.
167. Wilkie, I., *Variable tensility in echinoderm collagenous tissues: a review.* Marine & Freshwater Behaviour & Phy, 1984. **11**(1): p. 1-34.
168. Wilkie, I., G. Griffiths, and S. Glennie, *Morphological and physiological aspects of the autotomy plane in the aboral integument of Asterias rubens L.(Echinodermata).* Echinoderm research, 1990: p. 301-313.
169. Wilkie, I., M.C. Carnevali, and J. Trotter. *Mutable collagenous tissue: recent progress and an evolutionary perspective*. in *Echinoderms: Munchen: Proceedings of the 11th International Echinoderm Conference, 6-10 October 2003, Munich, Germany*. 2005. Taylor & Francis.
170. Szulgit, G., *The effects of calcium chelation and cell perforation on the mechanical properties of sea urchin ligaments.* Echinoderms through time, 1994: p. 887-892.
171. Dobson, W.E. and R.L. Turner, *Morphology and Histology of the Disk Autotomy Plane in Ophiophragmus-Filograneus (Echinodermata, Ophiurida).* Zoomorphology, 1989. **108**(6): p. 323-332.
172. Fontaine, A.R., *Neurosecretion in the Ophiuroid Ophiopholis aculeata.* Science, 1962. **138**(3543): p. 908-9.

173. Wilkie, I.C., *The juxtaligamental cells of Ophiocomina nigra (Abildgaard) (Echinodermata: Ophiuroidea) and their possible role in mechano-effector function of collagenous tissue.* Cell Tissue Res, 1979. **197**(3): p. 515-30.
174. Wilkie, I.C. and R.H. Emson, *The Tendons of Ophiocomina-Nigra and Their Role in Autotomy (Echinodermata, Ophiuroida).* Zoomorphology, 1987. **107**(1): p. 33-44.
175. Wilkie, I.C., *Functional Morphology of the Arm Spine Joint and Adjacent Structures of the Brittlestar Ophiocomina nigra (Echinodermata: Ophiuroidea).* PLoS One, 2016. **11**(12): p. e0167533.
176. MOTOKAWA, T., *Factors regulating the mechanical properties of holothurian dermis.* Journal of Experimental Biology, 1982. **99**(1): p. 29-41.
177. MOTOKAWA, T., *Connective tissue catch in echinoderms.* Biological Reviews, 1984. **59**(2): p. 255-270.
178. Birenheide, R. and T. Motokawa, *Contractile connective tissue in crinoids.* Biol Bull, 1996. **191**(1): p. 1-4.
179. Wilkie, I.C., *Is muscle involved in the mechanical adaptability of echinoderm mutable collagenous tissue?* Journal of Experimental Biology, 2002. **205**(2): p. 159-165.
180. Motokawa, T., O. Shintani, and R. Birenheide, *Contraction and stiffness changes in collagenous arm ligaments of the stalked crinoid Metacrinus rotundus (Echinodermata).* The Biological Bulletin, 2004. **206**(1): p. 4-12.
181. Motokawa, T., *Mechanical mutability in connective tissue of starfish body wall.* The Biological Bulletin, 2011. **221**(3): p. 280-289.
182. Wilkie, I., *Nervously mediated change in the mechanical properties of a brittlestar ligament.* Marine & Freshwater Behaviour & Phy, 1978. **5**(4): p. 289-306.
183. Smith, D.S., et al., *Structural features associated with movement and 'catch'of sea-urchin spines.* Tissue and Cell, 1981. **13**(2): p. 299-320.
184. HIDAKA, M. and K. TAKAHASHI, *Fine structure and mechanical properties of the catch apparatus of the sea-urchin spine, a collagenous connective tissue with muscle-like holding capacity.* Journal of Experimental Biology, 1983. **103**(1): p. 1-14.
185. Szulgit, G. and R. Shadwick, *The effects of calcium chelation and cell perforation on the mechanical properties of sea urchin ligaments.* Echinoderms through time, 1994: p. 887-892.
186. Trotter, J.A., et al., *Covalent composition of collagen fibrils from the dermis of the sea cucumber,< i> Cucumaria frondosa</i>, a tissue with mutable mechanical properties.* Comparative Biochemistry and Physiology Part A: Physiology, 1995. **112**(3): p. 463-478.
187. Trotter, J.A., et al., *Collagen fibril aggregation-inhibitor from sea cucumber dermis.* Matrix Biology, 1999. **18**(6): p. 569-578.
188. Tipper, J.P., et al., *Purification, characterization and cloning of tensilin, the collagen-fibril binding and tissue-stiffening factor from< i> Cucumaria frondosa</i> dermis.* Matrix biology, 2002. **21**(8): p. 625-635.
189. Koob, T.J., M.M. Koob-Emunds, and J.A. Trotter, *Cell-derived stiffening and plasticizing factors in sea cucumber (Cucumaria frondosa) dermis.* Journal of Experimental Biology, 1999. **202**(17): p. 2291-2301.
190. Junqueira, L.C.U. and G.S. Montes, *Biology of Collagen-Proteoglycan Interaction.* Archivum Histologicum Japonicum, 1983. **46**(5): p. 589-629.
191. Yamada, A., et al., *A novel stiffening factor inducing the stiffest state of holothurian catch connective tissue.* The Journal of experimental biology, 2010. **213**(20): p. 3416-3422.

192. Trotter, J.A., et al., *Stiparin: a glycoprotein from sea cucumber dermis that aggregates collagen fibrils.* Matrix biology, 1996. **15**(2): p. 99-110.
193. Wilkie, I., M.C. Carnevali, and J. Trotter. *Mutable collagenous tissue: recent progress and an evolutionary perspective*. in *Echinoderms: Munchen: Proceedings of the 11th International Echinoderm Conference, 6-10 October 2003, Munich, Germany*. 2006. Taylor & Francis.
194. Tamori, M., et al., *Tensilin-like stiffening protein from Holothuria leucospilota does not induce the stiffest state of catch connective tissue.* J Exp Biol, 2006. **209**(Pt 9): p. 1594-602.
195. Timmons, B., M. Akins, and M. Mahendroo, *Cervical remodeling during pregnancy and parturition.* Trends in Endocrinology & Metabolism, 2010. **21**(6): p. 353-361.
196. Ribeiro, A.R., et al., *Matrix metalloproteinases in a sea urchin ligament with adaptable mechanical properties.* PLoS One, 2012. **7**(11): p. e49016.
197. Yamada, A., et al., *A novel stiffening factor inducing the stiffest state of holothurian catch connective tissue.* Journal of Experimental Biology, 2010. **213**(20): p. 3416-3422.
198. Trotter, J.A., F.A. Thurmond, and T.J. Koob, *Molecular-Structure and Functional-Morphology of Echinoderm Collagen Fibrils.* Cell and Tissue Research, 1994. **275**(3): p. 451-458.
199. Motokawa, T. and Y. Fuchigami, *Coordination between catch connective tissue and muscles through nerves in the spine joint of the sea urchin Diadema setosum.* J Exp Biol, 2015. **218**(Pt 5): p. 703-10.
200. Inoue, M., et al., *Localization of the neuropeptide NGIWYamide in the holothurian nervous system and its effects on muscular contraction.* Proceedings of the Royal Society B-Biological Sciences, 1999. **266**(1423): p. 993-1000.
201. Guinier, A., *X-ray diffraction: in crystals, imperfect crystals, and amorphous bodies*. 2013: Courier Dover Publications.
202. Guinier, A., *X-ray diffraction in crystals, imperfect crystals, and amorphous bodies*. 1994: Courier Corporation.
203. Huang, B., et al., *Three-dimensional super-resolution imaging by stochastic optical reconstruction microscopy.* Science, 2008. **319**(5864): p. 810-813.
204. Wenk, H.R. and F. Heidelbach, *Crystal alignment of carbonated apatite in bone and calcified tendon: Results from quantitative texture analysis.* Bone, 1999. **24**(4): p. 361-369.
205. Petoukhov, M.V. and D.I. Svergun, *Applications of small-angle X-ray scattering to biomacromolecular solutions.* The international journal of biochemistry & cell biology, 2013. **45**(2): p. 429-437.
206. Glatter, O. and O. Kratky, *Small angle X-ray scattering*. 1982: Academic press.
207. Henrich, B., et al., *PILATUS: A single photon counting pixel detector for X-ray applications.* Nuclear Instruments and Methods in Physics Research Section A: Accelerators, Spectrometers, Detectors and Associated Equipment, 2009. **607**(1): p. 247-249.
208. Oster, G. and D. Riley, *Scattering from cylindrically symmetric systems.* Acta Crystallographica, 1952. **5**(2): p. 272-276.
209. Hulmes, D.J., et al., *Analysis of the primary structure of collagen for the origins of molecular packing.* Journal of molecular biology, 1973. **79**(1): p. 137-148.
210. Petruska, J.A. and A.J. Hodge, *A subunit model for the tropocollagen macromolecule.* Proceedings of the National Academy of Sciences, 1964. **51**(5): p. 871-876.

211. Hosemann, R., R. Bonart, and T. Nemetschek, *The inhomogeneous stretching process of collagen.* Colloid & Polymer Science, 1974. **252**(11): p. 912-919.
212. Hosemann, R. and T. Nemetschek, *Reaktionsabläufe zwischen Phosphorwolframsäure und Kollagen.* Kolloid-Zeitschrift und Zeitschrift für Polymere, 1973. **251**(1): p. 53-60.
213. Knörzer, E., et al., *New aspects of the etiology of tendon rupture.* Archives of Orthopaedic and Trauma Surgery, 1986. **105**(2): p. 113-120.
214. Mosler, E., et al., *Stress-induced molecular rearrangement in tendon collagen.* Journal of molecular biology, 1985. **182**(4): p. 589-596.
215. Hammersley, A., *FIT2D: a multi-purpose data reduction, analysis and visualization program.* Journal of Applied Crystallography, 2016. **49**(2): p. 646-652.
216. Basham, M., et al., *Data Analysis WorkbeNch (DAWN).* Journal of synchrotron radiation, 2015. **22**(3): p. 853-858.
217. Sokolov, A.A. and I.M. Ternov, *Synchrotron radiation.* Akademia Nauk SSSR, Moskovskoie Obshchestvo Ispytatelei prirody. Sektsia Fiziki. Sinkhrotron Radiation, Nauka Eds., Moscow, 1966 (Russian title: Sinkhrotronnoie izluchenie), 228 pp., 1966.
218. Als-Nielsen, J. and D. McMorrow, *Elements of modern X-ray physics*. 2011: John Wiley & Sons.
219. Bilderback, D.H., P. Elleaume, and E. Weckert, *Review of third and next generation synchrotron light sources.* Journal of Physics B: Atomic, molecular and optical physics, 2005. **38**(9): p. S773.
220. Mittemeijer, E.J. and U. Welzel, *Modern diffraction methods*. 2013: John Wiley & Sons.
221. Borie, B., *X-Ray Diffraction in Crystals, Imperfect Crystals, and Amorphous Bodies.* Journal of the American Chemical Society, 1965. **87**(1): p. 140-141.
222. Fratzl, P., et al., *Position-resolved small-angle X-ray scattering of complex biological materials.* Journal of Applied Crystallography, 1997. **30**(2): p. 765-769.
223. Follath, R. and F. Senf, *New plane-grating monochromators for third generation synchrotron radiation light sources.* Nuclear Instruments and Methods in Physics Research Section A: Accelerators, Spectrometers, Detectors and Associated Equipment, 1997. **390**(3): p. 388-394.
224. Mosselmans, J.F.W., et al., *I18–the microfocus spectroscopy beamline at the Diamond Light Source.* Journal of synchrotron radiation, 2009. **16**(6): p. 818-824.
225. Zhang, Y., et al., *Towards in situ determination of 3D strain and reorientation in the interpenetrating nanofibre networks of cuticle.* Nanoscale, 2017. **9**(31): p. 11249-11260.
226. Karunaratne, A., et al., *Significant deterioration in nanomechanical quality occurs through incomplete extrafibrillar mineralization in rachitic bone: Evidence from in‐situ synchrotron X‐ray scattering and backscattered electron imaging.* Journal of Bone and Mineral Research, 2012. **27**(4): p. 876-890.
227. Karunaratne, A., et al., *Hypophosphatemic rickets is associated with disruption of mineral orientation at the nanoscale in the flat scapula bones of rachitic mice with development.* Bone, 2012. **51**(3): p. 553-562.
228. Hubbell, J.H. and S.M. Seltzer, *Tables of X-ray mass attenuation coefficients and mass energy-absorption coefficients 1 keV to 20 MeV for elements Z= 1 to 92 and 48 additional substances of dosimetric interest*. 1995, National Inst. of Standards and Technology-PL, Gaithersburg, MD (United States). Ionizing Radiation Div.

229. Fratzl, P., et al., *Position-resolved small-angle X-ray scattering of complex biological materials.* Journal of Applied Crystallography, 1997. **30**(5): p. 765-769.
230. Karunaratne, A., *Analysis of Alterations in Matrix Quality at Nanoscale in Metabolic Bone Diseases using Synchrotron X-ray Diffraction.* Queen mary, University of London, 2012.
231. Gupta, H.S., et al., *Cooperative deformation of mineral and collagen in bone at the nanoscale.* Proceedings of the National Academy of Sciences, 2006. **103**(47): p. 17741-17746.
232. Krauss, S., et al., *Inhomogeneous fibril stretching in antler starts after macroscopic yielding: Indication for a nanoscale toughening mechanism.* Bone, 2009. **44**(6): p. 1105-1110.
233. Gupta, H., et al., *Intrafibrillar plasticity through mineral/collagen sliding is the dominant mechanism for the extreme toughness of antler bone.* Journal of the mechanical behavior of biomedical materials, 2013. **28**: p. 366-382.
234. Paris, O., et al., *A new experimental station for simultaneous X-ray microbeam scanning for small-and wide-angle scattering and fluorescence at BESSY II.* Journal of Applied Crystallography, 2006. **40**: p. s466-s470.
235. Siegel, S., *Manual: Microfocus Beamline at BESSY.* 2008.
236. Blanton, T., C. Barnes, and M. Lelental, *Preparation of silver behenate coatings to provide low-to mid-angle diffraction calibration.* Journal of applied crystallography, 2000. **33**(1): p. 172-173.
237. Gupta, H.S., et al., *Nanoscale deformation mechanisms in bone.* Nano Letters, 2005. **5**(10): p. 2108-2111.
238. Gupta, H., et al., *Synchrotron diffraction study of deformation mechanisms in mineralized tendon.* Physical review letters, 2004. **93**(15): p. 158101.
239. Gupta, H., et al., *< i> In situ</i> multi-level analysis of viscoelastic deformation mechanisms in tendon collagen.* Journal of structural biology, 2010. **169**(2): p. 183-191.
240. Screen, H., et al., *Extrafibrillar diffusion and intrafibrillar swelling at the nanoscale are associated with stress relaxation in the soft collagenous matrix tissue of tendons.* Soft Matter, 2011. **7**(23): p. 11243-11251.
241. Gupta, H.S., et al., *Intrafibrillar plasticity through mineral/collagen sliding is the dominant mechanism for the extreme toughness of antler bone.* Journal Of the Mechanical Behavior Of Biomedical Materials, 2013. **28**: p. 366-382.
242. Price, R.I., S. Lees, and D.A. Kirschner, *X-ray diffraction analysis of tendon collagen at ambient and cryogenic temperatures: role of hydration.* International journal of biological macromolecules, 1997. **20**(1): p. 23-33.
243. Fratzl, P., N. Fratzl-Zelman, and K. Klaushofer, *Collagen packing and mineralization. An x-ray scattering investigation of turkey leg tendon.* Biophysical journal, 1993. **64**(1): p. 260-266.
244. Hukins, D. and J. Woodhead-Galloway, *Liquid-crystal model for the organization of molecules in collagen fibrils [proceedings].* Biochemical Society transactions, 1977. **6**(1): p. 238-239.
245. Purslow, P.P., T. Wess, and D. Hukins, *Collagen orientation and molecular spacing during creep and stress-relaxation in soft connective tissues.* Journal of Experimental Biology, 1998. **201**(1): p. 135-142.
246. Meyers, M.A., et al., *Biological materials: Structure and mechanical properties.* Progress In Materials Science, 2008. **53**(1): p. 1-206.
247. Weinkamer R, D.J., Brechet Y, & Fratzl P, *All but diamonds-Biological materials are not forever.* Acta Mater, 2013. **61**(3): p. 880-889.

248. Eyre, D.R., *Collagen: Molecular Diversity in the Body's Protein Scaffold.* Science, 1980. **207**(4437): p. 1315-1322.
249. Harrington, M.J., et al., *Iron-Clad Fibers: A Metal-Based Biological Strategy for Hard Flexible Coatings.* Science, 2010. **328**(5975): p. 216-220.
250. Fratzl, P., N. Fratzlzelman, and K. Klaushofer, *Collagen Packing And Mineralization - an X-Ray-Scattering Investigation Of Turkey Leg Tendon.* Biophysical Journal, 1993. **64**(1): p. 260-266.
251. Ciarletta, P. and M.B. Amar, *A finite dissipative theory of temporary interfibrillar bridges in the extracellular matrix of ligaments and tendons.* Journal of the Royal Society Interface, 2009. **6**(39): p. 909-924.
252. Julicher, F., A. Ajdari, and J. Prost, *Modeling molecular motors.* Reviews Of Modern Physics, 1997. **69**(4): p. 1269-1281.
253. Motokawa, T., *Connective-Tissue Catch In Echinoderms.* Biological Reviews Of the Cambridge Philosophical Society, 1984. **59**(2): p. 255-270.
254. Wilkie, I.C., *Variable Tensility In Echinoderm Collagenous Tissues - a Review.* Marine Behaviour And Physiology, 1984. **11**(1): p. 1-34.
255. Motokawa, T., *Effects of ionic environment on viscosity of Triton-extracted catch connective tissue of a sea cucumber body wall.* Comparative Biochemistry and Physiology Part B: Comparative Biochemistry, 1994. **109**(4): p. 613-622.
256. Motokawa, T. and A. Tsuchi, *Dynamic mechanical properties of body-wall dermis in various mechanical states and their implications for the behavior of sea cucumbers.* Biological Bulletin, 2003. **205**(3): p. 261-275.
257. Di Benedetto, C., et al., *Production, Characterization and Biocompatibility of Marine Collagen Matrices from an Alternative and Sustainable Source: The Sea Urchin Paracentrotus lividus.* Marine Drugs, 2014. **12**(9): p. 4912-4933.
258. Wilkie, I.C., et al., *Mechanical Properties of the Compass Depressors of the Sea-Urchin Paracentrotus lividus (Echinodermata, Echinoidea) and the Effects of Enzymes, Neurotransmitters and Synthetic Tensilin-Like Protein.* Plos One, 2015. **10**(3).
259. Birenheide, R. and T. Motokawa, *Contractile connective tissue in crinoids.* Biological Bulletin, 1996. **191**(1): p. 1-4.
260. Takemae, N., F. Nakaya, and T. Motokawa, *Low Oxygen Consumption and High Body Content of Catch Connective Tissue Contribute to Low Metabolic Rate of Sea Cucumbers.* Biological Bulletin, 2009. **216**(1): p. 45-54.
261. Jordan, H., *Die Holothurien als hohlorganartige Tiere und die Tonusfunktion ihrer Muskulatur.* Zool. Jahrb. Abt., 1914. **34**: p. 365-436.
262. Motokawa, T., *The stiffness change of the holothurian dermis caused by chemical and electrical stimulation.* Comparative Biochemistry and Physiology Part C: Comparative Pharmacology, 1981. **70**(1): p. 41-48.
263. Motokawa, T., *Factors regulating the mechanical properties of holothurian dermis.* Journal of Experimental Biology, 1982. **99**: p. 29-41.
264. Wilkie, I.C., M.D.C. Carnevali, and F. Bonasoro, *The Compass Depressors Of Paracentrotus-Lividus (Echinodermata, Echinoida) - Ultrastructural And Mechanical Aspects Of Their Variable Tensility And Contractility.* Zoomorphology, 1992. **112**(3): p. 143-153.
265. M, H. and T. K, *Fine structure and mechanical properties of the catch apparatus of the sea-urchin spine, a collagenous connective tissue with muscle-like holding capacity.* Journal of Experimental Biology, 1983. **103**(1): p. 1-14.
266. Diab, M. and W.F. Gilly, *Mechanical properties and control of non-muscular catch in spine ligaments of the sea urchin, Strongelocentrotus franciscanus.* Journal of Experimental Biology, 1984. **111**(1): p. 155-170.

267. Trotter, J.A. and T.J. Koob, *Collagen and proteoglycan in a sea urchin ligament with mutable mechanical properties.* Cell and tissue research, 1989. **258**(3): p. 527-539.
268. Trotter, J.A., et al., *Covalent composition of collagen fibrils from the dermis of the sea cucumber, Cucumaria frondosa, a tissue with mutable mechanical properties.* Comparative Biochemistry and Physiology a-Molecular & Integrative Physiology, 1995. **112**(3-4): p. 463-478.
269. Oji, T. and T. Okamoto, *Arm autotomy and arm branching pattern as anti-predatory adaptations in stalked and stalkless crinoids.* Paleobiology, 1994. **20**(1): p. 27-39.
270. Trotter, J.A., et al., *Growth of sea cucumber collagen fibrils occurs at the tips and centers in a coordinated manner.* Journal of Molecular Biology, 1998. **284**(5): p. 1417-1424.
271. Cluzel, C., et al., *Characterization of fibrosurfin, an interfibrillar component of sea urchin catch connective tissues.* Journal Of Biological Chemistry, 2001. **276**(21): p. 18108-18114.
272. Motokawa, T., *Factors Regulating the Mechanical-Properties of Holothurian Dermis.* Journal of Experimental Biology, 1982. **99**(Aug): p. 29-41.
273. Koob, T.J., M.M. Koob-Emunds, and J.A. Trotter, *Cell-derived stiffening and plasticizing factors in sea cucumber (Cucumaris frondosa) dermis.* Journal Of Experimental Biology, 1999. **202**(17): p. 2291-2301.
274. Tipper, J.P., et al., *Purification, characterization and cloning of tensilin, the collagen-fibril binding and tissue-stiffening factor from Cucumaria frondosa dermis.* Matrix biology, 2002. **21**(8): p. 625-635.
275. Ribeiro, A.R., et al., *Matrix Metalloproteinases in a Sea Urchin Ligament with Adaptable Mechanical Properties.* Plos One, 2012. **7**(11).
276. Cluzel, C., et al., *Distinct Maturations of N-propeptide Domains in Fibrillar Procollagen Molecules Involved in the Formation of Heterotypic Fibrils in Adult Sea Urchin Collagenous Tissues.* Journal Of Biological Chemistry, 2004. **279**: p. 9811-9817.
277. Zimmermann, E.A., et al., *Mechanical adaptability of the Bouligand-type structure in natural dermal armour.* Nature Communications, 2013. **4**.
278. Zimmermann, E.A., et al., *Age-related changes in the plasticity and toughness of human cortical bone at multiple length scales.* Proc Natl Acad Sci U S A, 2011. **108**(35): p. 14416-21.
279. Hulmes, D., et al., *Electron microscopy shows periodic structure in collagen fibril cross sections.* Proceedings of the National Academy of Sciences, 1981. **78**(6): p. 3567-3571.
280. Stock, S.R. and J.D. Almer, *Strains in bone and tooth via high energy X-ray scattering.* Bone, 2009. **44**(2): p. S270-S270.
281. Puxkandl, R., et al., *Viscoelastic properties of collagen: synchrotron radiation investigations and structural model.* Philosophical Transactions of the Royal Society of London B: Biological Sciences, 2002. **357**(1418): p. 191-197.
282. Gasser, T.C., et al., *Spatial orientation of collagen fibers in the abdominal aortic aneurysm's wall and its relation to wall mechanics.* Acta Biomaterialia, 2012. **8**(8): p. 3091-3103.
283. Linari, M., et al., *Force generation by skeletal muscle is controlled by mechanosensing in myosin filaments.* Nature, 2015. **528**(7581): p. 276-9.
284. Vincent, J.F., *Structural biomaterials*. 2012: Princeton University Press.
285. Narayanan, T., O. Diat, and P. Boesecke, *SAXS and USAXS on the high brilliance beamline at the ESRF.* Nuclear Instruments and Methods in Physics Research

Section A: Accelerators, Spectrometers, Detectors and Associated Equipment, 2001. **467**: p. 1005-1009.
286. Jeffries, C.M., et al., *Limiting radiation damage for high-brilliance biological solution scattering: practical experience at the EMBL P12 beamline PETRAIII.* Journal of Synchrotron Radiation, 2015. **22**: p. 273-279.
287. Hammersley, A., *FIT2D: an introduction and overview.* European Synchrotron Radiation Facility Internal Report, 1997. **68**.
288. Karunaratne, A., et al., *Significant deterioration in nanomechanical quality occurs through incomplete extrafibrillar mineralization in rachitic bone: evidence from in-situ synchrotron X-ray scattering and backscattered electron imaging.* J Bone Miner Res, 2012. **27**(4): p. 876-90.
289. Karunaratne, A., et al., *Multiscale alterations in bone matrix quality increased fragility in steroid induced osteoporosis.* Bone, 2016. **84**: p. 15-24.
290. Eppell, S.J., et al., *Nano measurements with micro-devices: mechanical properties of hydrated collagen fibrils.* Journal of the Royal Society Interface, 2006. **3**(6): p. 117-121.
291. Fratzl, P., *Collagen: structure and mechanics, an introduction*. 2008: Springer US.
292. Jager, I. and P. Fratzl, *Mineralized collagen fibrils: A mechanical model with a staggered arrangement of mineral particles.* Biophysical Journal, 2000. **79**(4): p. 1737-1746.
293. Gao, H.J., et al., *Materials become insensitive to flaws at nanoscale: Lessons from nature.* Proceedings of the National Academy of Sciences of the United States of America, 2003. **100**(10): p. 5597-5600.
294. Fratzl, P., *Nature's hierarchical materials.* Nature's hierarchical materials, 2007. **52**(8): p. 1263–1334.
295. Masic, A., et al., *Osmotic pressure induced tensile forces in tendon collagen.* Nature Communications, 2015. **6**: p. 5942.
296. Scott, J.E., *Proteoglycan: collagen interactions and subfibrillar structure in collagen fibrils. Implications in the development and ageing of connective tissues.* Journal of Anatomy, 1990. **169**: p. 23-35.
297. Ottani, V., M. Raspanti, and A. Ruggeri, *Collagen structure and functional implications.* Micron, 2001. **32**(3): p. 251-260.
298. Bell, J., et al., *The hierarchical response of human corneal collagen to load.* Acta biomaterialia, 2018. **65**: p. 216-225.
299. Elphick, M.R., *The protein precursors of peptides that affect the mechanics of connective tissue and/or muscle in the echinoderm Apostichopus japonicus.* Plos One, 2012. **7**(8).
300. Motokawa, T., *The stiffness change of the holothurian dermis caused by chemical and electrical stimulation.* Comp Biochem Physiol C, 1981. **70**(1): p. 41-8.
301. Eylers, J.P., *Ion-dependent viscosity of holothurian body wall and its implications for the functional morphology of echinoderms.* Journal of Experimental Biology, 1982. **99**(1): p. 1-8.
302. Shibayama, R., et al., *Stiffness changes of holothurian dermis induced by mechanical vibration.* Zoological science, 1994. **11**(4): p. 511-515.
303. Greenberg, A. and J. Eylers, *Influence of ionic environment on the stress relaxation behavior of an invertebrate connective tissue.* Journal of biomechanics, 1984. **17**(3): p. 161-166.
304. Trivedi, D., et al., *Soft robotics: Biological inspiration, state of the art, and future research.* Applied Bionics and Biomechanics, 2008. **5**(3): p. 99-117.

305. Hill, R., *A self-consistent mechanics of composite materials.* Journal of the Mechanics and Physics of Solids, 1965. **13**(4): p. 213-222.
306. Laws, N. and R. McLaughlin. *Self-consistent estimates for the viscoelastic creep compliances of composite materials*. in *Proceedings of the Royal Society of London A: Mathematical, Physical and Engineering Sciences*. 1978. The Royal Society.
307. Sasaki, N. and S. Odajima, *Elongation mechanism of collagen fibrils and force-strain relations of tendon at each level of structural hierarchy.* J Biomech, 1996. **29**(9): p. 1131-6.
308. Antipova, O. and J.P.R.O. Orgel, *In Situ D-periodic Molecular Structure of Type II Collagen.* The Journal of Biological Chemistry, 2010. **285**(10): p. 7087-7096.
309. Cullity, B. and S. Stock, *Elementary of X-ray Diffraction.* Englewood Cliffs, 3rd, 2001.
310. Eshelby, J.D. *The determination of the elastic field of an ellipsoidal inclusion, and related problems*. in *Proceedings of the Royal Society of London A: Mathematical, Physical and Engineering Sciences*. 1957. The Royal Society.
311. Screen, H.R.C., *Investigating load relaxation mechanics in tendon.* Journal of the Mechanical Behavior of Biomedical Materials, 2008. **1**(1): p. 51-58.
312. Machiraju, C., et al., *Viscoelastic studies of human subscapularis tendon: relaxation test and a Wiechert model.* Computer methods and programs in biomedicine, 2006. **83**(1): p. 29-33.
313. Balooch, M., et al., *Viscoelastic properties of demineralized human dentin measured in water with atomic force microscope (AFM)-based indentation.* Journal of biomedical materials research, 1998. **40**(4): p. 539-544.
314. Thorpe, C.T., et al., *Specialization of tendon mechanical properties results from interfascicular differences.* Journal of The Royal Society Interface, 2012: p. rsif20120362.
315. Thorpe, C.T., et al., *The interfascicular matrix enables fascicle sliding and recovery in tendon, and behaves more elastically in energy storing tendons.* Journal of the mechanical behavior of biomedical materials, 2015. **52**: p. 85-94.
316. Gupta, H., et al., *In situ multi-level analysis of viscoelastic deformation mechanisms in tendon collagen.* Journal of structural biology, 2010. **169**(2): p. 183-191.
317. Wilkie, I., *Design for disaster: the ophiuroid intervertebral ligament as a typical mutable collagenous structure.* Echinoderm biology, 1988: p. 25-38.
318. Feinberg, A.W., *Biological Soft Robotics.* Annual Review of Biomedical Engineering, 2015. **17**(1): p. 243-265.
319. Stuart, M.A., et al., *Emerging applications of stimuli-responsive polymer materials.* Nat Mater, 2010. **9**(2): p. 101-13.
320. Jeong, B. and A. Gutowska, *Lessons from nature: stimuli-responsive polymers and their biomedical applications.* Trends in biotechnology, 2002. **20**(7): p. 305-311.
321. Osada, Y. and J. Gong, *Stimuli-responsive polymer gels and their application to chemomechanical systems.* Progress in Polymer Science, 1993. **18**(2): p. 187-226.
322. Holtz, J.H. and S.A. Asher, *Polymerized colloidal crystal hydrogel films as intelligent chemical sensing materials.* Nature, 1997. **389**(6653): p. 829.
323. Bae, Y.H., T. Okano, and S.W. Kim, *Insulin permeation through thermo-sensitive hydrogels.* Journal of Controlled Release, 1989. **9**(3): p. 271-279.
324. Wijnen, B., et al., *Open-source syringe pump library.* PLoS One, 2014. **9**(9): p. e107216.

325. Heim, A.J., W.G. Matthews, and T.J. Koob, *Determination of the elastic modulus of native collagen fibrils via radial indentation.* Applied physics letters, 2006. **89**(18): p. 181902.

Appendix

1. **Tolerance test for tissue strain ε_T:**

   I estimated the error by considering it to have two sources: error in the measurement of gauge length of sample, and error in the determination of incremental length movement during the tensile deformation. The length increment is applied by the PI DC-motor with encoder, and the gauge length via measurement by Vernier callipers.

   - $\Delta L0$ = error in Vernier callipers = 0.01 mm; L0 = 3 mm
   - Δ movement of PI motor = precision in micron of PI stage=0.1 µm; Total movement = 45 µm (calculated from 1.5/100 * 3 mm)
   - error in ε_T = (Δ movement of PI motor/ movement) + ($\Delta L0/L0$) = 0.0001 mm /0.045 mm + 0.01 mm /3 mm=0.005=0.5%

2. **Initial estimation of Φ_1 and E_{IF}:**

Equations (1) and (2) in the main text are reproduced below with additions:

$$\frac{\varepsilon_T}{\varepsilon_F} = 1 + \frac{4}{\rho_1^2}\frac{1-\Phi_1}{\Phi_1}\frac{E_F}{\gamma_{IF}E_{IF}} \qquad \textbf{Equation S1}$$

$$E_T = \Phi_1 E_F \frac{\varepsilon_F}{\varepsilon_T} + (1-\Phi_1)E_{IF} = \frac{\Phi_1 E_F}{1 + \frac{4}{\rho_1^2}\frac{1-\Phi_1}{\Phi_1}\frac{E_F}{\gamma_{IF}E_{IF}}} + (1-\Phi_1)E_{IF} \quad \textbf{Equation S2}$$

From Figure 4 it is observed that $\varepsilon_F/\varepsilon_T$ is of the order of 0.01, hence

$$\frac{\varepsilon_T}{\varepsilon_F} \sim 100 >> 1 \qquad \textbf{Equation S3}$$

Hence, we can neglect the "1" term in Equation (1), leading to

$$\frac{\varepsilon_T}{\varepsilon_F} \approx \left(\frac{4}{\rho_1^2} \frac{1-\Phi_1}{\Phi_1} \frac{1}{\gamma_{IF} E_{IF}} \right) E_F$$ **Equation S4**

$$\frac{\varepsilon_F}{\varepsilon_T} \approx \left(\frac{\rho_1^2}{4} \frac{\Phi_1}{1-\Phi_1} \frac{\gamma_{IF}}{E_F} \right) E_{IF}$$ **Equation S4'**

The above amounts to approximating:

$$1 + \frac{4}{\rho_1^2} \frac{1-\Phi_1}{\Phi_1} \frac{E_F}{\gamma_{IF} E_{IF}} \approx \frac{4}{\rho_1^2} \frac{1-\Phi_1}{\Phi_1} \frac{E_F}{\gamma_{IF} E_{IF}}$$ **Equation S5**

As estimates for fibril modulus E_F = 600 MPa and experimental values for $\varepsilon_F/\varepsilon_T \sim 0.01$ are known, the term in parentheses below can be estimated as

$$\left(\frac{\rho_1^2}{4} \frac{\Phi_1}{1-\Phi_1} \gamma_{IF} E_{IF} \right) \approx \frac{E_F}{100}$$ **Equation S6**

where the RHS is a known quantity. In an analogous manner, the approximation in **Equation S5** can be used in **Equation S2** to get:

$$E_T = \frac{\Phi_1 E_F}{1 + \frac{4}{\rho_1^2} \frac{1-\Phi_1}{\Phi_1} \frac{E_F}{\gamma_{IF} E_{IF}}} + (1-\Phi_1) E_{IF} \approx \frac{\Phi_1 E_F}{\frac{4}{\rho_1^2} \frac{1-\Phi_1}{\Phi_1} \frac{E_F}{\gamma_{IF} E_{IF}}} + (1-\Phi_1) E_{IF}$$

$$\Rightarrow E_T \approx \left(\frac{\rho_1^2 \Phi_1 \gamma_{IF} E_{IF}}{4(1-\Phi_1)} \right) \Phi_1 + (1-\Phi_1) E_{IF}$$

Equation S7

The expression in parentheses in the last line is the same as that estimated in **Equation S6**. Further, as the aspect ratio $\rho_1 >> 1$, the 1st term on the second line is much larger than the second term, which can be neglected:

$$E_T \approx \left(\frac{\rho_1^2 \Phi_1 \gamma_{IF} E_{IF}}{4(1-\Phi_1)} \right) \Phi_1 = \frac{E_F}{100} \Phi_1$$ **Equation S8**

where **Equation S6** has been used in the last step. Since the tissue modulus (or tangent modulus) is known to be $E_T \sim 3.23$ MPa for ASW (Figure 4, main text), and $E_F \sim 600$ MPa, an estimate for the fibril volume fraction is obtained:

$$\Phi_1 \approx \frac{100E_T}{E_F} = 0.54 \qquad \textbf{Equation S9}$$

Using this value for Φ_1 in **Equation S6**, along with estimates of the fibril aspect ratio $\rho_1 \sim 1000$ and the numerical pre-factor $\gamma_{IF} = 0.4$, an estimate for the interfibrillar modulus E_{IF} is obtained:

$$E_{IF} \approx \frac{E_F}{100}\frac{4(1-\Phi_1)}{\Phi_1\rho_1^2\gamma_{IF}} \qquad \textbf{Equation S10}$$

leading to $E_{IF} \sim 50 \times 10^{-6}$ MPa.

From the foregoing, the required estimates for fibril volume fraction Φ_1 and interfibrillar modulus E_{IF} are obtained.

3. Sensitivity of fibril strain ratio and tissue modulus to model parameters:

Variation in aspect ratio ρ:

Fibril strain ratio $\varepsilon_F/\varepsilon_T$: By taking a differential of the inverse of **Equation S1**, we obtain

$$\Delta\left(\frac{\varepsilon_F}{\varepsilon_T}\right) = \Delta\left(\frac{1}{1+\frac{4}{\rho_1^2}\frac{1-\Phi_1}{\Phi_1}\frac{E_F}{\gamma_{IF}E_{IF}}}\right) \approx \Delta\left(\frac{\rho_1^2\Phi_1\gamma_{IF}E_{IF}}{4(1-\Phi_1)E_F}\right) = \frac{2\Delta\rho_1}{\rho_1}\left(\frac{\rho_1^2\Phi_1\gamma_{IF}E_{IF}}{4(1-\Phi_1)E_F}\right) \approx \frac{2\Delta\rho_1}{\rho_1}\left(\frac{\varepsilon_F}{\varepsilon_T}\right)$$

where the approximation sign is because (for all experimentally observed fibril strain ratios), $\varepsilon_F/\varepsilon_T << 1$ as stated in the main text, and as a result $1 << \frac{4}{\rho_1^2}\frac{1-\Phi_1}{\Phi_1}\frac{E_F}{\gamma_{IF}E_{IF}}$ and can be neglected. Hence, we have

$$\frac{\Delta\left(\frac{\varepsilon_F}{\varepsilon_T}\right)}{\left(\frac{\varepsilon_F}{\varepsilon_T}\right)} \approx 2\frac{\Delta\rho_1}{\rho_1}$$

As a result, a 10% variation in aspect ratio will lead to a 20% variation in the fibril strain ratio. This relatively large variation with aspect ratio is expected on physical grounds, as increased aspect ratio will increase the interfacial area over which shear stress will be transferred to the fibril.

Tissue modulus E_T: Using **Equation S2**, we have:

$$\Delta E_T = \Delta\left(\frac{\Phi_1 E_F}{1+\frac{4}{\rho_1^2}\frac{1-\Phi_1}{\Phi_1}\frac{E_F}{\gamma_{IF}E_{IF}}} + (1-\Phi_1)E_{IF}\right) \approx \Delta\left(\frac{\rho_1^2\Phi_1\gamma_{IF}E_{IF}}{4(1-\Phi_1)E_F}\Phi_1 E_F + (1-\Phi_1)E_{IF}\right)$$

(using the same approximation for the denominator as above):

$$\Delta E_T \approx \Delta\left(\left[\frac{\rho_1^2\Phi_1^2\gamma_{IF}}{4(1-\Phi_1)} + (1-\Phi_1)\right]E_{IF}\right)$$

Considering the first term within rectangular parentheses on the RHS, because $\rho_1 >> 1$ while the other terms are of the order of 1 ($\Phi_1 \sim 0.54$ and $\gamma_{IF} = 0.4$), it is clear that the first term will be much larger than the second term which can be neglected in comparison. We obtain

$$\Delta E_T \approx \Delta\left(\frac{\rho_1^2\Phi_1^2\gamma_{IF}}{4(1-\Phi_1)}E_{IF}\right)$$

As a result, on a variation in aspect ratio ρ_1 we have – similar to $\varepsilon_F/\varepsilon_T$ –

$$\frac{\Delta E_T}{E_T} \approx 2\frac{\Delta \rho_1}{\rho_1}$$

with the similar consequence that a 10% variation in aspect ratio will lead to a 20% variation in the fibril strain ratio.

Variation in fibril volume fraction Φ_1:

Fibril strain ratio $\varepsilon_F/\varepsilon_T$: Similarly, we can show that

$$\Delta\left(\frac{\varepsilon_F}{\varepsilon_T}\right) \approx \Delta\left(\frac{\rho_1^2 \Phi_1 \gamma_{IF} E_{IF}}{4(1-\Phi_1)E_F}\right) = \frac{\Delta\Phi_1}{\Phi_1(1-\Phi_1)}\left(\frac{\rho_1^2 \Phi_1 \gamma_{IF} E_{IF}}{4(1-\Phi_1)E_F}\right) \approx \frac{\Delta\Phi_1}{\Phi_1(1-\Phi_1)}\left(\frac{\varepsilon_F}{\varepsilon_T}\right)$$

Therefore, at a fibril volume fraction of Φ_1~0.54, a 10% variation in volume fraction leads to a ~21.7% variation in fibril strain ratio.

Tissue modulus E_T: Similarly, we can show that

$$\Delta E_T \approx \left(\frac{\rho_1^2\left(2\Phi_1 - \Phi_1^2\right)\gamma_{IF}}{4(1-\Phi_1)^2} E_{IF}\Delta\Phi_1\right) = \left(\frac{\rho_1^2 \gamma_{IF}\Phi_1^2}{4(1-\Phi_1)} E_{IF}\right)\Delta\Phi_1\left(2\Phi_1 - \Phi_1^2\right)\frac{1}{(1-\Phi_1)\Phi_1^2}$$

$$\frac{\Delta E_T}{E_T} = \frac{\Delta\Phi_1}{\Phi_1}\frac{(2-\Phi_1)}{(1-\Phi_1)}$$

which implies that a 10% variation of fibril volume fraction (initial volume fraction of Φ_1~0.54) leads to a 31.7% variation in tissue modulus. This high rate of variation highlights the increased efficiency of the fibrils in reinforcing the tissue (and increasing the modulus).

4. From ε_{T0} to ε_T:

The incremental strain due to a small increase in stress is defined as the ratio of the differential increase in length to the sample length. The

total strain is, therefore, the sum of all these incremental strains. When the sample length does not change significantly over the course of the test, the total strain can therefore be approximated as the change in length divided by the *original* length, which is the engineering tissue strain ε_{T0}:

$$\varepsilon_{T0} = \frac{l_1 - l_0}{l_0}$$

where l_1 is the final length and l_0 the initial length. This approximation will not hold if the sample length does change significantly over the course of the test, as occurs in many soft biological tissues. For this case, the exact definition of strain (true strain ε_T) is the sum of all the incremental strains, defined by the integral:

$$\varepsilon_T = \int_{l_0}^{l_f} \frac{dl}{l} = \ln\left(\frac{l_f}{l_0}\right) = \ln\left(\frac{l_0(1+\varepsilon_{T0})}{l_0}\right) = \ln(1+\varepsilon_{T0})$$

where in the last step the definition for engineering strain is used.

5. $\varepsilon_F/\varepsilon_T$ for each individual sample

Ionic treatment	Sample index	Fit estimate of $\varepsilon_F/\varepsilon_T$ [no units]	Std. error of $\varepsilon_F/\varepsilon_T$ estimate [no units]
ASW	1	0.0074	0.0003
	2	0.0039	0.0002
	3	0.0042	0.0003
	4	0.0007	0.0003
KASW	5	0.0166	0.0018
	6	0.1060	0.0068
	7	0.0032	0.0011
	8	0.0166	0.0015

CAF	9	9.36E-05	0.0003
	10	0.0018	0.0004
	11	0.0010	0.0005

6. Radial intensities of different meridional Bragg peaks in I(q):

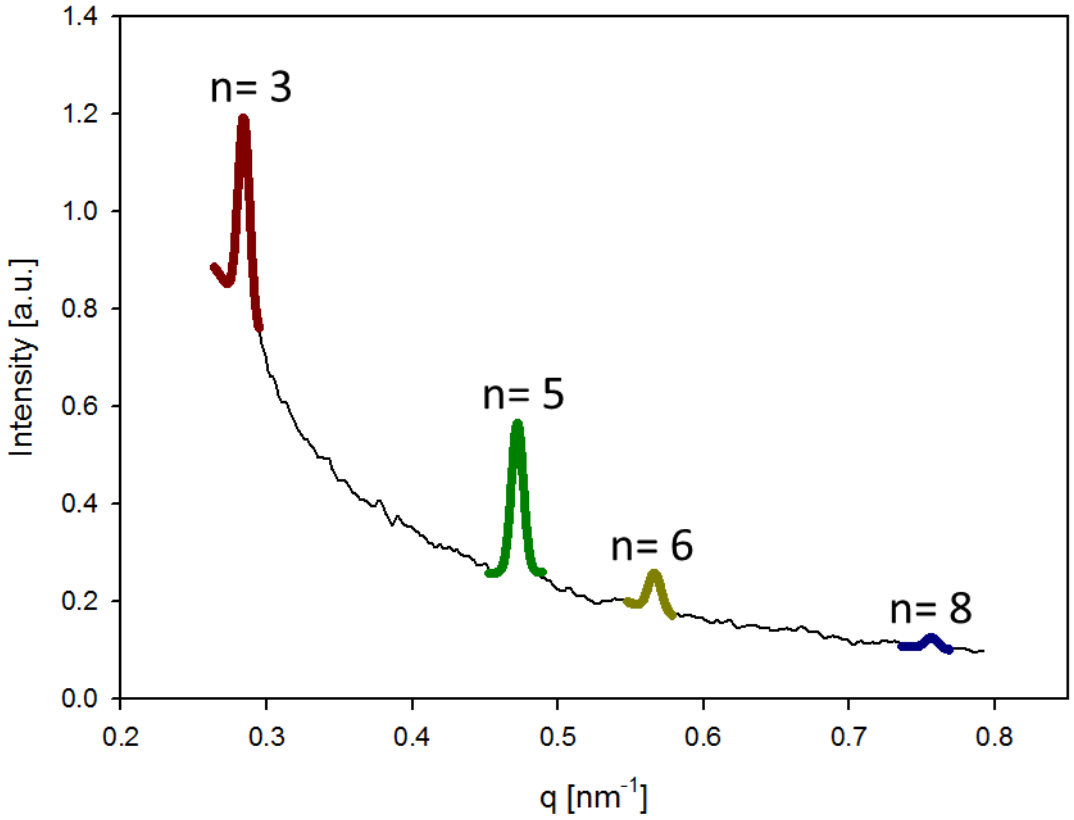

Figure S1: *Radial intensity profile I(q) for sea cucumber dermis, with wavevector ranging from 0.26 to 0.79 nm^{-1}, showing all visible peaks (3rd, 5th , 6th and 8th).*

As the 5th peak has the highest peak intensity, the peak fitting is most accurate when using the 5th order rather than a much weaker peak such as the 6th order.

Further, it is also not as close to the primary beam and the region of strong diffuse background scattering compared to the lower Bragg orders like n = 2 or 3. As seen in the **Figure S1** above, at low orders,

the background intensity is strongly nonlinear as a function of wavevector q. As a result, it is more difficult to subtract the background for such lower orders, and the fit function used here (Gaussian and linear background) does not fit the data as well.

Lastly, the 5^{th} order peak is also better for measuring peak shifts than lower Bragg orders (e.g. 3) because the shift in the peak due to fibril strain is linearly proportional to the order. I.e. the 5^{th} order will shift by $-5(2\pi/D_0)\varepsilon_F$, compared to $3(2\pi/D_0)\varepsilon_F$ for the 3^{rd} order. As the detection of larger peak shifts via peak fitting is more accurate compared to smaller peak shifts, this makes determination of fibril strain from peak shifts more accurate when using the 5^{th} order peak compared to the 3^{rd} order.

7. Figure SI 2: Spread of I(χ) data with three different number of bins

In order to show that the choice of the number of bins does not significantly affect the fitted curve, we have plotted the azimuthal intensity profile for the same SAXD pattern with three different choices of bin numbers: 300, 150 and 75. Concurrently, the fitted curve for each I(χ) data set, along with the fit parameters, is shown in **Figure S2**. It can be seen that the fitted curves overlap very well, and that the fit parameters are nearly identical for the choice of the different bins. This result indicates that choice of different bin numbers does not alter the fit results.

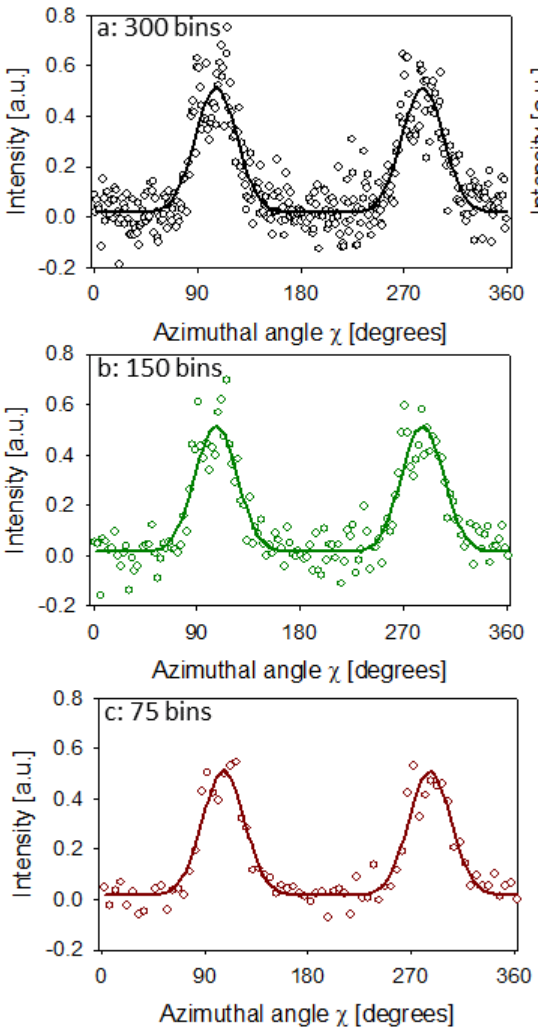

Fit parameters

Number of bins	$I_{0\chi}$ [a.u.]	$\Delta\chi_0$ [deg.]	χ_0 [deg.]	I_0
300	0.49	18.21	106.29	0.016
150	0.50	18.35	106.76	0.014
75	0.49	18.39	106.37	0.016

Figure S2*: Left (a)-(c): Plots of azimuthal intensity profiles I(χ) for a single SAXD pattern with three different numbers of azimuthal bins, along with the fits to the model function of 2 Gaussians with a constant. (d) Superimposition of the fit functions for (a)-(c), showing that the functions are close to identical. (e) Likewise, the fit parameters for the model function are shown in the Table below to be very similar.*